INVERTED MICELLES: A NOVEL METHOD OF THERANOSTIC AGENT ENCAPSULATION FOR ENHANCED NANO-DELIVERY

BY

ENRIQUE ALEJANDRO DAZA

DISSERTATION

Submitted in fulfillment of the requirements
for the degree of Science in Bioengineering
in the Graduate College of the
University of Illinois at Urbana-Champaign, 2018

Urbana, Illinois

Doctoral Committee:

Professor Dipanjan Pan, Chair and Director of Research
Professor Joseph Irudayaraj
Professor Wawrzyniec Dobrucki
Professor Gregory H. Underhill

Abstract

This thesis outlines an innovative solution for packaging an expansive set of theranostic agents for high-throughput intracellular delivery, which offers numerous advantages over liposomes and other contemporary encapsulation modalities. This encapsulation method works by using a simple 2-step phase-transfer chemistry. The first step consists of enveloping the agents within an inverted micelle capsule, and in the second step, they are repackaged with an outer lipid-based shell to produce a structure termed the NanoCapsule (NCAP).

Our encapsulation procedure is adaptable and robust, with modifiable size, chemistry, and surface properties and it is compatible with agents such as ions, small molecules, and ~10 nm nanoparticles. This method greatly simplifies hydrophobic encapsulation and surface modification, which is otherwise a costly and technically challenging procedure that relies on anaerobic reactions in an organic medium. Our encapsulation procedure can also be scaled with high-throughput efficacy. Furthermore, the inverted micelles and NCAP coating consist of materials that have been shown to provide excellent biocompatibility.

With this methodology, agents are encapsulated without a significant amount of aqueous solvent in the lumen of the nanoparticle, thus, delivering a more concentrated and stable payload to the tumor site without the leaky tendencies of liposomal encapsulation. Within this thesis, we show how the NCAP architecture retains long-term stability and quantifiably enhances payload delivery intracellularly through *in vitro* and *in vivo* investigations. Furthermore, the highly customizable nature of our encapsulation methodology is especially desirable for theranostic applications in personalized medicine. Therefore, our strategy could become a widely-used

methodology for encapsulating and delivering personalized theranostics, customized to match precise therapeutic needs.

Keywords: Nanomedicine, Nanoparticles, Inverted Micelles, Theranostics, Drug Delivery, Nano-Delivery.

Acknowledgements

The author would like to acknowledge his advisor Professor Dipanjan Pan, as well as all post docs, graduate students, undergrads, and fellows that are, or have been, a part of the Pan Lab. The author would also like to acknowledge his family, mentors (such as Santosh K. Misra), and all supporters of the author's endeavors, as well as financial support from the University of Illinois at Urbana-Champaign, the Institute for Sustainability, Energy, and Environment, and the Children's Discovery Institute. Many characterization techniques were carried out in part in the Frederick Seitz Materials Research Laboratory Central Research Facilities, University of Illinois. Lastly, none of this would have been possible without caffeine, Soylent, polyphasic sleep cycles, and Google.

This thesis is hereby dedicated to my fellow engineer

and brother, Brandon Alan Clore. May we go out into

the world and be successful.

TABLE OF CONTENTS

Abbreviations and Acronyms ix

List of Figures xiii

List of Equations xxiii

Chapter 1: Introduction 1

Introduction 2

Specific Aims 12

References to Introduction 16

Chapter 2: Nano-Cesium for Anti-Cancer Properties: An Investigation into Cesium Induced Metabolic Interference 22

Abstract 23

Introduction 24

Results and Discussion 26

Conclusion 77

Methods 78

References to Chapter 2 88

Chapter 3: Combinatorial Nanoencapsulation of Silver Ions via Levofloxacin Prodrug for Bactericidal Applications 95

Abstract 96

Introduction 97

Results and Discussion 98

Conclusion 120

Methods 121

Author Contributions 124

References to Chapter 3 125

Chapter 4: Nanocapsulation for Improved Intracellular Delivery of Hydrophilic Agents 128

Abstract 129

Introduction 131

Results and Discussion 133

Conclusion 155

Methods 156

References to Chapter 4 160

Chapter 5: A Facile Chemical Strategy to Hydrophobically Modify Solid Nanoparticles using Inverted Micelles for Efficient Intracellular Delivery 162

Abstract 163

Introduction 164

Results and Discussion 166

Conclusion 202

Methods 203

References to Chapter 5 208

Chapter 6: Conclusion 215

Final Note 218

References to Conclusion 220

ABBREVIATIONS AND ACRONYMS

2-NBDG	2-deoxy-2-[(7-nitro-2,1,3-benzoxadiazol-4-yl)amino]-D-glucose
ζ	Electrophoretic Potential or Zeta Potential
AI-Pro-NP	Ag^{+} Ion – Prodrug - Nanoparticle
AFM	Atomic Force Microscopy
Ag	Silver
AI-NP	Ag Ion-Nanoparticle
ATG	Autophagy-Related Proteins
ATP	Adenosine Triphosphate
AuNP	Gold Nanoparticles
BHI	Heart Infusion Broth
CB	Cytochalasin B
CNP	Carbon Nanoparticle
CP	Control Particle
Cs	Cesium
CsCl	Cesium Chloride
D_{ah}	Anhydrous Diameter
DCFH-DA	2', 7'-Dichlorodihydrofluorescein Diacetate
D_{hy}	Hydrodynamic Diameters
DLS	Dynamic Light Scattering
DMSO	Dimethyl Sulfoxide
DOG	2-Deoxyglucose
dPBS	Dulbecco's Phosphate Buffered Saline

EDC	N-(3-dimethylaminopropyl)-N′-ethylcarbodiimide hydrochloride
EDS	Energy Dispersive X-ray Spectroscopy
EDX	Energy Dispersive X-ray
EPR	Enhanced Permeability and Retention Effect
FBS	Fetal Bovine Serum
FTIR	Fourier Transform Infrared
FITC	Fluorescein Isothiocyanate
Gd-DTPA	Gadopentetic Acid
GLUT	Glucose Transport Proteins
H&E	Hematoxylin and Eosin
IM-AuNP	Inverted Micelle Encapsulated Gold Nanoparticles
IACUC	Institutional Animal Care and Use Committee
ICP-OES	Inductively Coupled Plasma Optical Emission Spectrometry
MRI	Magnetic Resonance Imaging
MTT	3-(4,5-dimethylthiazole-2-yl)-2,5-diphenyltetrazolium bromide
MWCO	Molecular Weight Cut Off
NaN_3	Sodium Azide
NanoCs	Nanoparticle of Ionic Cesium
NCAP	NanoCapsule
NIH	National Institutes of Health
NIR	Near-infrared spectrum
NMC	Nano-MultiCapsule
NMC-AuNP	Nano-MultiCapsule Gold Nanoparticle

NMC-CNP	Nano-MultiCapsule Carbon Nanoparticle
NMC-AgNP	Nano-MultiCapsule Silver Nanoparticle
PALS	Phase Analysis Light Scattering
PC	Phosphatidylcholine
PCD	Programmed Cell Death
PCL-*b*-P2VP	Copolymer (ϵ-caprolactone)-*block*-poly(2-vinyl pyridine)
PDI	Polydispersity Index
PE	1,2-dioleoyl-*sn*-glycero-3-phosphatidylethanolamine
PEG	Polyethylene Glycol
PEGCE	Polyethylene Glycol Cetyl Ether
PEI	Polyethyleneimine
PI	Propidium Iodide
PIPR	Pixel Intensity Peak Ratio
PLGA	Poly(lactide-co-glycolide)
ppm	Part per Million
PS	Phosphatidylserine
PtIr	Platinum–Iridium
F-PE	Fluorescent lipid 1,2-Dioleoyl-sn-Glycero-3-Phosphoethanolamine-N-(Carboxyfluorescein)
RES	Reticuloendothelial System
RFU	Relative Fluorescent Unit
RME	Receptor Mediated Endocytosis
ROS	Reactive Oxygen Species

SAXS	Small Angle X-Ray Scattering
SEM	Scanning Electron Microscopy
TEM	Transmission Electron Microscopy
THF	Tetrahydrofuran
VEGFR	Vascular Endothelial Growth Factor Receptor
SNARF-1	Seminaphtharhodafluor

LIST OF FIGURES

Figure 2.1: Schematic representation of NanoCs synthesis. Cs^+ ions interact with negatively charged acrylic acid groups in the particle. 29

Figure 2.2: Bar graph representation of Cs^+ entrapment optimization via hydrodynamic diameter analysis. 30

Figure 2.3: Overlaid histogram representing the number averaged (%) of CP and NanoCs particles. 31

Figure 2.4: EDS analysis on (a) CP and (b) NanoCs to identify cesium peaks (shown with black arrow). 32

Figure 2.5: SEM image of NanoCs used for EDS. 33

Figure 2.6: a) NanoCs Cesium release profile over the course of three days as measured by ICP-OES in parts per million (ppm). b) Percent of cesium released as a function of time. 34

Figure 2.7: Surface charge as measured by Zeta potential of CP and NanoCs. Student's T test was used to measure statistical significance ($p< 0.05$). 35

Figure 2.8: TEM micrograph of CP. Within the figure is an inset of a particle at higher magnification for detail. 36

Figure 2.9: TEM micrograph of NanoCs. Black arrow shows cesium collection within NanoCs particle. Within the figure is an inset of a particle at higher magnification for detail. 36

Figure 2.10: ImageJ analysis of anhydrous particle diameter (n=100). 37

Figure 2.11: Long term shelf life stability analysis (measured over 30 days) of CP and NanoCs hydrodynamic diameter. X-axis is in Log_2 scale. 38

Figure 2.12: Hydrodynamic diameter stability of CP in various environments measured over the course of seven days. 39

Figure 2.13: Hydrodynamic diameter stability of NanoCs in various environments measured over the course of seven days. 40

Figure 2.14: FTIR analysis of CP composition. (a) Near-mid infrared spectrum of respective samples. (b) Near-infrared spectrum close up of black boxed outline in (a). Peaks are assigned to common molecular structures found in CP particles. 41

Figure 2.15: FTIR analysis of NanoCs composition. (a) Near-mid infrared spectrum of respective samples. (b) Near-infrared spectrum close up of black boxed outline in (a). Peaks are assigned to common molecular structures found in NanoCs particles. 42

Figure 2.16: Raman analysis of (a) CP and (b) NanoCs composition. Peaks are assigned to common molecular structures found in CP particles. 43

Figure 2.17: ImageJ analysis of pixel intensity of particles TEM micrographs (white pixel = high intensity, black pixel = low intensity). 44

Figure 2.18: AFM plot of anhydrous NanoCs particles. 45

Figure 2.19: Bright field images of MCF-7 cells at 20X. The treatment concentration is 62.5 µM (Scale bar: 50 µm). 47

Figure 2.20: Cell viability of NanoCs, CP, and CsCl as a percent ratio to control cells. Concentrations of NanoCs were treated in molar equivalence to CsCl, and CP was treated in volume equivalence to NanoCs. 48

Figure 2.21: Bar graph detailing IC_{50} values of NanoCs as compared to CsCl alone (t-test for significance, $p<<0.01$). 49

Figure 2.22: Investigations of NanoCs mechanism of cellular internalization. a) Control cells treated with inhibitors of various endocytic pathways. b) Cells treated with endocytic inhibitors for 1h followed by incubation with NanoCs particles for 24 h. 51

Figure 2.23: Dot plot of CsCl concentration versus pH when added to pH 4 water. 53

Figure 2.24: SNARF-1 AM structure. 55

Figure 2.25: SNARF-1 confocal images and pixel intensity peak analysis of MCF-7 and MCF-10A for investigations into possible CsCl induced pH change. (a-h) Confocal images of MCF-7 cells loaded with SNARF-1 and treated with respective samples at 100 µM of CsCl concentration equivalence. b, d, f, h, and j is each treatment's unmodified pixel intensity with calculated peak ratios. (i, j) Positive control of SNARF-1 loaded MCF-10A cells (non-cancerous cell line) with a physiologically higher intracellular pH. 56

Figure 2.26: Bar chart of respective samples PIPR value. 57

Figure 2.27: RFU analysis of 2-NBDG uptake by MCF-7 cells at various concentrations of NanoCs, CsCl, CP, and CB. 60

Figure 2.28: Absorbance graph of 2-NBDG loaded and lysed MCF-7 cells treated at various concentrations with respective samples for 4 hours. 61

Figure 2.29: Flow cytometry RFU histogram of MCF-7 cells treated with respective samples. . 63

Figure 2.30: Differential interference contrast microscopy images and confocal images of MCF-7 cells treated with respective samples and then exposed to 10 µM 2-NBDG for four hours. Final image per row is an overlay including DAPI stain. White arrows indicate localized glucose storage in intracellular vesicles (63X Objective, Scale bar: 20 µm). 64

Figure 2.31: Bar graph of average per cell pixel intensity of confocal 2-NBDG emission only as measured by ImageJ (t-test of NanoCs and CB to CsCl, $p<<0.01$). 65

Figure 2.32: ROS Standard curve in Log_{10} form for assessing actual ROS content within cells. 67

Figure 2.33: Graph depicting intracellular ROS content of 10k cells post four-hour exposure to respective samples at varying concentrations. Control values were subtracted from each data point to eliminate the physiological ROS concentrations from the data set. 68

Figure 2.34: Flow cytometry RFU histogram analysis of apoptotic cells labeled with Annexin V-FITC. 70

Figure 2.35: Flow cytometry dot plot of (a) control cells and (b) NanoCs treated cells plotted as Annexin V-FITC intensity (x-axis) versus PI intensity (y-axis). 71

Figure 2.36: *In vivo* tumor regression analysis post NanoCs injections in xenograft mouse model. Formulations were injected in tumors developed from MCF-7 cells. 74

Figure 2.37: Timeline of experimental procedures performed on animals and tumors treated with (a) CP; (b) CsCl; (c) NanoCs and (d) tumor volume after excision post euthanasia from animals treated with (d2) CP; (d3) CsCl and (d4) NanoCs on cm scale (d1). 75

Figure 2.38: Tumor volume regression analysis for all the animals treated with various used formulations. ONE-WAY ANOVA was performed on tumor sizes and found as $p = 0.0546$ between tumor volume size from tumors treated with CP and NanoCs. 75

Figure 2.39: H&E stained tumor sections after microtomy on waxed tumors from animals treated with (a) CP, (b) CsCl and (c) NanoCs. Arrows show the location of the apoptotic cell population with fragmented nuclei. 76

Figure 3.1: Histogram comparing the mM of silver transferred from aqueous $AgNO_3$ to chloroform with and without dodecanoic acid. 100

Figure 3.2: Schematic representation of the lipid wrapping process to produce the AI-NP. 101

Figure 3.3: Histogram representing the number averaged (%) of AI-NPs. 103

Figure 3.4: A 7-day shelf life stability assessment of the nanoparticle's Hydrodynamic diameter (stored at 4° C). 104
Figure 3.5: TEM micrograph to visualize nanoparticle morphology; Ag^+ inverted micelle capsule is indicated by blue arrow. 105
Figure 3.6: Ag^+ release profile against a 10k MWCO dialysis cassette, and measured by ICP. 106
Figure 3.7: Schematic showing the prodrug synthesis procedure. The final chemical structure is representative of the lipid used to form the AI-Pro-NP. 108
Figure 3.8: Electrospray ionization mass spectrometry of levofloxacin prodrug ($C_{42}H_{69}FN_4O_{10}P^+$). Theoretical peak calculated at 839.4730 MW, and experimental peak was measured to be 839.4715 MW. 109
Figure 3.9: NMR spectrums of the levofloxacin prodrug constituents. 110
Figure 3.10: FTIR spectral analysis of each levofloxacin prodrug constituent paired with its near infrared spectrum. Peaks are assigned to common molecular structures found in each chemical compound. 111
Figure 3.11: Seven-day stability assessment of each nanoparticle's hydrodynamic diameter in BHI media. 112
Figure 3.12: Percent change in *B. subtilis* viability after treatment with each sample. 115
Figure 3.13: Fluorescence image of an agarose gel with DNA samples of bacteria treated with each nanoparticle variation. Order of wells from the left: 1) DNA Ladder, 2) positive control 3) negative control (untreated bacterial DNA), 4) CP, 5) AI-NP, 6) Pro-NP, 7) AI-Pro-NP 116
Figure 3.14: TEM micrograph of bacterial cells treated with CP. Inset is added from other imaging samples to show reproducibility. White artifacts in the center of cells are consequence of slicing samples at 60 nm thin. 117

Figure 3.15: TEM micrograph of bacterial cells treated with AI-Pro-NP. Inset is added from other imaging samples to show reproducibility. White artifacts in the center of cells are consequence of slicing samples at 60 nm thin. Blue arrows indicate AI-Pro-NP, while purple arrows point to compromised cell walls..... 118

Figure 3.16: Cellular samples stained with either SYTO 9 (green) or propidium iodide (red). Each image represents a bacterial sample treated with a separate nanoparticle variation. (40x objective). 119

Figure 4.1: Schematic representation of rhodamine B transferring from aqueous to organic layers into inverted micelle capsules. Image of actual samples are shown adjacent to schematic. 134

Figure 4.2: Histogram representing the number averaged (%) of dodecanoic acid inverted micelles as measured by DLS. 135

Figure 4.3: Sample image of aqueous Methylene Blue suspension and transfer into dodecanoic acid inverted micelles. Dye structure is provided in ionic form for reference. 137

Figure 4.4: Sample image of aqueous FITC suspension and transfer attempts into dodecanoic acid and dodecyl amine. Dye structure is provided in ionic form for reference. 138

Figure 4.5: Sample image of aqueous Doxorubicin suspension and transfer into dodecanoic acid inverted micelles. 139

Figure 4.6: Absorbance levels and quantification of dye transferred into dodecanoic acid inverted micelles, as compared to control samples. 140

Figure 4.7: a) Doxorubicin concentration-absorbance calibration curve, accompanied by b) the absorbance peak measurements 141

Figure 4.8: Schematic representation of the NCAP synthesis process from the inverted micelle capsule to the NMC particle. 143

Figure 4.9: Histogram representing the number averaged (%) of NCAPs with an overlaid image of a TEM micrograph of the NCAPSs for nanoparticle visualization. 144
Figure 4.10: One week assessment of the NCAP's Hydrodynamic diameter stability in various environments. 146
Figure 4.11: Dialysis release profile of doxorubicin from liposome and NCAP samples over 7 hours, compared to free doxorubicin. 147
Figure 4.12: Percent change in MCF-7 cell viability at different treatment concentrations. 149
Figure 4.13: Flow cytometry histogram analysis of cells treated with an F-PE labeled Liposome, and an F-PE labeled NCAP. The liposome histogram was subtracted from the NCAP histogram by Cumulative Overton method, and NCAP-Treated cells which were identified to have more fluorescence expression than liposome-treated cells are labeled in dark red. A histogram of control cells is shown for reference 150
Figure 4.14: Confocal images of MCF-7 cells treated with an F-PE labeled a) liposome or b) NCAP. Both samples were loaded with rhodamine to visualize delivery capability. (40x objective). 152
Figure 4.15: Still confocal images of MCF-7 cells while treated with an F-PE labeled liposome. Stills were taken from live recording at 0, 5, and 300 Seconds. White arrows point to collection of F-PE liposomes which were collected on cell surfaces. Arrows are maintained through the time series for consistency (40x objective). 154
Figure 4.16: Still confocal images of MCF-7 cells while treated with an F-PE labeled NCAP. Stills were taken from live recording at 0, 5, and 300 Seconds. White arrows point to fluorescent NCAP artifacts being consumed by cells. Arrows are maintained through the time series for consistency (40x objective). 154

Figure 5.1: Histogram representing the number averaged (%) of AuNPs with an inset of a TEM micrograph for nanoparticle visualization. 169
Figure 5.2: An overlaid histogram comparing the intensity averaged (%) of the AuNP stock suspension (magenta) and the 'post-transfer' supernatant (dark purple). 170
Figure 5.3: UV-Vis absorbance measurements of the AuNP stock suspension (magenta) and post transfer organic layer (dark purple). 171
Figure 5.4: Schematic representation of solid nanoparticles transferring from aqueous to organic layers into inverted micelle capsules. Image of actual samples are shown adjacent to schematic. 172
Figure 5.5: FTIR Spectral analysis of AuNP, dodecylamine ($C_{12}H_{25}NH_2$), and IM-AuNP with respective peak wavenumbers. 173
Figure 5.6: Histogram representing the number averaged (%) of CNPs with an overlaid image of a TEM micrograph of the CNPs for nanoparticle visualization. 174
Figure 5.7: A characteristic EEM fluorescence spectral map of the CNP. 175
Figure 5.8: Raman spectral analysis of the CNP's graphitic and diamond-like characteristics with respective peak wavenumbers. 176
Figure 5.9: a) FTIR spectral analysis of CNP's chemical composition and (b) a near infrared spectrum of black box outlined in (a) Peaks are assigned to common molecular structures found in CNP. 178
Figure 5.10: Sample image of aqueous CNP suspension and transfer into dodecylamine organic solution. 179
Figure 5.11: Schematic representation of the NMC synthesis process from the inverted micelle capsule to the NMC particle. 180

Figure 5.12: An overlaid histogram representing the number averaged (%) of the NMC-AuNP and NMC-CNP colloidal hydrodynamic diameters. 182
Figure 5.13: Surface charge as measured by Zeta potential of each nanoparticle formulation. . 183
Figure 5.14: Seven-day assessment of (a) NMC-AuNP and (b) NMC-CNP Hydrodynamic diameter stability in various environments. 185
Figure 5.15: A 30-day assessment of the NMC Hydrodynamic diameter shelf life stability at 4 °C. 185
Figure 5.16: TEM micrographs of NMC-AuNP with an inset at a higher magnification. 186
Figure 5.17: UV-Vis absorbance measurements of the AuNP stock suspension (Magenta) and NMC-AuNP (dark purple). The direction of the shifted peak is labeled with an arrow..... 187
Figure 5.18: a) SAXS intensity versus q (nm^{-1}) with visible feature indicated by black arrow. a) SAXS band formation colored by intensity. 188
Figure 5.19: TEM micrographs of NMC-CNP with an inset at a higher magnification. Arrows reveal individual particles entrapped within the NMC-CNP complex. 189
Figure 5.20: UV-Vis absorbance measurements of the CNP stock suspension (dark) and NMC-AuNP (light). The direction of peak shift is labeled with an arrow. 190
Figure 5.21: a) Percent change in MCF-7 cell viability of AuNP and CNP. b) Percent change in MCF-7 cell viability of NMC-AuNP, NMC-CNP, and an NMC control particle..... 192
Figure 5.22: a-c) Bright field images of MCF-7 cells treated at 0.1 mg/ml of the labeled samples. Images were taken with a 10x objective (Scale bar: 50 µm). 193
Figure 5.23: ICP histogram analysis of elemental gold per cell after treatments with AuNP, NMC-AuNP, and a duplicate of each variation with an added heparin sulfate wash (indicated by '-H' after the treatment name). 195

Figure 5.24: a-b) TEM micrographs of cells treated with AuNP alone. Both images contain insets at higher magnifications. 197

Figure 5.25: a-b) TEM micrographs of cells treated with NMC-AuNP. Both images include insets at higher magnifications. 197

Figure 5.26: Raman-generated intensity heat maps (and respective bright field images) of MCF-7 cells treated with the labeled formulations. 199

Figure 5.27: Raman-generated spectral analysis of cells with their respective chemical peak associations. 200

Figure 5.28: Bar chart representing pixel intensity per cell of respective treatment formulations measured by Image J. 201

LIST OF EQUATIONS

Equation 2.1 52

Equation 2.2 79

Equation 2.3 79

Equation 2.4 80

Equation 2.5 82

Equation 2.6 86

Equation 3.1 123

Equation 4.1 157

Equation 4.2 158

Equation 5.1 181

Equation 5.2 205

Equation 5.3 207

CHAPTER 1: INTRODUCTION

Introduction

Worldwide, several leading causes of deaths are classified as preventable diseases according to a study published in 2016.[1] The statistics estimated for the top five leading causes of death in people below 80 years of age were identified as heart diseases (30% of 87,950 were preventable), cancer (15% of 63,209 were preventable), unintentional injuries (43% of 29,232 were preventable), chronic lower respiratory disease (36% of 45,331 were preventable), and stroke (28% of 15,175 were preventable).[1] The number of cancer cases worldwide has been projected to increase to 21.7 million new cases by 2030 (50% increase) with 13 million deaths (60% increase).[2] Despite this grim scenario, the death rate due to cancer decreased by 1.5% between 2005 and 2014 while the overall cancer death rate fell by 25% between 1991 and 2014, which is equivalent to 2,143,200 fewer deaths.[3] This significant reduction in deaths from cancer can be largely attributed to increased access to medicine within developing countries and recent medical advances in diagnosis and therapy.

Current State of Cancer Treatments and Their Challenges

Modern hospitals have access to an array of cancer treatments such as surgery, exposure to radiation, chemotherapy, hormone therapy, immune therapy, and targeted therapy. The use of surgery to treat cancer can include advancements such as cryosurgery, lasers, or laparoscopy for minimally invasive surgery. However, the use of surgery often carries a great cost to the patient due to risks accompanied by pain, infections, bleeding, or reactions to anesthesia.[4]

Radiation therapy is another form of treatment which close to two-thirds of all cancer patients receive, although the use of radiation has been linked to several serious side effects,

including damage to vital organs and microbiomes, and increased risk to subsequent cancers as indicated by radiation epidemiology studies.[5]

The use of chemotherapy (small molecule drug agents) to target cancer cells is a common treatment method used to shrink tumors, followed by surgical excision with further rounds of chemotherapy. Unfortunately, this process is inherently destructive and invasive; it is also associated with several side effects such as weakness, nausea, loss of hair, and vomiting.[6] Furthermore, any healthy cells that show rapid division are also damaged in the process, thus causing further deterioration to the patient.[7]

Overall, the current state of cancer imaging and treatment techniques is not yet perfect, but many treatments are balanced with predictable benefits and challenges. These challenges, as well as the referenced numbers of cancer cases and deaths, call for advanced treatment options to further minimize deaths that could have been preventable.[8]

The Benefits of Nanotechnology in Medicine

The field of "nanotechnology" (10^{-9} meters) is opening new strategies in biomedicine that advance research towards the design of precise and personalized medicine.[9] Specifically, nanoparticles have revolutionized personalized medicine by their ability to physically interact with tissues at the molecular level, either for therapy or imaging applications. Several advantages of delivering agents at the nanoscale level include enhanced bioavailability of poorly soluble agents, lower concentrations of drugs or imaging agents, prolonged systemic retention rates (which increases treatment activity), and higher absorption rates (due to facilitated delivery across the cell membrane).[9] For these presumed benefits, a combined therapeutic and imaging-based approach, enhanced by nanotechnology, has been the target of considerable research.[9]

This field, known as nano-theranostics, uses a combination of nanomaterials combined with chemical modification and agent entrapment. Such dual-purpose theranostic nanoparticles can streamline therapeutic nano-medicine through simultaneous treatment of the disease and monitoring of the treatment progress with imaging techniques.[10] The imaging modality depends on the type of nanoparticle; for example, the luminescent properties of carbon nanoparticles make them ideal for infrared imaging agents,[11] whereas the surface plasmon resonance of different sized gold nanoparticles are excellent for photoacoustic imaging and photothermal ablation therapy.[12] For nanoparticles to function as theranostic agents, they must also effectively treat the target diseased tissue; this can be accomplished in several different ways. For example, some gold nanoparticles can be functionalized with tumor-targeting agents[13] while tuned with a specific diameter that enhances surface plasmon characteristics, which allows them to generate heat when excited by light in the near-infrared spectrum (NIR).[14,15] If these nanoparticles have been internalized within target cells and exposed to NIR light, the heat is able to destroy the cells, thus functioning as a photo-ablative agent.[16] Another option is to use the nanoparticles as a vehicle to carry and deliver disease-treating agents via surface binding or entrapment, be it in ionic, small-molecule, or pro-drug form.[17]

The Role of Theranostic Nanoparticles towards Cancer

Cancer is an extremely complex disease. For example, cancers across different patients, yet within similar tissue, can have very different phenotypic expressions of malignancy. This creates difficulties in treatment; inhibiting one element, such as vasculature growth, cellular receptors, or DNA, will not always have the same effect across all cells or affected patients.[18] Therefore, nano-theranostics must be personalized or redesigned for broad applications on several treatment levels, such as size/shape of particles, type of payload, material composition, and

delivery mechanism. The adaptability of nanoparticle design makes them an ideal platform for delivering personalized theranostics and allows for comprehensive preclinical studies of these agents.[19] However, complex chemistries and synthesis procedures hinder the design of theranostic agents for efficient delivery towards a variety of disease types and patients. These considerable obstacles point to a need for a universal platform as part of the solution.

The design of nanoparticles can involve programming of their physical properties, such as size, mass, and zeta potential, to facilitate different applications and targets. In passive targeting, the blood vessels of tumor cells are leakier than those of normal cells because of abnormalities in the basement membrane of cancer cells.[20] The latter thus require higher levels of resources to continue propagation of the tumor mass. An additional problematic feature of tumors is poor lymphatic drainage, which is known as the enhanced permeability and retention effect (EPR). Consequently, the preferred dimensions for molecules to penetrate tumors via EPR and be retained long enough to treat the tumor mass efficiently is reported to be between 10–150 nm.[21,21]

The active version of cancer cell targeting is based on unique targeting proteins found on the cell membrane's surface that differentiate them from healthy cells. In the active targeting approach, nanoparticles are engineered to possess targeting ligands for cell receptors on a specific type of cancer cell strain. Several other molecules that have been used to target nanoparticles include tumor-specific antigens, transferrin, growth factor receptors, nucleic acid aptamers, monoclonal antibodies, and death receptors.[13]

With a combined design and targeting approach, the nanomedicine research community has developed a breadth of theranostic nanoparticles for various applications such as imaging, therapeutics, targeting, and enhanced delivery. For example, Jin et al. recently investigated an

intrinsic, biodegradable, and liposome-mimicking theranostic nanoparticle called the porphysome nanostructure. In their report, folate-conjugated porphysome nanostructures were designed to target folate receptors that are overexpressed in ovarian and breast cancer cells and initiate folate-receptor-mediated endocytosis. Once the porphysome nanostructures disassembled within the cell, the authors used thermal ablation to destroy the cell while initiating photodynamic activity, which is monitorable with *in vivo* fluorescence microscopy.[22]

In another example, Chen et al. designed peptide-modified ferritin nanocages and used them to target integrin $\alpha_v\beta_3$ on tumor cells. These protein-based nanoparticles were composed of 24 subunits that assembled as a cage-like structure to deliver imaging agents (e.g., radiometal isotopes and fluorescent dyes) and therapeutic agents (e.g., photosensitizers and doxorubicin) to tumor cells.[23] The nanocages were co-loaded with copper-precomplexed doxorubicin and a near-infrared dye (ZW800) to demonstrate an augmentation of optical imaging and chemotherapeutic effects in mice models.[24,25]

A 2014 study by Liu et al. investigated pH-sensitive theranostic nanoparticles designed for both magnetic resonance imaging (MRI) and therapy. The particles were developed by the use of multi-block polymer poly(lactic acid)-polyethylene glycol-poly(L-lysine)-diethylenetriamine penta-acetic acid and the pH-sensitive material poly(L-histidine)-polyethylene glycol-biotin. This polymer nanoarchitecture was used to encapsulate the anti-hepatocellular carcinoma drug sorafenib and MRI-active Gd-DTPA (Gadopentetic acid), while antibodies were used simultaneously to facilitate VEGFR (vascular endothelial growth factor receptor) targeting. The results of nanoparticle treatment in mice xenografted with the H22 tumor cell line showed higher MRI resolution and imaging time with an increased treatment efficacy of the tumor as compared to the contrast agent Magnevist®, which is used with MRI to visualize lesions.[26]

Nanoparticles and the Importance of Nano-Delivery

As we have discussed here, nanoparticles offer a versatile vessel for the transportation of various agent types and material compositions. Without such a delivery vehicle, imaging or therapeutic agents would suffer on several dimensions that nano-delivery strategies can alleviate, such as increased half-life of systemic clearance, bioavailability, controlled release, and active/passive targeting.[27] Therefore, each application must use a carefully designed and versatile nano-delivery system to achieve a specific purpose, either for imaging or therapy. There are several popular nano-based delivery systems such as liposomes, polymeric micelles, dendrimers, nanospheres, nanocapsules, inorganic nanoparticles, protein-derived nanoparticles, and nanotubes.

Liposomes are lipid bilayers that enclose water-soluble agents within the nanoparticle's hydrophilic core, whereas micelles can package water-insoluble agents within their hydrocarbon-rich hydrophobic core. Another classification of nanoarchitectures includes dendrimers, which are defined as branched, three-dimensional, tree-like structures developed from artificial or natural materials such as nucleotides or sugars. Dendrimers can be loaded with agents to target cancer cells, whereas their branching nature is also convenient for conjugating several molecules on the surface. Nanospheres are matrices infused with agents and functionalized with targeting ligands. While, nanocapsules have a lipid shell with a central core composed of polymers or other fatty molecules, which enables efficient packaging of agents for systemic delivery.[9]

Apart from polymers or lipid-based systems, inorganic materials can also be explored as nano-delivery vehicles. For instance, non-polymer or non-lipid based nano-delivery vehicles include monodisperse inorganic nanoparticles such as gold or iron oxide nanoparticles. These inorganic nanoparticles have strong zeta potentials and a large surface-area-to-volume ratio, which

makes them easily passivated with theranostic agents. Furthermore, inorganic nanoparticles are well known for their strong covalent surface modification properties.[27] Biomolecules such as proteins are also considered as nano-delivery systems on account of their biocompatibility, biodegradability, and surface modification ability.[23] For example, albumin is used as a nanocapsule in the FDA-approved drug Abraxane to deliver the water-insoluble chemotherapeutic agent Paclitaxel for cancer therapy.[23]

The most popular nano-delivery vehicles for theranostic applications are liposomes. These nanoparticles offer advantages such as transport of water-soluble agents where their inherent nanoarchitectural properties make hydrophilic molecules face the core, and hydrophobic molecules are kept within the lipid membrane. Liposomes are ideal for systemic use because of their biocompatibility, ability to self-assemble, large loading capacities, and their ability to be modified for different theranostic applications.[28]

One of the most cited case studies showing the success of liposomal use for systemic cancer treatment is the pharmaceutical product called Doxil® (Ben Venue Laboratories, Inc., Bedford, OH), which was granted FDA approval in 1995. Doxil is a liposome packed with the anti-cancer drug doxorubicin and has been mainly used in the treatment for breast cancer and other aggressive tumors. Doxil has increased circulation time and higher treatment efficacy at lower concentrations when compared to treatment using unpackaged doxorubicin alone (Ben Venue Laboratories, Inc., Bedford, OH).

While several liposome-based delivery methods have been advantageous in the therapeutic world, liposomes have several limitations that restrict their effectiveness for theranostic applications. First, liposomes tend to be "leaky," which is defined as the passive and unintentional

release of the contents. This "leakiness" depends on several variables such as drug-to-lipid ratio, vesicle diameter, and cholesterol content.[29,30] Therefore, the "leakiness" reduces the efficiency and potency of drugs or agents needed to reach their desired targets, decreasing their overall therapeutic effectiveness and potentially contributing to unintended side effects. Furthermore, liposomes are foreign objects that are quickly cleared by the reticuloendothelial system (RES). Coating of liposomes with polyethylene glycol (PEG) can increase stability and minimize the uptake by RES;[31] however, pegylation hinders the particles' controlled release ability at the intended tissue.[32,33] Unfortunately, as current research advances the complexity of liposomal architectures, and as theranostic agents become more intricate to serve a variety of purposes, the nanoparticles' complex chemistry and synthesis procedures hinder their ability to move into clinical trials and become FDA approved.[28]

The Need for a Redesigned Nano-Architecture

One significant barrier of nano-theranostics that limits their translation into clinical applications is the lack of a broad platform for encapsulation and delivery of the theranostic agents. Current research is continuously producing novel theranostic agents of several calibers, with various applications, and with high possibilities to revolutionize modern medicine. Yet, the use of novel theranostic agents in practice is often hindered by their inability to properly reach their target with high bioavailability and biocompatibility, even with the aid of popular nano-delivery techniques such as liposomes. Nonetheless, an ideal, universal, and biocompatible nanoparticle for multi-purpose, high-throughput delivery has yet to come to fruition. Despite the progress in this field, there are several challenges that must be improved, such as the development of a robust package with high packaging capacity, simpler chemical synthesis, material compatibility with

molecularly diverse agents, material biocompatibility with cells, and ligand conjugation efficiency.[34]

From our research, we believe that a universal nanoparticle – with significant improvements in the delivery throughput of theranostic agents – can be achieved by a two-pronged approach, which are i) the development of a highly efficient, robust, and universal vehicle for theranostic agent encapsulation; and ii) the wrapping of the encapsulated agent with a modifiable, stable, and biocompatible shell.

Development of a highly efficient, robust, and universal vehicle for theranostic agent encapsulation

To address this methodology, we looked towards the use of inverted micelles for their ease of preparation, encapsulation, and versatility with various materials.[35] By definition, regular micelles are self-assemblies of amphiphilic molecules in an aqueous medium, whereas inverted micelles are self-assemblies of amphiphilic molecules in an organic medium. Such inverted micelles have been explored as encapsulating systems for hydrophilic agents,[35] yet are not exhaustively investigated regarding *in vitro* or *in vivo* agent delivery. To highlight the effectiveness of inverted micelles as robust encapsulation and delivery systems, one study performed spontaneous acid-base self-assembly to achieve nano-encapsulation of small molecules and inorganic nanoparticles that circumvented the use of chemical modification.[36] The first subject for phase transfer into the organic solvent toluene was a fourth-generation amine-terminated PAMAM dendrimer (G4–NH_2) passivated with the hydrophilic organic dye, methyl orange (previously unable to transfer into toluene). The inverted-micelle-initiating molecule was a dodecanoic acid, which electrostatically interacts with the amine-terminated PAMAM dendrimer. The use of UV-

vis spectroscopy confirmed the nearly complete transfer of the dye into toluene containing >10% dodecanoic acid. This inverted micelle encapsulation was pursued with Pd nanoparticles and proved successful.[36] A second article expanded on Chechik et al.'s work with the formation of supramolecular, hyperbranched polyethyleneimine (PEI) with encapsulation with other fatty acids, showing the versatility and possibilities of this mechanism to encapsulate water-soluble agents efficiently within organic solvents.[37]

To highlight the robust packaging ability of inverted micelle structures, Qiu et al. found that the use of amphiphilic phosphazene polymers in an inverted micelle form was able to retain 70% of its packaged contents over a 60-day period as compared to regular poly(lactide-co-glycolide) (PLGA) microparticles, which only retained 50% of the enclosed agent within the first day.[38] Thus, the inverted micelle architecture showed robust encapsulation and retention abilities; unfortunately, this study did not address critical factors such as systemic retention time, biocompatibility, and ability to encapsulate multiple agent types and material compositions.

To highlight an example of protein encapsulation in inverted micelles, Miller et al. studied micelles composed of a hydrophilic and hydrophobic block-copolymer (ϵ-caprolactone)-*block*-poly(2-vinyl pyridine) (PCL-*b*-P2VP), which were used to transfer model globular proteins between aqueous and organic (toluene) phases. Thus, such polymer-based inverted micelles could also serve as nano-encapsulation vehicles.[39]

Wrapping of the encapsulated agent with a modifiable, stable, and biocompatible shell

In a previous section, we saw that lipids are ideal wrapping agents for systemic nano-delivery vehicles on account of stability and biocompatibility.[40] Hence, here we venture into combining the use of lipids as a shell to wrap the inverted micelle capsule to create a modified

version of nanocapsules, which we have termed the NCAP, NanoCS, AI-NP, or NMC depending on the project and application. With this combined architecture consisting of a robust inverted micelle capsule wrapped with a biocompatible lipid shell, many types of agents would be capable of being efficiently entrapped and become subject to high-throughput systemic delivery.

For example, the use of inverted micelles is not challenged by encapsulating hydrophobic or hydrophilic agents because hydrophobic molecules can occupy positions between the hydrocarbon sections of the lipids and the inverted-micelle-initiating molecule, while hydrophilic molecules can be enclosed within the micelle's hydrophilic core. Furthermore, an appropriate selection of a molecule that initiates the inverted micelle in an organic medium can facilitate the incorporation of a diverse range of molecules of various charges, chemical structures, or weights.

Specific Aims

Within this literature review, we have seen examples of current research discussing the advantages of inverted micelles and their packaging efficiency with small molecules, inorganic nanoparticles, and biological material. We have also discussed the difficulties associated with creating ideal nano-architectures built with materials suitable for clinical translation. Therefore, with these factors in play, we believe that this area of research is ripe for disruption with the novel nanoarchitecture that we have termed the NanoCapsule.

This thesis will outline an innovative approach for creating a novel nanoparticle architecture with robust chemistry with a streamlined 2-step process adaptable for a variety of agents. By using phase transfer to facilitate hydrophobic modification and lipid wrapping, this approach has the potential to eliminate many of the challenges facing encapsulation of chemically different theranostic agents. Furthermore, the proposed approach uses materials with proven

biocompatibility, which greatly improves the prospects for similar methodologies needing FDA approval. The overarching goal of this thesis seeks to create a universal and highly efficient encapsulation and delivery vehicle, which can be used to overcome the barriers of current clinical techniques. Ideally, this research is an advantageous step in facilitating the use of theranostic agents in personalized medicine for the entire nanomedicine community. We have followed the following aims to defend our hypothesis:

Aim 1: Develop an efficient nanoparticle architecture capable of encapsulating and delivering various types of agents

For this aim, we engineered a novel encapsulation nanoarchitecture, developed and optimized synthesis methods, and characterized the physical and material properties of the nanoparticles. The facile 2-step process began with an aqueous-to-organic phase transfer used to envelop agents within an amphiphilic hydrocarbon-based inverted micelle. The resulting encapsulation depends on the electrostatic reactions between charged heads of fatty acids, such as dodecanoic acid, or fatty amines, such as dodecylamine, and the charge of the encapsulated agent. This approach could efficiently create a robust hydrophobic shell to protect the packaged agents from leakage and harsh denaturing environments.

Aim 2: Determine the ability of nanoparticle architecture to encapsulate specific types of agents

After developing and optimizing the methodology to create the NCAP, we tested its encapsulation capability with six different types of agents that have potential theranostic applications: cesium ions (Cs^+), silver ions (Ag^+), a small molecule drug (doxorubicin), inorganic gold nanoparticles (AuNPs), and organic carbon nanoparticles (CNPs). Each of these agents has very different chemical and functional properties and applications that span anti-cancer therapies,

nano-imaging, and even anti-microbial remedies. The variety of agents' characteristics will, therefore, thoroughly test the adaptability of our novel delivery vehicle.

Aim 3: Evaluate the theranostic potential of encapsulated agents

Once the protocols have been optimized, and the nanoarchitecture characterized, each type of encapsulated agent was tested for their effectiveness in a biological setting.

Within our first project, we published an article in 2016 where we investigated the intracellular delivery of cesium chloride (CsCl) through the nanocapsulation technique mentioned above and compared it to the unamended cesium salt towards cancer therapy. The nano-based system, which we termed NanoCs (for Nano-Cesium), proved to be more efficient at intracellular delivery of cesium ions as compared to the unamended salt alone, and the mechanism for cancer therapy was glucose uptake inhibition rather than the expected high-pH therapy. This nanoparticle containing ionic cesium was developed for the first time for delivery to tumor cells *in vitro* as well as *in vivo.*[41]

To address antibiotic resistance on the nano level, our team designed a unique combinatorial approach to impair antimicrobial activity by encapsulating ionic silver within the inverted-micelle-initiated nanocapsule and wrapping the encapsulated agent with a lipid-based levofloxacin prodrug; we termed this new nanoarchitecture AI-NP (for Ag ion-nanoparticle). Our rationale was to use the antimicrobial activity of silver ions to disrupt the bacterial cell wall and deliver the topoisomerase inhibitor molecule levofloxacin in the form of a prodrug cleavable by common intracellular esterases.

As outlined, the liposomal anti-cancer agent Doxil has many weaknesses; therefore, we investigated the encapsulation, treatment efficiency, and imaging capabilities of inverted micelle

(NCAP) containing doxorubicin and the popular small-molecule fluorescent probe Rhodamine. Here, we visualized the interactions of the NCAP with a breast cancer cell line through various fluorescent imaging modalities and analyzed the NCAP's effectiveness as cancer therapeutic compared to treatments with free doxorubicin or doxorubicin within a liposome.

Finally, we recently published an article delving into nanoparticle-based imaging with separate encapsulations and treatments of surface-plasmon-rich gold nanoparticles or Raman-active carbon nanoparticles. We focused on ~10 nm gold and carbon nanoparticles because such small particles are usually unable to activate enough receptors for receptor-mediated endocytosis.[42,43] These nanoparticles were encapsulated within nanocapsules, termed NMCs (for Nano-MultiCapsules), in a simple 2-step process to form a unique particle-in-particle complex. We found that the NMCs enable efficient encapsulation of numerous ~10 nm nanoparticles for high-throughput intracellular delivery within a breast cancer cell line.[44]

In the following chapters, we will cover each project in depth with details on the motivations behind each project, their methodologies, and the explanation of how the novel NCAP architecture can revolutionize the packaging and delivery of theranostic agents for clinical use.

References to Introduction

(1) García, M. C.; Bastian, B.; Rossen, L. M.; Anderson, R.; Miniño, A.; Yoon, P. W.; Faul, M.; Massetti, G.; Thomas, C. C.; Hong, Y.; et al. Potentially Preventable Deaths Among the Five Leading Causes of Death — United States, 2010 and 2014. *MMWR. Morb. Mortal. Wkly. Rep.* **2016**, *65* (45), 1245–1255.

(2) American Cancer Society. *Global Cancer Facts and Figures 3rd Edition.*; American Cancer Society: Atlanta, 2015.

(3) Siegel, R. L.; Miller, K. D.; Jemal, A. Cancer Statistics, 2017. *CA. Cancer J. Clin.* **2017**, *67* (1), 7–30.

(4) Surgery for Cancer - National Cancer Institute https://www.cancer.gov/about-cancer/treatment/types/surgery.

(5) Newhauser, W. D.; Berrington de Gonzalez, A.; Schulte, R.; Lee, C. A Review of Radiotherapy-Induced Late Effects Research after Advanced Technology Treatments. *Front. Oncol.* **2016**, *6*, 11.

(6) Shahbaz Aslam, M.; Naveed, S.; Ahmed, A.; Abbas, Z.; Gull, I.; Athar, M. A.; Aslam, M. S. Side Effects of Chemotherapy in Cancer Patients and Evaluation of Patients Opinion about Starvation Based Differential Chemotherapy. *J. Cancer Ther. Jour-nal Cancer Ther.* **2014**, *5* (5), 817–822.

(7) Zhao, G.; Rodriguez, L. B. Molecular Targeting of Liposomal Nanoparticles to Tumor Microenvironment. *Int. J. Nanomedicine* **2012**, *8*, 61–71.

(8) Ferlay, J.; Shin, H.-R.; Bray, F.; Forman, D.; Mathers, C.; Parkin, D. M. Estimates of

Worldwide Burden of Cancer in 2008: GLOBOCAN 2008. *Int. J. Cancer* **2010**, *127* (12), 2893–2917.

(9) Bishwajit Sutradhar, K.; Lutful Amin, M.; Lecturer, S. Nanoemulsions: Increasing Possibilities in Drug Delivery. *Eur. J. Nanomed* **2013**, *5* (2), 97–110.

(10) Xie, J.; Lee, S.; Chen, X. Nanoparticle-Based Theranostic Agents. *Adv. Drug Deliv. Rev.* **2010**, *62* (11), 1064–1079.

(11) Mukherjee, P.; Misra, S. K.; Gryka, M. C.; Chang, H.-H.; Tiwari, S.; Wilson, W. L.; Scott, J. W.; Bhargava, R.; Pan, D. Tunable Luminescent Carbon Nanospheres with Well-Defined Nanoscale Chemistry for Synchronized Imaging and Therapy. *Small* **2015**, *11* (36), 4691–4703.

(12) Singh, M.; Harris-Birtill, D. C. C.; Markar, S. R.; Hanna, G. B.; Elson, D. S. Application of Gold Nanoparticles for Gastrointestinal Cancer Theranostics: A Systematic Review. *Nanomedicine Nanotechnology, Biol. Med.* **2015**, *11* (8), 2083–2098.

(13) Gmeiner, W. H.; Ghosh, S. Nanotechnology for Cancer Treatment. *Nanotechnol. Rev.* **2015**, *3* (2), 111–122.

(14) Huang, X.; El-Sayed, I. H.; Qian, W.; El-Sayed, M. A. Cancer Cell Imaging and Photothermal Therapy in the Near-Infrared Region by Using Gold Nanorods. *J. Am. Chem. Soc.* **2006**, *128* (6), 2115–2120.

(15) Zharov, V. P.; Letfullin, R. R.; Galitovskaya, E. N. Microbubbles-Overlapping Mode for Laser Killing of Cancer Cells with Absorbing Nanoparticle Clusters. *J. Phys. D. Appl. Phys.* **2005**, *38* (15), 2571–2581.

(16) Huff, T. B.; Tong, L.; Zhao, Y.; Hansen, M. N.; Cheng, J.-X.; Wei, A. Hyperthermic Effects of Gold Nanorods on Tumor Cells. *Nanomedicine (Lond).* **2007**, *2* (1), 125–132.

(17) Cho, K.; Wang, X.; Nie, S.; Chen, Z. G.; Shin, D. M. Therapeutic Nanoparticles for Drug Delivery in Cancer. *Clin. Cancer Res.* **2008**, *14*, 1310–1316.

(18) Baird, R. D.; Caldas, C. Genetic Heterogeneity in Breast Cancer: The Road to Personalized Medicine? *BMC Med.* **2013**, *11* (1), 151.

(19) Ryu, J. H.; Lee, S.; Son, S.; Kim, S. H.; Leary, J. F.; Choi, K.; Kwon, I. C. Theranostic Nanoparticles for Future Personalized Medicine. *J. Control. Release* **2014**, *190*, 477–484.

(20) McDonald, D. M.; Baluk, P. Significance of Blood Vessel Leakiness in Cancer. *Cancer Res.* **2002**, *62* (18), 5381–5385.

(21) Chauhan, V. P.; Jain, R. K. Strategies for Advancing Cancer Nanomedicine. *Nat. Mater.* **2013**, *12* (11), 958–962.

(22) Jin, C. S.; Cui, L.; Wang, F.; Chen, J.; Zheng, G. Targeting-Triggered Porphysome Nanostructure Disruption for Activatable Photodynamic Therapy. *Adv. Healthc. Mater.* **2014**, *3* (8), 1240–1249.

(23) Lohcharoenkal, W.; Wang, L.; Chen, Y. C.; Rojanasakul, Y. Protein Nanoparticles as Drug Delivery Carriers for Cancer Therapy. *Biomed Res. Int.* **2014**, *2014*, 12.

(24) Zhen, Z.; Tang, W.; Chen, H.; Lin, X.; Todd, T.; Wang, G.; Cowger, T.; Chen, X.; Xie, J. RGD-Modified Apoferritin Nanoparticles for Efficient Drug Delivery to Tumors. *ACS Nano* **2013**, *7* (6), 4830–4837.

(25) Zhen, Z.; Tang, W.; Guo, C.; Chen, H.; Lin, X.; Liu, G.; Fei, B.; Chen, X.; Xu, B.; Xie, J. Ferritin Nanocages To Encapsulate and Deliver Photosensitizers for Efficient Photodynamic Therapy against Cancer. *ACS Nano* **2013**, *7* (8), 6988–6996.

(26) Liu, Y.; Feng, L.; Liu, T.; Zhang, L.; Yao, Y.; Yu, D.; Wang, L.; Zhang, N. Multifunctional pH-Sensitive Polymeric Nanoparticles for Theranostics Evaluated Experimentally in Cancer. *Nanoscale* **2014**, *6* (6), 3231–3242.

(27) Mudshinge, S. R.; Deore, A. B.; Patil, S.; Bhalgat, C. M. Nanoparticles: Emerging Carriers for Drug Delivery. *Saudi Pharm. J.* **2011**, *19* (3), 129–141.

(28) Sercombe, L.; Veerati, T.; Moheimani, F.; Wu, S. Y.; Sood, A. K.; Hua, S. Advances and Challenges of Liposome Assisted Drug Delivery. *Front. Pharmacol.* **2015**, *6*, 286.

(29) Luo, D.; Carter, K. A.; Razi, A.; Geng, J.; Shao, S.; Lin, C.; Ortega, J.; Lovell, J. F. Porphyrin-Phospholipid Liposomes with Tunable Leakiness. *J. Control. Release Off. J. Control. Release Soc.* **2015**, *220* (Pt A), 484–494.

(30) Subramanian, S.; Khan, I.; Korale, O.; Alhnan, M. A.; Ahmed, W.; Najlah, M.; Taylor, K. M. G.; Elhissi, A. A Simple Approach to Predict the Stability of Phospholipid Vesicles to Nebulization without Performing Aerosolization Studies. *Int. J. Pharm.* **2016**, *502* (1–2), 18–27.

(31) Ishida, T.; Harashima, H.; Kiwada, H. Interactions of Liposomes with Cells in Vitro and in Vivo: Opsonins and Receptors. *Curr. Drug Metab.* **2001**, *2* (4), 397–409.

(32) Ulrich, A. S. Biophysical Aspects of Using Liposomes as Delivery Vehicles. *Biosci. Rep.* **2002**, *22* (2), 129–150.

(33) Forssen, E.; Willis, M. Ligand-Targeted Liposomes. *Adv. Drug Deliv. Rev.* **1998**, *29* (3), 249–271.

(34) Chen, F.; Ehlerding, E. B.; Cai, W. Theranostic Nanoparticles. *J. Nucl. Med.* **2014**, *55* (12), 1919–1922.

(35) Trivedi, R.; Kompella, U. B. Nanomicellar Formulations for Sustained Drug Delivery: Strategies and Underlying Principles. *Nanomedicine* **2010**, *5* (3), 485–505.

(36) Chechik, V.; Zhao, M.; Crooks, R. M. Self-Assembled Inverted Micelles Prepared from a Dendrimer Template: Phase Transfer of Encapsulated Guests. *J. Am. Chem. Soc.* **1999**, *121* (20), 4910–4911.

(37) Chen, Y.; Shen, Z.; Frey, H.; Pérez-Prieto, J.; Stiriba, S.-E.; Tzschucke, C. C.; Markert, C.; Bannwarth, W.; Roller, S.; Hebel, A.; et al. Synergistic Assembly of Hyperbranched Polyethylenimine and Fatty Acids Leading to Unusual Supramolecular Nanocapsules. *Chem. Commun.* **2005**, *41* (6), 755–757.

(38) Qiu, L.; Zhang, J.; Yan, M.; Jin, Y.; Zhu, K. Reverse Self-Assemblies Based on Amphiphilic Polyphosphazenes for Encapsulation of Water-Soluble Molecules. *Nanotechnology* **2007**, *18* (47), 475602.

(39) Miller, A. C.; Bershteyn, A.; Tan, W.; Hammond, P. T.; Cohen, R. E.; Irvine, D. J. Block Copolymer Micelles as Nanocontainers for Controlled Release of Proteins from Biocompatible Oil Phases. *Biomacromolecules* **2009**, *10* (4), 732–741.

(40) Kalepu, S.; Manthina, M.; Padavala, V. Oral Lipid-Based Drug Delivery Systems – an Overview. *Acta Pharm. Sin. B* **2013**, *3* (6), 361–372.

(41) Daza, E. A.; Misra, S. K.; Schwartz-Duval, A. S.; Ohoka, A.; Miller, C.; Pan, D. Nano-Cesium for Anti-Cancer Properties: An Investigation into Cesium Induced Metabolic Interference. *ACS Appl. Mater. Interfaces* **2016**, *8* (40), 26600–26612.

(42) Decuzzi, P.; Ferrari, M. The Receptor-Mediated Endocytosis of Nonspherical Particles. *Biophys. J.* **2008**, *94* (10), 3790–3797.

(43) Park, J. H.; Oh, N. Endocytosis and Exocytosis of Nanoparticles in Mammalian Cells. *Int. J. Nanomedicine* **2014**, *9 Suppl 1*, 51–63.

(44) Daza, E. A.; Schwartz-Duval, A. S.; Volkman, K.; Pan, D. Facile Chemical Strategy to Hydrophobically Modify Solid Nanoparticles Using Inverted Micelle-Based Multicapsule for Efficient Intracellular Delivery. *ACS Biomater. Sci. Eng.* **2018**, *4* (4), 1357–1367.

CHAPTER 2: NANO-CESIUM FOR ANTI-CANCER PROPERTIES: AN INVESTIGATION INTO CESIUM INDUCED METABOLIC INTERFERENCE[1]

Graphical Abstract

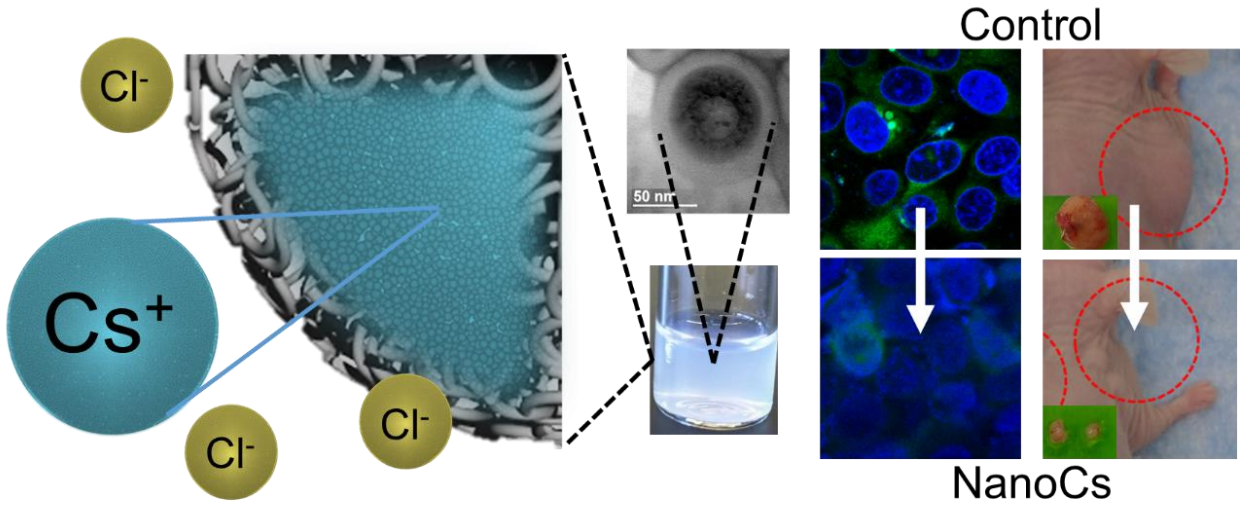

[1] This chapter was published in *Applied Materials & Interfaces* journal by Enrique A. Daza, Santosh K. Misra, Aaron S. Schwartz-Duval, Ayako Ohoka, Callie Miller, and Dipanjan Pan. DOI: 10.1021/acsami.6b09887

Abstract

The use of cesium chloride (CsCl) for cancer therapy ("high pH therapy") has been theorized to produce anti-cancer properties by raising intracellular pH to induce apoptosis. Although considered as "alternative medicine", little scientific evidence supports this theory. Alternatively, cells have no cesium ion (Cs^+) mediated channels for clearance. Thus, such unstable electrochemical distributions have the potential severe potential to disrupt electrochemical dependent cellular processes, such as glucose co-transporters. Hence, a detailed investigation of pH changing effects and glucose uptake inhibition are warranted as a possible cesium-induced anti-cancer therapy. We developed and characterized cesium nanoparticles (38 ± 6 nm), termed NanoCs, for nanoparticle-mediated internalization of the ion, and compared its treatment to free CsCl. Our investigations suggest that neither NanoCs nor CsCl drastically changed the intracellular pH, negating the theory. Alternatively, NanoCs lead to a significant decrease in glucose uptake when compared to free CsCl, suggesting cesium inhibited glucose uptake. An apoptosis assay of observed cell death affirms that NanoCs leads tumor cells to initiate apoptosis rather than follow necrotic behavior. Furthermore, NanoCs lead to *in vivo* tumor regression, where H&E analysis confirmed apoptotic cell populations. Thus, NanoCs persuaded pH-independent anti-cancer therapy by inducing metabolic stasis.

Keywords: Cesium, Nano Particles, Cancer Therapy, Metabolic Therapy.

Introduction

High pH therapy (also known as "cesium therapy") is an alternative cancer treatment approach,[1] wherein the cesium chloride (CsCl) salt is taken orally or injected intravenously and intended to raise the intracellular pH of tumor cells leading to cell-mediated apoptosis. Changing the acidic pH range of the cancerous cells towards weak alkalinity is expected to imperil its endurance by neutralizing and excluding the generation of essential acidic proteins and molecules. This theory has been tagged as an "Underground Cure for Cancer"[1–3] although scientific evidence is severely lacking. Not to be confused with conventional and orthodox cesium-137 radiation therapy,[4] or nano-enabled extracellular pH modulation,[5] "cesium therapy" is mostly prescribed by nutritionists and pseudo-doctors. Existing studies of CsCl therapy report patient and animal consumption of CsCl leading to a decrease in symptoms and pain,[6–8] Although most of these patients were terminal cases, a post-mortem follow-up autopsy revealed cesium accumulation within vital organs. [9] Investigations into the health risks of high CsCl consumption have shown a direct correlation to cardiac arrhythmia,[9–12] hypokalemia,[13] and death,[9,10] In response to these health risks, many licensed physicians emphasize that cesium therapy should not be used to treat tumors until further research has been conducted.

Besides "high pH therapy", other scientific reports have indicated CsCl interacts with important ion dependent cellular mechanisms [13,14] which are upregulated in cancerous systems and as such pose as potential targets for tumor inhibition. One possible mechanism to investigate uses Cs^+ to disrupt the ion dependent facilitated glucose transport proteins (GLUT) (sodium (Na^+)/glucose co-transport proteins), which are overexpressed in tumor cells.[15] An increase in inner membrane charge by Cs^+ exposure could reduce, Na^+/K^+ channel activity leading to a decreased amount of Na^+ and glucose influx *via* the Na^+/glucose cotransport proteins. This decline

in glucose influx, if significant, can result in cellular starvation and apoptosis initiation, thus deeming Cs^+ a metabolic therapy agent. A strong indication of starvation is the production of reactive oxygen species (ROS) which can lead to intracellular damage and oxidative stress, and thus cellular autophagy.[16] One known ROS target of interest is the aforementioned Na^+/K^+ pump[17,18] which indirectly aids Na^+/glucose cotransporters by increasing extracellular Na^+ and thus leads to a chain reaction of starvation-mediated apoptosis.

The free CsCl salt lacks specific tumor targeting tactics, whether taken orally or intravenously as its transport is purely determined by diffusion, physiological filtration, and immune recognition. Due to its high water solubility (1865 g/L at 20 °C) the free ions are left to interact throughout all reliant systems including normal bystander cells, posing detrimental effects that can lead to severe off target toxicity.[11–13] To address this issue and to further investigate the role of CsCl in metabolic therapy, a nanomedicine approach was envisioned, since nanoparticles tend to accumulate passively in tumor tissue much more than normal tissues.[19–23] This is due to the rapid and entropic metastasis of *in vivo* tumor growth which leads to poor formation of blood and drainage vessels in adjacent tissue; a phenomenon commonly known as the enhanced permeability and retention effect (EPR).[24] Nanoparticles of certain sizes tend to accumulate passively in tumor tissue much more than they do in normal tissues.[19–23] Towards this aim, we developed a nanoparticle of ionic cesium (NanoCs) for delivery to tumor cells *in vitro* and *in vivo* for the first time. The NanoCs particle was used to investigate any possible intracellular pH change from intracellular delivery of ionic cesium, mechanistic influence on glucose uptake and ROS generation, as well as method of cellular death. Furthermore, *in vivo* studies revealed significant tumor regression *via* induced apoptosis in nude mice xenograft model treated with NanoCs.

Results and Discussion

Design of Cesium Based Nanoparticle and Subsequent Analysis of Metal Entrapment, Optimization, and Stability

NanoCs was prepared following a synthetic procedure to encapsulate and trap a high concentration of cesium ions (Cs^+) within polymeric micellar particles with excellent retention and stability. Polymers were chosen based on their ability to capture high quantities of agents varying in molecular structures from small molecules[25,26] and peptides.[21,27] These vast interstitial spaces combined with strong negative charges associated with the poly acrylic acid residues create a favorable environment for entrapment of the positively charged cesium ions. The process involves the stepwise formation of a micelle from polyethylene glycol cetyl ether (2 mg/ml, Average M_n 1124) in a CsCl/water solution and subsequent addition of a solution of poly(styrene)$_{67}$-block-poly(acrylic acid)$_{27}$ in THF (Figure 2.1). The water to THF volume ratio was optimized to 4:1 for ideal particle formation, size, and long-term stability. In order to maximally enrich Cs^+ within the particle, various amounts of the salt were applied during particle synthesis (0, 10, 20, 50, and 100 mg/ml). Using dynamic light scattering (DLS), we identified that the salt concentration limit to produce stable particles was 50 mg/ml and produced NanoCs with an average hydrodynamic diameters (D_{hy}) at 38 ± 6 nm accompanied by a polydispersity index of 0.2 ± 0.0 (Figure 2.2 and Figure 2.3). Higher concentrations of CsCl during particle synthesis resulted in polymeric particles with a D_{hy} of 548 ± 229 nm accompanied by a high polydispersity index of 0.8 ± 0.1 (Figure 2.2). Control particles (CP) lacking Cs^+ (D_{hy}: 19 ± 4 nm with a polydispersity index of 0.3 ± 0.0) (Figure 2.3) were produced *via* the same methods (using 18 MΩ nanopure water instead of the CsCl solution). CP was used as controls during various experiments to ensure that polymer interaction and surface chemistry did not interfere with experimental hypotheses. To eliminate any free Cs^+

ions present, post particle synthesis, NanoCs underwent dialysis for a prolonged period and subsequently filtered. To confirm the presence of cesium, energy dispersive X-ray spectroscopic measurements (EDS) on anhydrous particles imaged *via* SEM, enabled us to see cesium signals within NanoCs particle mass (Figure 2.4, Figure 2.5). In order to quantify the cesium entrapped within NanoCs post dialysis, a hydrochloric acid digestion of the particles followed by inductively coupled plasma optical emission spectrometry (ICP-OES) measurements were performed. This data showed that the NanoCs had a capture efficiency of 250 Cs^+ per nanoparticle or 1:0.21 weight per weight (w/w) of nanoparticle to Cs^+ respectively which remained constant during long-term shelf storage at ambient temperature. Quantitative analysis of cesium release, post dialysis revealed that ~85% of cesium discharged within 72 hours (Figure 2.6). This cesium release can be described as a two-phase release system, whereby the first burst discharged 42% of the cesium ion within 8 hours of dialysis, which was followed by an extended cesium release of 43% over the next 64 hours. A Zeta analysis of the particle's electrophoretic potential (ζ) showed that both the NanoCs and CP have a negative surface charges (-24 ± 4 and -42 ± 5 mV, respectively). Since both particle variants (CP and NanoCs) had zeta potentials below -20 mV, they are predicted to have strong colloidal stability[28,29] (Figure 2.7). Furthermore, the significantly more negative ζ of CP compared to NanoCs indicates that NanoCs will have a lower probability of developing a protein corona before reaching its intended target.[30] Anhydrous diameter (D_{ah}) and morphology of NanoCs particles were assessed by Transmission Electron Microscopy (TEM). These TEM micrographs determined that CP and NanoCs both possess spherical traits in nature (Figure 2.8, Figure 2.9) and furthermore displayed D_{ah} of 25 ± 6 and 27 ± 6 nm, respectively as measured by ImageJ analysis (n=100 each) (Figure 2.10). NanoCs and CP were analyzed for D_{hy} stability over the course of 30 days (stored at 4 °C) and were found to maintain significant integrity (Figure

2.11). In order to assess its systemic stability, hydrodynamic diameter of both NanoCS and CP were monitored over the course of 7 days at 37 °C in pH 4.5 (HCl), 7.4, and 12 (NaOH), nanopure water (0.2µm), and fetal bovine serum (FBS, 10%). Over the course of one week, CP integrity remained consistent (Figure 2.12), while NanoCs particle diameter increased slightly in lower pH but persisted under other conditions (Figure 2.13). This result ensured the systemic stability of the particles minimizing the possibility of aggregation.

Cesium's high atomic z number (z=55) led to an increased electron density within NanoCs particles which could be observed *via* electron microscopy, as compared to organic moieties consisting of carbon, hydrogen, and oxygen that are found in CP (as confirmed by FTIR (Figure 2.14, Figure 2.15) and Raman spectrometry (Figure 2.16a, b)). Further ImageJ analysis on TEM images revealed that the contrast within CP was orders of magnitude higher than NanoCs (Figure 2.17). This difference in white (high intensity) versus black (low intensity) pixels indicates that NanoCs particles have a higher atomic density due to the presence of cesium ions (z=55) and thus leads to a lower pixel value within TEM micrographs. After hydrated and anhydrous state characterization through light scattering and electron microscopy, atomic force microscopy (AFM) was used to determine particle height and surface topography (Figure 2.18). The measured CP and NanoCs heights were 11 ± 5 and 25 ± 3 nm respectively, confirming that the particles were indeed morphologically spherical.

Figure 2.1: Schematic representation of NanoCs synthesis. Cs^+ ions interact with negatively charged acrylic acid groups in the particle.

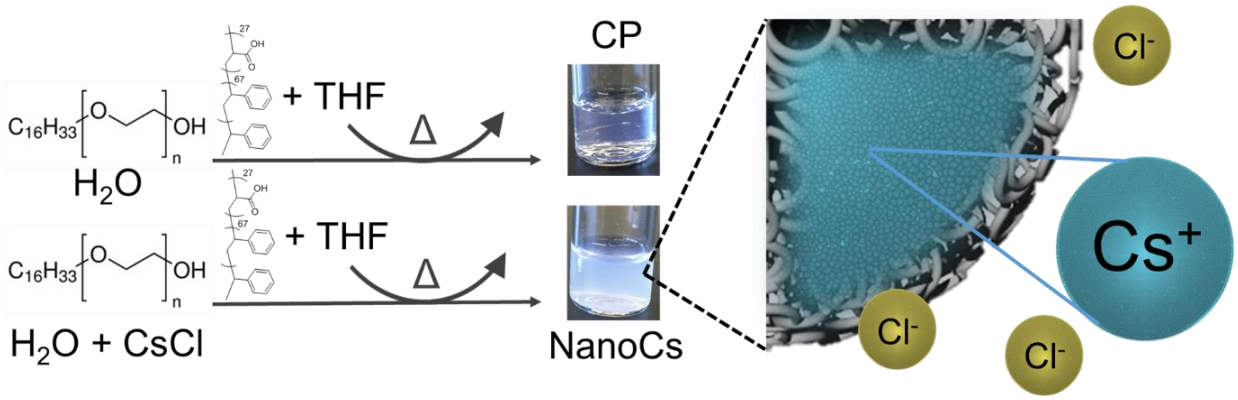

Figure 2.2: Bar graph representation of Cs^+ entrapment optimization via hydrodynamic diameter analysis.

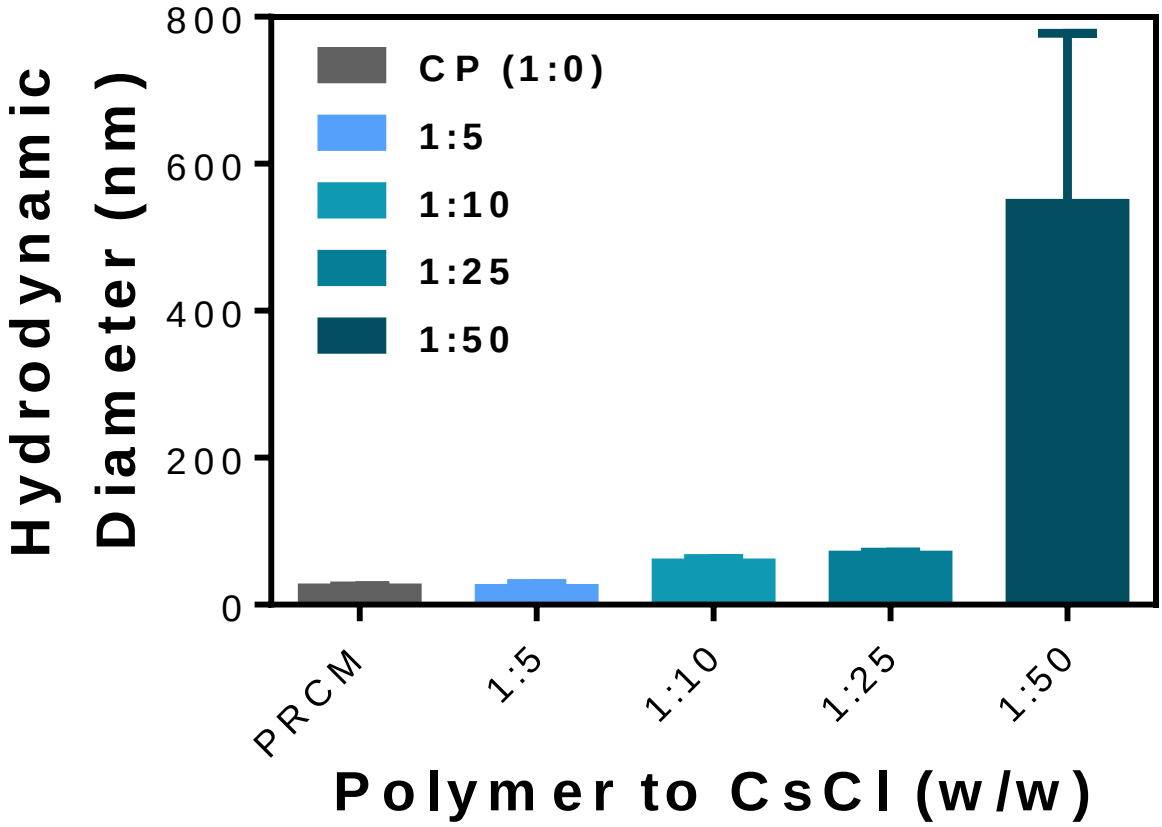

Figure 2.3: Overlaid histogram representing the number averaged (%) of CP and NanoCs particles.

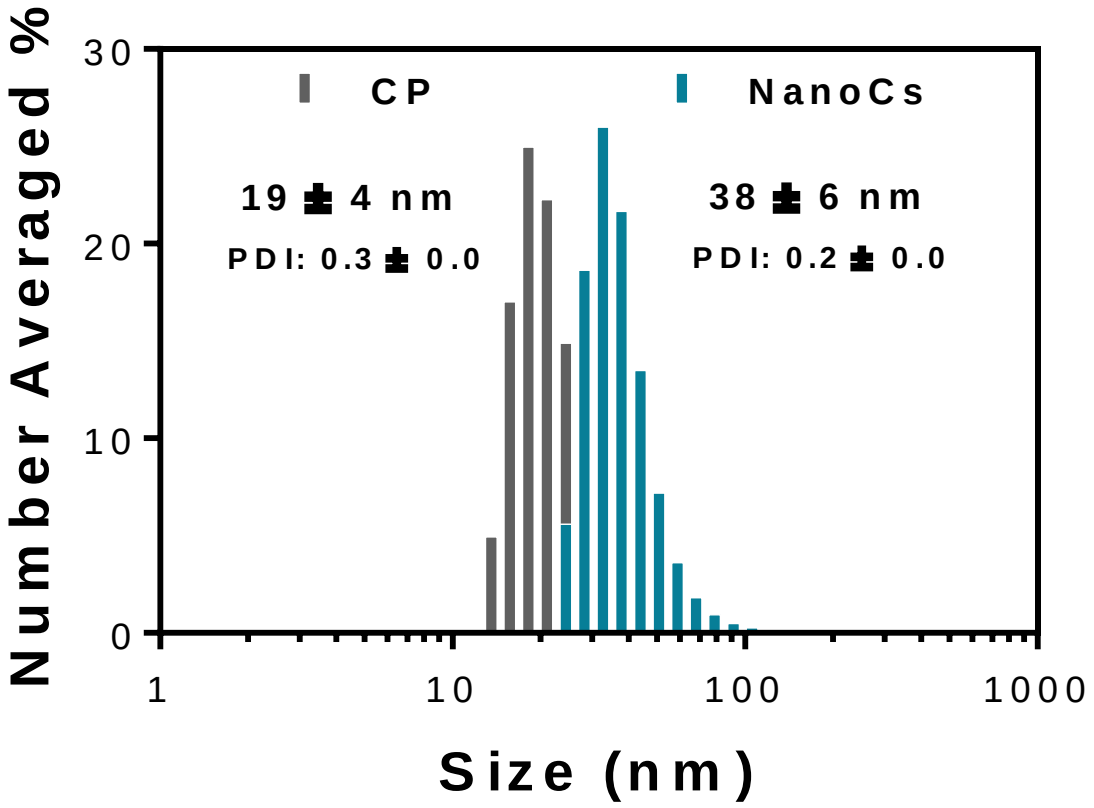

Figure 2.4: EDS analysis on (a) CP and (b) NanoCs to identify cesium peaks (shown with black arrow).

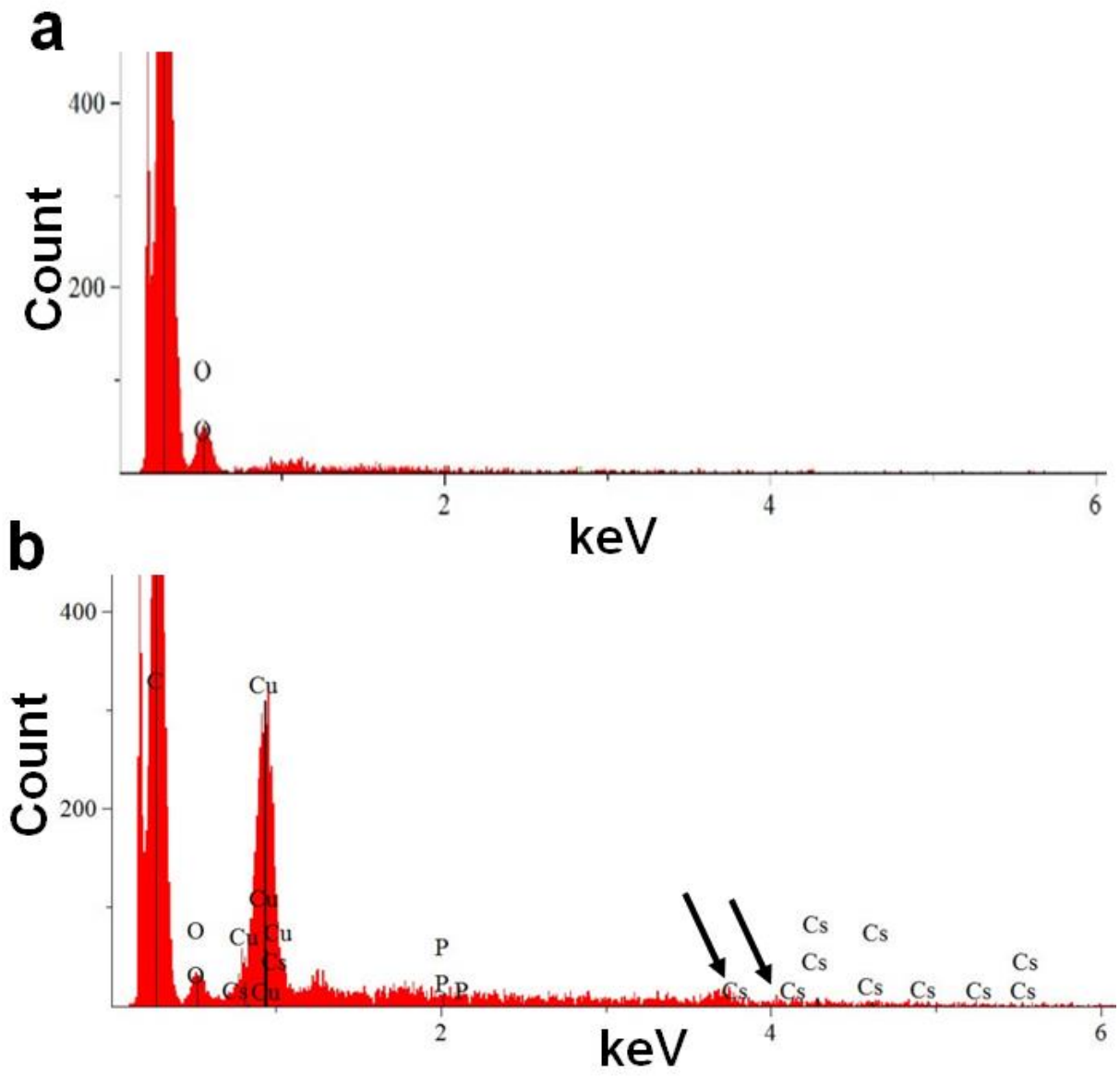

Figure 2.5: SEM image of NanoCs used for EDS.

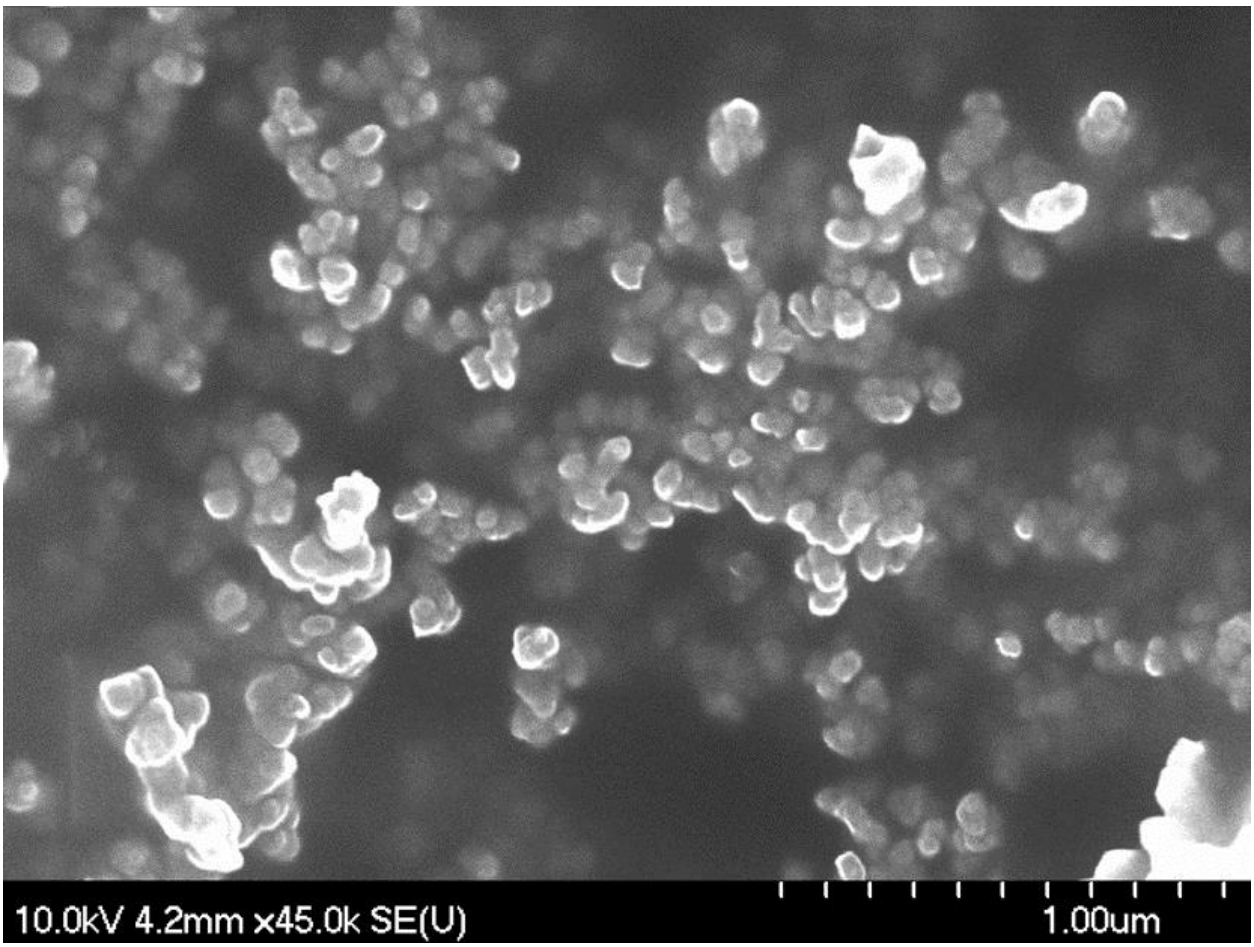

Figure 2.6: a) NanoCs Cesium release profile over the course of three days as measured by ICP-OES in parts per million (ppm). b) Percent of cesium released as a function of time.

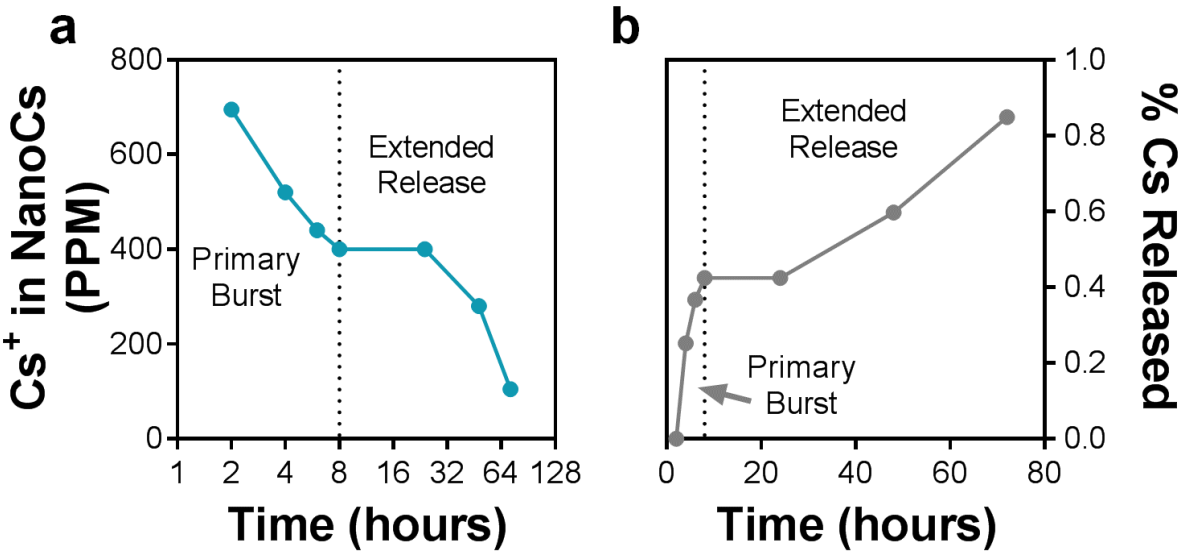

Figure 2.7: Surface charge as measured by Zeta potential of CP and NanoCs. Student's T test was used to measure statistical significance ($p < 0.05$).

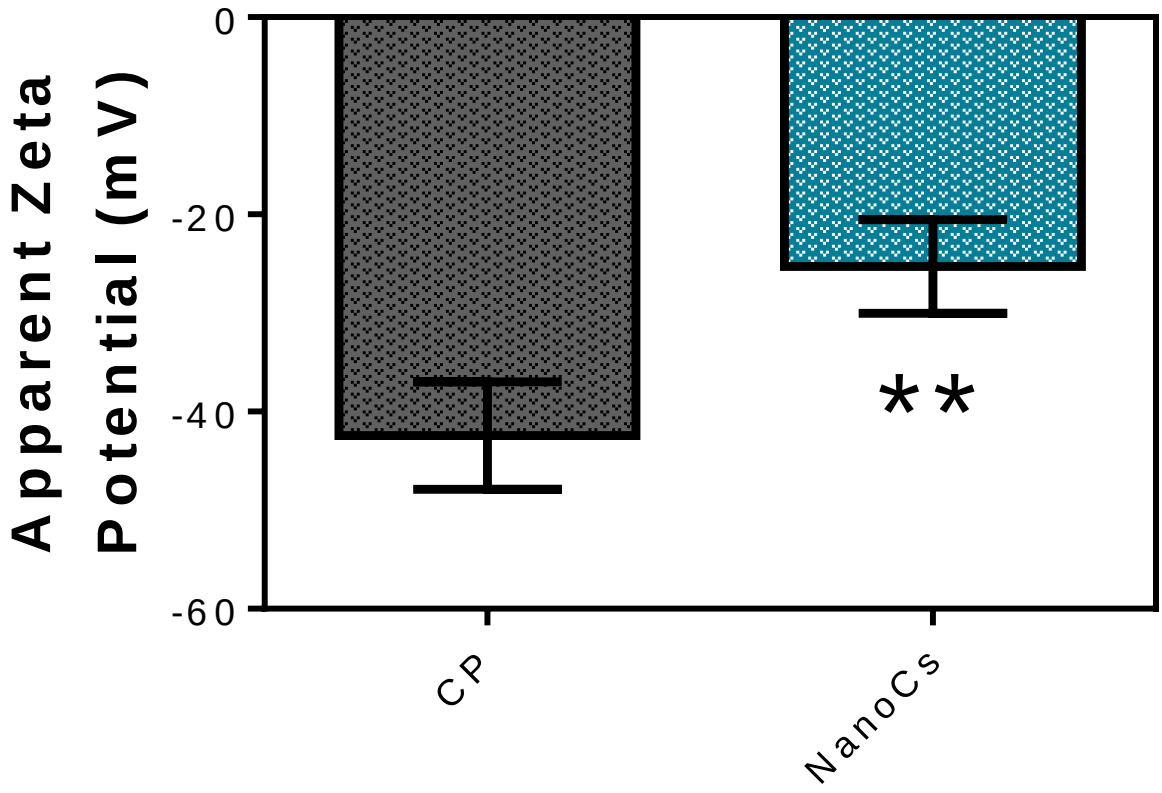

Figure 2.8: TEM micrograph of CP. Within the figure is an inset of a particle at higher magnification for detail.

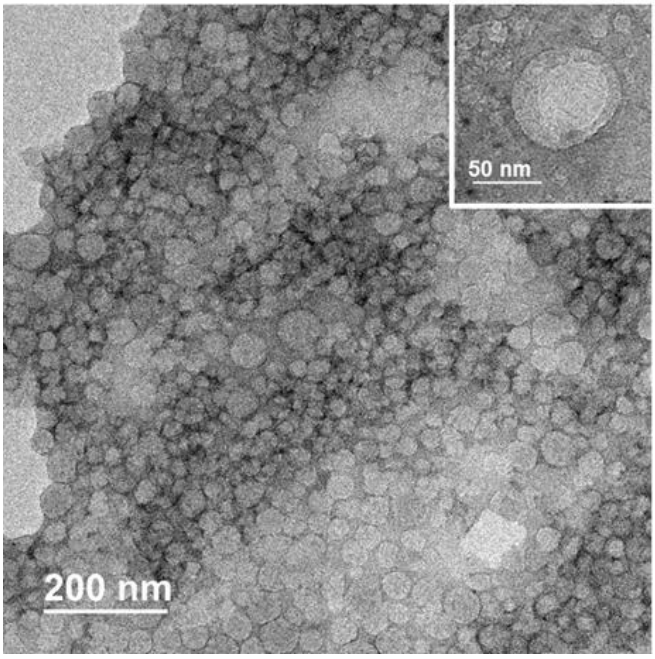

Figure 2.9: TEM micrograph of NanoCs. Black arrow shows cesium collection within NanoCs particle. Within the figure is an inset of a particle at higher magnification for detail.

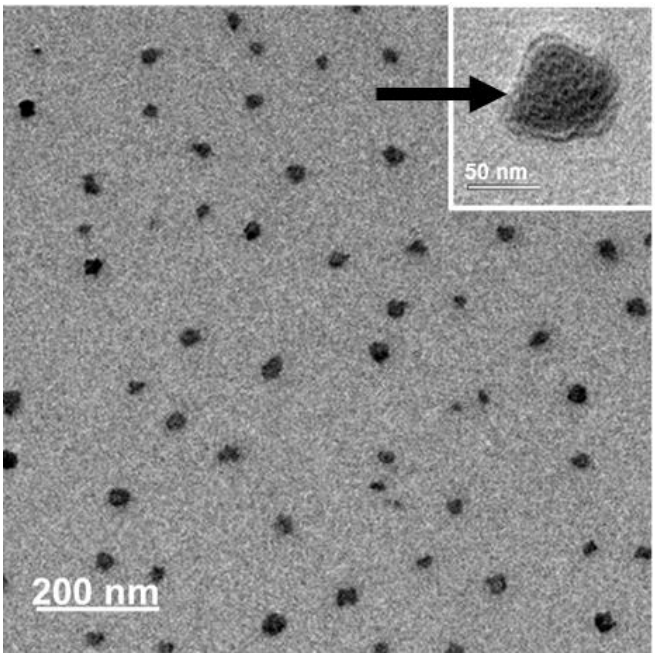

Figure 2.10: ImageJ analysis of anhydrous particle diameter (n=100).

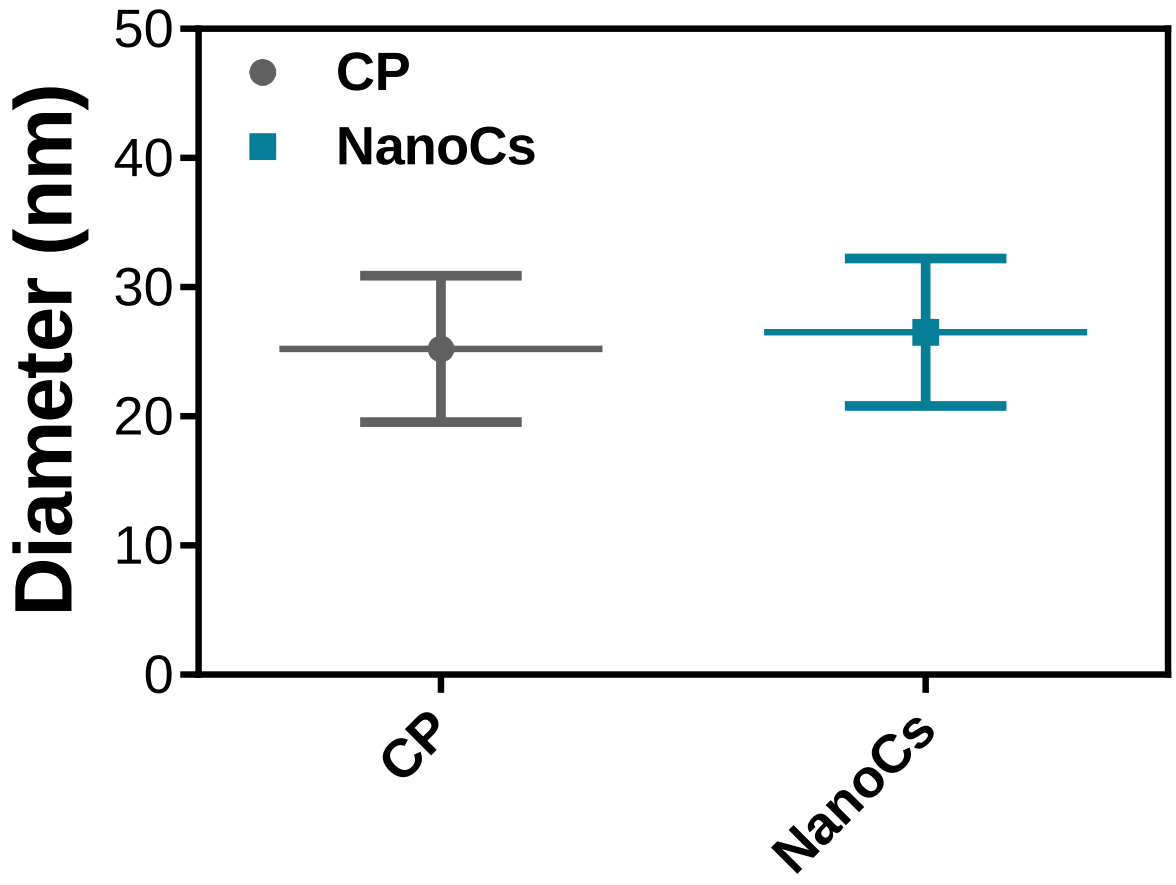

Figure 2.11: Long term shelf life stability analysis (measured over 30 days) of CP and NanoCs hydrodynamic diameter. X-axis is in Log_2 scale.

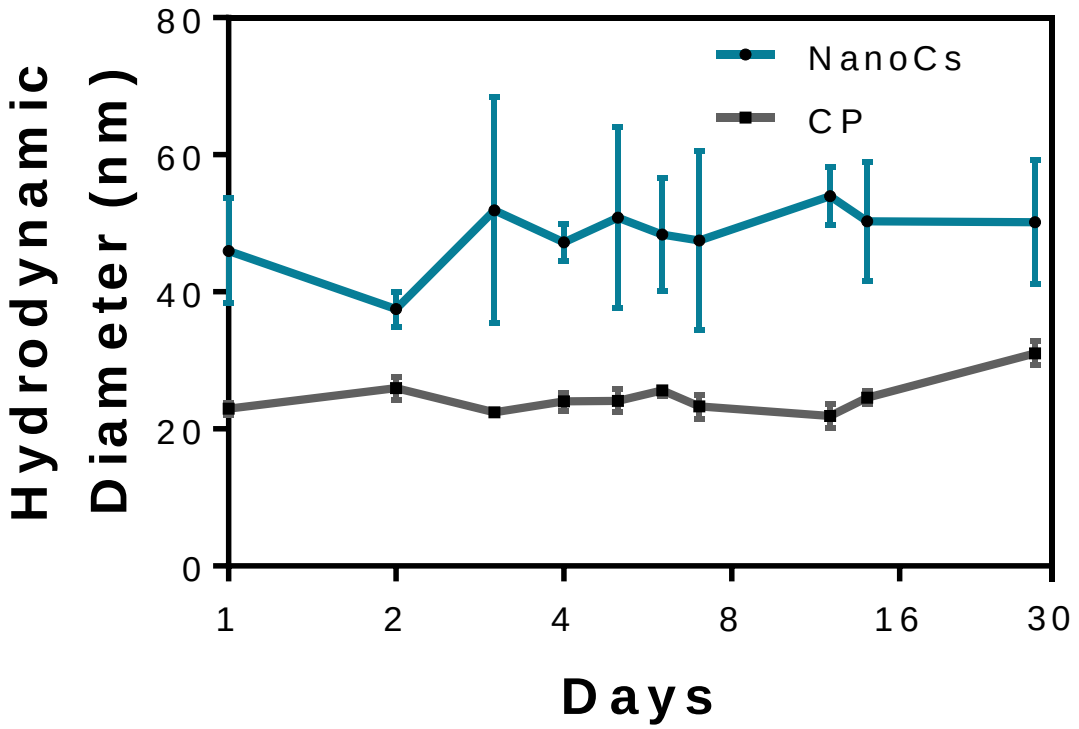

Figure 2.12: Hydrodynamic diameter stability of CP in various environments measured over the course of seven days.

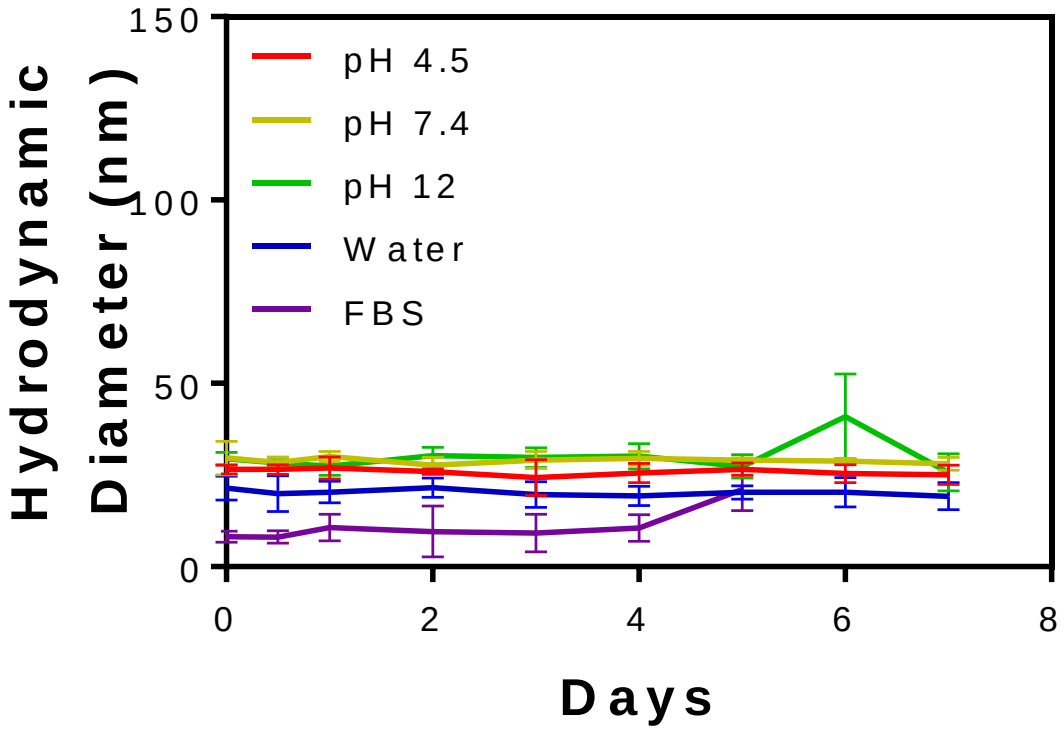

Figure 2.13: Hydrodynamic diameter stability of NanoCs in various environments measured over the course of seven days.

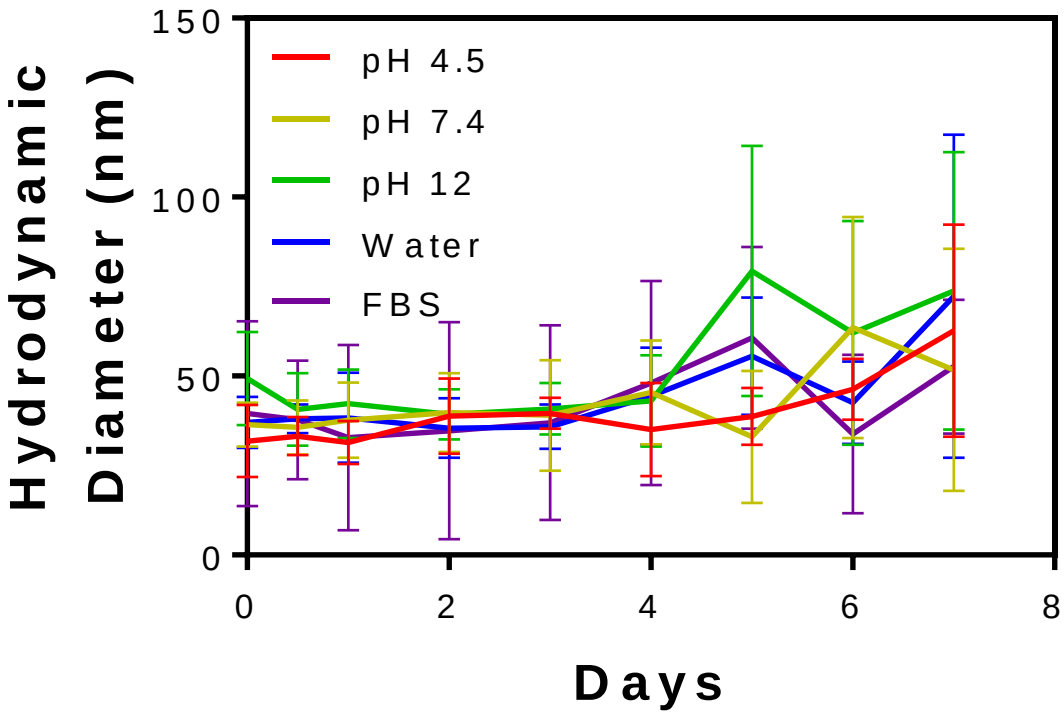

Figure 2.14: FTIR analysis of CP composition. (a) Near-mid infrared spectrum of respective samples. (b) Near-infrared spectrum close up of black boxed outline in (a). Peaks are assigned to common molecular structures found in CP particles.

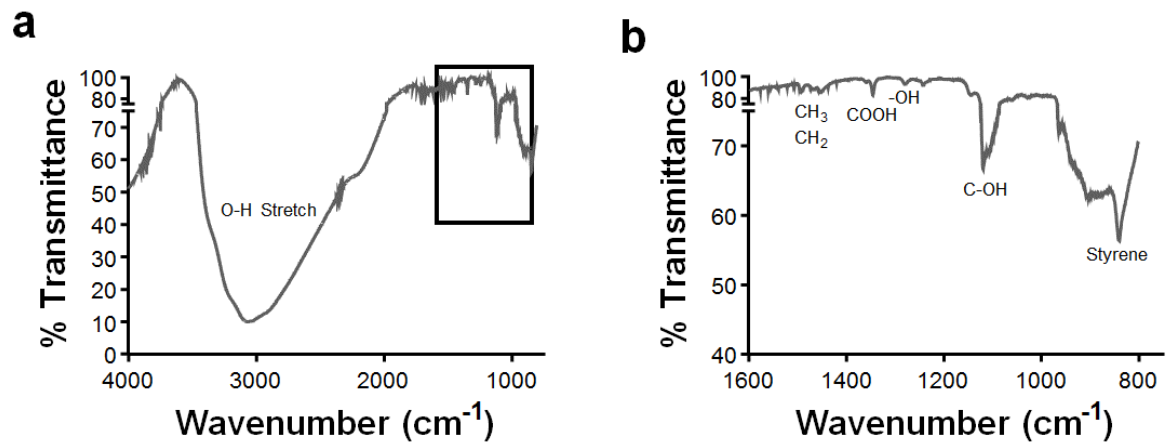

Figure 2.15: FTIR analysis of NanoCs composition. (a) Near-mid infrared spectrum of respective samples. (b) Near-infrared spectrum close up of black boxed outline in (a). Peaks are assigned to common molecular structures found in NanoCs particles.

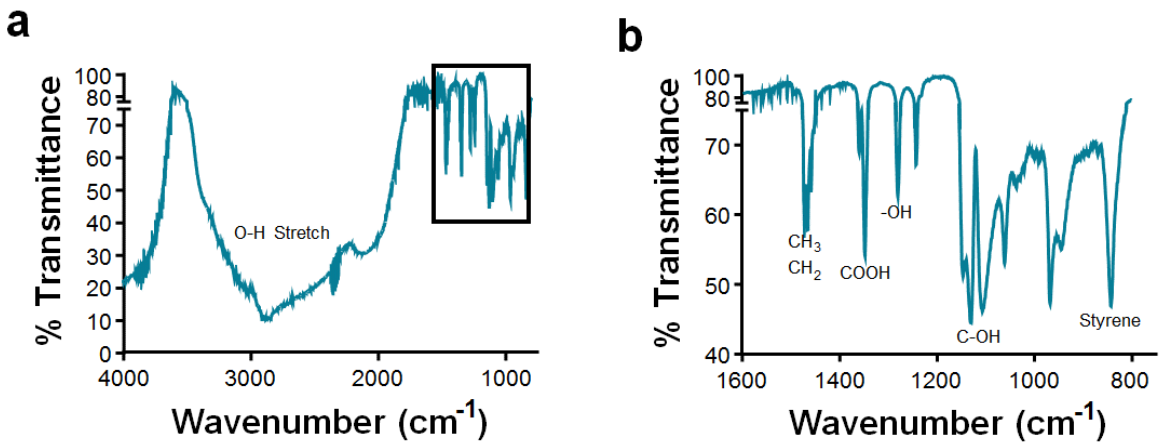

Figure 2.16: Raman analysis of (a) CP and (b) NanoCs composition. Peaks are assigned to common molecular structures found in CP particles.

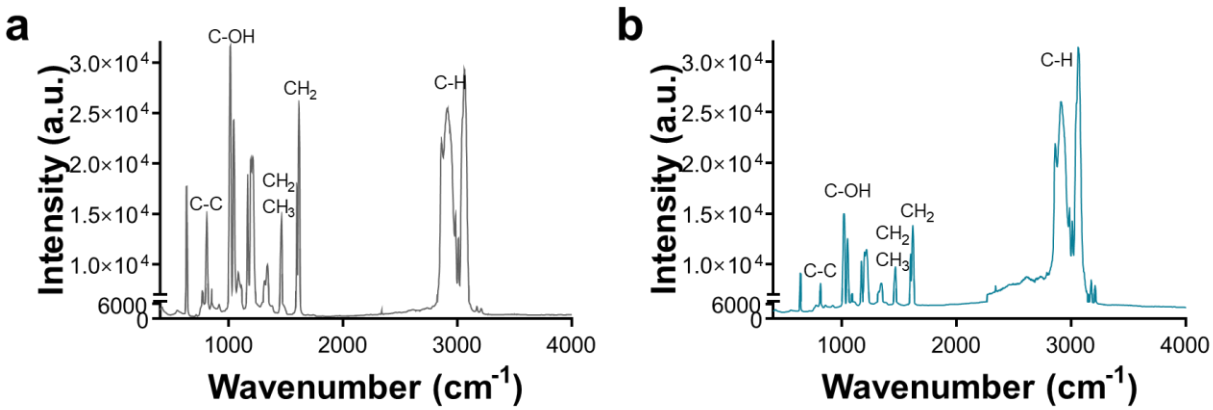

Figure 2.17: ImageJ analysis of pixel intensity of particles TEM micrographs (white pixel = high intensity, black pixel = low intensity).

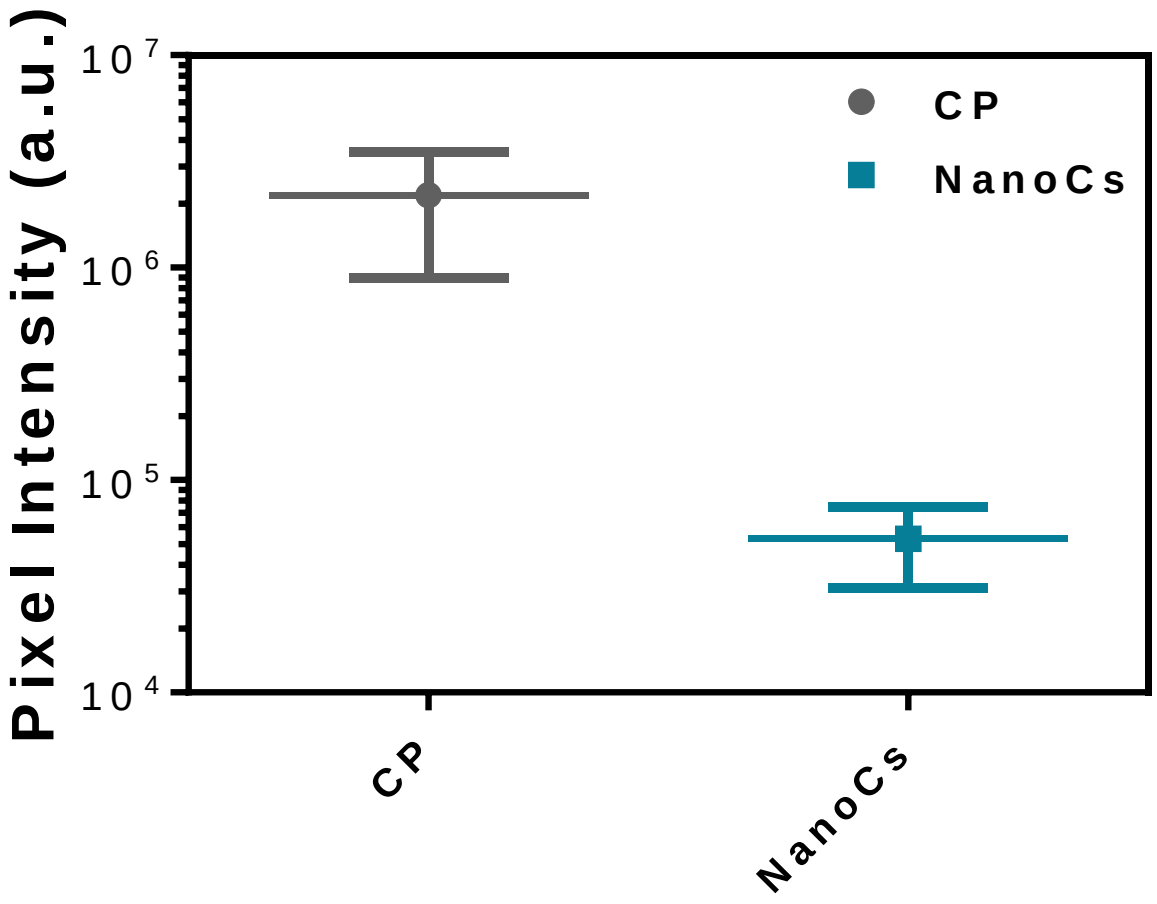

Figure 2.18: AFM plot of anhydrous NanoCs particles.

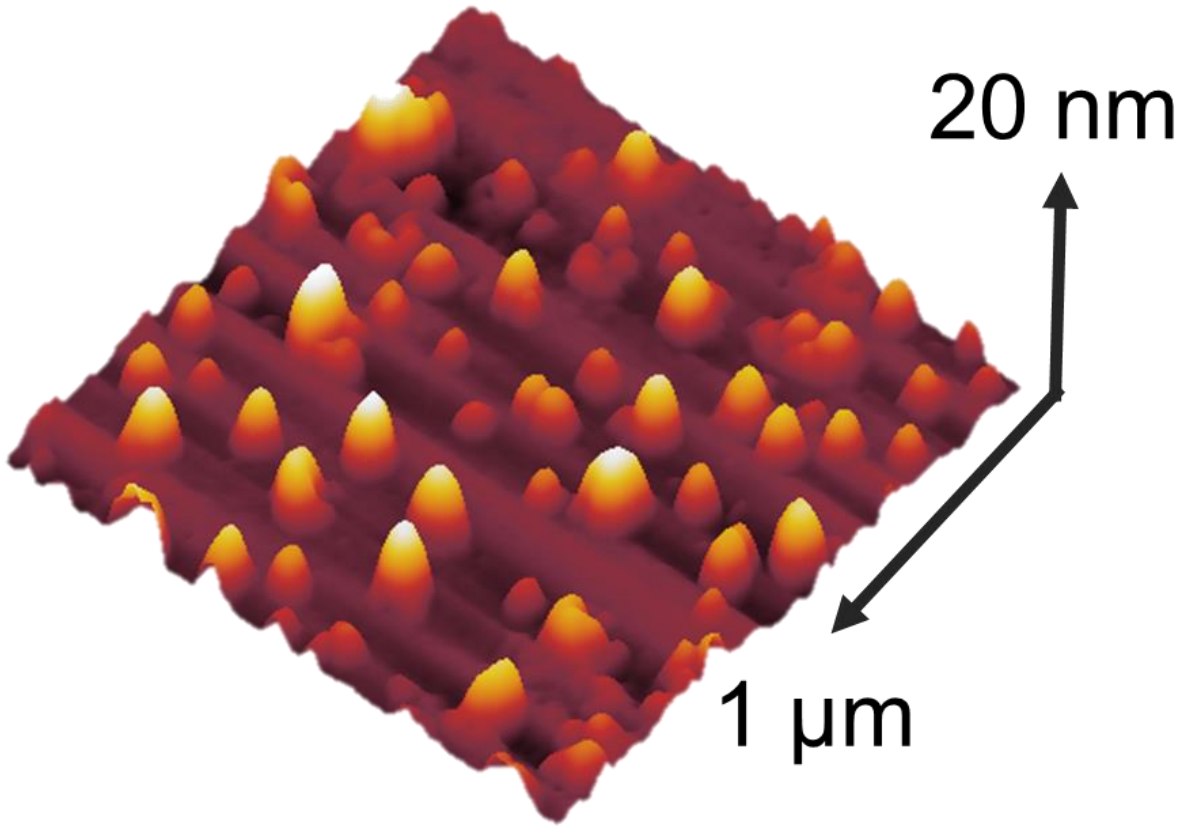

Biocompatibility Profile and Cellular Response to Cesium Chloride and NanoCs Treatments

To fully capitalize on the *in vivo* nanoparticle – EPR effect combination, an *in vitro* biocompatibility assay was necessary to understand NanoCs and free CsCl toxicity. An estrogen receptor positive, human breast cancer cell line (MCF-7) was cultured in triplicate at a density of 10,000 cells per well for cytotoxicity measurements *via* MTT reduction assay. MCF-7 cells were treated with various concentrations of CsCl from 1000 µM to 15.6 µM. NanoCs samples used to treat cells were calculated at a CsCl equivalence concentration from 1000 µM to 15.6 µM based on concentrations of Cs^+ within particles as determined by ICP-OES. Finally, CP samples used to treat cells were calculated based on volume equivalence of NanoCs samples, in order to keep particle concentration, the same (Figure 2.19). Cell viability, as measured by percent difference from control, in the presence of free CsCl returned a 48-hour exposure IC_{50} of 250 µM, while NanoCs showed significantly higher toxicity with a 48 hour IC_{50} of 77 µM (Figure 2.20, Figure 2.21). As expected, MCF-7 cells remained largely unresponsive to CP samples. These variations in cell viability between free CsCl solution and NanoCs are considered biologically significant with a p-value less than 0.001. As a result, we can conclude that NanoCs is outperforming the delivery of Cs^+ ions to the cells.

Figure 2.19: Bright field images of MCF-7 cells at 20X. The treatment concentration is 62.5 µM (Scale bar: 50 µm).

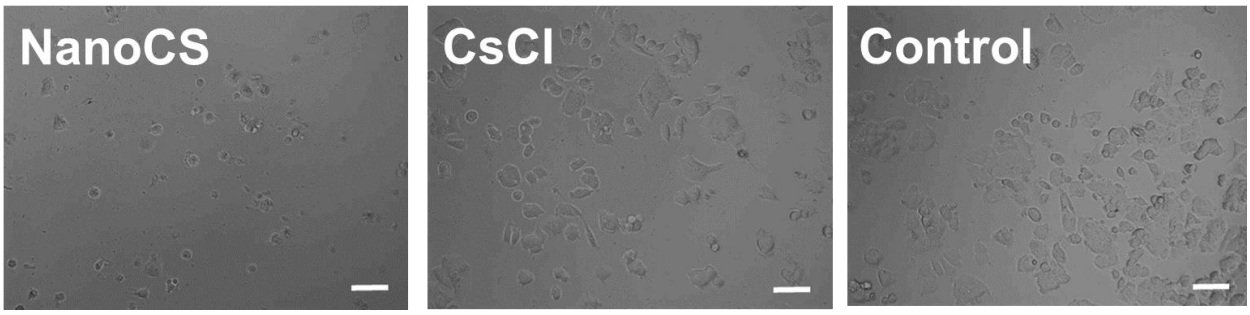

Figure 2.20: Cell viability of NanoCs, CP, and CsCl as a percent ratio to control cells. Concentrations of NanoCs were treated in molar equivalence to CsCl, and CP was treated in volume equivalence to NanoCs.

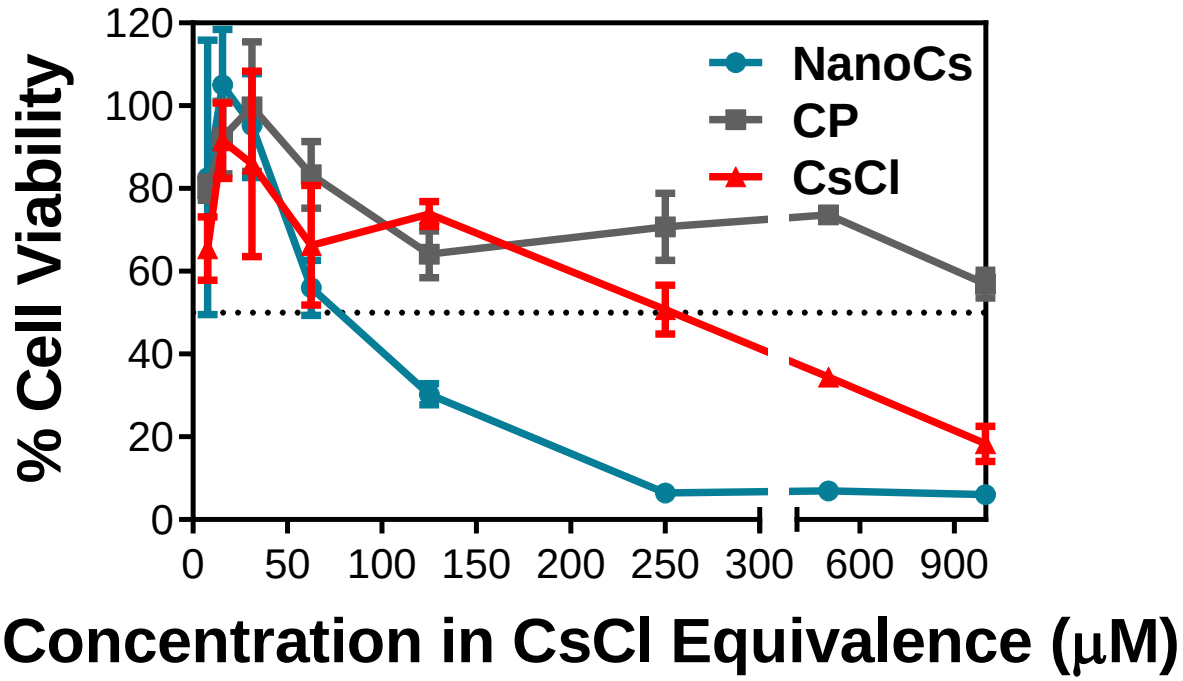

Figure 2.21: Bar graph detailing IC_{50} values of NanoCs as compared to CsCl alone (t-test for significance, $p<<0.01$).

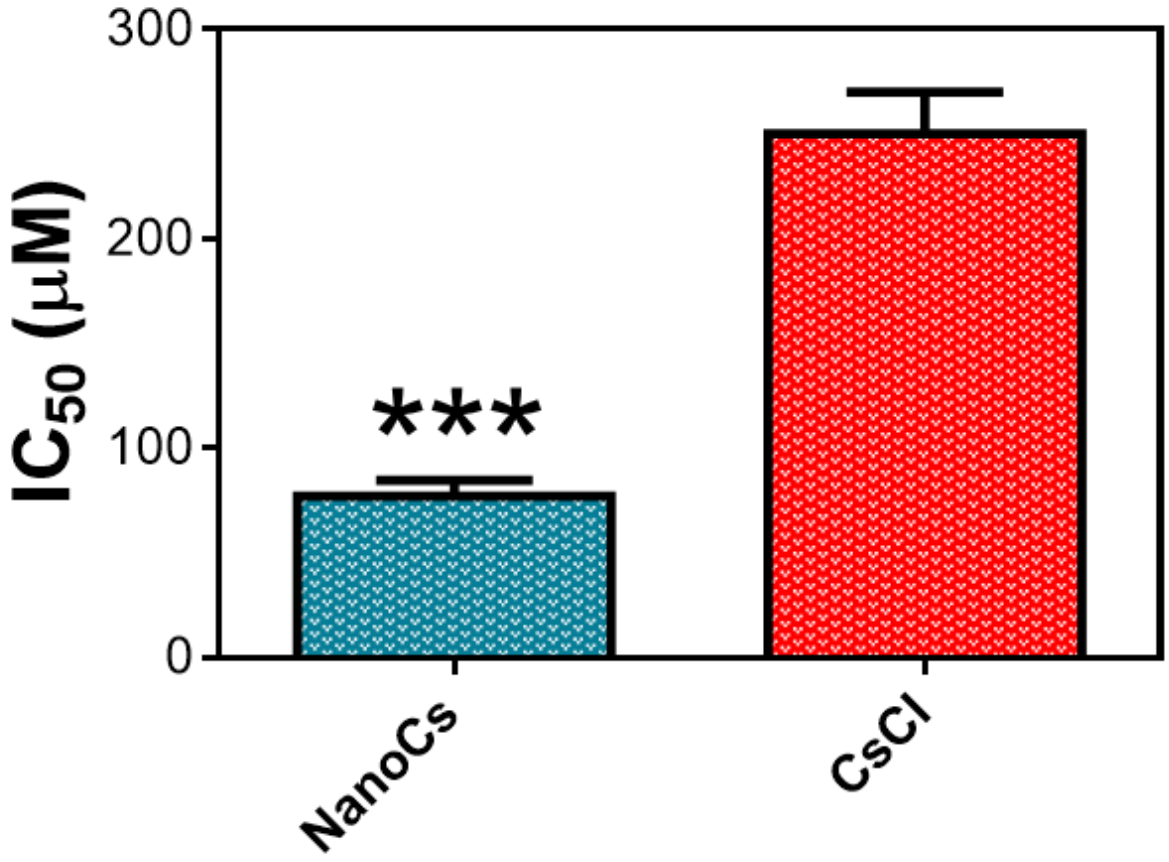

Further investigations into the cellular entry mechanisms of NanoCs particles were performed via independent endocytic inhibitors to predict the primary internalization pathway. Of inhibitors, we considered clathrin mediated entry inhibition by chlorpromazine and Dynasore, clathrin-independent endocytosis inhibition by Nystatin, and energy dependent uptake inhibition by sodium azide with 2-deoxyglucose (NaN_3/DOG). Since NanoCs internalization directly correlates to cell viability, we used an MTT reduction assay to compare inhibition effects with control samples. MCF-7 cells were first exposed to inhibitors for one hour before dPBS washing and 24 hour NanoCs incubation (Figure 2.22). Chloropromazine, a clathrin protein translocator,[31] nystatin, a caveolae disassembly agent,[32] and NaN_3/DOG, an inhibition combination of glycogenolysis and cellular respiration,[33] all showed the highest cell viability. Contrarily, dynasore, an inhibitor of dynamin dependent clathrin mediated endocytosis,[34] showed lower cell viability compared to the other formulations. This information indicates that the NanoCs particle is versatile transportation vehicle for cellular internalization and takes part in multiple endocytic pathway for delivering cesium ions within the cell.

Figure 2.22: Investigations of NanoCs mechanism of cellular internalization. a) Control cells treated with inhibitors of various endocytic pathways. b) Cells treated with endocytic inhibitors for 1h followed by incubation with NanoCs particles for 24 h.

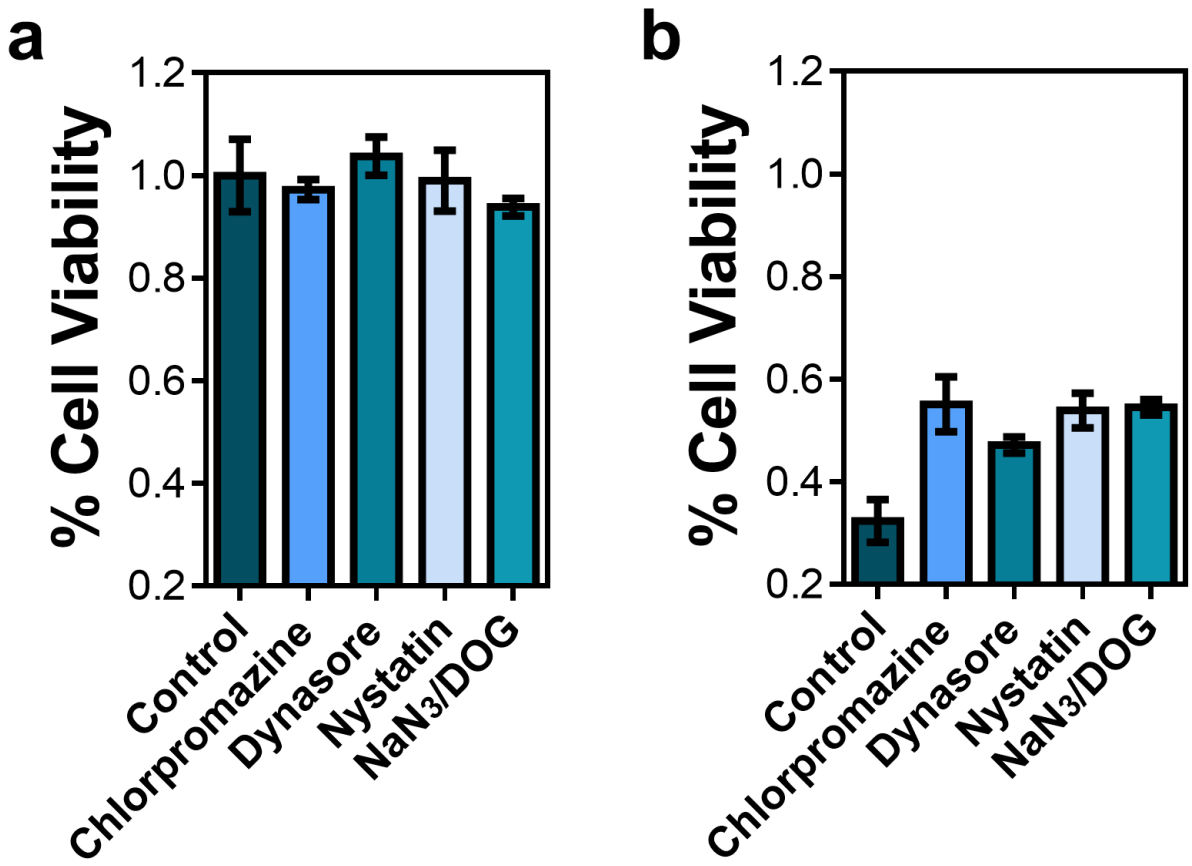

Experimental Validation of Proposed 'High pH Therapy' Theory

A common assumption, of CsCl when used as an "alternative therapy", was that free Cs^+ would lead to an increase in intracellular pH where cellular mechanisms cease leading to cell death.[6–8] Experimental proof in support of this mechanism is rather weak as conflicting literature reports exist.[6–8] However, it was theorized that the acidic nature of tumor cells, due to high cellular activity and glucose decomposition to lactic acid (also known as the Warburg effect[35]), will cause the cell membrane to act as a moderately strong electron donor and thus drastically enhance the permeability for Cs^+ [6,8]. As a salt, CsCl does not have the ability to change the pH of neutral water due to its role as a spectator ion. To grasp CsCl's effect on a low pH solution, an unbuffered nanopure water sample was decreased to pH 4.1 with hydrochloric acid and monitored *via* pH probe while supplemented with the gradual addition of CsCl salt. Interestingly, as the concentration of CsCl increased, we observed the pH of the system moderately increase until it reached 300 mM and subsequently flat lined without surpassing pH 4.8 (650 mM being the maximum concentration tested) (Figure 2.23). This noticeable increase in observed pH can be explained by the Debye-Huckel equation (Equation 2.1), whereby increasing the ionic concentration of a solution decreases the activity of the hydrogen ions, not the actual content[36–38].

Equation 2.1 $$\alpha_C = \gamma \frac{C}{C^e}$$

Will the decline in hydrogen ion activity *via* CsCl exposure lead to anti-cancer properties? The observed pH phenomena raised a larger issue regarding the extraneous amount of CsCl needed to reduce the activity of hydrogen ions in a non-buffered environment by a few units. Knowing that cells contain natural buffers, a large intake of this salt could lead to various other cellular issues

before hydrogen ion activity decreases enough for the theorized pH-driven apoptosis becomes the cause of cell death.

Figure 2.23: Dot plot of CsCl concentration versus pH when added to pH 4 water.

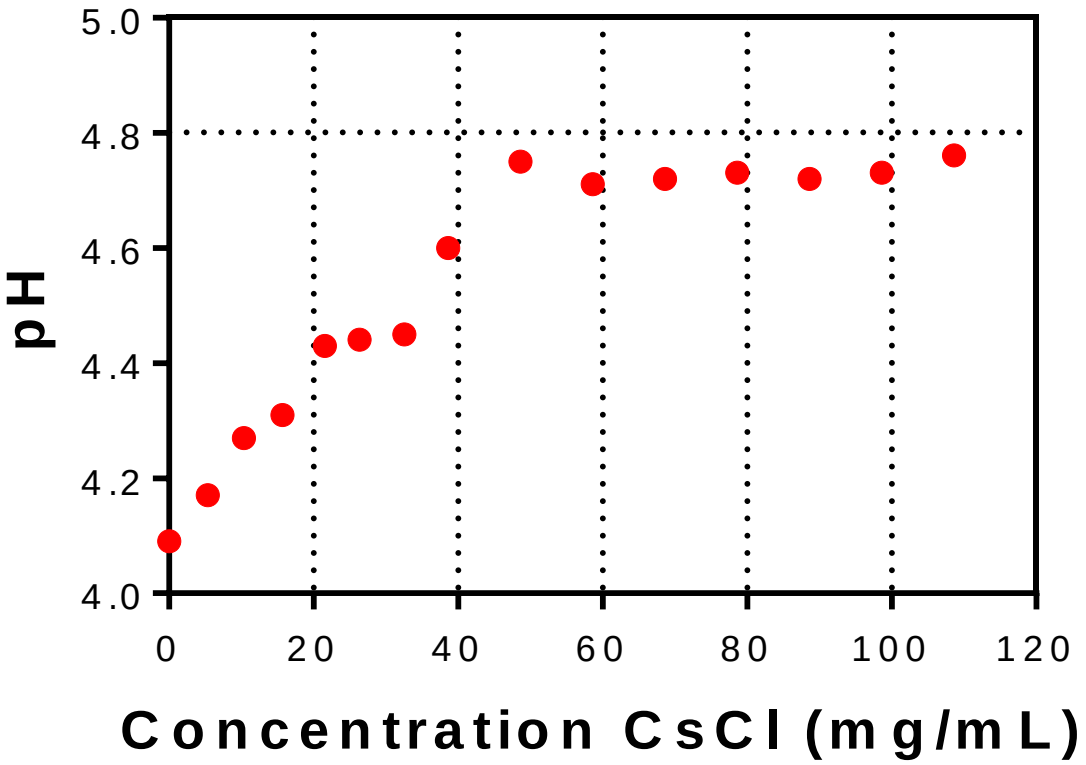

To further probe any possible intracellular pH change due to decreased hydrogen ion activity during CsCl exposure, the cell permeable pH sensitive fluorescent dye carboxy seminaphtharhodafluor (SNARF-1), was used to quantify NanoCs and CsCl pH transitions within the MCF-7 breast cancer cell line. Carboxy SNARF-1 (Figure 2.24) is known to alter its fluorescent properties under different cellular pH conditions.[39] SNARF-1 produces an emission peak at 585 nm (green fluorescence) for acidic conditions (maximum emission at pH 6) and 640 nm (red fluorescence) for basic conditions (maximum emission at pH 9) when excited at 488 nm. Before confocal imaging, MCF-7 cells were exposed to SNARF-1,[40], washed and then treated with respective samples at 100 µM CsCl, 100 µM CsCl equivalent of NanoCs, and CP at NanoCs volume equivalence. Treated cells were incubated at 37 °C and 5% CO_2 for 4 hours, then washed and fixed for confocal imaging. All images in the 585 emission window were corrected for cellular auto-fluorescence (Figure 2.25a-j). A non-cancerous breast cancer cell line (MCF-10A) prepared in a similar fashion, was loaded with SNARF-1 and imaged as a positive control since non-cancerous cells possess a close to neutral intracellular pH as compared to the acidic intracellular nature of tumor cells (Figure 2.25i-j). Confocal images and intensity quantifications were performed by a Zeiss 700, 20X objective, with gain and laser power consistency among all samples. The ZEN Blue image processing program was used to quantify MCF-7 intensity readings per pixel and revealed that the pixel intensity peak ratio (PIPR) of protonated (acidic environment) to the deprotonated (basic environment) form of SNARF-1 did not drop below 2 (Figure 2.25b, d, f, h, Figure 2.26) indicating that the amount of Cs^+ delivered did not significantly change the intracellular pH. Given that we had delivered Cs^+ above IC_{50} value (70 µM), any higher concentrations of CsCl would have led to cellular death and unreliable SNARF-1 intensity

comparisons. As expected, the non-malignant MCF-10A cell line produced a much lower PIPR value (0.29 ratio of deprotonated to protonated SNARF-1) (Figure 2.25i, j).

Figure 2.24: SNARF-1 AM structure.

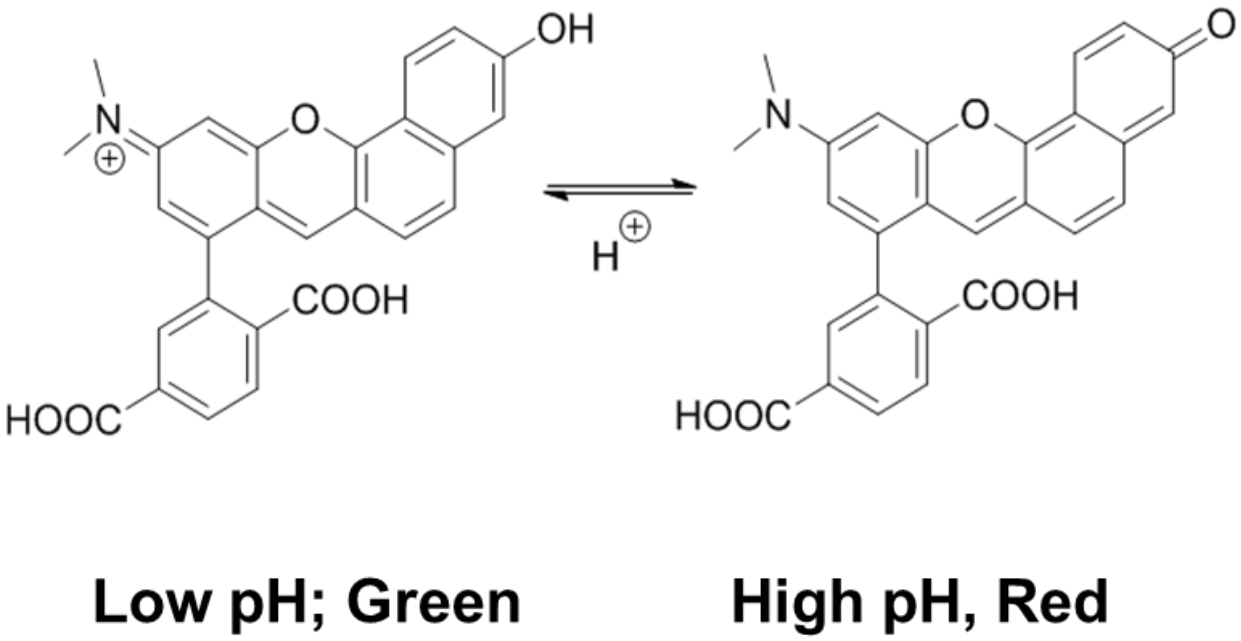

Figure 2.25: SNARF-1 confocal images and pixel intensity peak analysis of MCF-7 and MCF-10A for investigations into possible CsCl induced pH change. (a-h) Confocal images of MCF-7 cells loaded with SNARF-1 and treated with respective samples at 100 µM of CsCl concentration equivalence. b, d, f, h, and j is each treatment's unmodified pixel intensity with calculated peak ratios. (i, j) Positive control of SNARF-1 loaded MCF-10A cells (non-cancerous cell line) with a physiologically higher intracellular pH.

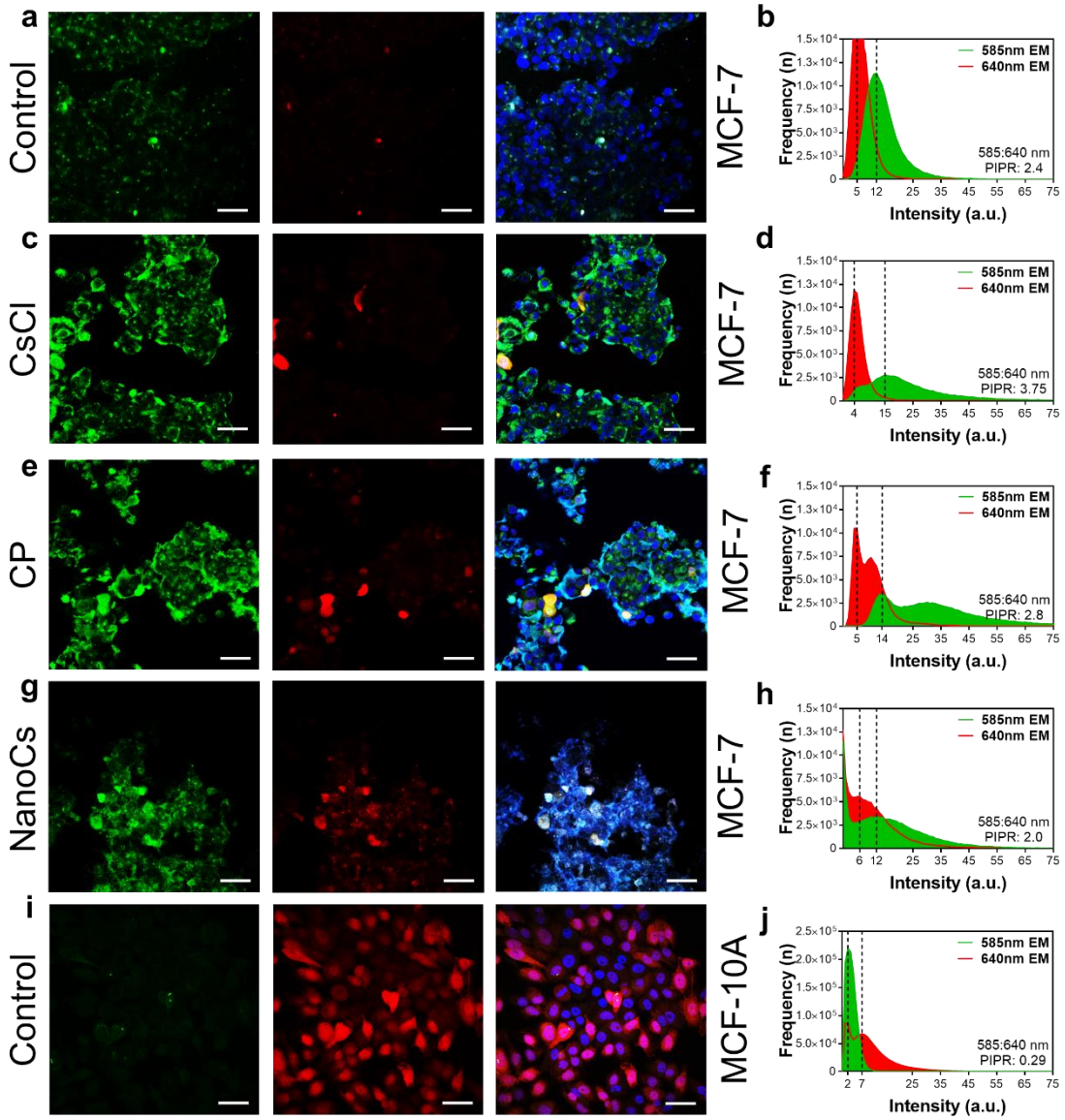

Figure 2.26: Bar chart of respective samples PIPR value.

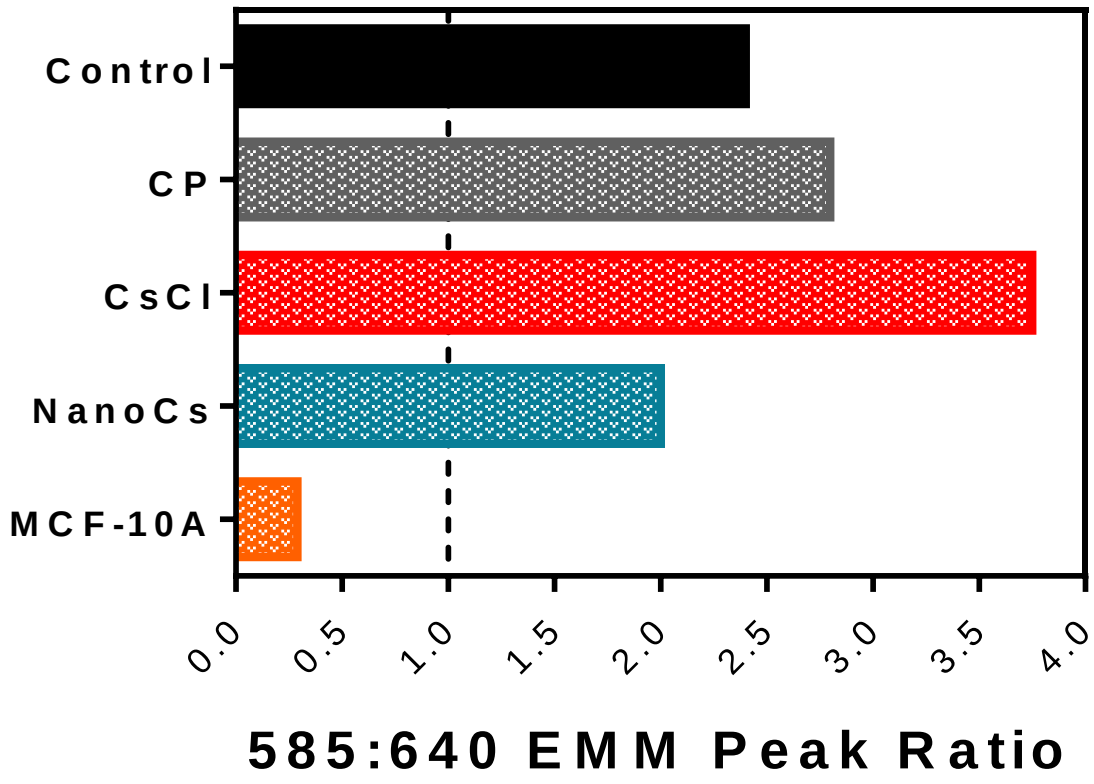

Investigation of NanoCs for Metabolic Therapy

In oncology, the Warburg effect[35] states that the high metabolic activity of cells is an incident characteristic of malignant cancer which leads to a vast and rapid consumption of the energy molecule adenosine triphosphate (ATP) necessary for rapid cellular division. As a result, tumor cells upregulate GLUT expression to keep up with glucose intake for ATP generation.[15] This consequence makes the targeting and inhibition of the GLUT pathway an area of high interest for treating basic to malignant forms of cancer. The GLUT pathway, and more specifically the Na^+/glucose cotransporter, is highly dependent on the electrochemical gradient, which can be disturbed if there was an imbalance of charges across the membrane due to an intake of foreign ions, or any disruption in Na^+/K^+ pump activity.

Internalization of Cs^+ (a positive ion), *via* NanoCs uptake, might initiate the destabilization of the electrochemical gradient as cells have no viable means of clearing Cs^+ from their system, and it would contribute to the internal membrane charge. Additionally, since CsCl leads to a decrease of free K^+,[13,14] which reduces the extracellular transport of Na^+ by the Na^+/K^+ pump, the Na^+/glucose cotransporter could cease to replenish the cells energy source and lead to cellular starvation.[41] Thus, metabolic therapy in the form of Cs^+ *via* reduction of GLUT activity could result in metabolic stasis, and induce cellular apoptosis.

To further examine this phenomenon, we used the fluorescently labeled marker 2-deoxy-2-[(7-nitro-2,1,3-benzoxadiazol-4-yl)amino]-D-glucose (2-NBDG) to visualize and quantify glucose uptake. This fluorescent 2-deoxy glucose analog has the ability to accumulate within living cells since it cannot be fully utilized in glycolysis following phosphorylation by hexokinase. Hence, 2-NBDG makes for an optimal marker in identifying any incidental glucose uptake

inhibition. An initial culture of MCF-7 was treated with a high dose of 2-NBDG (300 µM).[42,43] in order to obtain an understanding of its uptake activity at varied concentrations of CsCl, NanoCs, and CP after a four-hour exposure. Cytochalasin B (CB), a known GLUT inhibitor.[44] was used as a negative control for all 2-NBDG uptake investigations. The MCF-7 line was cultured in triplicate at a density of 12,000 cells per well in a 96 well plate. Before fluorescence analysis, cells were washed with dPBS and lysed with 50 µL of cell lysis buffer. A Synergy HT (Biotek, USA) plate reader, measured the fluorescent output (RFU) of each well's contents with an excitation wavelength of 488 nm. The fluorescence intensity readings were processed as percentage ratios to the control (RFU sample/RFU control) and revealed that cells treated with the NanoCs and CB samples had fluorescent intensities at less than 80% for all concentrations above 125 µM, indicating that NanoCs is presumably restricting glucose uptake comparatively to CB (Figure 2.27). Additional confirmation of glucose uptake inhibition through absorbance measurement of the sample at 480 nm was taken to confirm fluorescent results, and showed a similar pattern where CB caused the largest deficiency in 2-NBDG within cells followed by NanoCs, CsCl, and CP (Figure 2.28).

Figure 2.27: RFU analysis of 2-NBDG uptake by MCF-7 cells at various concentrations of NanoCs, CsCl, CP, and CB.

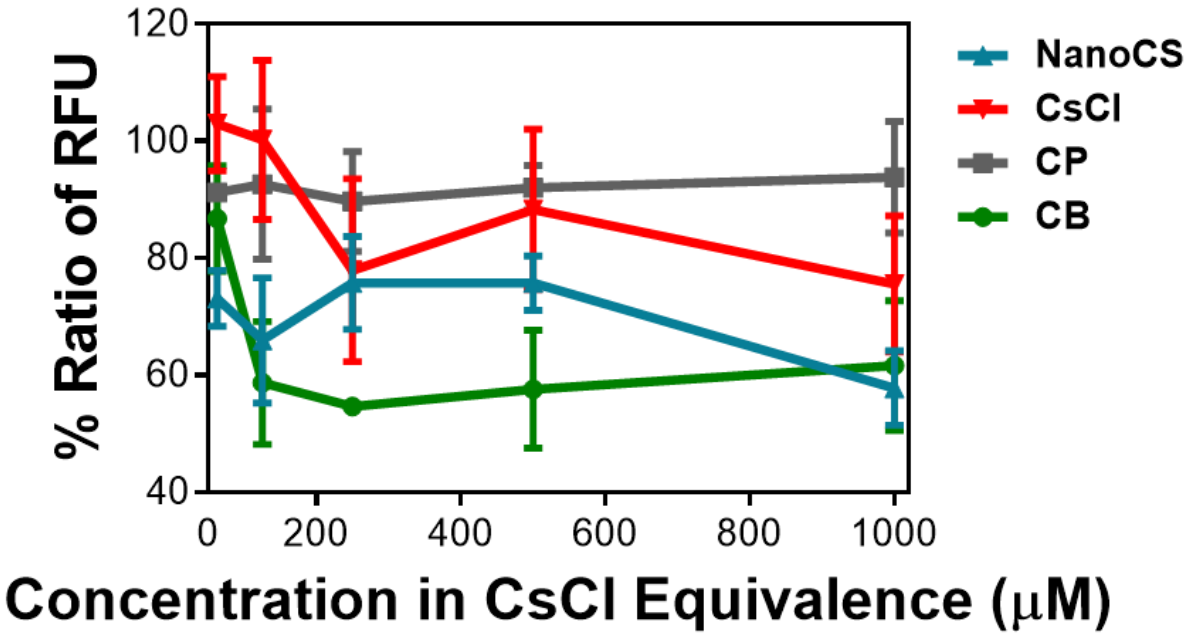

Figure 2.28: Absorbance graph of 2-NBDG loaded and lysed MCF-7 cells treated at various concentrations with respective samples for 4 hours.

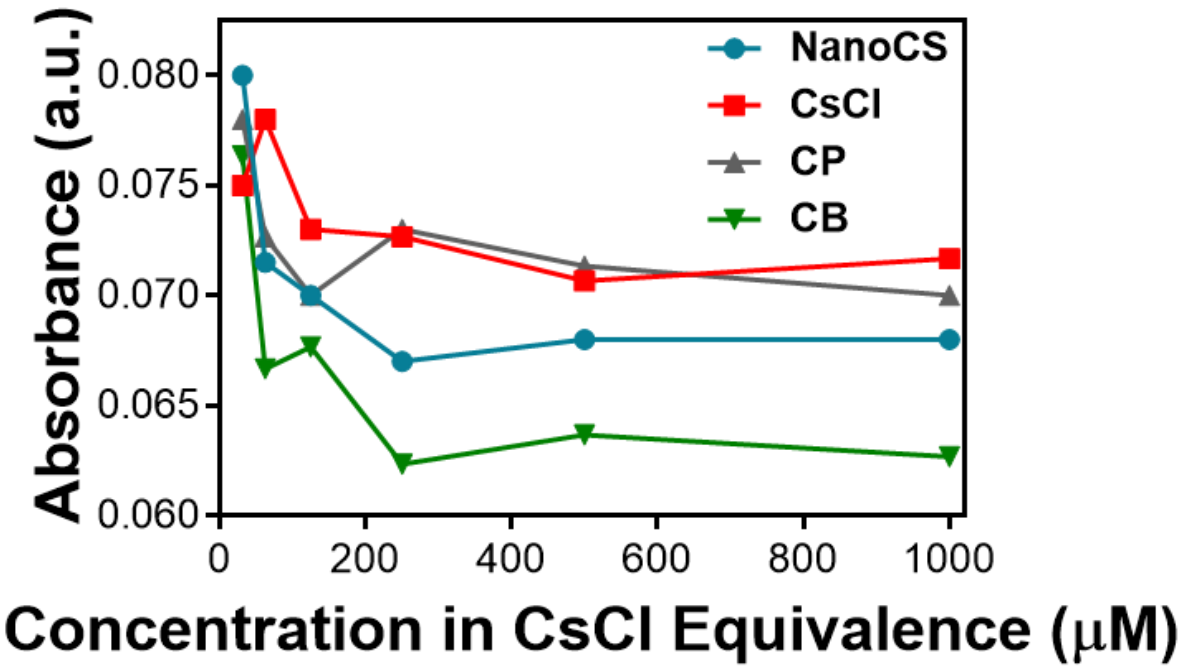

Flow cytometry of cells exposed to 2-NBDG can provide specific information on possible subpopulations affected by NanoCs exposure. Thus, MCF-7 cells were treated with 10 µM of 2-NBDG as previously reported,[42] prior to a four-hour incubation with 100 µM CB, CsCl, NanoCs at CsCl equivalence, and CP at volume equivalence to NanoCs at 37 °C. A Guava® EasyCyte Plus Flow Cytometer was used to count 5000 single cell events at an excitation of 488 nm for 2-NBDG fluorescence intensity readings. Since samples were being measured at the green emission wavelength of the flow cytometer, all samples were histogram subtracted from control values to eliminate any cellular autofluorescence signal. As previous data had suggested, CB exposure resulted in a highly effective suppression of 2-NBDG uptake, with NanoCs being the second most effective and followed closely by CsCl. CP and control samples showed high 2-NBDG uptake, with no apparent shift (Figure 2.29). To analyze how single-cell interactions with NanoCs may lead to inhibition of 2-NBDG uptake, confocal imaging, and single-cell fluorescent intensity analysis was performed on cellular samples treated in a similar fashion to the flow cytometry assay. Fixed and DAPI stained MCF-7 cells were excited at 488 nm for 2-NBDG fluorescence excitation. All images were corrected for cellular autofluorescence and analyzed for individual cellular intensity *via* ZEN Blue image processing software. Within control, CP, and CsCl samples it was evident that the 2-NBDG primary area of localization and accumulation was in the cytosol and not within cell nucleus or surrounding extracellular matrix. Additionally, each of these samples also showed evidence of high 2-NBDG localization within intracellular vesicles (Figure 2.30a-c). Nonetheless, NanoCs and CB samples both largely lacked signs of 2-NBDG accumulation and had no signs of vesicular entrapment within the cells (Figure 2.30d, e). Cells were measured for individual fluorescent intensities and averaged *via* ImageJ processing software, which reiterated

our hypothesis that NanoCs and CB had significantly decreased cellular 2-NBDG uptake with p values less than 0.001 (Figure 2.31).

Figure 2.29: Flow cytometry RFU histogram of MCF-7 cells treated with respective samples.

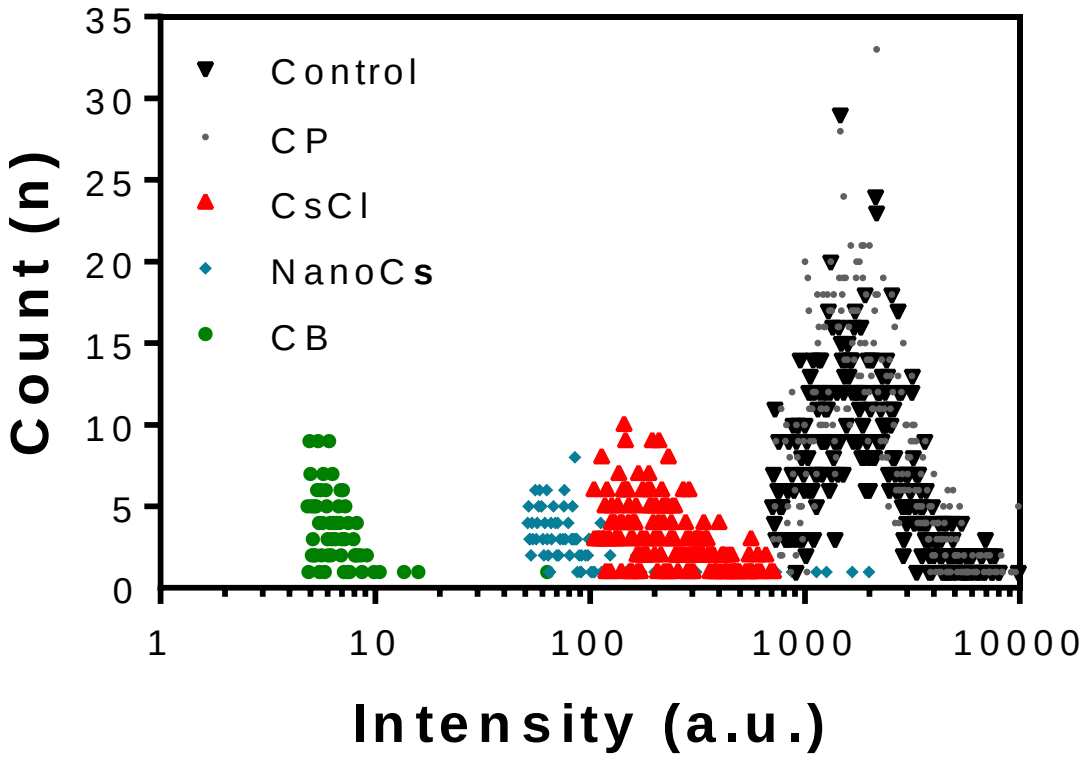

Figure 2.30: Differential interference contrast microscopy images and confocal images of MCF-7 cells treated with respective samples and then exposed to 10 µM 2-NBDG for four hours. Final image per row is an overlay including DAPI stain. White arrows indicate localized glucose storage in intracellular vesicles (63X Objective, Scale bar: 20 µm).

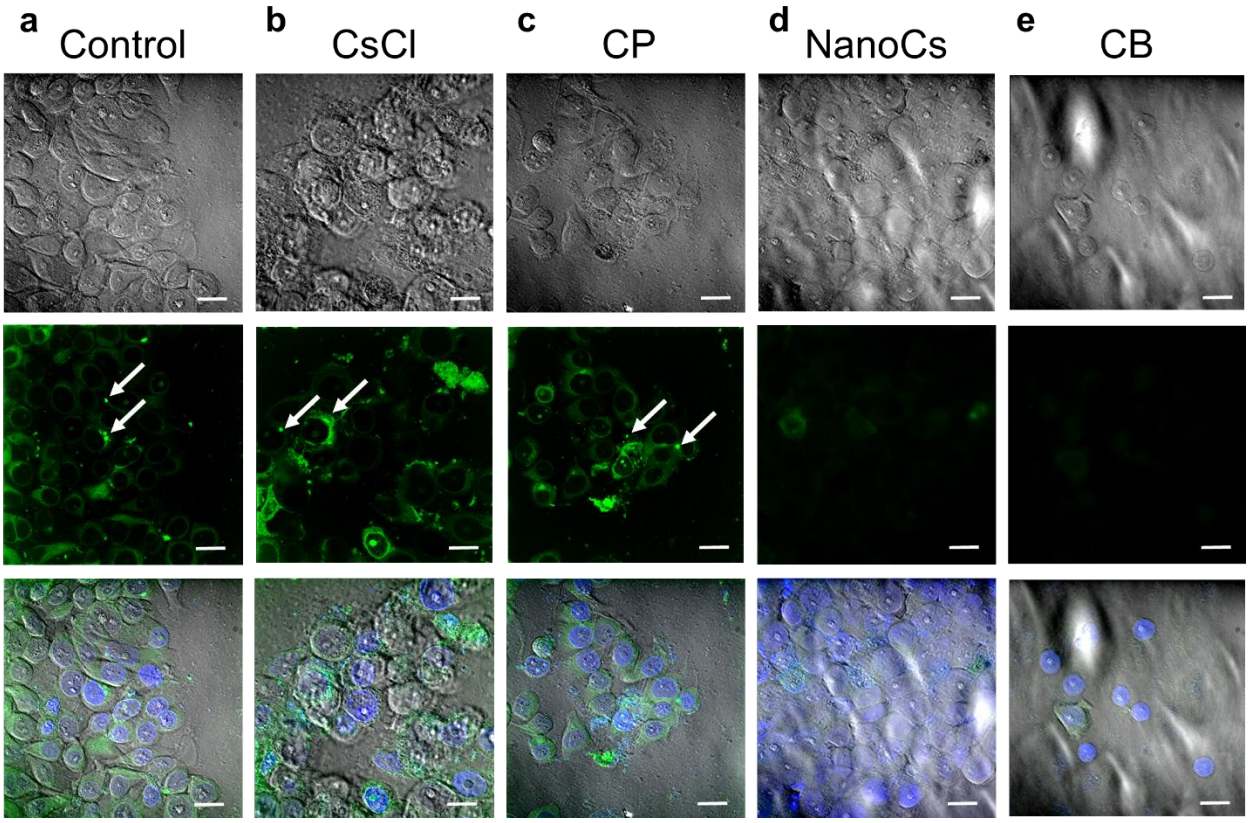

Figure 2.31: Bar graph of average per cell pixel intensity of confocal 2-NBDG emission only as measured by ImageJ (t-test of NanoCs and CB to CsCl, p<<0.01).

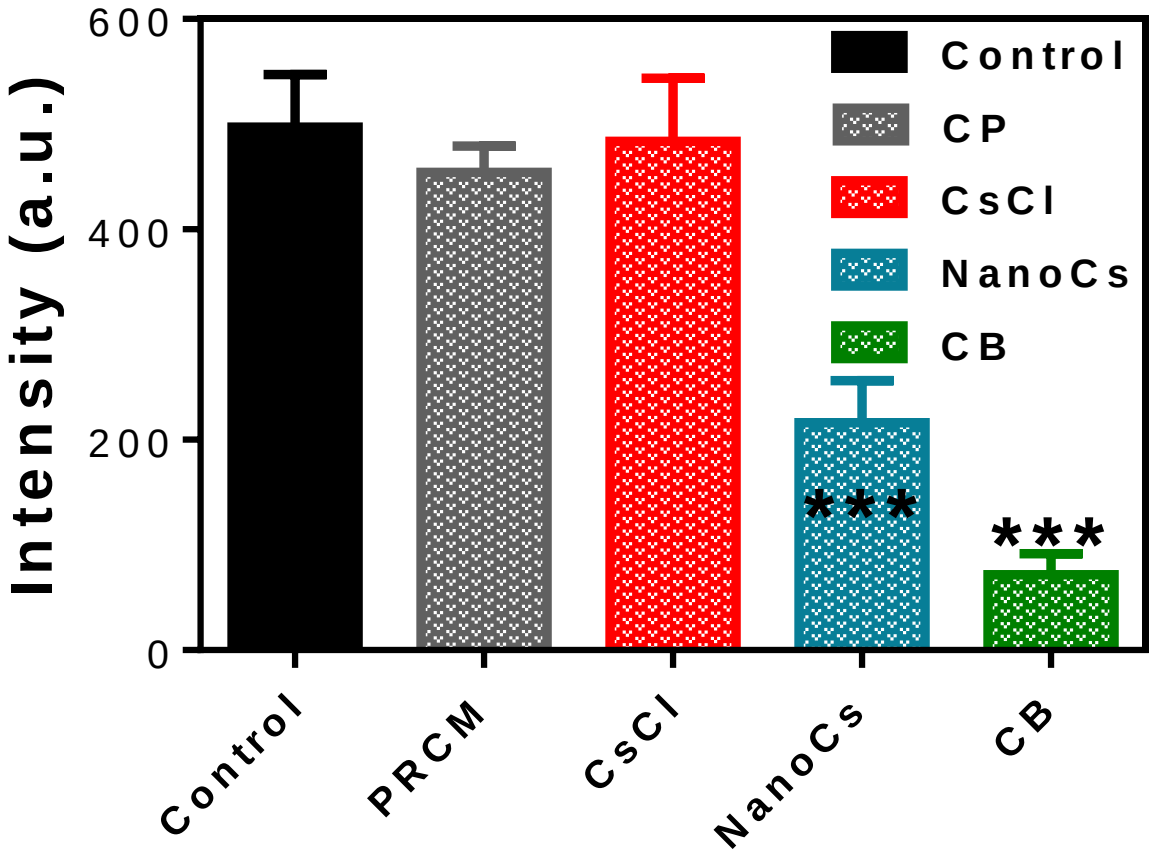

Generation of Intracellular Reactive Oxygen Species in Response to Starvation

Reactive oxygen species (ROS) are important molecules for identifying cellular stress due to their nature as products of mitochondrial starvation and signaling activators of autophagy-related proteins (ATG) for programmed cell death (PCD).[16] High concentrations of ROS within cells can also lead to increased oxidative damage of proteins with cysteine residues.[16] One specific ROS target is the Na^+/K^+ symporter,[18] which, if damaged, will further exacerbate the intracellular ion gradients and glucose import inhibition. Since Cs^+ exposure showed evidence of reduced glucose uptake, we quantified cellular starvation *via* the production of intracellular ROS generated after NanoCs treatment. An ROS assay (Cell Biolabs Inc., San Diego, CA) on MCF-7 cells at a density of 12,000 cells per sample was performed using a known protocol that takes advantage of ROS oxidation on the cell-permeable dye 2', 7'-Dichlorodihydrofluorescein diacetate (DCFH-DA) to measure ROS content with 10 ppM sensitivity.[45,46] Cells were pre-loaded with DCFH-DA, washed with dPBS, and then exposed to various concentrations of NanoCs as CsCl equivalence, and CP as volume equivalence to NanoCs, from 1000 to 31.25 μM in media for four hours. An ROS standard calibration curve was performed to calculate molar concentration of ROS within cell species and produced the curve Y = 9.87*X+1.077 (Figure 2.32). The DCFH-DA intensity values were subsequently translated to molar values and control values subtracted to eliminate noise from normal physiological ROS concentrations. The assay revealed that NanoCs did indeed initiate the production of a significant amount of ROS as compared to the CP sample which contained near physiological ROS concentrations (Figure 2.33). This suggests that the decreased glucose uptake caused by Cs^+ exposure is driving high mitochondrial production of ROS, which in turn will lead to PCD.

Figure 2.32: ROS Standard curve in Log_{10} form for assessing actual ROS content within cells.

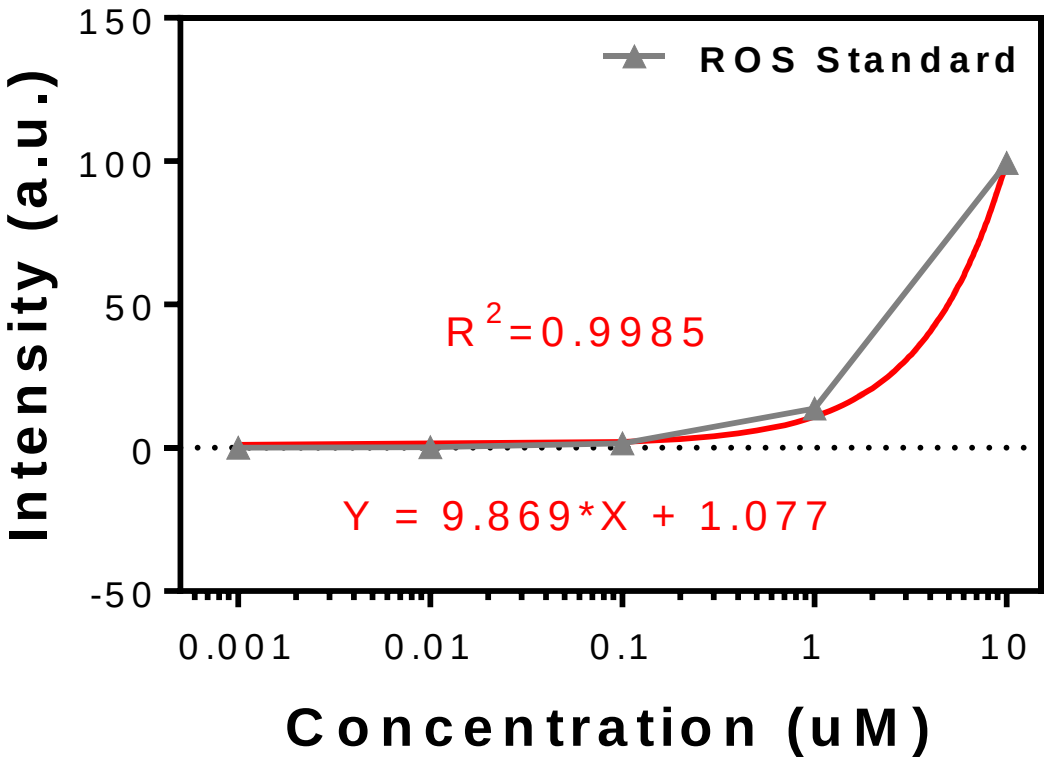

Figure 2.33: Graph depicting intracellular ROS content of 10k cells post four-hour exposure to respective samples at varying concentrations. Control values were subtracted from each data point to eliminate the physiological ROS concentrations from the data set.

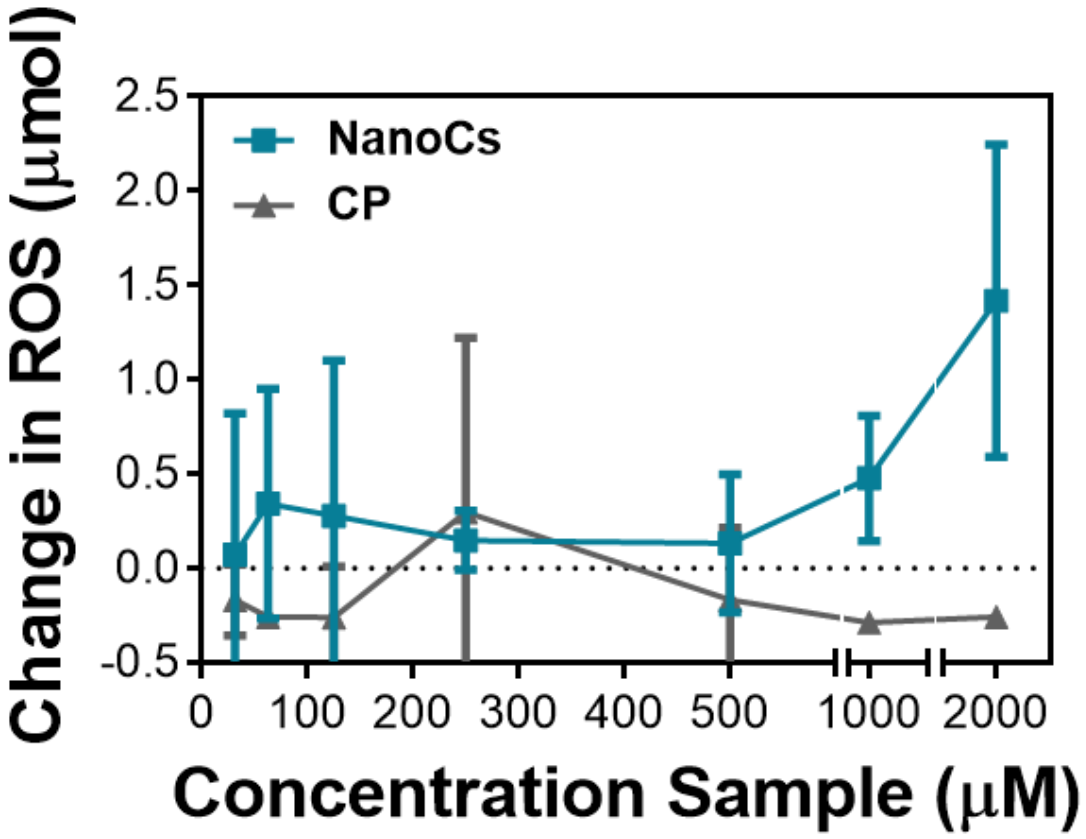

Investigations of NanoCs Initiation of Apoptosis versus Cellular Death by Necrosis

Since CsCl is known to be toxic at high doses as revealed by our MTT assay, we investigated the possibility that the NanoCs enabled delivery of Cs^+ is causing a mutual initiation of apoptosis *via* cellular starvation, and ROS-activated autophagy, rather than general toxicity and induced cellular death *via* necrosis. To prove the possibilities, an Annexin V-FITC based apoptosis assay paired with propidium iodide (PI) and measured *via* Flow cytometry, unveiled cellular properties that indicate the mechanism of cell death. Annexin V is a non-cell permeable binding protein with high affinity for the lipid phosphatidylserine (PS) normally expressed on the inner leaflet of the cell membrane. However, cells have been shown to expose PS on the outer side of the membrane during early stages of apoptosis,[47] which makes the fluoro-labeled Annexin V-FITC a perfect candidate for apoptotic cell tagging at early stages. PI is a well-documented fluorescent dye only permeable to dead cells. Thus, sole PI expression indicates necrotic cells only, while sole Annexin V-FITC expression indicates early stage apoptotic cells, and finally, dual expression indicates late stages of apoptosis.

An apoptosis assay kit (eBioscience Inc, San Diego, CA) was performed on MCF-7 cells at a density of 100,000 cells per sample for a 48 hour 37 °C exposure of 100 µM CsCl, NanoCs as CsCl equivalence, and CP as volume equivalence to NanoCs. After the 48 hour incubation, cells were washed with dPBS and resuspended in 195 µL provided binding buffer, followed by exposure to 5 µL of Annexin V-FITC for PS binding. Cells were resuspended in fresh binding buffer and exposed to PI before processing *via* a Guava® EasyCyte Plus Flow Cytometer. Since FITC intensity was measured at the flow cytometers green spectral filter, all samples were histogram subtracted from control values to eliminate any cellular autofluorescent signal. A histogram analysis of FITC intensity among samples uncovered that both CsCl and NanoCs produced high-

intensity readings, while NanoCs produced the highest counts of Annexin V-FITC binding (Figure 2.34), indicating that NanoCs was a major influence in initiating apoptosis among cells. Further analysis and comparison to PI expression revealed that many cells exposed to NanoCs had a significant subpopulation that expressed higher amounts of Annexin V-FITC binding than expressed PI fluorescence. Thus, this subpopulation was in the beginning stages of apoptosis after 48 hours of exposure, when compared to the control sample (Figure 2.35a, b).

Figure 2.34: Flow cytometry RFU histogram analysis of apoptotic cells labeled with Annexin V-FITC.

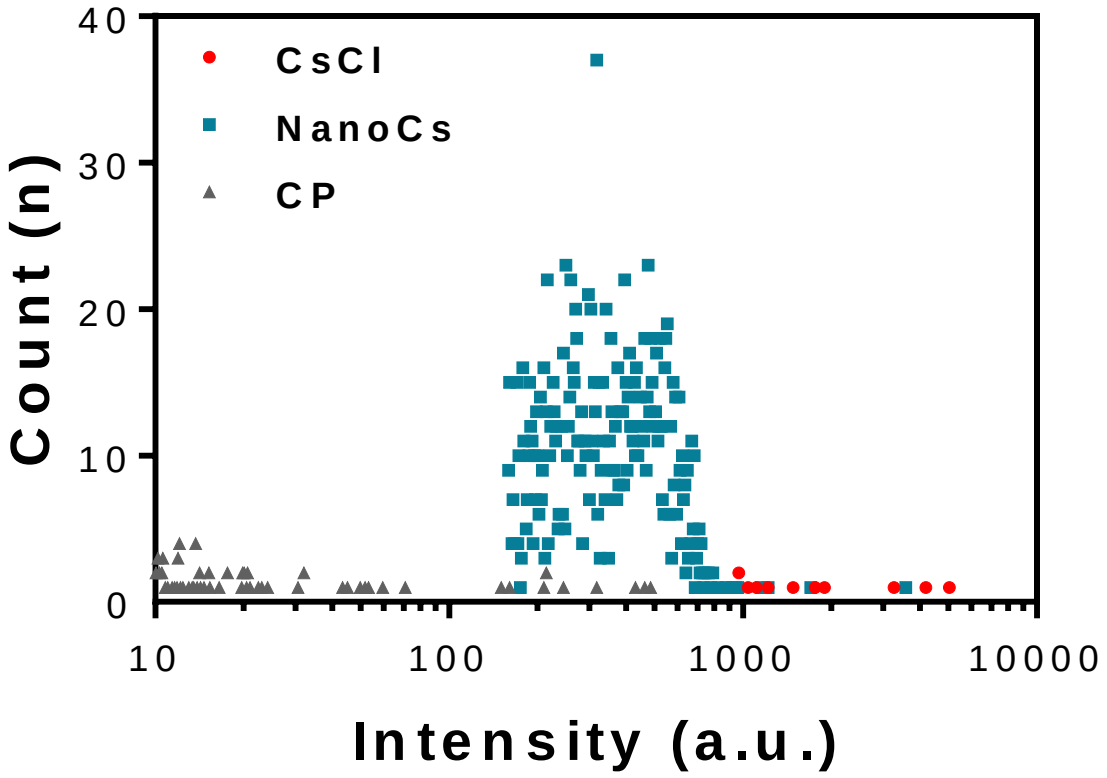

Figure 2.35: Flow cytometry dot plot of (a) control cells and (b) NanoCs treated cells plotted as Annexin V-FITC intensity (x-axis) versus PI intensity (y-axis).

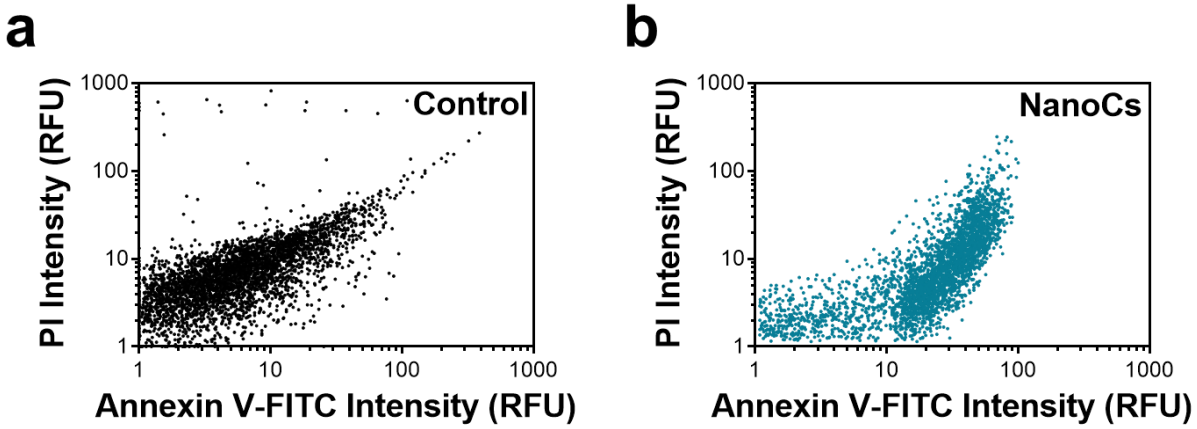

In Vivo Tumor Regression in a Xenografted Athymic Nude Mice Model

While advanced 3D cell culture techniques can mimic some of the aspects of the *in vivo* tumor environment, these techniques are still lacking in the complexity found *in vivo*. In addition to tumor architecture, the global setting of the tumor in the animal cannot be replicated yet with cell culture techniques. Thus, after optimizing treatment strategies *in vitro*, it had to be established in animal models to get a real picture of treatment efficiency. Thus, to evaluate the efficacy of our Cs^+ loaded nanoparticle system for anti-cancer properties, tumor regression efficiency experiments were performed *in vivo* (Figure 2.36). Nude mice were subcutaneously injected with MCF-7 cells to develop tumors of 5mm x 5mm size before starting the intratumoral injections with various treatments. Grown tumors were injected with 40 µL of CsCl solution and NanoCs suspension with 3.0 mM cesium concentration, as well as 40 µL of CP. Injections and tumor size tracking were followed using a caliper through on the 14, 18, 22 and 26^{th} day of tumor growth, while further size tracking continued for an additional 9 days. Animals were allowed to feed on food and water with no specific control. At the end of the experiment, average tumor sizes were found to be 250, 150 and 125 mm^3 in animals treated with CP, CsCl, and NanoCs, respectively. These changes in final tumor volumes were of critical importance based on their treatment type and significance. The significance of these changes was proven bio-statistically by ONE WAY ANNOVA performed on various tumor sizes at different time points. It revealed a value for $p = 0.0546$ between tumor sizes for CP and NanoCs treated animals (Figure 2.37a-d, Figure 2.38). To verify the mechanism of tumor regression, an H&E staining protocol was performed by following standard method supplied by core facility IGB. It showed presence of an apoptotic population with fragmented nuclei of tumors treated with CsCl and NanoCs formulation. The presence of vacuoles (white areas) in tissue sections from tumors, which were treated with CsCl (Figure 2.39b) and NanoCs (Figure 2.39c),

indicated the cell starvation.[48] This result further strengthens the chances of assuming that probably Cs inducing apoptosis *via* cellular starvation. It will be a matter of further investigation in future studies. Thus, *in vivo* study clearly supported the *in vitro* observation of cancer cell growth inhibition *via* apoptosis induction in terms of decreased tumor size and presence of fragmented nuclei in the apoptotic cell population. It verified the role of NanoCs as an effective anticancer nanomedicine with success in tumor regression in a rodent model. To the best of our knowledge, this is the first report to study the nano-enabled delivery of cesium. Although more detailed *in vivo* studies are warranted, we anticipate this early investigation will trigger a further exploration of cesium as a therapeutic agent.

Figure 2.36: *In vivo* tumor regression analysis post NanoCs injections in xenograft mouse model. Formulations were injected in tumors developed from MCF-7 cells.

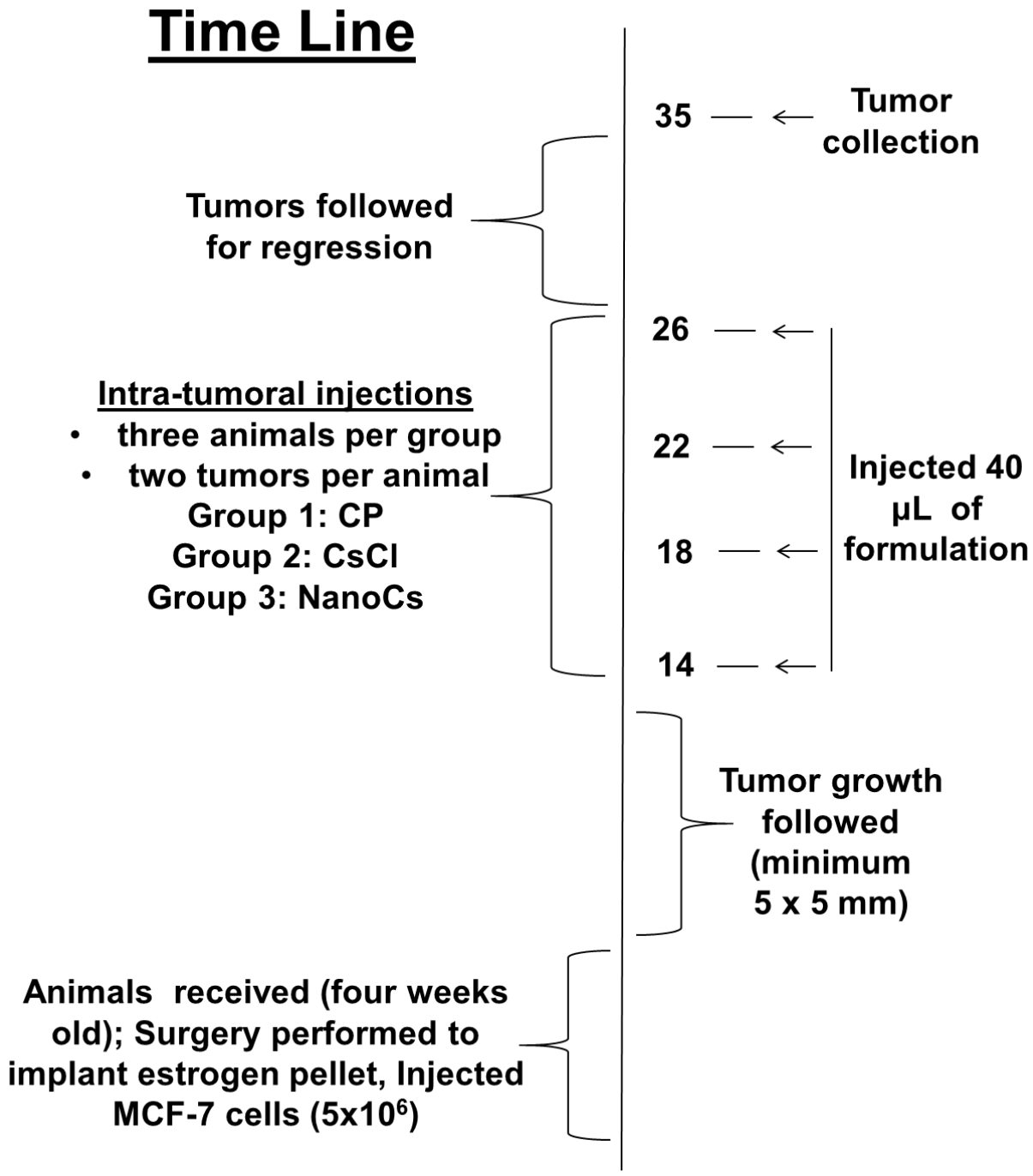

Figure 2.37: Timeline of experimental procedures performed on animals and tumors treated with (a) CP; (b) CsCl; (c) NanoCs and (d) tumor volume after excision post euthanasia from animals treated with (d2) CP; (d3) CsCl and (d4) NanoCs on cm scale (d1).

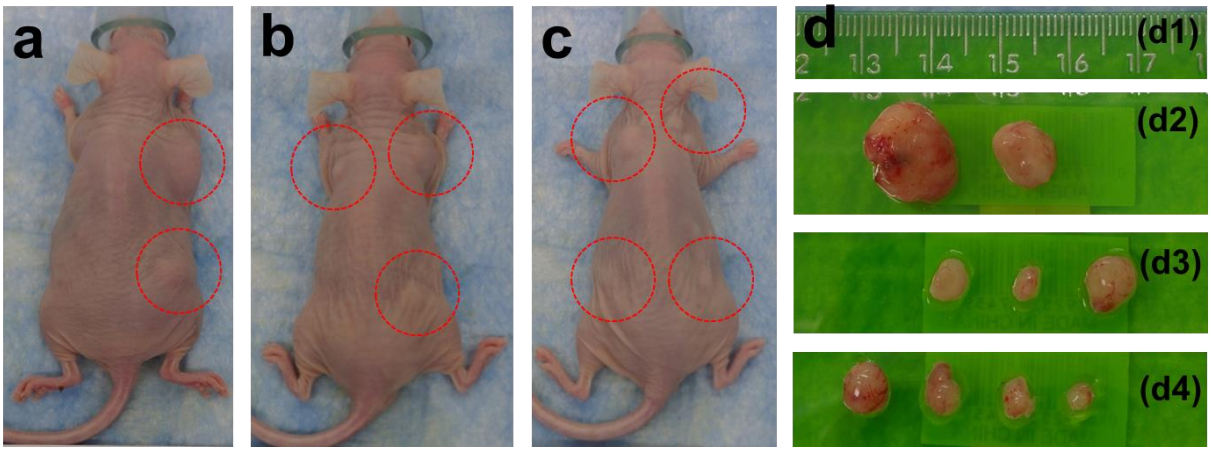

Figure 2.38: Tumor volume regression analysis for all the animals treated with various used formulations. ONE-WAY ANOVA was performed on tumor sizes and found as p = 0.0546 between tumor volume size from tumors treated with CP and NanoCs.

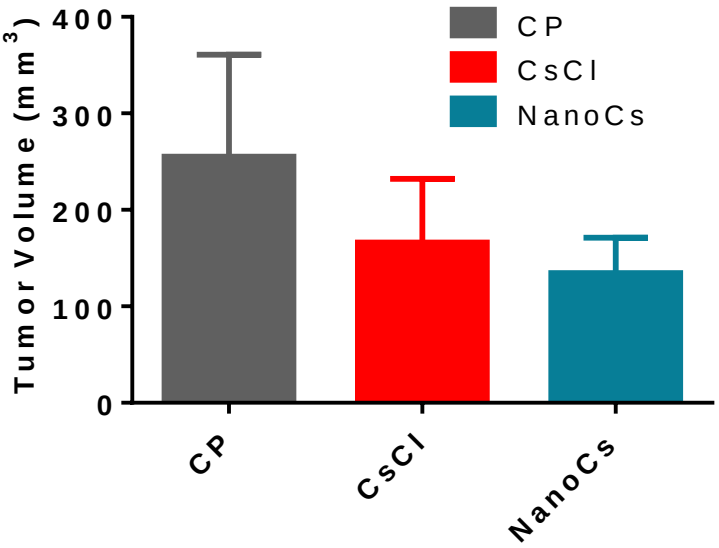

Figure 2.39: H&E stained tumor sections after microtomy on waxed tumors from animals treated with (a) CP, (b) CsCl and (c) NanoCs. Arrows show the location of the apoptotic cell population with fragmented nuclei.

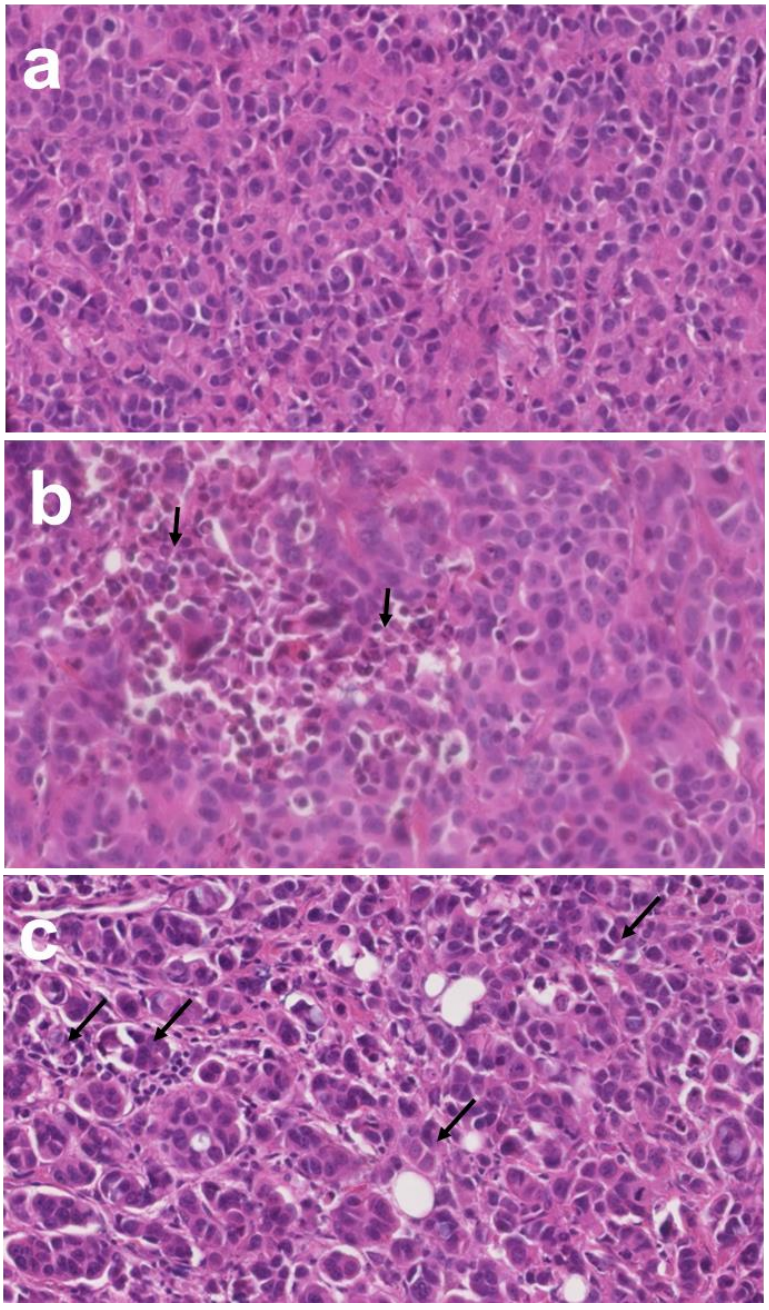

Conclusion

Within this study, we have investigated the highly theorized concept of "high pH therapy" lead by CsCl supplementation, as well as other possible mechanisms initiated *via in vitro* and *in vivo* CsCl delivery. For a detailed scientific understanding of cesium delivery, we used proper scientific procedures and analysis on a model breast cancer cell line to resemble tumor treatment. For the first time, we have identified a facile and amenable procedure for the synthesis of cesium-based nanoparticles for efficient delivery of cesium ion to cancer cells as compared to a free CsCl salt solution. Our data indicates that although CsCl has the ability to decrease hydrogen ion activity for an observed pH raise of an acidic non-buffered solution, the amount necessary to initiate programmed cell death is far out of reach. Intracellular delivery of Cs^+, *via* the optimized nano-delivery vehicle: NanoCs, still did not cause a pH change as previously expected and no high pH initiated cell death was observed. Furthermore, alternative hypothesized mechanisms have been identified as different forms of CsCl mediated cell death than previously expected. Our data suggests that Cs^+ internalization *via* NanoCs limits glucose internalization. Additionally, this consequential cellular starvation leads to the mitochondrial generation of ROS, an autophagy activator and precursor to PCD. A further investigation into the hypothesized method of cell death using a popular flow cytometry analysis method revealed that Cs^+ delivery *via* NanoCs, indeed causes high rates of cellular initiated apoptosis rather than death by toxicity induced necrosis. *In vivo* studies showed that xenograft tumors grown in nude mice regressed to a statistically significant level after intra-tumoral injection of NanoCs. H&E analysis of tumor sections characterizes with apoptotic cell population with fragmented nuclei. Further investigations into the exact mechanism of Cs^+ induced membrane potential disruption and inhibition of ion dependent glucose co-transporters is essential for translation into clinical settings. Additionally, studies

regarding the NanoCs long term effects and biodistribution properties *in vivo* are vital for validation of the system.

Methods

Unless stated otherwise, all material and reagents were purchased from Sigma–Aldrich, St. Louis, MO, and were used without further purification. Solvents were used as received and without further purification.

NanoCs and CP Synthesis

Polyethylene glycol cetyl ether (2 mg) was melted at 65 °C for 5 min followed by the dropwise addition of 2 ml of water (approximately 1 drop/sec) (for NanoCs, 2 ml of 50 mg/ml CsCl in water was added dropwise). The solution was allowed to stir for 20 min at 1150 rpm. Simultaneously, a solution of poly(styrene)$_{67}$-block-poly(acrylic acid)$_{27}$ (PS_{67}-*b*-PAA_{27}, Mn 1,600–1,950 (poly(acrylic acid)), Mn 6,500–7,000 (polystyrene), Mn 8,100–9,100, average Mn 8,700, mp: 192–197 °C; Mw/Mn = 1.2) was prepared by adding 2 mg of the amphiphilic polymer dissolved in 0.5 ml of tetrahydrofuran (THF) to a glass vial. After the polyethylene glycol cetyl ether micellar suspension was stirred for 20 min, 500 μL of PS_{67}-*b*-PAA_{27}/THF solution was added drop-wise (approximately 1 drop/10 sec) to the solution. The solution was left stirring overnight to allow THF evaporation. At the end of the procedure, volume was increased up to 2 ml with autoclaved nanopure water (0.2 μM). The suspension was further stirred for 10 minutes. Finally, the suspension was stored at 4 °C overnight to cure the core of the particle. The NanoCs were purified by dialysis against nanopure (0.2 μM) water using a 10,000 Da MWCO cellulose membrane for a prolonged period of time to release free CsCl ions from the nanoparticle solution (CP was also dialyzed for consistent preparation). Furthermore, nanoparticles were passed through

a 0.45 μm Acrodisc Syringe filter. Nanoparticles were stored under argon atmosphere at 4 °C in order to prevent bacterial growth.

Inductively Coupled Plasma Optical Emission Spectroscopy (ICP-OES)

ICP-OES was performed on NanoCs particles, post dialysis, to measure cesium content entrapped within polymer solution with a Perkinelmer 2000DV ICP-OES (Noyes Microanalysis Laboratory, UIUC). For the cesium release study, NanoCs post routine dialysis was further dialyzed in Nano pure H_2O (18MΩ) at room temperature. Various samples were extracted from inside the dialysis cassette and measured via ICP-OES for cesium concentration.

Calculating the Amount of Cs^+ per Nanoparticle

Johansson et al.[49] reports that poly ethylene glycol cetyl ether (PEGCE, Average M_n 1124) has an average micellar M_n = 79,000. At 1 mg/ml polyethylene glycol cetyl ether:

Equation 2.2

$$1\,\frac{mg\ PEGCE}{ml}\Big/79{,}000\,\frac{mg\ PEGCE}{mmol} = 12.66\ \frac{nmol\ micelles}{ml}$$

One milliliter of NanoCs has 0.42 mg or 3,160.27 nmol Cesium

Equation 2.3

$$\frac{3{,}160.27\ nmol\ Cesium}{12.66\ nmol\ micelles} = 249.63 \sim 250\ \frac{Cesium}{Micelle}$$

Dynamic Light Scattering Measurements

Hydrodynamic diameters were determined using a Malvern Zetasizer ZS90 particle size analyzer, while scattered light was collected at a fixed angle of 90°. A photomultiplier aperture of

400 μm was used with the incident laser power adjusted to obtain a photon counting rate between 200 and 300 kcps. Diameter values depended on measurements whereupon the measured and calculated baselines of the intensity autocorrelation function had to agree within +0.1%. All determinations were made in multiples of three consecutive measurements at 15 runs each.

Determination of Surface Zeta Potential

Zeta potential (ζ) values for NanoCS and CP were determined with a nano series Malvern Zetasizer zeta potential analyzer (Fredrick Seitz Material Research Laboratory, University of Illinois at Urbana Champaign, (MRL facility, UIUC)). Data were acquired in the phase analysis light scattering (PALS) mode following solution equilibration at 25 °C when calculation of ζ from the measured electrophoretic mobility (μ) employed the Smoluchowski equation (Equation 2.4), which is expressed as:

Equation 2.4 $$\mu = \varepsilon\zeta/\eta$$

where ε and η are the dielectric constant and the absolute viscosity of the medium, respectively.

Measurements of ζ were reproducible to within ± 6 mV of the mean value given by three determinations of 15 data accumulations.

Transmission Electron Microscopy Measurements

Two μL of particle suspension was applied to carbon coated TEM grids. Grids were then blotted, air dried, and imaged on a JEOL 2100 Cryo TEM machine *via* a Gatan UltraScan 2k × 2k CCD camera (MRL facility, UIUC).

Atomic Force Microscopy

A Digital Instruments Dimension 3000 series AFM (MRL facility, UIUC) was used for scanning the samples using standard Veeco tapping mode silicon probes with a platinum–iridium (PtIr) coating. In a typical experiment, suspended NanoCS or CP samples were dried in a desiccator on freshly cleaved mica. Dried samples were placed on the AFM platform and scanned. Pertinent scanning parameters were fixed as follows: Example of tip velocity: 4 m/s for 2 m, 15 m/s for 5 m, 30 m/s for 10 m; resonant frequency (probe): 60–80 kHz. Aspect ratio: 1:1; resolution: 512 samples/line, 256 lines.

EDX Analysis

Energy dispersive X-ray (EDX) spectrum analysis was performed to demonstrate the presence of cesium with nanoparticles in addition to carbon and oxygen found in particle preparations. Samples were prepared on metal stubs decorated with silicon block. Suspension of particles were drop cast on carbon tape and allowed to air-dry before vacuum desiccation for 5 hrs. EDX was carried out on an ISIS EDS X-ray Microanalysis System, Oxford Instruments (MRL facility, UIUC).

Raman and FTIR Spectroscopy

All Raman measurements were taken on a Nanophoton Raman instrument (MRL facility, UIUC) with a 532 nm wavelength laser for one min at 0.2% laser power using a 20x objective. For each spectrum a grating (600 l mm^{-1}) scan was taken over the range of 120–2700 cm^{-1}. An average of 20 spectra were recorded and averaged per sample.

For Fourier Transform Infrared (FTIR) analysis, aqueous suspensions of particles were drop cast onto MirrIR IR-reflective glass slides (Kevley Technologies, Chesterland, Ohio, USA) for measurements using a Nicolet Nexus 670 FTIR (MRL facility, UIUC). For each measurement 100×100 μm images were collected at 1 cm^{-1} spectral resolution with 64 scans per pixel and a 25×25 μm pixel size and individual spectra were corrected for atmospheric contributions.

MTT Assay

The cytotoxic effect of CP and those of NanoCs were investigated with a 3-(4,5-dimethylthiazole-2-yl)-2,5-diphenyltetrazolium bromide (MTT) assay (Sigma-Aldrich, MO, USA). An MCF-7 human estrogen receptor positive breast cancer cell line was plated on a 96-well plate at a density of 10,000 cells per well (Greiner Cellstar® 96 well plates, Sigma-Aldrich, MO, USA) and exposed to CP and NanoCs after 24 hr at 37 °C. Followed by a 48 hr exposure time, 20 μL (5 mg/mL) of MTT solution was added to each well and cells were further incubated for another 4 hours. After exposure, media was aspirated and 200 μL of dimethyl sulfoxide (DMSO, ≥99%, MP Biomedicals, USA) was added to dissolve formazan crystals. Optical density of samples was determined by Synergy HT (BioTek, USA) with a reference wavelength of 570 nm. Percentage cell viability was determined by the following equation (Equation 2.5):

Equation 2.5
$$\%Viability = \frac{A_{570}(treated) - A_{570}(background)}{A_{570}(control) - A_{570}(background)}$$

For inhibitor studies, MCF-7 cells were plated on a 96-well plate in triplicate at a density of 10,000 cells per well (Greiner Cellstar® 96 well plates, Sigma-Aldrich, MO, USA) and exposed to each inhibitor for one hour. Inhibitor concentrations are as follows; 28 μM chlorpromazine, 80

μM Dynasore, 180 nM Nystatin, 10 μM NaN_3 and 50 μM DOG. Cells were then washed and incubated with a 100 μM NanoCs equivalent of CsCl. The cytotoxic effects of the NanoCs particles were measured using the same methods as the MTT reduction assay.

Confocal Microscopy

SNARF and NBDG cell internalization measurements were carried out using a Zeiss 710 confocal scanner. For all samples, the MCF-7 cell line was plated on poly-L-lysine coated circular coverslips at a cell density of 400,000 cells per 25 mm coverslip. After 24 hours, cells were treated with respective components and fixed using 8% paraformaldehyde. Cells were then stained with DAPI containing Vectashield mounting medium prior to imaging. In both experiments, the sample was excited at 405 nm and the emission was measured at 461 nm using suitable filters to locate and image cell nuclei.

Cellular pH Change Using SNARF

Cells were treated with 0.5 μg of 5-(and-6) Carboxy SNARF®-1 AM 24 hours post plating and incubated at 37 °C for 30 minutes. After dye loading, cells were washed with dPBS and treated with respective samples with an incubation time of 4 hours. Cells were then washed with dPBS and fixed for confocal imaging as described above. For SNARF imaging and analysis, samples were excited at 488 and imaged at 535 nm and 640 nm gates to visualize dye intensity corresponding to pH change. An MCF-10A sample was prepared similarly as a positive pH change control.

NBDG Glucose Uptake

For 96 well plate reading of 2-deoxy-2-[(7-nitro-2,1,3-benzoxadiazol-4-yl)amino]-D-glucose (NBDG) (Cayman Chemicals, Michigan USA), MCF-7 Cells were plated at a cell density of 12,000 cells per well. 24 hours after plating, cells were treated with respective samples at varying concentrations and incubated at 37 °C for 30 min. Cells were subsequently treated with 300 µM of NBDG and incubated at 37 °C for an additional 3.5 hours. After treatment, cells were washed with dPBS and lysed in 50 µL lysis buffer. The fluorescence spectra of each well were measured with a Synergy HT (BioTek, USA) Plate reader at 488 excitation and 535 emission. Each respective well was additionally measured for absorption at 480 nm.

Flow Cytometry samples were performed on cells (cell density: 500 cells/µL) treated with 10 µM NBDG on a Guava® EasyCyte Plus Flow Cytometer. For each sample data from 5000 single cell events were collected within 1 minute at an excitation of 488 nm.

Confocal samples were also treated in a similar fashion as mentioned above with 10 µM NBDG treatment and fixed similarly to SNARF samples. NBDG exposed cells were imaged at 488 excitation and 535 emission.

Intracellular Reactive Oxygen Species Assay (ROS)

ROS Assay was purchased from Cell Biolabs Inc., San Diego, CA. MCF-7 was plated on a 96 well plate at a cell density of 10,000 cells per well for 24 hours. Cells were then washed with dPBS and treated with 1mM DCFH-DA in media at 37 °C for 60 minutes. Cells were then washed with dPBS and treated with respective samples at varying concentrations for 4 hours at 37 °C. Cells were then re-washed with dPBS, lysed with lysis buffer and incubated at room temperature for 5 minutes. The fluorescence was then read by a Synergy HT (BioTek, USA) plate reader at

488 excitation and 535 emission. A standard was created to correlate the molarity of ROS found in cell samples.

Apoptosis Detection Assay

Apoptosis detection kit was purchased from eBioscience Inc, San Diego, CA. MCF-7 cells were plated in a 24 well plate at a cell density of 100,000 cells per well for 24 hours. Cells were then treated with respective samples at varying concentrations and incubated at 37 °C for an additional 24 hours. Cells were then washed with dPBS and suspended in binding buffer with 5 µL of Annexin V-FITC and allowed to incubate at room temperature for 10 minutes. Cells were washed with and resuspended in binding buffer for treatment of Propidium Iodide (20 µg/ml). Samples were then analyzed *via* a Guava® EasyCyte Plus Flow Cytometer. For each sample, data from 2000 single cell events were collected within 1 minute at an excitation of 488 nm.

Animal Studies

To evaluate the efficacy of adopted strategy of loading Cs in nanoparticle system animal experiments were performed on the least amount of animals necessary for significant results. The experimental protocol was approved by the Institutional Animal Care and Use Committee (IACUC), University of Illinois, Urbana–Champaign, and satisfied all University and National Institutes of Health (NIH) rules for the humane use of laboratory animals. All the animal experiments were carried out in accordance with the approved guidelines. Athymic mice were bought from Charles River Laboratories International, Inc. USA. Upon arrival, athymic mice are allowed 1 week for acclimation. Animals were single-cage housed and had free access to food and water. Animals were housed in Integrative Genomic Biology, University of Illinois at Urbana-Champaign. Animals were anesthetized with isoflurane before injecting the 5×10^6 MCF-7 cells

suspended in matrigel (50%, v/v) using a Hamilton auto-injector or standard syringe tipped with a 26 gauge 1/2" long needle. Mice were monitored during recovery from the anesthesia in a clean cage.

Mice were monitored daily for signs of discomfort and behavioral change. The mice's body weight was measured every week. Criteria for interventions were set up as animal body weight drops by 20% or tumor increase to 17 x 17 mm^2. Tumor size was determined by measuring the length and width of the tumor and then calculating the tumor volume *via* the formula

Equation 2.6

$$Tumor\ Volume = \frac{length^2\ x\ width}{2}$$

Intra-Tumoral Injections and Tumor Regression Analysis

Animals were followed till tumors grew to a minimum of 5 x 5 mm^2 before starting the treatment protocol. Isoflurane-oxygen mixture was used to anesthetize the animals with 3-4% isoflurane gas from a vaporizer and constant anesthesia maintained with 1-2% isoflurane *via* an inlet tube. A second tube was used to remove carbon dioxide and excess anesthetic. All the personnel involved wore protective lab coats, face masks, sterile gloves during experimental procedures. A total of 40 µL particle suspensions were injected to each tumor on every 4th day till 26th day while following the tumor size growth and regression for the next 9 days. At the end of experiment, animals were euthanized, tumors collected and stored in tissue cassettes dipped in 10% formalin before performing the tissue fixation protocol in Leica ASP300 tissue processor. Embedded tumor blocks were clamped in microtome (Leica) and sectioned at 7 µm thickness. Paraffin-embedded sections (7 µm) were subjected to hematoxylin and eosin (H&E) staining. H&E

staining was performed by following standard protocol supplied by core facility IGB. In brief, sections were processed by deparaffinize sections, in xylene, absolute alcohol, 95% alcohol and 70% alcohol before staining in mayer hematoxylin solution and counterstaining in eosin Y solution. Mounted the section in xylene based mounting medium. The morphological changes of H&E-stained tissue with each fixation were analyzed at magnification 40X.

References to Chapter 2

(1) Binzel, P.; Day, L.; Kehr, W. DMSO | Cesium Chloride http://www.cancertutor.com/faq_cesium_cure_rate/ (accessed Mar 22, 2016).

(2) Author, U. Cancer Cover-Up (Cesium Science): Cesium - A High Ph Therapy For Cancer http://www.cancer-coverup.com/%0Afighters/cesium-science.htm (accessed Mar 22, 2016).

(3) Kehr, W. pH Therapy (a.k.a. Cesium Chloride Protocol) http://www.cancertutor.com/alkaline/ (accessed Mar 22, 2016).

(4) Horwitz, H.; Kereiakes, J. G.; Bahr, G. K.; Cluxton, S. E.; Barrett, C. M. An After-Loading System Utilizing Cesium 137 for the Treatment of Carcinoma of the Cervix. *Am. J. Roentgenol., Radium Ther. Nucl. Med.* **1964**, *Vol: 91*.

(5) Som, A.; Raliya, R.; Tian, L.; Akers, W.; Ippolito, J. E.; Singamaneni, S.; Biswas, P.; Achilefu, S. Monodispersed Calcium Carbonate Nanoparticles Modulate Local pH and Inhibit Tumor Growth in Vivo. *Nanoscale* **2016**, *8* (25), 12639–12647.

(6) Sartori, H. E. Cesium Therapy in Cancer Patients. *Pharmacol. Biochem. Behav.* **1984**, *21*, 11–13.

(7) Sartori, H. E. Nutrients and Cancer: An Introduction to Cesium Therapy. *Pharmacol. Biochem. Behav.* **1984**, *21*, 7–10.

(8) Brewer, A. K. The High pH Therapy for Cancer Tests on Mice and Humans. *Pharmacol. Biochem. Behav.* **1984**, *21*, 1–5.

(9) Centeno, J. A.; Pestaner, J. P.; Omalu, B. I.; Torres, N. L.; Field, F.; Wagner, G.; Mullick, F. G. Blood and Tissue Concentration of Cesium after Exposure to Cesium Chloride: A Report of Two Cases. *Biol. Trace Elem. Res.* **2003**, *94* (2), 97–104.

(10) Nierenberg, C. Woman's Death Linked to Alternative Cancer Treatment http://www.livescience.com/42266-death-alternativecancer-%0Atreatment-cesium-chloride.html (accessed Mar 22, 2016).

(11) Lyon, A. W.; Mayhew, W. J. Cesium Toxicity: A Case of Self-Treatment by Alternate Therapy Gone Awry http://journals.lww.com/drug-monitoring/Abstract/2003/02000/Cesium_Toxicity__A_%0ACase_of_Self_Treatment_by.18.aspx (accessed Mar 22, 2016).

(12) Dalal, A. K.; Harding, J. D.; Verdino, R. J. Acquired Long QT Syndrome and Monomorphic Ventricular Tachycardia after Alternative Treatment with Cesium Chloride for Brain Cancer. *Mayo Clin. Proc.* **2004**, *79* (8), 1065–1069.

(13) Horn, S.; Naidus, E.; Alper, S. L.; Danziger, J. Cesium-Associated Hypokalemia Successfully Treated with Amiloride. *Clin. Kidney J.* **2015**, *8* (3), 335–338.

(14) Lazarev, N. V.; Gadaskina, I. D. Harmful Substances in Industry. Manual for Chemists, Engineers and Physicians. *St. Petersburg, Khimiya* **1977**, *3* (7), 328–329.

(15) Brown, R. S.; Wahl, R. L. Overexpression of Glut-1 Glucose Transporter in Human Breast Cancer an Immunohistochemical Study. *Cancer* **1993**, *72* (10), 2979–2985.

(16) Scherz-Shouval, R.; Shvets, E.; Fass, E.; Shorer, H.; Gil, L.; Elazar, Z. Reactive Oxygen Species Are Essential for Autophagy and Specifically Regulate the Activity of Atg4. *EMBO*

J. **2007**, *26* (7), 1749–1760.

(17) Huang, W.; Wang, Y.; Askari, A.; Zolotarjova, N.; Ganjeizadeh, M. Different Sensitivities of the Na+/K+-ATPase Isoforms to Oxidants. *Biochim. Biophys. Acta - Biomembr.* **1994**, *1190* (1), 108–114.

(18) Bogdanova, A.; Petrushanko, I.; Boldyrev, A.; Gassmann, M. Oxygen- and Redox-Induced Regulation of the Na/K ATPase http://www.eurekaselect.com/55314/article (accessed Mar 22, 2016).

(19) Ostadhossein, F.; Daza, E. A.; Frankowski, D.; Goatz, D.; Imgruet, M.; Kus, J.; Lake, R.; Modak, M.; Olsen, N.; Schwartz-Duval, A.; et al. Nano-Enabled Delivery of Intracellular Therapeutics. **2015**, 1–15.

(20) Misra, S. K.; Ghoshal, G.; Gartia, M. R.; Wu, Z.; De, A. K.; Ye, M.; Bromfield, C. R.; Williams, E. M.; Singh, K.; Tangella, K. V.; et al. Trimodal Therapy: Combining Hyperthermia with Repurposed Bexarotene and Ultrasound for Treating Liver Cancer. *ACS Nano* **2015**, *9* (11), 10695–10718.

(21) Misra, S. K.; Ye, M.; Kim, S.; Pan, D. Defined Nanoscale Chemistry Influences Delivery of Peptido-Toxins for Cancer Therapy. *PLoS One* **2015**, *10* (6), e0125908.

(22) Zhang, R.; Pan, D.; Cai, X.; Yang, X.; Senpan, A.; Allen, J. S.; Lanza, G. M.; Wang, L. V. alphaVbeta3-Targeted Copper Nanoparticles Incorporating an Sn 2 Lipase-Labile Fumagillin Prodrug for Photoacoustic Neovascular Imaging and Treatment. *Theranostics* **2015**, *5* (2), 124–133.

(23) Zhou, H.; Yan, H.; Hu, Y.; Springer, L. E.; Yang, X.; Wickline, S. A.; Pan, D.; Lanza, G.

M.; Pham, C. T. N. Fumagillin Prodrug Nanotherapy Suppresses Macrophage Inflammatory Response *via* Endothelial Nitric Oxide. *ACS Nano* **2014**, *8* (7), 7305–7317.

(24) Iyer, A. K.; Khaled, G.; Fang, J.; Maeda, H. Exploiting the Enhanced Permeability and Retention Effect for Tumor Targeting. *Drug Discov. Today* **2006**, *11* (17–18), 812–818.

(25) Misra, S. K.; Jensen, T. W.; Pan, D. Enriched Inhibition of Cancer and Stem-like Cancer Cells via STAT-3 Modulating Niclocelles. *Nanoscale* **2015**, *7* (16), 7127–7132.

(26) Hu, Y.; Jiang, X.; Ding, Y.; Ge, H.; Yuan, Y.; Yang, C. Synthesis and Characterization of Chitosan–poly(acrylic Acid) Nanoparticles. *Biomaterials* **2002**, *23* (15), 3193–3201.

(27) Misra, S. K.; Ye, M.; Kim, S.; Pan, D. Highly Efficient Anti-Cancer Therapy Using Scorpion "NanoVenin". *Chem. Commun. (Camb).* **2014**, *50* (87), 13220–13223.

(28) Riddick, T. Control of Colloid Stability through Zeta Potential. *Blood* **1968**.

(29) Hunter, R. J. *Zeta Potential in Colloid Science: Principles and Applications*; Academic Press, 2013.

(30) Cedervall, T.; Lynch, I.; Lindman, S.; Berggård, T.; Thulin, E.; Nilsson, H.; Dawson, K. A.; Linse, S. Understanding the Nanoparticle-Protein Corona Using Methods to Quantify Exchange Rates and Affinities of Proteins for Nanoparticles. *Proc. Natl. Acad. Sci. U. S. A.* **2007**, *104* (7), 2050–2055.

(31) Wang, L. H.; Rothberg, K. G.; Anderson, R. G. Mis-Assembly of Clathrin Lattices on Endosomes Reveals a Regulatory Switch for Coated Pit Formation. *J. Cell Biol.* **1993**, *123* (5), 1107–1117.

(32) Sigismund, S.; Woelk, T.; Puri, C.; Maspero, E.; Tacchetti, C.; Transidico, P.; Di Fiore, P. P.; Polo, S. Clathrin-Independent Endocytosis of Ubiquitinated Cargos. *Proc. Natl. Acad. Sci. U. S. A.* **2005**, *102* (8), 2760–2765.

(33) Allen, C.; Yu, Y.; Eisenberg, A.; Maysinger, D. Cellular Internalization of PCL20-B-PEO44 Block Copolymer Micelles. *Biochim. Biophys. Acta - Biomembr.* **1999**, *1421* (1), 32–38.

(34) Kirchhausen, T.; Macia, E.; Pelish, H. E. Use of Dynasore, the Small Molecule Inhibitor of Dynamin, in the Regulation of Endocytosis. *Methods Enzymol.* **2008**, *438*, 77–93.

(35) Warburg, O. On the Origin of Cancer Cells. *Sci. (Washington, DC, U.S).* **1956**, *123* (3191), 309–314.

(36) Robinson, H. W. The Influence of Neutral Salts on the pH of Phosphate Buffer Mixtures. *J. Biol. Chem.* **1929**, *82* (3), 775–802.

(37) Sereshti, H.; Aliakbarzadeh, G. Response Surface Methodology Optimized Dispersive Liquid–liquid Microextraction Coupled with UV-Vis Spectrophotometry for Determination of Quinine. *Anal. Methods* **2013**, *5* (19), 5253–5259.

(38) Fisher, M.; Levin, Y. Criticality in Ionic Fluids: Debye-Hückel Theory, Bjerrum, and Beyond. *Phys. Rev. Lett.* **1993**, *71* (23), 3826–3829.

(39) Buckler, K. J.; Vaughan-Jones, R. D. Application of a New pH-Sensitive Fluoroprobe (Carboxy-SNARF-1) for Intracellular pH Measurement in Small, Isolated Cells. *Pflügers Arch. Eur. J. Physiol.* **1990**, *417* (2), 234–239.

(40) Lerch, S.; Ritz, S.; Bley, K.; Messerschmidt, C.; Weiss, C. K.; Musyanovych, A.;

Landfester, K.; Mailänder, V. Nanoprobing the Acidification Process during Intracellular Uptake and Trafficking. *Nanomedicine* **2015**, *11* (6), 1585–1596.

(41) Fu, Y.; Li, J.; Lee, A. S. GRP78/BiP Inhibits Endoplasmic Reticulum BIK and Protects Human Breast Cancer Cells against Estrogen Starvation-Induced Apoptosis. *Cancer Res.* **2007**, *67* (8), 3734–3740.

(42) Zou, C.; Wang, Y.; Shen, Z. 2-NBDG as a Fluorescent Indicator for Direct Glucose Uptake Measurement. *J. Biochem. Biophys. Methods* **2005**, *64* (3), 207–215.

(43) O'Neil, R. G.; Wu, L.; Mullani, N. Uptake of a Fluorescent Deoxyglucose Analog (2-NBDG) in Tumor Cells. *Mol. Imaging Biol.* **2005**, *7* (6), 388–392.

(44) Klip, A.; Paquet, M. R. Glucose Transport and Glucose Transporters in Muscle and Their Metabolic Regulation. *Diabetes Care* **1990**, *13* (3), 228–243.

(45) Keston, A. S.; Brandt, R. The Fluorometric Analysis of Ultramicro Quantities of Hydrogen Peroxide. *Anal. Biochem.* **1965**, *11* (1), 1–5.

(46) Misra, S. K.; Kus, J.; Kim, S.; Pan, D. Nanoscopic Poly-DNA-Cleaver for Breast Cancer Regression with Induced Oxidative Damage. *Mol. Pharm.* **2014**, *11* (11), 4218–4227.

(47) Vermes, I.; Haanen, C.; Steffens-Nakken, H.; Reutellingsperger, C. A Novel Assay for Apoptosis Flow Cytometric Detection of Phosphatidylserine Expression on Early Apoptotic Cells Using Fluorescein Labelled Annexin V. *J. Immunol. Methods* **1995**, *184* (1), 39–51.

(48) He, Z.; Liu, H.; Agostini, M.; Yousefi, S.; Perren, A.; Tschan, M. P.; Mak, T. W.; Melino, G.; Simon, H. U. p73 Regulates Autophagy and Hepatocellular Lipid Metabolism through a Transcriptional Activation of the ATG5 Gene. *Cell Death Differ.* **2013**, *20* (10), 1415–

1424.

(49) Johansson, F.; Olbe, M.; Sommarin, M.; Larsson, C. Brij 58, a Polyoxyethylene Acyl Ether, Creates Membrane Vesicles of Uniform Sidedness. A New Tool to Obtain inside-out (Cytoplasmic Side-out) Plasma Membrane Vesicles. *Plant J.* **1995**, *7* (1), 165–173.

CHAPTER 3: COMBINATORIAL NANOENCAPSULATION OF SILVER IONS *VIA* LEVOFLOXACIN PRODRUG FOR BACTERICIDAL APPLICATIONS

Abstract

Bacterial-based infectious diseases continue to worsen as instances of antibiotic resistance rise. Research into silver-based or drug-based approaches shows promise, but their clinical translation is hindered by their low incremental effectiveness over currently used treatments. To address these issues, a combinatorial approach using both silver and a fluoroquinolone drug could provide a more suitable substitute for current techniques. For a truly synergistic treatment, however, the packaging and delivery of these agents must be chosen strategically. Here, we investigate a nano-level approach by packaging ionic silver within inverted micelle capsules and subsequently wrapping these capsules with a lipid shell composed of a synthesized levofloxacin prodrug. Our procedure yielded 192 ± 31 nm particles, which we termed the AI-Pro-NP. During bacterial tests, the combination of silver ions and the levofloxacin prodrug had an enhanced and additive antimicrobial effect over each constituent alone. Furthermore, the AI-Pro-NP showed evidence of disrupting vital cell structures as imaged by transmission electron microscopy of bacteria and measured by gel electrophoresis of extracted DNA and proteins. Finally, a live/dead cell assay confirmed the combinatorial effects of the AI-Pro-NP and its ability to serve as an integral antibiotic.

Keywords: Nanoparticles, Drug Delivery, Nanomedicine, Antibiotics.

Introduction

With the wealth of antibacterial agents in clinical use, instances of antibiotic resistance continue to rise and are becoming a growing concern for the future of infectious disease treatments. Both gram-positive and gram-negative bacteria have become resistant to various antibiotics such as macrolides[1] and quinolones.[2] The need to design and develop new agents and methods of delivery with potent antimicrobial activity is urgent.

Fluoroquinolones, a derivative of quinolones with a C-6 fluorinated and a C-7 piperazine ring residue, have had major successes across gram-positive and gram-negative bacteria.[3] Yet, not even these antimicrobial agents are immune to resistance.[4] Therefore, independent investigations have expanded the fluoroquinolone family by developing multiple sub-derivatives to diversify their antimicrobial mechanism. For example, the chemically versatile piperazine ring enabled facile modification of levofloxacin, a topoisomerase inhibitor with significant anti-gram-positive activity,[5] which resulted in the synthesis of countless derivative structures.[6,7] One particular fluoroquinolone derivative of interest is prulifloxacin modified to a lipid tail for prodrug functionality, which is a method that has rapidly gained popularity for drug delivery.[8,9] This prulifloxacin prodrug was found to have a greater potency towards the gram-negative bacteria *E. coli*, and an ofloxacin-resistant strain of *Enterobacter cloacae* than the unmodified form.[10]

Another efficient and popularized method for combatting bacterial infections is the use of silver-based platforms. For example, Panacek et al. synthesized 25 nm silver nanoparticles that exhibited high antibacterial and bactericidal activity against both gram-positive and gram-negative bacteria, including multi-resistant strains.[11] Furthermore, Jung et al. have shown that solutions of ionic silver have incredibly strong antimicrobial potential against *Escherichia coli* and

Staphylococcus aureus[12] due to the silver ions' high affinity for thiol groups on essential biomolecules, such as the amino acid, cysteine.[13]

Here we introduce a unique combinatorial strategy for enhanced antibiotic treatment. We developed a nanocapsule derived from inverted micelle packaging and a levofloxacin-prodrug lipid wrapping for delivering ionic silver, termed the AI-Pro-NP. Our motivation for this design is to simultaneously disrupt the bacterial cell wall and other cellular mechanisms, while delivering levofloxacin intracellularly. With our research methodologies, we found that this nanocapsule is robust, and its antibiotic activity is quantifiably superior to either silver (Ag^+) ions or the levofloxacin prodrug alone. Furthermore, DNA gel assays showed that the AI-Pro-NP disrupted vital cell structures at the molecular level. Finally, transmission electron microscopy (TEM) and *in vitro* imaging of AI-Pro-NP treatments provided visual evidence of their antibiotic activity at the cellular level. Altogether, the AI-Pro-NP technique shows that a multi-mechanistic approach is a superior measure for infectious disease therapy.

Results and Discussion

Nanoparticle Synthesis

At the inception of the AI-Pro-NP synthesis, a solution of 600 mM $AgNO_3$ was vigorously shaken in equal parts volume with 50 mM dodecanoic acid ($C_{12}H_{24}O_2$) solubilized in anhydrous chloroform. The two layers were allowed to settle for a prolonged period before the aqueous layer was extracted. Dodecanoic acid was chosen as the optimal inverted micelle constituent since the electrostatic interactions between the positive Ag^+ ions and the negatively charged carboxylic acid groups would lead to a higher degree of encapsulation. To analyze the transfer capability of Ag^+ from an aqueous solution to the organic solvent chloroform, we performed inductively coupled

plasma optical emission spectrometry (ICP-OES) on the transfer of aqueous $AgNO_3$ (600 mM) to an anhydrous chloroform layer with or without dodecanoic acid (50 mM). Measurements of the control sample (absent of dodecanoic acid) revealed that 7.2 ± 0.6 mM Ag^+ inevitably transferred to chloroform layer due to a reduced integrity of the chloroform's anhydrous state after contact with H_2O. Nonetheless, vigorous shaking of aqueous $AgNO_3$ with the dodecanoic acid solubilized in the chloroform layer, initiated the transfer of 22.0 ± 2.2 mM Ag^+ ions into self-assembled dodecanoic acid inverted micelles (Figure 3.1).

After the Ag^+ ions have been encapsulated by the reverse micelles within the organic chloroform layer, they were mixed with a lipid cocktail consisting of phosphatidylcholine (PC), 1,2-dioleoyl-*sn*-glycero-3-phosphatidylethanolamine (PE), and cholesterol at an optimized mM ratio of 3:0.23:0.03:0.03 of dodecanoic acid:PC:PE:cholesterol. The organic layer was then evaporated to form a thin film, which was flushed with nanopure water (18 MΩ, pH 7.4) and subjected to probe sonication to produce nanoparticles with a final mass concentration of 0.81 mg/ml (Figure 3.2). For naming conventions, this non-prodrug, lipid-wrapped inverted micelle capsule carrying Ag^+ ions is termed the Ag Ion Nanoparticle (AI-NP). From the encapsulation efficiency stated above, we can calculate the w/w percent of silver in the AI-NPs to be 19.3%.

Figure 3.1: Histogram comparing the mM of silver transferred from aqueous $AgNO_3$ to chloroform with and without dodecanoic acid.

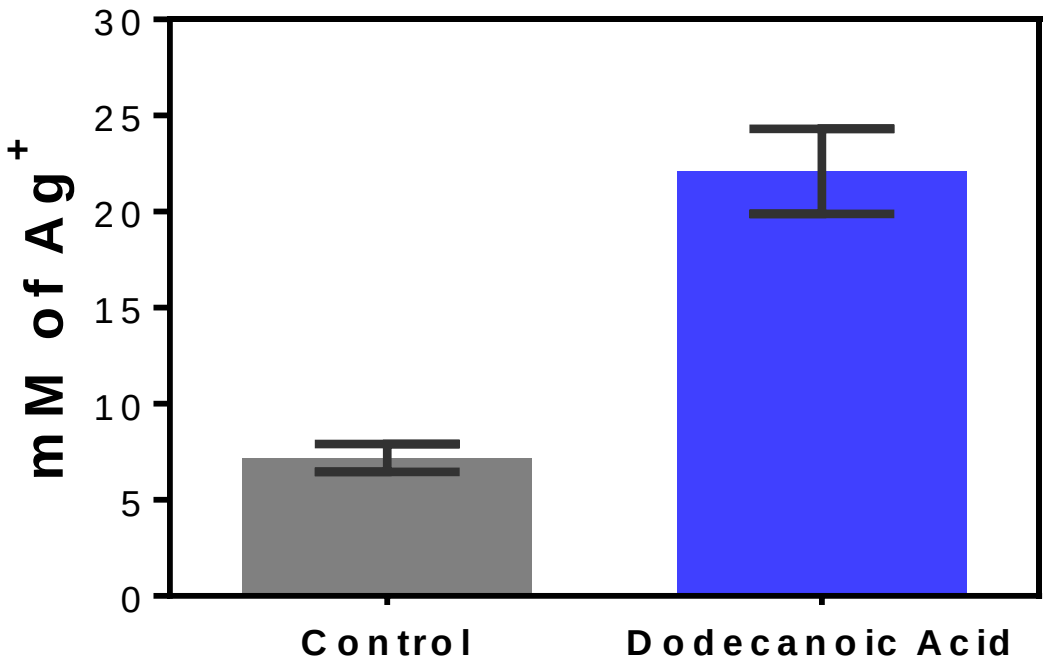

Figure 3.2: Schematic representation of the lipid wrapping process to produce the AI-NP.

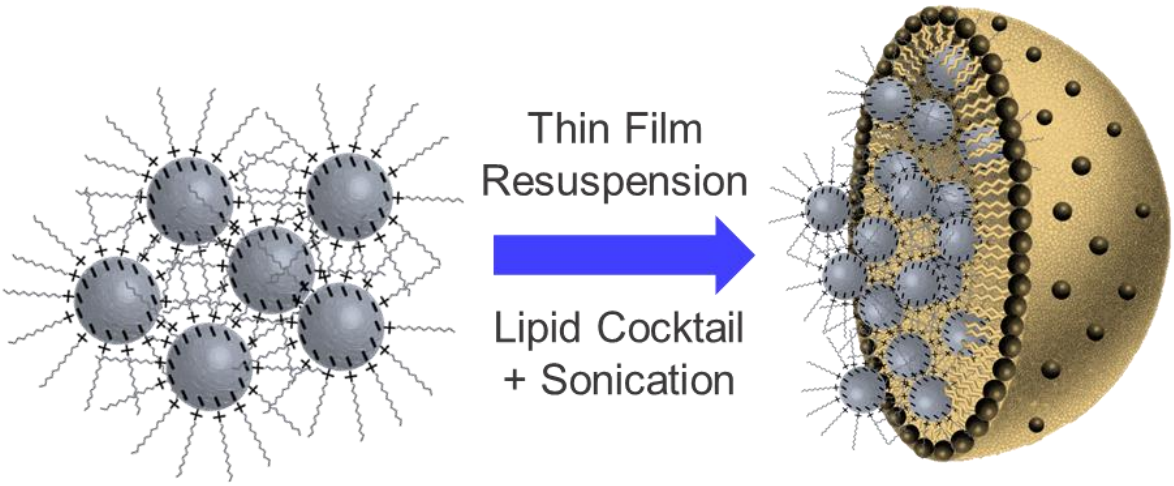

To ensure nanoparticle formation and size consistency, we performed dynamic light scattering measurements, which revealed the AI-NPs' average hydrodynamic diameter to be 192 ± 31 nm with a polydispersity index (PDI) of 0.2 ± 0.1 (Figure 3.3). Moreover, a one-week stability analysis of the AI-NPs stored in the dark at 4 °C showed consistent hydrodynamic diameter integrity, indicating that these particles are suitable for multi-day storage (Figure 3.4). Transmission electron micrographs of AI-NPs supported the nanoparticle formation and the presence of encapsulated silver (Figure 3.5). Within these micrographs, the encapsulated Ag^+ was visually contrasted against the outer nanoparticle material which is explained by the silver's higher electron density (Z = 47).

To measure the AI-NPs' silver release profile, we dialyzed the nanoparticles with 10,000 molecular weight cut off (MWCO) cassettes against nanopure water (18 MΩ, 7.4 pH) at room temperature (25 °C). The nanoparticles were compared to an $AgNO_3$ solution of an equivalent concentration. Over the course of 48 hours, the AI-NP sample maintained 60.9% of its original Ag^+ ion concentration, while the $AgNO_3$ sample lost the majority of its silver content in the first hour (Figure 3.6). This observation demonstrates the AI-NPs' robust ability to encapsulate and hold their contents without compromising their potency as a silver delivery vehicle.

As discussed above, both fluoroquinolone drugs and silver have excellent bactericidal properties stemming from their ability to disrupt different, yet key mechanisms in bacteria needed for bacterial survival. Therefore, we aimed to combine the topoisomerase inhibitor, levofloxacin, with the silver's capability of physically disrupting cell walls, DNA, and Protein. We thus modified a Lyso-PC lipid into a levofloxacin prodrug, cleavable by esterases secreted by common bacterial strains.

Figure 3.3: Histogram representing the number averaged (%) of AI-NPs.

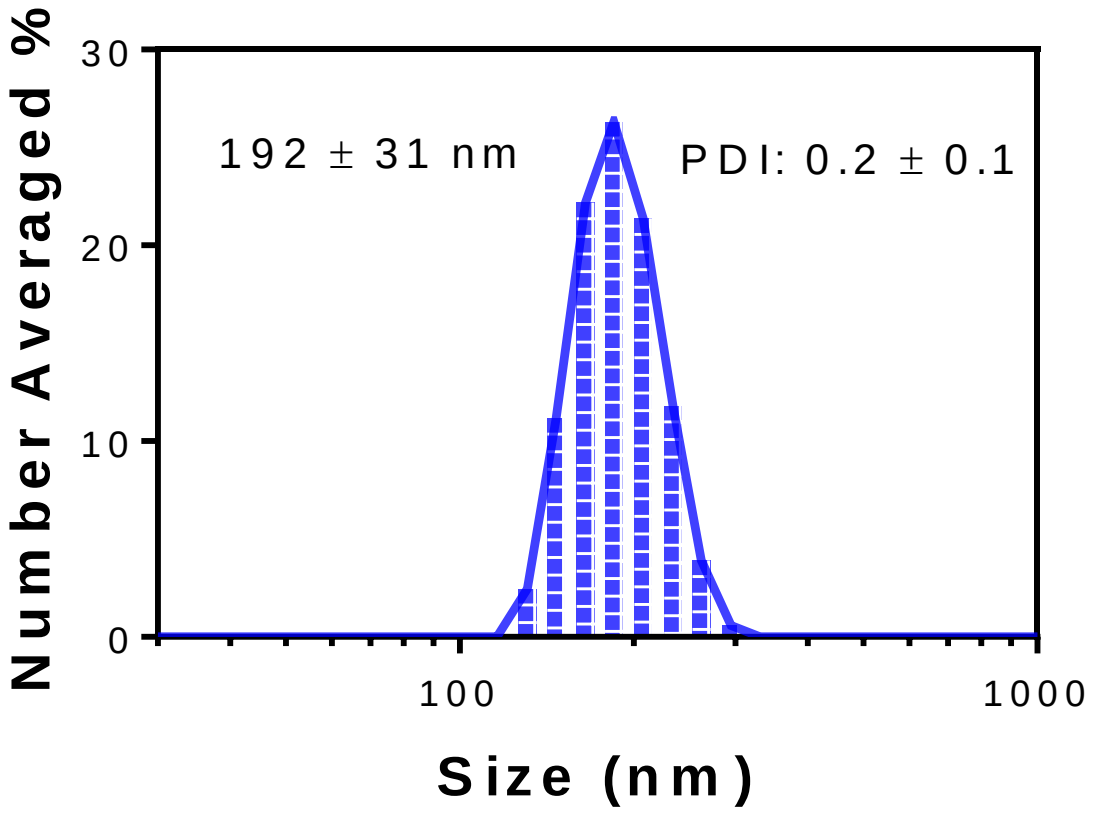

Figure 3.4: A 7-day shelf life stability assessment of the nanoparticle's Hydrodynamic diameter (stored at 4° C).

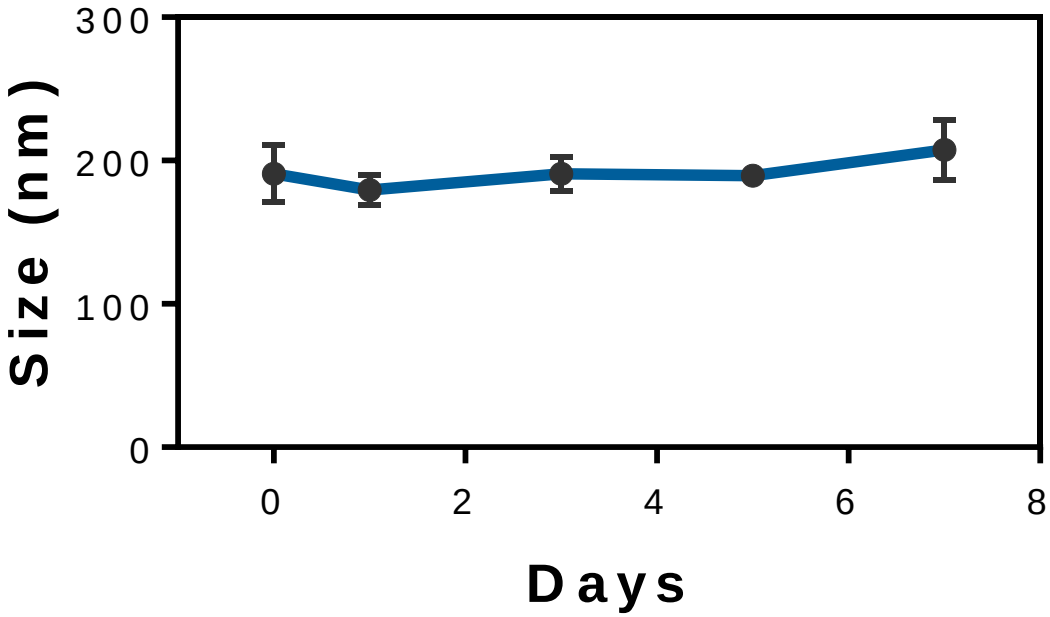

Figure 3.5: TEM micrograph to visualize nanoparticle morphology; Ag^{+} inverted micelle capsule is indicated by blue arrow.

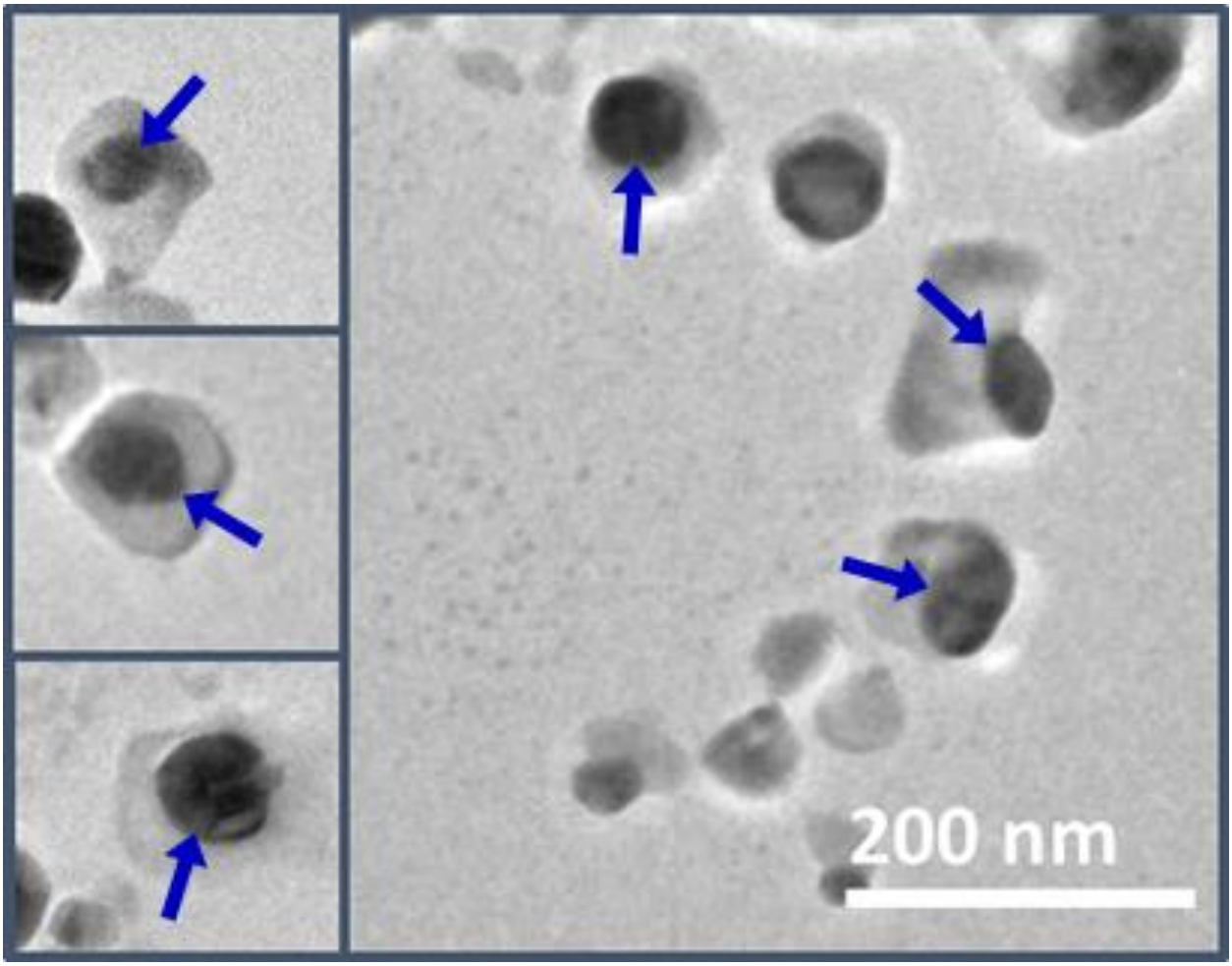

Figure 3.6: Ag^{+} release profile against a 10k MWCO dialysis cassette, and measured by ICP.

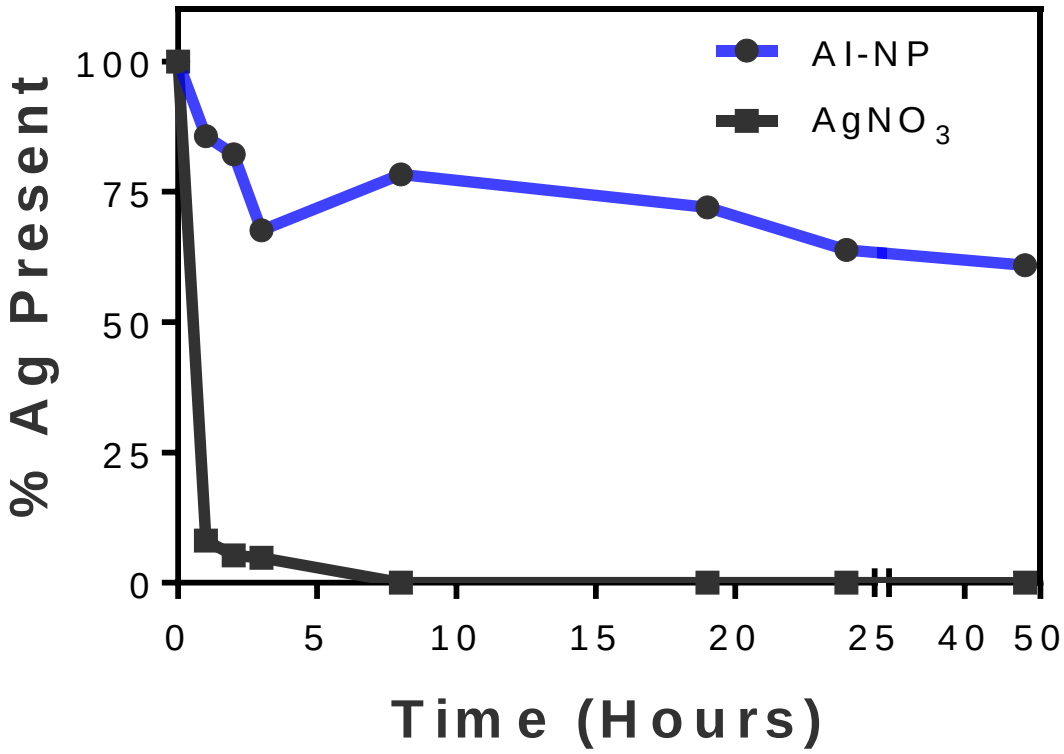

The levofloxacin prodrug synthesis began with Lyso-PC (>99%), Levofloxacin (≥98.0%), N-(3-dimethylaminopropyl)-N′-ethylcarbodiimide hydrochloride (EDC), and 4-dimethylaminopyridine, incubated and stirred at room temperature in chloroform for three days (Figure 3.7). The formation of prodrug was confirmed by Electrospray ionization mass spectrometry (Figure 3.8) ^{1}H –NMR (Figure 3.9), and FTIR (Figure 3.10), spectroscopies results. The peak at m/z value of 839.4715 was identified, indicating the formation of prodrug.

The levofloxacin prodrug was then combined with the AI-NP by replacing the PC lipid molecule and creating the combinatorial nanoparticle termed AI-Pro-NP. This was carried out with the new lipid cocktail consisting of an optimized mM ratio of 3:0.57:0.03:0.03 of dodecanoic acid:prodrug:PE:cholesterol.

To expand the characterization of the AI-Pro-NPs, we investigated the nanoparticles' stability and robustness for *in vito* applications requiring bacterial treatment, through zeta potential measurements and tracking of their hydrodynamic diameter within bacterial media. Zeta measurements of control particles (made of the lipid cocktail with no Ag^{+} or prodrug), AI-NPs, and AI-Pro-NPs remained at 9 ± 2 mV, 9 ± 2 mV, and 9 ± 0 mV, respectively, indicating that the encapsulated contents and the levofloxacin surface modification did not significantly change the stability profile of the AI-Pro-NP nanoarchitecture. When the nanoparticles were kept in Brain Heart Infusion Broth (BHI) at 37 °C over the course of one week, we observed slight variations but no significant increases in their hydrodynamic diameter. This points to aggregation of the nanoparticles' protein corona rather than the aggregation of nanoparticles themselves due to instability (Figure 3.11). Such a result was expected since the zeta potential of each nanoparticle sample (mentioned above) is below 20 mV, which makes it a target for protein aggregation.

Figure 3.7: Schematic showing the prodrug synthesis procedure. The final chemical structure is representative of the lipid used to form the AI-Pro-NP.

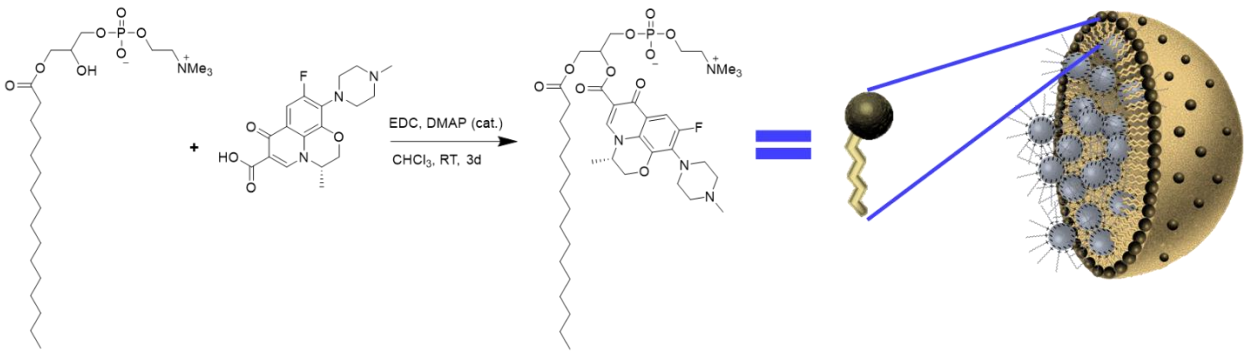

Figure 3.8: Electrospray ionization mass spectrometry of levofloxacin prodrug ($C_{42}H_{69}FN_4O_{10}P^+$). Theoretical peak calculated at 839.4730 MW, and experimental peak was measured to be 839.4715 MW.

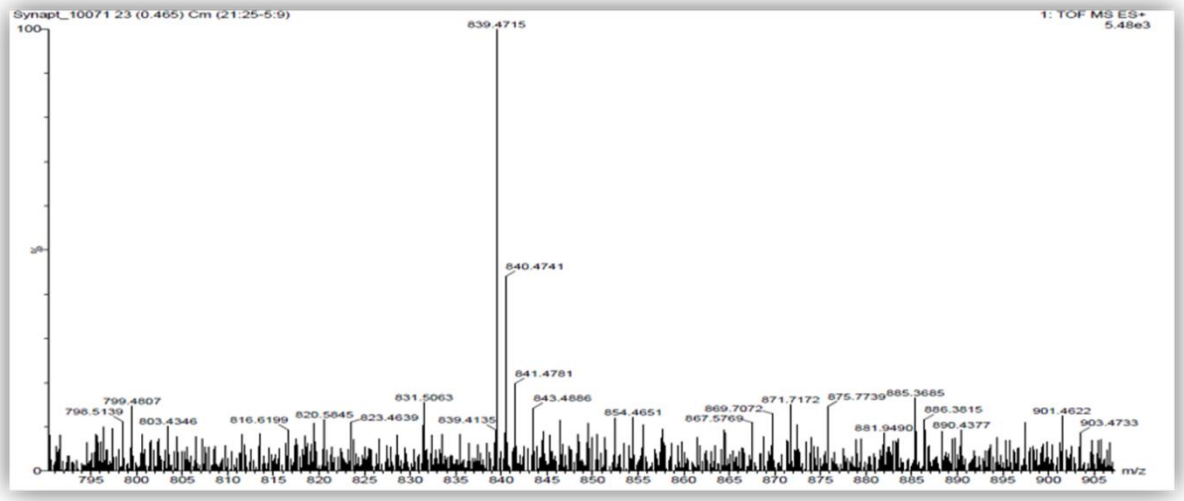

Figure 3.9: NMR spectrums of the levofloxacin prodrug constituents.

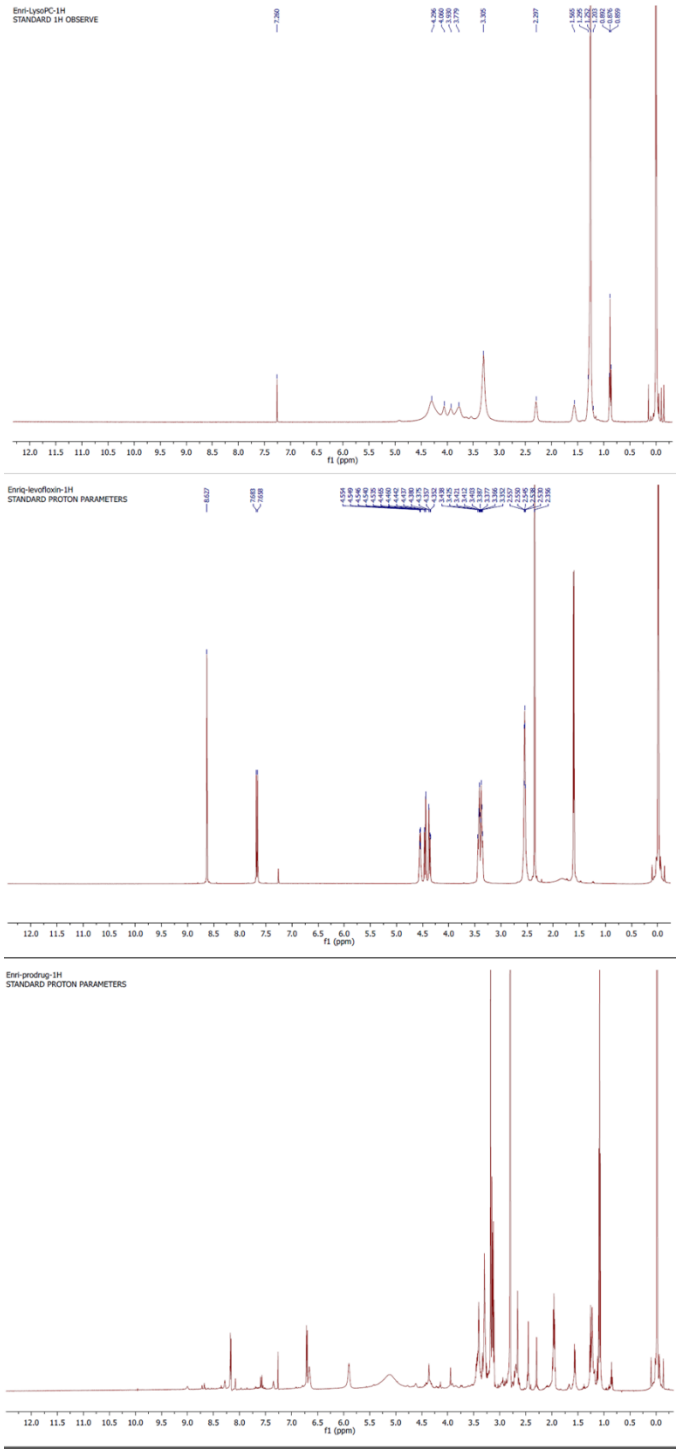

Figure 3.10: FTIR spectral analysis of each levofloxacin prodrug constituent paired with its near infrared spectrum. Peaks are assigned to common molecular structures found in each chemical compound.

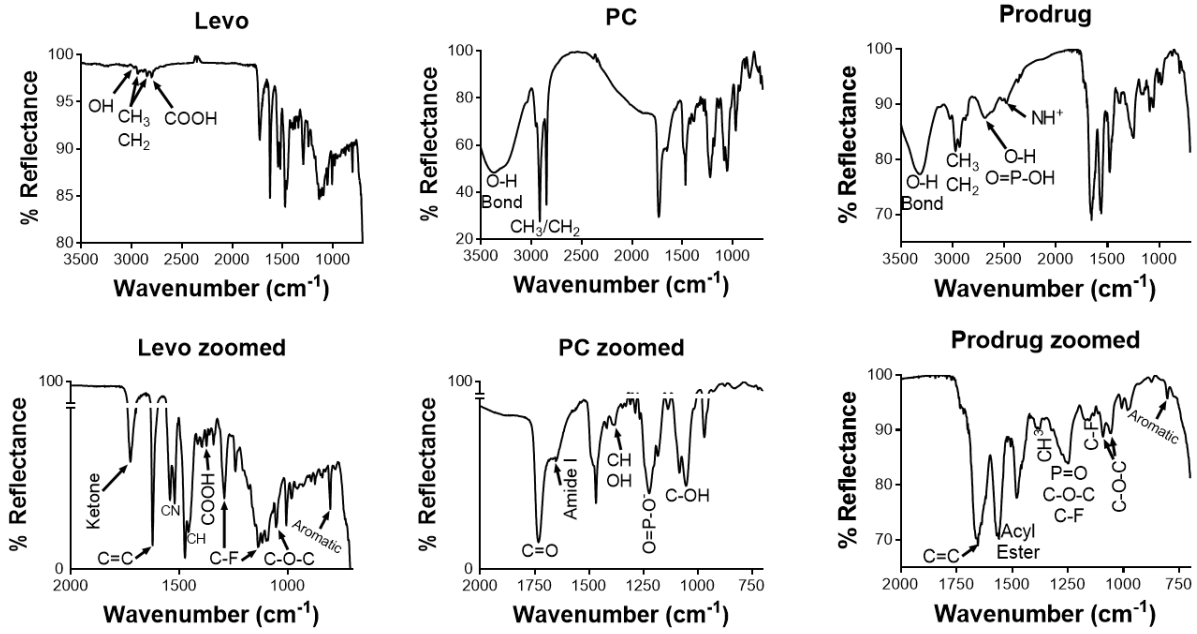

Figure 3.11: Seven-day stability assessment of each nanoparticle's hydrodynamic diameter in BHI media.

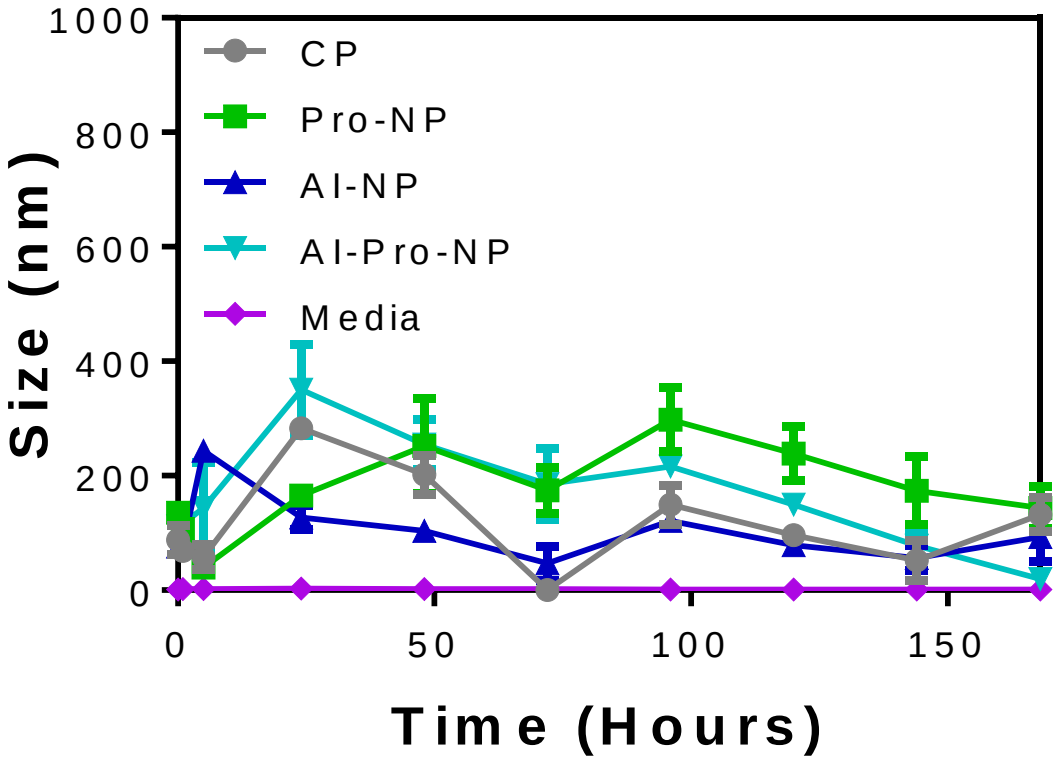

Antibacterial Performance

To compare the AI-Pro-NPs' antimicrobial effects to each of its separate constituents, we tested the LD_{50} level of each nanoparticle variation at a 10% v/v treatment with the bacterium *Bacillus subtilis* (ATCC 6633*)*. This species was chosen because of its history as an exceptional bacterial model for studying resiliency against anti-microbial agents,[14,15] as well as its ability to secrete large amounts of industrially important enzymes to cleave the prodrug ester bond.[16] By tracking the optical density of *B. subtilis* in BHI media at 546 nm over several time points, we gathered that the combinatorial effect of Ag^+ ions and the levofloxacin prodrug led to an additive toxic effect, with the combinatorial approach making the most significant impact (Figure 3.12). Specifically, the AI-Pro-NPs reached the LD_{50} level at 1.3 h, while the AI-NP and the levofloxacin prodrug reached the LD_{50} at 2 h and 4.5 h, respectively.

Although we showed that the levofloxacin prodrug works as an effective topoisomerase inhibitor, the purpose of combining levofloxacin with Ag^+ is to simultaneously disrupt the bacterial cell wall and other critically important cellular mechanisms, in parallel with delivering levofloxacin intracellularly. To investigate this disruptive process, we extracted DNA from treated bacterial samples and performed gel electrophoresis to visualize the effects of Ag^+ ions at the molecular level. For DNA samples, the control particle (CP) and levofloxacin prodrug produced similar results as the control; this is expected because neither CP nor the prodrug are physically destroying cellular mechanisms. As for the AI-NP-treated and AI-Pro-NP-treated samples, DNA bands disappeared from the electrophoresis gels (Figure 3.13). This interesting phenomenon can be explained by the Ag^+ ions breaking the DNA into pieces small enough to run off the gel. Another likely explanation is that amine-based groups of DNA reduced the Ag^+ ions to create

macromolecular silver structures that are too large to migrate through the gel and thus remain confined to the gel well.

To examine the disruptive capabilities of Ag^+ ions at the cellular level, we investigated bacterial cells with TEM. While control samples looked healthy in TEM micrographs (Figure 3.14), the micrographs of the AI-Pro-NP-treated bacterial samples show cross-sections of bacteria with compromised cell walls emptied of bacterial cytoplasm (Figure 3.15). In many of these micrographs, the AI-Pro-NPs can be seen inside disrupted cells, which provides evidence that the damage was due to Ag^+ ions.

Finally, to visualize the effectiveness of the combinatorial AI-Pro-NPs against *B. subtilis*, we assessed the treated bacteria with a live/dead confocal assay. For control and CP samples, cells remained intact and expressed green fluorescence (Figure 3.16a, b), indicating healthy unaffected cellular functions. Contrarily, cells exposed to the levofloxacin prodrug showed low viability yet remained intact, as evidenced by a high population of cells expressing red fluorescence (Figure 3.16c). Finally, both AI-NP-treated and AI-Pro-NP-treated cells had damaged cellular anatomies, with a combination of red and green fluorescence, which resulted in a yellow/orange expression (Figure 3.16d, e). This yellow/orange expression can be explained by the compromised cell wall, which does not have selectivity towards either dye. Even more so, the AI-Pro-NP-treated samples showed very little evidence of any live or intact cells as compared to AI-NP-treated samples alone. This bolstered our assessment that a combinatorial approach with our novel nanoarchitecture leads to more efficient antibacterial treatment.

Figure 3.12: Percent change in *B. subtilis* viability after treatment with each sample.

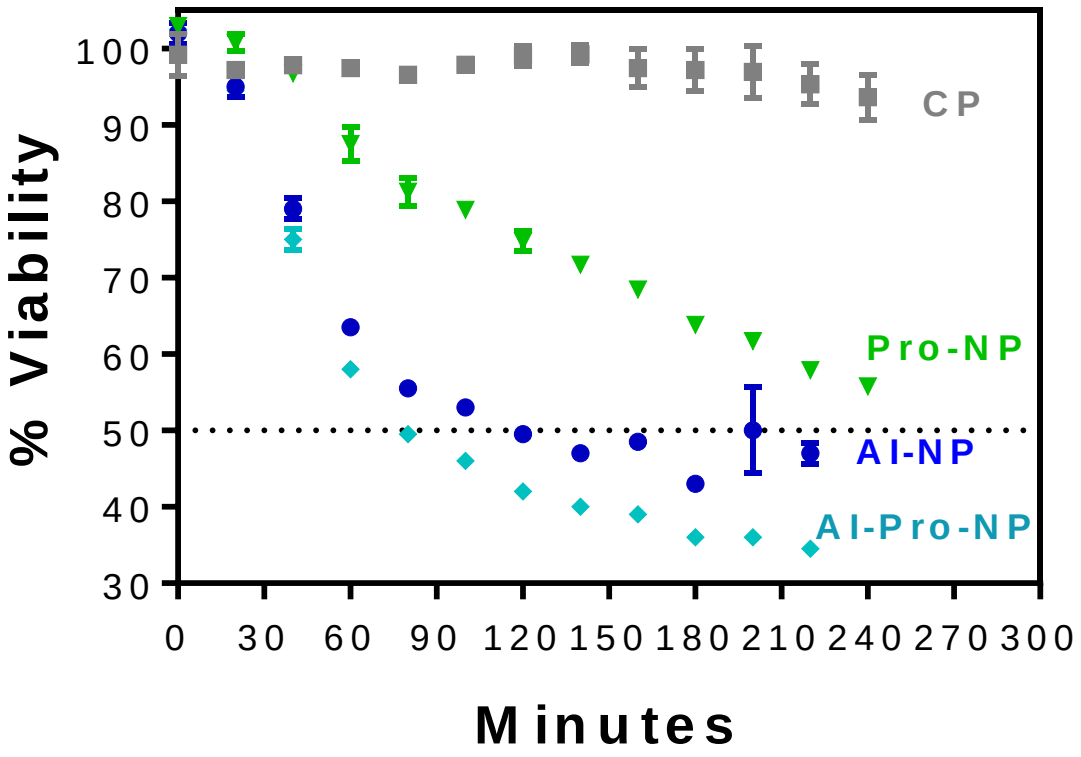

Figure 3.13: Fluorescence image of an agarose gel with DNA samples of bacteria treated with each nanoparticle variation. Order of wells from the left: 1) DNA Ladder, 2) positive control 3) negative control (untreated bacterial DNA), 4) CP, 5) AI-NP, 6) Pro-NP, 7) AI-Pro-NP

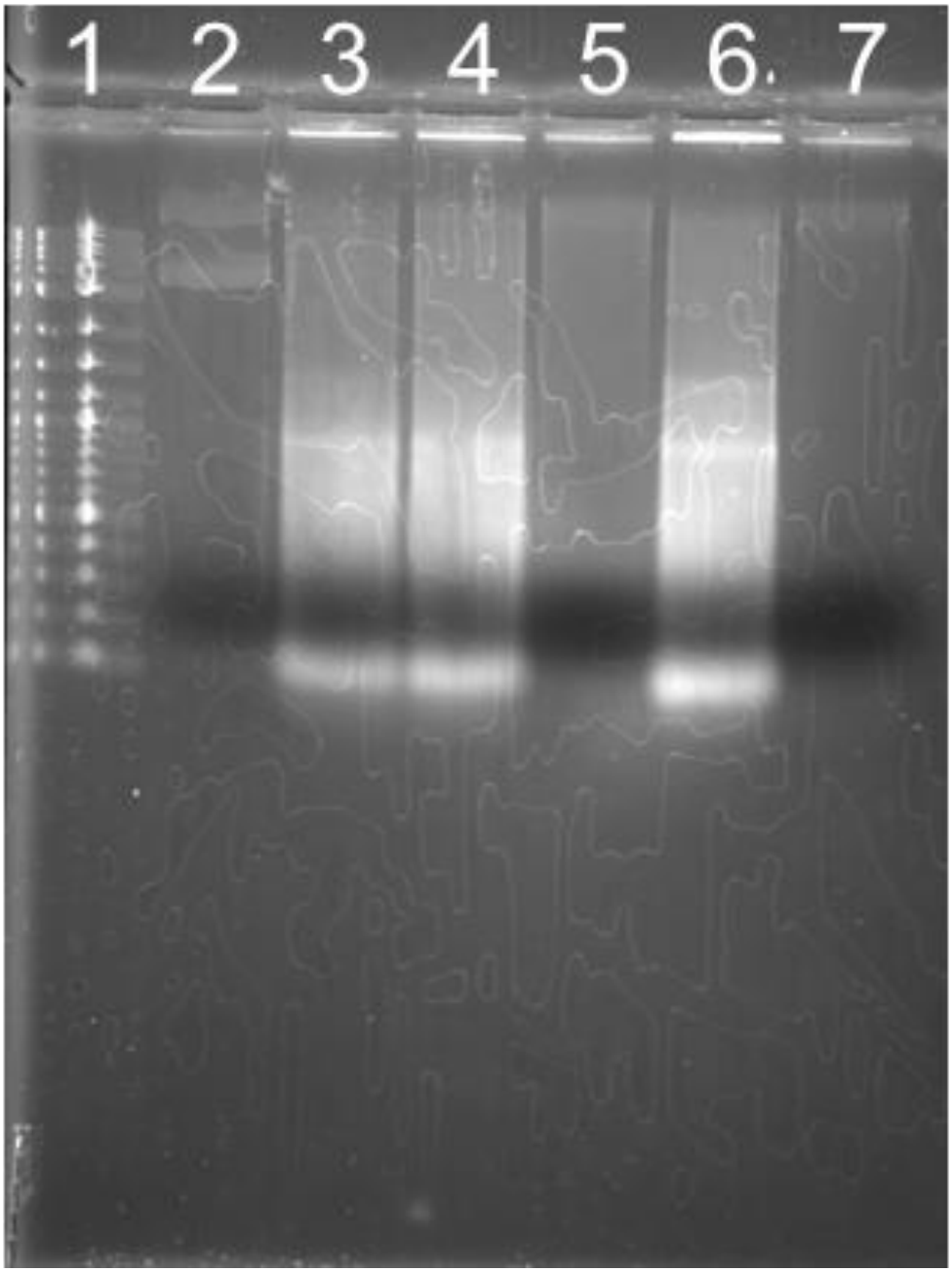

Figure 3.14: TEM micrograph of bacterial cells treated with CP. Inset is added from other imaging samples to show reproducibility. White artifacts in the center of cells are consequence of slicing samples at 60 nm thin.

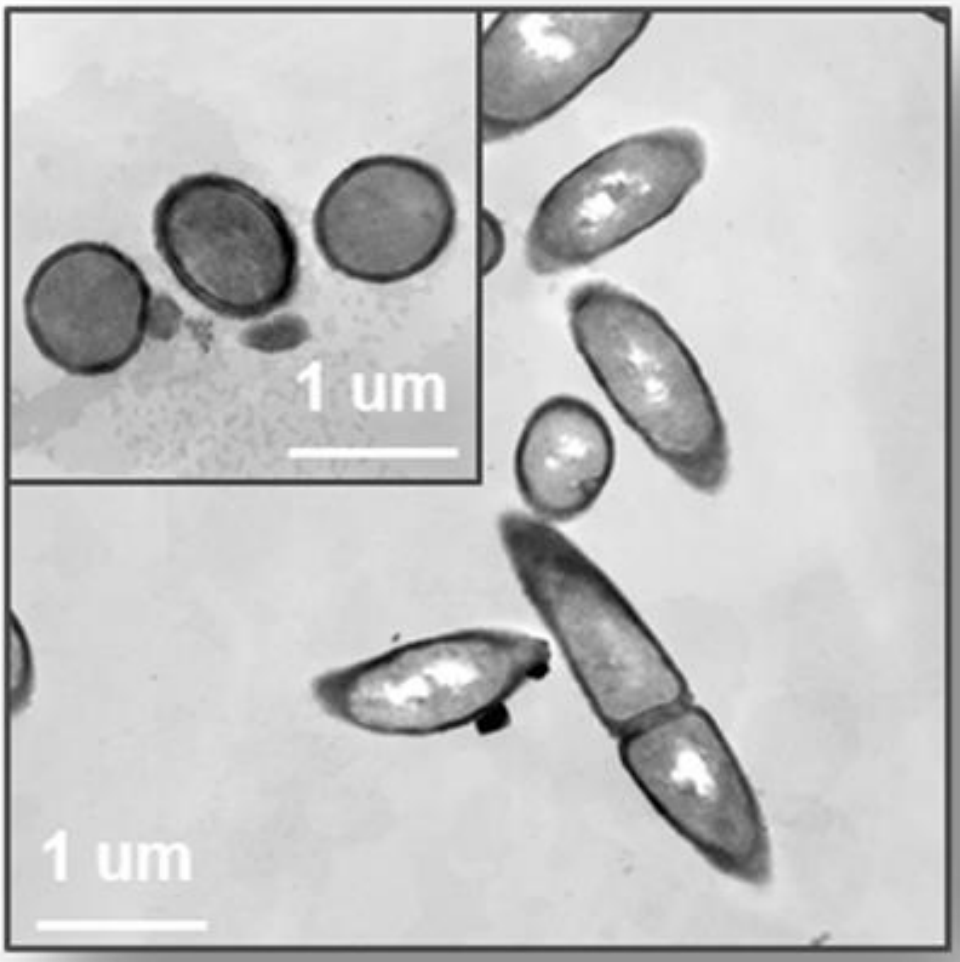

Figure 3.15: TEM micrograph of bacterial cells treated with AI-Pro-NP. Inset is added from other imaging samples to show reproducibility. White artifacts in the center of cells are consequence of slicing samples at 60 nm thin. Blue arrows indicate AI-Pro-NP, while purple arrows point to compromised cell walls.

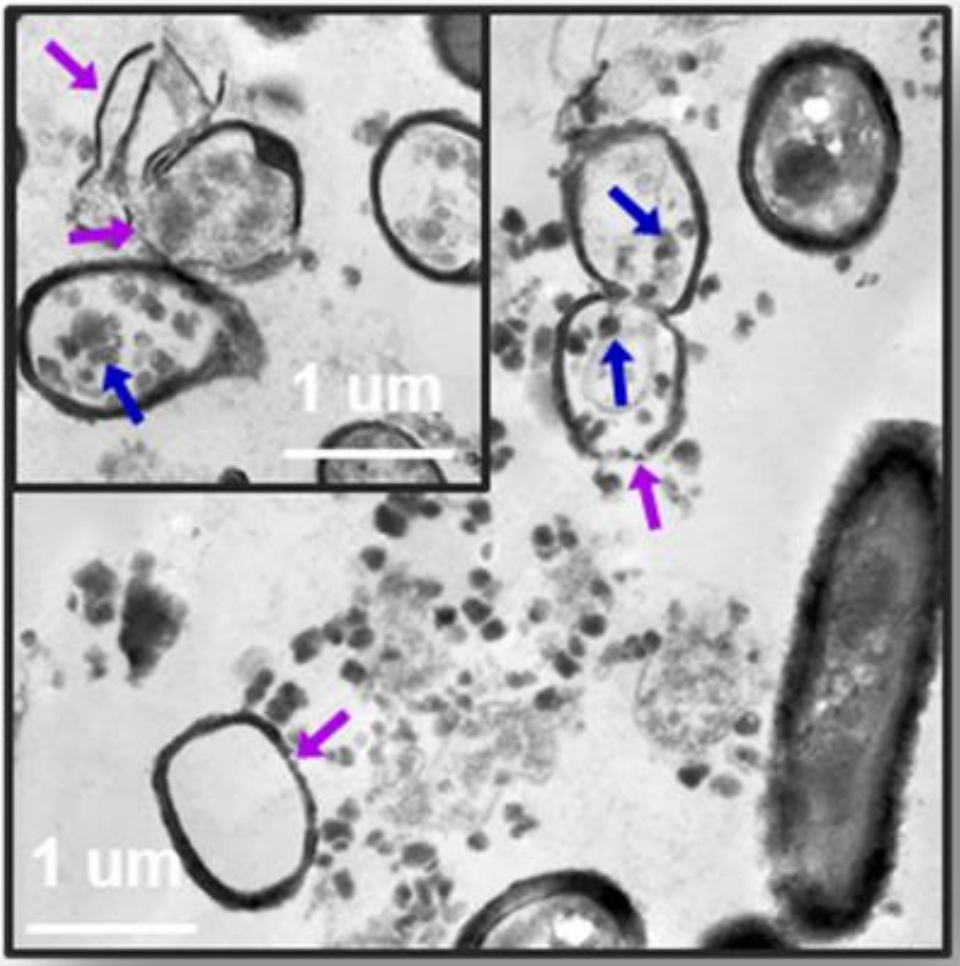

Figure 3.16: Cellular samples stained with either SYTO 9 (green) or propidium iodide (red). Each image represents a bacterial sample treated with a separate nanoparticle variation. (40x objective).

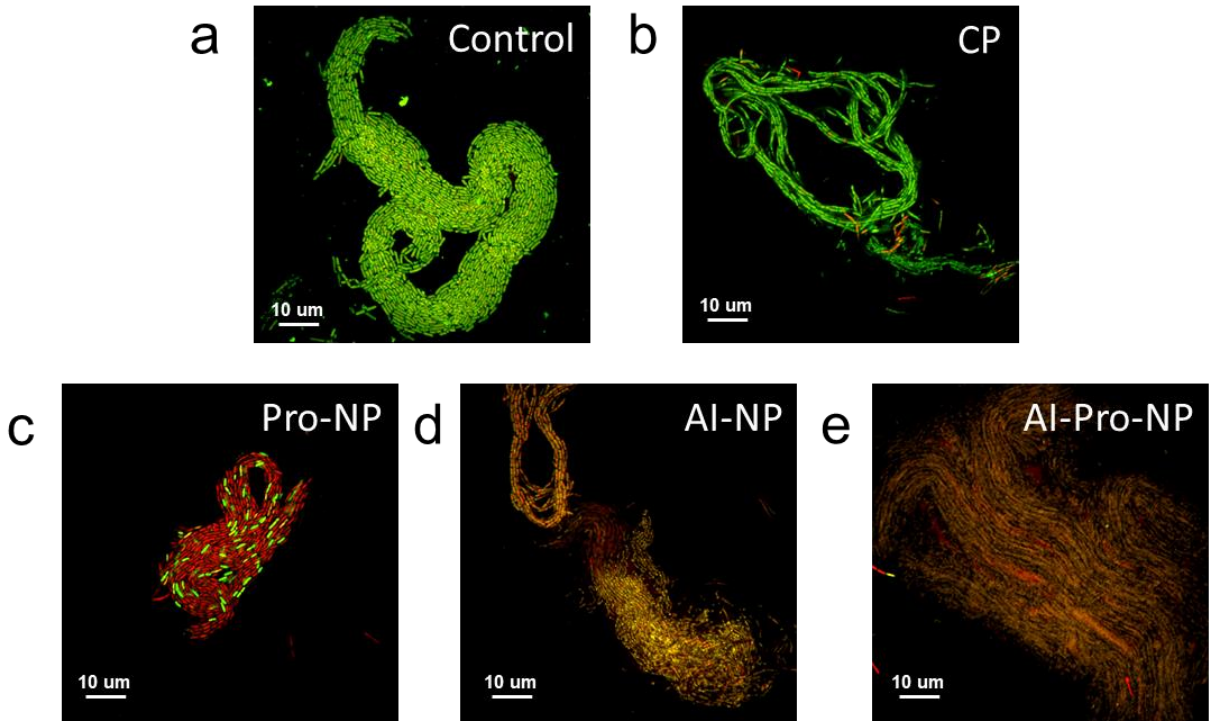

Conclusion

In conclusion, we have demonstrated a combinatorial approach which uses the destructive properties of Ag^+ combined with a prodrug derivative of the popular antibiotic, levofloxacin, for bactericidal applications. This combined approach is strengthened by the novel nano-based packaging and delivery system, which uses inverted micelle self-assembly and lipid wrapping to ensure both Ag^+ ions and levofloxacin are jointly delivered to bacteria at the cellular level. We thoroughly characterized these nanoparticles and measured their bactericidal effectiveness in multiple experimental mediums. Thorough quantification showed that the combinatorial effects of Ag^+ ions and the levofloxacin prodrug in the AI-Pro-NPs are additive and yield a higher toxic effect than each constituent alone. After analyzing the integrity of the bacterial DNA and proteins, we showed that the AI-Pro-NPs exhibited further antibacterial destructive effects at the molecular level. Furthermore, we visualized the effective antibacterial properties of Ag^+ delivered by the AI-NPs with bacterial TEM, which confirmed the bacterial cell wall was, in fact, compromised. Finally, live/dead assays confirmed that the combinatorial AI-Pro-NPs had a powerful antibacterial outcome as compared to Ag^+ ions or the prodrug alone.

Moving forward, additional investigations are warranted for future applications with the AI-Pro-NPs or similar combinatorial techniques. For example, this nanoarchitecture can be used to entrap material other than ionic silver, such as biological matter or other molecular compounds. Additionally, the adaptability of AI-Pro-NPs to other *in vivo* antibiotic applications should be investigated to upgrade this novel delivery platform towards a multifunctional, all-purpose solution to bacterial-based infectious diseases.

Methods

Unless stated otherwise, all material and reagents were purchased from Sigma–Aldrich, St. Louis, MO, and were used without further purification. Solvents were used as received and without further purification.

Inverted Micelle Transfer

An equal volume ratio of 50 mM of dodecanoic acid dissolved in chloroform and an aqueous suspension of 600 mM silver nitrate ($AgNO_3$) was added into a 1-dram (3.7 ml) vial and vigorously shaken for several seconds to homogenously mix the layers. The vials were then allowed to separate and settle for a prolonged period of time. At this point, the organic layer became cloudy indicating the successful transfer and encapsulation of the silver ion.

Nanocapsule Formation

The inverted micelle and silver ion composite (while suspended in chloroform), was added to a glass bulb along with a lipid cocktail. For control samples, this lipid cocktail consisted of phosphatidylcholine (PC, Coatsome, NOF Corporation, Tokyo, Japan) 1,2-Dioleoyl-sn-glycero-3-phosphatidylethanolamine (PE, Cayman Chemical Company, MI, USA), and cholesterol at an optimized mM ratio of 3 : 0.23 : 0.03 : 0.03 of dodecanoic acid:PC:PE:cholesterol. For samples requiring the Levofloxacin Prodrug (NP-Pro or Ag-Pro samples), the lipid cocktail consisted of the Levofloxacin/Lyso-PC derived prodrug (Molecular weight 839.4715 g/mol) at an optimized mM ratio of 3 : 0.57 : 0.03 : 0.03 of dodecanoic acid:Prodrug:PE:cholesterol.

The chloroform in the glass bulb was evaporated by a rotary evaporator (RE200, Yamato Scientific Co., Ltd. Japan) in a 55 °C water bath to produce a thin film layer of the materials. The

sample was then placed in a desiccator (Labconco, Kansas City, MO, USA) for 30 minutes. Water (pH 7.4, 18 MΩ Millipore H_20) was added to the bulb at a volume to produce a final concentration of 0.8 mg/ml. The sample was subject to probe sonication for 30 seconds (Amp: 1, On: 2 sec, Off: 2 sec). The samples were then immediately placed in an ice-bath and incubated for one hour at 4 °C. Following incubation, the samples were filtered through a 0.22 μm PTFE syringe filter and dialyzed against a 10,000 molecular weight cut off cassette (Thermo Scientific Product # 87730, Rockford IL, USA).

Dynamic Light Scattering Measurements

Hydrodynamic diameters were determined using a Malvern Zetasizer ZS90 particle size analyzer, while the scattered light was collected at a fixed angle of 90°. A photomultiplier aperture of 400 μm was used with the incident laser power adjusted to obtain a photon counting rate between 200 and 300 kcps. Diameter values depended on measurements whereupon the measured and calculated baselines of the intensity autocorrelation function had to agree within ±0.1%. All determinations were made in multiples of three consecutive measurements of 15 runs each.

Determination of Electrophoretic Zeta Potential

Zeta potential (ζ) values for each nanoparticle formulation were determined with a nano series Malvern Zetasizer Zeta potential analyzer (Fredrick Seitz Material Research Laboratory, University of Illinois at Urbana-Champaign, (MRL facility, UIUC)). Data were acquired in the phase analysis light scattering (PALS) mode following solution equilibration at 25 °C when calculation of ζ from the measured electrophoretic mobility (μ) employed the Smoluchowski equation, which is expressed as

Equation 3.1 $\mu = \varepsilon\zeta/\eta$

where ε and η are the dielectric constant and the absolute viscosity of the medium, respectively.

Measurements of ζ were reproducible to within ± 2 mV of the mean value given by three determinations of 15 data accumulations.

Transmission Electron Microscopy Imaging

Two µL of particle suspension was applied to carbon-coated TEM grids. Grids were then blotted, air dried, and imaged on a JEOL 2100 Cryo-TEM machine via a Gatan UltraScan 2k × 2k CCD camera (MRL facility, UIUC). For bacterial TEM, Bacterial samples were treated at concentrations that yielded 50% viability for 3 hours of exposure. Bacteria were then centrifuged and washed 3x with dPBS before being flushed with Karnovsky's Fixative and stored at 4°C until imaged.

Raman and FTIR spectroscopy

All Raman measurements were taken on a Nanophoton Raman instrument (MRL facility, UIUC) with a 532 nm wavelength laser. For each spectrum, a grating (600 l mm^{-1}) scan was taken over the range of 120–2700 cm^{-1}. Point scans were performed at 0.2% laser power for one minute using a 20x objective. An average of 20 spectra were recorded and averaged per sample.

For FTIR analysis, aqueous suspensions of particles were drop cast onto MirrIR IR-reflective glass slides (Kevley Technologies, Chesterland, Ohio, USA) and measured using a Nicolet Nexus 670 FTIR (MRL facility, UIUC). For each measurement 100 × 100 µm images were collected at 1 cm^{-1} spectral resolution with 64 scans per pixel and a 25 × 25 µm pixel size and individual spectra were corrected for atmospheric contributions.

Live/Dead Assay with Confocal Microscopy

After nanoparticle treatments, bacterial cells were washed with 3x with 0.85% NaCl. We then used the LIVE/DEAD BacLight Bacterial Viability Kit (Molecular Probes, L7012) to stain cells with both SYTO 9 dye (green) and propidum iodide (red). These cells incubated at room temperature in the dark for 15 minutes before confocal imaging. Imaging was carried out using a Zeiss LSM 710 confocal scanner with a 488 nm laser for both SYTO 9 and Propidium Iodide (all lasers were used at 2% laser power).

Author Contributions

EAD, SM and DP designed experimental procedures and performed analysis. EAD and SM wrote the manuscript. EAD synthesized and characterized particles. GV performed chemical synthesis of the prodrug. DS performed NMR measurements. ASD performed electron microscopy. EAD and SM performed bacterial experiments and analysis. SM and IT performed Animal Experiments.

References to Chapter 3

(1) Coleman, K. Recent Advances in the Treatment of Gram-Positive Infections. *Drug Discov. Today Ther. Strateg.* **2004**, *1* (4), 455–460.

(2) Martínez-Martínez, L.; Eliecer Cano, M.; Manuel Rodríguez-Martínez, J.; Calvo, J.; Pascual, Á. Plasmid-Mediated Quinolone Resistance. *Expert Rev. Anti. Infect. Ther.* **2008**, *6* (5), 685–711.

(3) Wolfson, J. S.; Hooper, D. C. The Fluoroquinolones: Structures, Mechanisms of Action and Resistance, and Spectra of Activity in Vitro. *Antimicrob. Agents Chemother.* **1985**, *28* (4), 581–586.

(4) Hooper, D. C. Mechanisms of Action and Resistance of Older and Newer Fluoroquinolones. *Clin. Infect. Dis.* **2000**, *31 Suppl 2* (Supplement 2), S24–S28.

(5) Segatore, B.; Setacci, D.; Perilli, M.; Franceschini, N.; Marchetti, F.; Amicosante, G. Bactericidal Activity of Levofloxacin and Ciprofloxacin on Clinical Isolates of Different Phenotypes of Pseudomonas Aeruginosa. *Int. J. Antimicrob. Agents* **2000**, *13* (3), 223–226.

(6) Mohammadhosseini, N.; Alipanahi, Z.; Alipour, E.; Emami, S.; Faramarzi, M.; Samadi, N.; Khoshnevis, N.; Shafiee, A.; Foroumadi, A. Synthesis and Antibacterial Activity of Novel Levofloxacin Derivatives Containing a Substituted Thienylethyl Moiety. *DARU J. Pharm. Sci.* **2012**, *20* (1), 16.

(7) Foroumadi, A.; Emami, S.; Mansouri, S.; Javidnia, A.; Saeid-Adeli, N.; Shirazi, F. H.; Shafiee, A. Synthesis and Antibacterial Activity of Levofloxacin Derivatives with Certain Bulky Residues on Piperazine Ring. *Eur. J. Med. Chem.* **2007**, *42* (7), 985–992.

(8) Zhang, R.; Pan, D.; Cai, X.; Yang, X.; Senpan, A.; Allen, J. S.; Lanza, G. M.; Wang, L. V. alphaVbeta3-Targeted Copper Nanoparticles Incorporating an Sn 2 Lipase-Labile Fumagillin Prodrug for Photoacoustic Neovascular Imaging and Treatment. *Theranostics* **2015**, *5* (2), 124–133.

(9) Zhou, H.; Yan, H.; Hu, Y.; Springer, L. E.; Yang, X.; Wickline, S. A.; Pan, D.; Lanza, G. M.; Pham, C. T. N. Fumagillin Prodrug Nanotherapy Suppresses Macrophage Inflammatory Response *via* Endothelial Nitric Oxide. *ACS Nano* **2014**, *8* (7), 7305–7317.

(10) Tomii, Y.; Ozaki, M.; Matsuda, M.; Honmura, T.; Nishimura, I.; Yamaguchi, R.; Adachi, T.; Okawa, Y.; Nishino, T. Therapeutic Effect of the Quinolone Prodrug Prulifloxacin against Experimental Urinary Tract Infections in Mice. *Arzneimittelforschung.* **1996**, *46* (12), 1169–1173.

(11) Panáček, A.; Kvítek, L.; Prucek, R.; Milan Kolář; Renata Večeřová, ‡; Naděžda Pizúrová, §; Virender K. Sharma, *; Tat‘jana Nevěčná, † and; Zbořil†, R. Silver Colloid Nanoparticles: Synthesis, Characterization, and Their Antibacterial Activity. **2006**.

(12) Jung, W. K.; Koo, H. C.; Kim, K. W.; Shin, S.; Kim, S. H.; Park, Y. H. Antibacterial Activity and Mechanism of Action of the Silver Ion in Staphylococcus Aureus and Escherichia Coli. *Appl. Environ. Microbiol.* **2008**, *74* (7), 2171–2178.

(13) Bragg, P. D.; Rainnie, D. J. The Effect of Silver Ions on the Respiratory Chain of *Escherichia Coli*. *Can. J. Microbiol.* **1974**, *20* (6), 883–889.

(14) Stein, T. Bacillus Subtilis Antibiotics: Structures, Syntheses and Specific Functions. *Mol. Microbiol.* **2005**, *56* (4), 845–857.

(15) Kim, D.; Yu, B. J.; Kim, J. A.; Lee, Y.-J.; Choi, S.-G.; Kang, S.; Pan, J.-G. The Acetylproteome of Gram-Positive Model Bacterium *Bacillus Subtilis*. *Proteomics* **2013**, *13* (10–11), 1726–1736.

(16) Kunst, F.; Ogasawara, N.; Moszer, I.; Albertini, A. M.; Alloni, G.; Azevedo, V.; Bertero, M. G.; Bessières, P.; Bolotin, A.; Borchert, S.; et al. The Complete Genome Sequence of the Gram-Positive Bacterium *Bacillus Subtilis*. *Nature* **1997**, *390* (6657), 249–256.

CHAPTER 4: NANOCAPSULATION FOR IMPROVED INTRACELLULAR DELIVERY OF HYDROPHILIC AGENTS

Abstract

Nanoparticles designed as theranostic delivery vehicles have the potential to revolutionize personalized medicine. However, the use of theranostic agents in clinical practice is considerably hindered by their complex chemistries and synthesis procedures, which create difficulties for their encapsulation and delivery efficacy in systemic applications. Although a common solution for nano-delivery is the use of liposomes, they tend to release water-soluble payloads accidentally during their systemic circulation. The liposome leakage reduces the overall potency of water-soluble drugs or agents.

Here we introduce a unique chemical combinatorial solution for enhancing the encapsulation and nano-delivery efficiency of water-soluble theranostic agents. Our encapsulation procedure is a simple 2-step nanoparticle synthesis method that uses inverted micelle self-assembly as the agent encapsulation mechanism followed by wrapping in an amphiphilic and biocompatible lipid shell, termed the NanoCapsule (NCAP). This method greatly enhances hydrophilic encapsulation without sacrificing structural integrity or biocompatibility. A thorough nanoparticle characterization revealed that the NCAPs' architecture maintained long-term stability and integrity across different environmental media. Additionally, we showed that the NCAP could be adapted to encapsulate a variety of imaging and therapeutic agents by tweaking the chemistries of the inverted micelle capsules. Finally, we employed fluorescent methods to measure the encapsulation and delivery efficiency of the NCAPs as compared to conventional liposomes on a breast cancer cell line. Flow cytometry results showed the NCAPs had a 69.93% greater efficiency in cellular labeling over liposomes, whereas live confocal videos confirmed the NCAPs' ability of intracellular delivery as opposed to interacting with the cell membrane alone. Our data supports the highly customizable nature of the NCAPs' architecture, which is especially desirable for

combinatorial theranostics requiring labeled lipids and agent delivery and presents an ideal platform for clinical translation.

Keywords: Nanomedicine, Nanoparticles, Inverted Micelles, Theranostics, Nanodelivery.

Introduction

Because of their high adaptability, nanoparticles are an ideal platform for delivering personalized theranostics to patients and for performing comprehensive preclinical studies of these agents.[1] Nanoparticles are capable of delivering a range of therapeutic agents to specific locations in the body, while they simultaneously facilitate imaging and tracking of the affected tissues. This capability has been welcomed by the scientific community, while spurring considerable research and advancement. Unfortunately, complex chemistry and synthesis procedures hinder the ability of nanoparticles to encapsulate certain agents necessary for specific clinical applications. This significant barrier to nanoparticle adoption highlights the lack of a broad and effective platform for the encapsulation and delivery of theranostic agents.

The current solution for packaging and delivering theranostic agents is to trap them within the lumen bilayer of liposomes, which enhances biocompatibility and targets tumors via the enhanced permeability and retention effect.[2] In fact, the first nanomedicine, liposomal doxorubicin (Doxil), was approved by the FDA in 1995 and has been used since in a clinical setting for the treatment of cancer for the last 20 years.[3]

However, liposomes have several limitations that restrict their effectiveness for theranostic applications. First, liposomes tend to be "leaky," which is defined as the passive and unintentional release of the contents. This "leakiness" depends on several variables such as water solubility of the agent, drug-to-lipid ratio, vesicle diameter, and cholesterol content.[4,5] Therefore, the "leakiness" reduces the efficiency and potency of water-soluble drugs or agents for reaching their desired targets, decreases their overall therapeutic effectiveness, and potentially contributes to unintended side effects. Furthermore, large (10–300 nm) and small (<10 nm) liposomes face

clearance from the blood by the reticuloendothelial system (RES) and renal clearance, respectively.[6,7] Coating the liposomes with polyethylene glycol (PEG) can mitigate RES clearance, but PEG can also hinder the particles' controlled release ability at the intended tissue.[8,9]

This investigation outlines an innovative solution for packaging water-soluble agents, which offers numerous advantages over liposomes and other encapsulation modalities currently in use. This encapsulation method employs a simple 2-step phase-transfer chemistry for enveloping agents within an inverted micelle capsule and repackaging them with a lipid-based shell to maintain biocompatibility for systemic use. These inverted micelles are composed of 12-carbon fatty acids where the head groups electrostatically interact with the intended encapsulated agent. These inverted micelles are then resuspended within a lipid coating to produce the structure termed the NanoCapsule (NCAP).

Throughout our investigation, we tested the NCAPs' encapsulation efficiency, stability, longevity, biocompatibility, and treatment efficacy. Since most drug varieties come in small molecule form, we chose various dyes and the popular chemotherapeutic agent Doxorubicin as our agent of encapsulation. We found that the electrostatic interactions between the inverted micelle material and the agent of interest (dye or drug) is a significant determinant of the types of molecular structures that can be encapsulated. Additionally, the NCAPs' architecture showed to maintain long-term stability and integrity across different environmental mediums. Furthermore, we established a biological profile of the NCAP and proved its superior ability as a nanodelivery vehicle against liposomes with fluorescent techniques. Specifically, in a flow cytometry experiment, the NCAP surpassed the liposome treatments in delivery efficiency by 69.93%.

Based on our findings, we believe our strategy can become a widely-used methodology for encapsulating and delivering water-soluble theranostic agents in systemic applications, replacing the commonly used liposome variant.

Results and Discussion

Our initial experiments began with the aqueous-to-organic transfer of the commonly used dye Rhodamine B to test the inverted micelle capabilities for encapsulating and retaining a simple molecular structure. A solution of 0.1 mg/ml Rhodamine B was vigorously shaken in equal parts volume with 50 mM dodecanoic acid ($C_{12}H_{24}O_2$) solubilized in anhydrous chloroform. The two layers are allowed to settle for a prolonged period until the phase transfer was visibly complete (Figure 4.1) and is followed by the extraction of the aqueous layer. Dodecanoic acid was chosen as the optimal reverse micelle constituent, which resulted in a high amount of Rhodamine B transfer. The concentration of Rhodamine B was optimized to ensure that the dodecanoic acid inverted micelles were at full payload capacity while ensuring that the presence of residual dye in the aqueous layer was less than 1%. The mol/mol optimization ratio between dodecanoic acid and Rhodamine B helped control the concentration of dye within the organic layer.

Once the Rhodamine B molecules have been encapsulated by the inverted micelles within the organic chloroform layer, the sample was measured by dynamic light scattering (DLS) to compare the diameters of the inverted micelles to their theoretical values. The dodecanoic acid inverted micelles had a measured diameter of 3 ± 1 nm with a polydispersity index (PDI) of 0.1 ± 0.1 (Figure 4.2), whereas the theoretical diameter of the inverted micelle is 3.6 nm (the length of dodecanoic acid is 1.8 nm). Therefore, the DLS measurements coincided with theoretical predictions.

Figure 4.1: Schematic representation of rhodamine B transferring from aqueous to organic layers into inverted micelle capsules. Image of actual samples are shown adjacent to schematic.

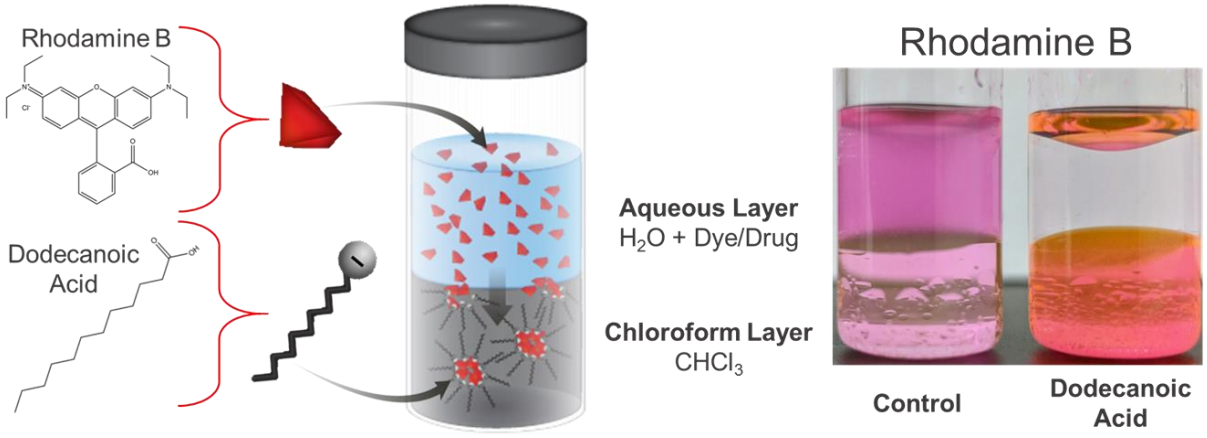

Figure 4.2: Histogram representing the number averaged (%) of dodecanoic acid inverted micelles as measured by DLS.

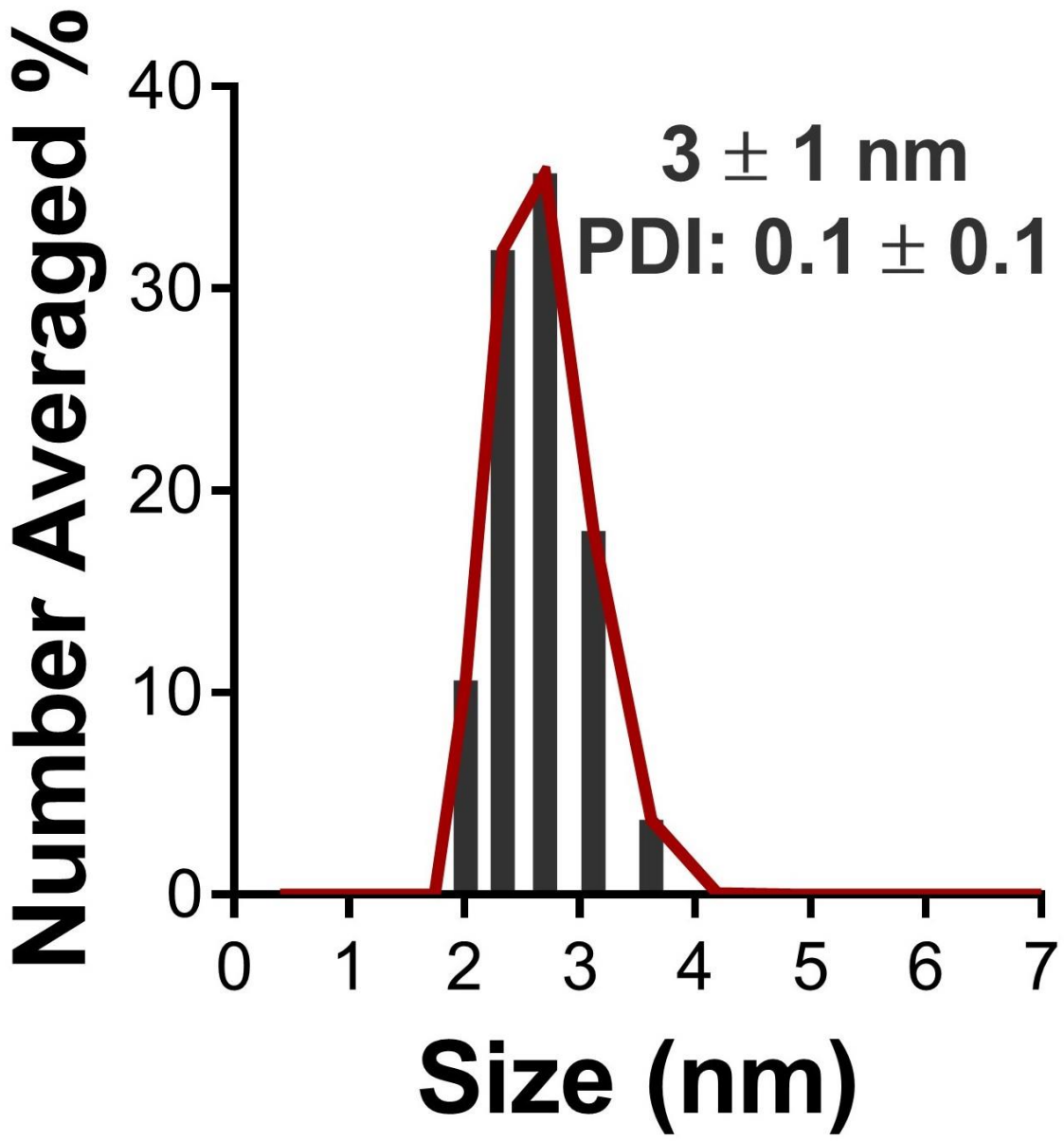

To evaluate the selectivity of the dodecanoic acid inverted micelle capsulation, we tested two separate solutions of Methylene Blue and fluorescein isothiocyanate (FITC) for their transfer capabilities, both at the same concentration of 0.1 mg/mL. Surprisingly, while Methylene Blue did transfer from the aqeuous layer to the organic layer (Figure 4.3), FITC did not (Figure 4.4). It can be seen from the chemical structure of each dye that the negatively charged dodecanoic acid head favors the positively charged amine groups of both Rhodamine B and Methylene Blue. To test this observation with FITC, we kept all parameters of the dye transfer process the same, except that dodecanoic acid was replaced with dodecylamine ($C_{12}H_{27}N$); the latter contains a primary amine instead of a carboxylic acid on its head group. As expected, FITC did transfer from the aqueous layer to the organic chloroform layer only in the presence of dodecylamine, since dodecylamine favors the electrostatic interactions with FITC's negatively charged carboxylic acid group (Figure 4.4).

To demonstrate the NCAPs' applicability in the field of nanomedicine, we chose to test the transfer of the popular chemotherapeutic drug Doxorubicin at 0.1 mg/ml using the inverted micelle initiating agent dodecanoic acid at 50 mM (Figure 4.5). Our UV-VIS results demonstrate that dodecanoic acid facilitated the transfer of 242% more doxorubicin than the control sample (control: 34.5 µg; with dodecanoic acid: 83.5 µg) (Figure 4.6). Concentrations of doxorubicin in the aqueous layer post transfer were fitted to a calibration curve (Figure 4.7).

Figure 4.3: Sample image of aqueous Methylene Blue suspension and transfer into dodecanoic acid inverted micelles. Dye structure is provided in ionic form for reference.

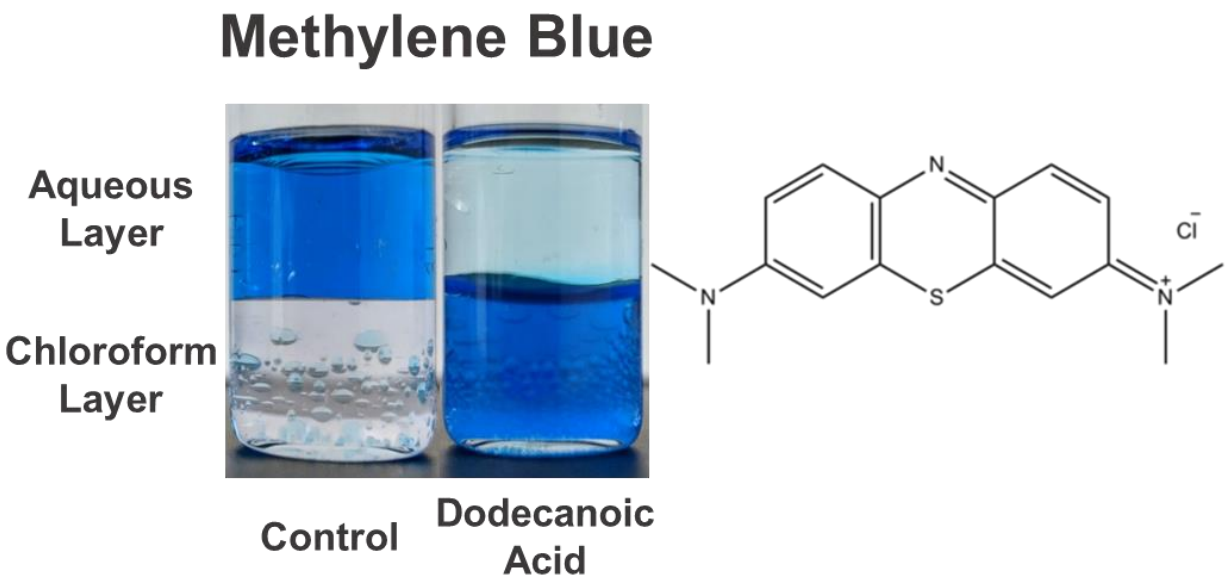

Figure 4.4: Sample image of aqueous FITC suspension and transfer attempts into dodecanoic acid and dodecyl amine. Dye structure is provided in ionic form for reference.

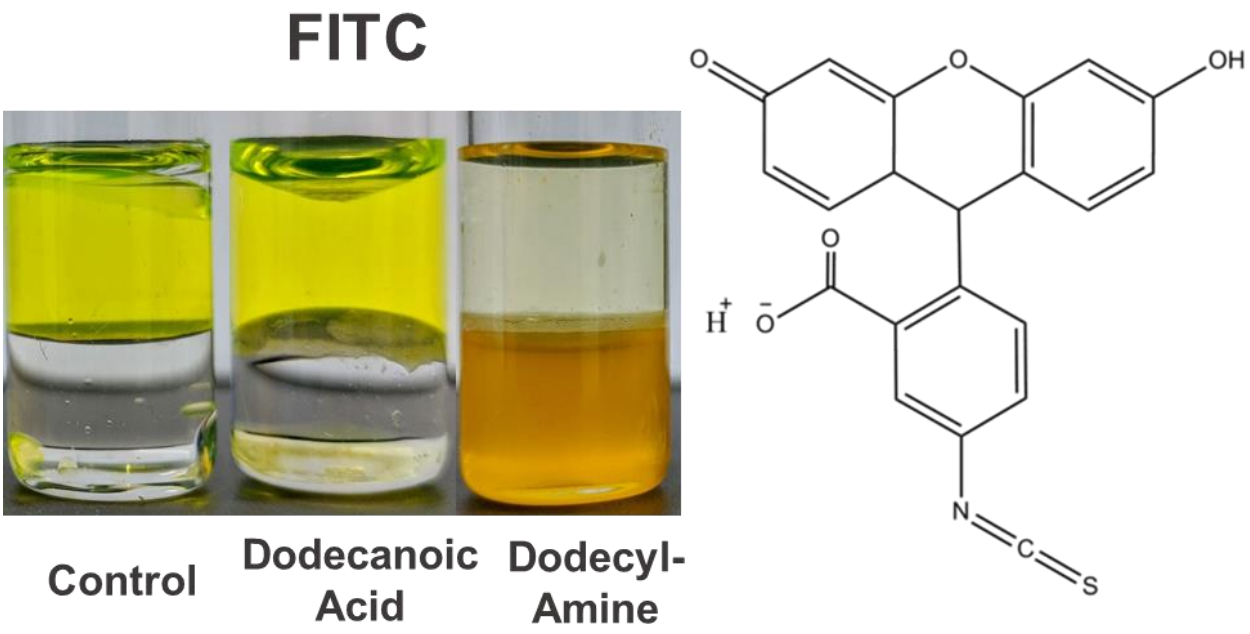

Figure 4.5: Sample image of aqueous Doxorubicin suspension and transfer into dodecanoic acid inverted micelles.

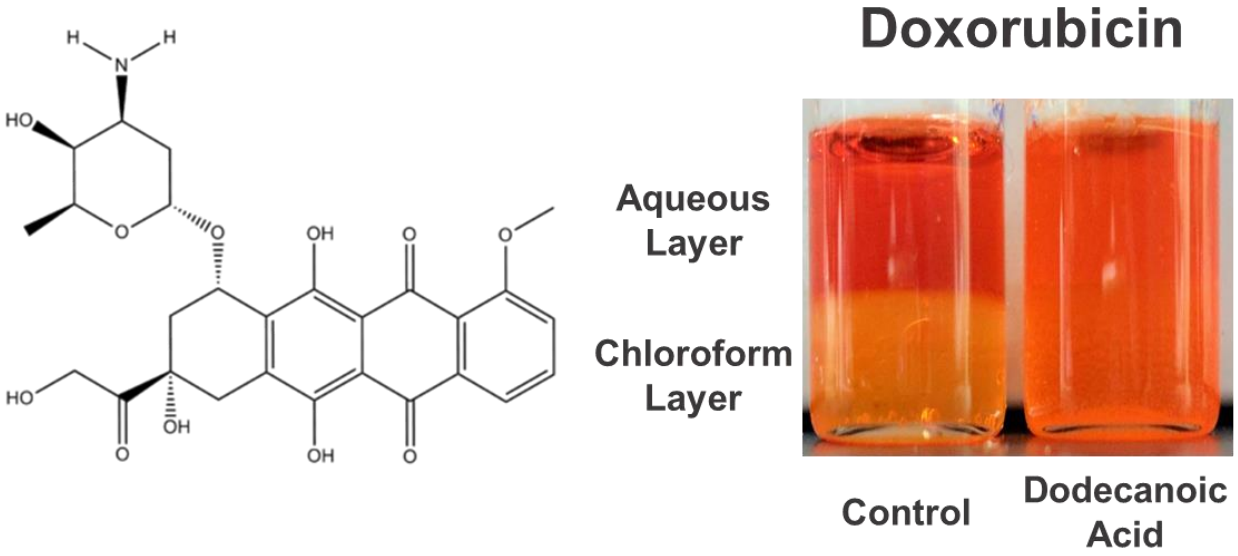

Figure 4.6: Absorbance levels and quantification of dye transferred into dodecanoic acid inverted micelles, as compared to control samples.

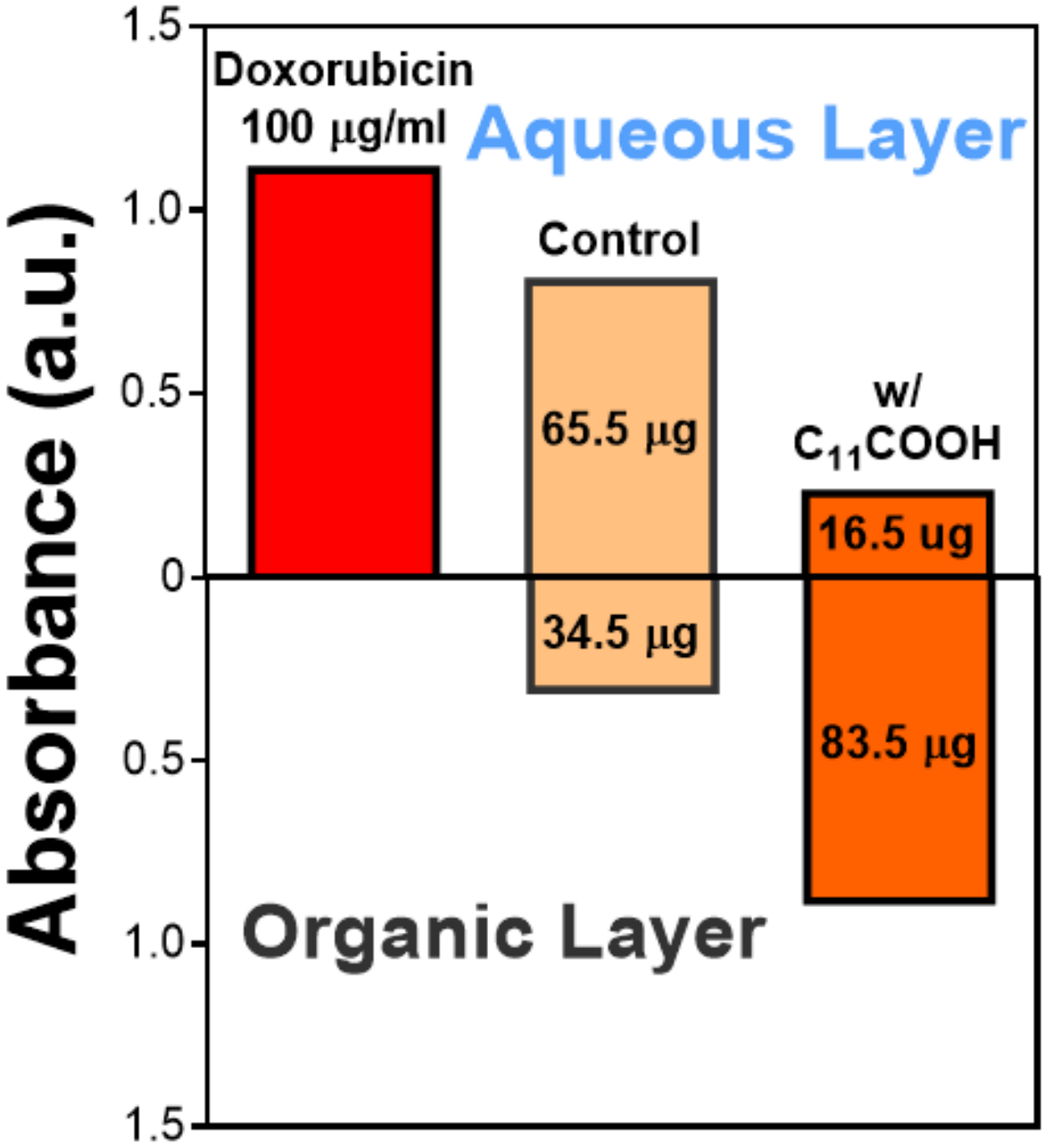

Figure 4.7: a) Doxorubicin concentration-absorbance calibration curve, accompanied by b) the absorbance peak measurements

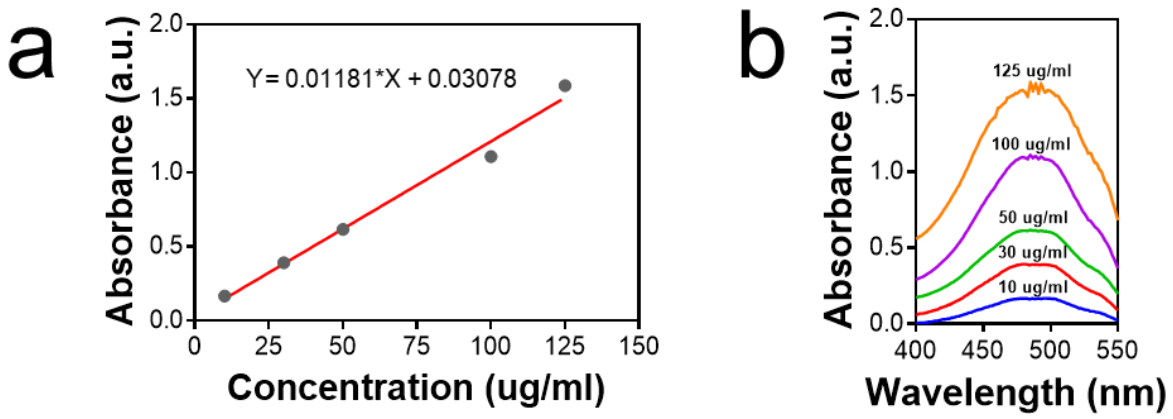

After the doxorubicin has been encapsulated into dodecanoic acid inverted micelles, 60 µL of the organic chloroform phase was added to a glass bulb along with phosphatidylcholine, 1,2-dioleoyl-*sn*-glycero-3-phosphatidylethanolamine, and cholesterol at an optimized w/w ratio of 10:9:1:0.5 of dodecanoic acid:PC:PE:cholesterol. The organic layer was evaporated to form a thin film. This film was flushed with nanopure water (18 MΩ, pH 7.4) and then subjected to probe sonication to produce nanoparticles with a final mass concentration of 0.6 mg/mL (Figure 4.8). Fresh samples were incubated for 1 h at 4 °C, then filtered (0.22 µm, PTFE) and dialyzed (10,000 MW) for a prolonged period.

After the synthesis, the samples were analyzed by DLS to compare their colloidal hydrodynamic size changes from the inverted micelle capsules. The NCAPs' hydrodynamic diameter was measured to be 29 ± 10 nm with a PDI of 0.5 ± 0.1 (Figure 4.9). This was followed by cryogenic transmission electron microscopy (cryo-TEM) to visualize nanoparticle formation and observe their morphology (Figure 4.9).

Figure 4.8: Schematic representation of the NCAP synthesis process from the inverted micelle capsule to the NMC particle.

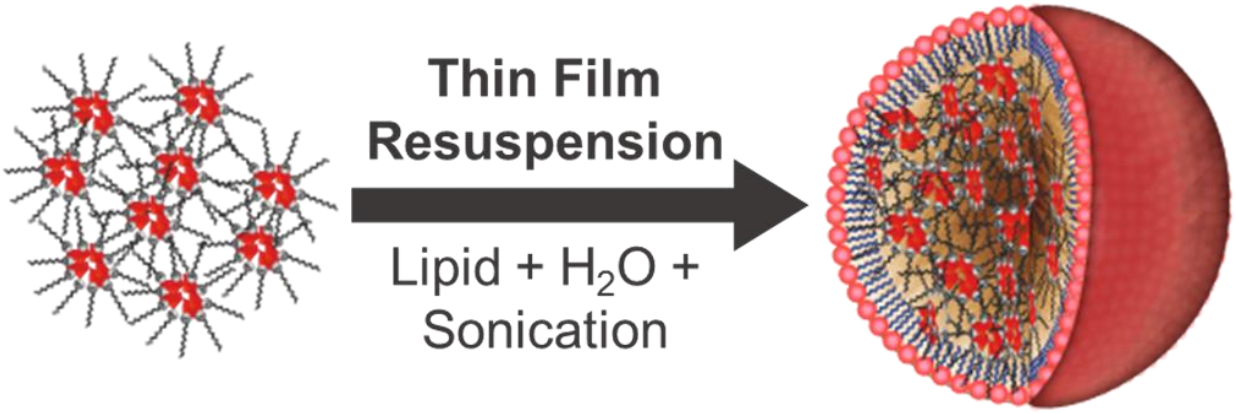

Figure 4.9: Histogram representing the number averaged (%) of NCAPs with an overlaid image of a TEM micrograph of the NCAPSs for nanoparticle visualization.

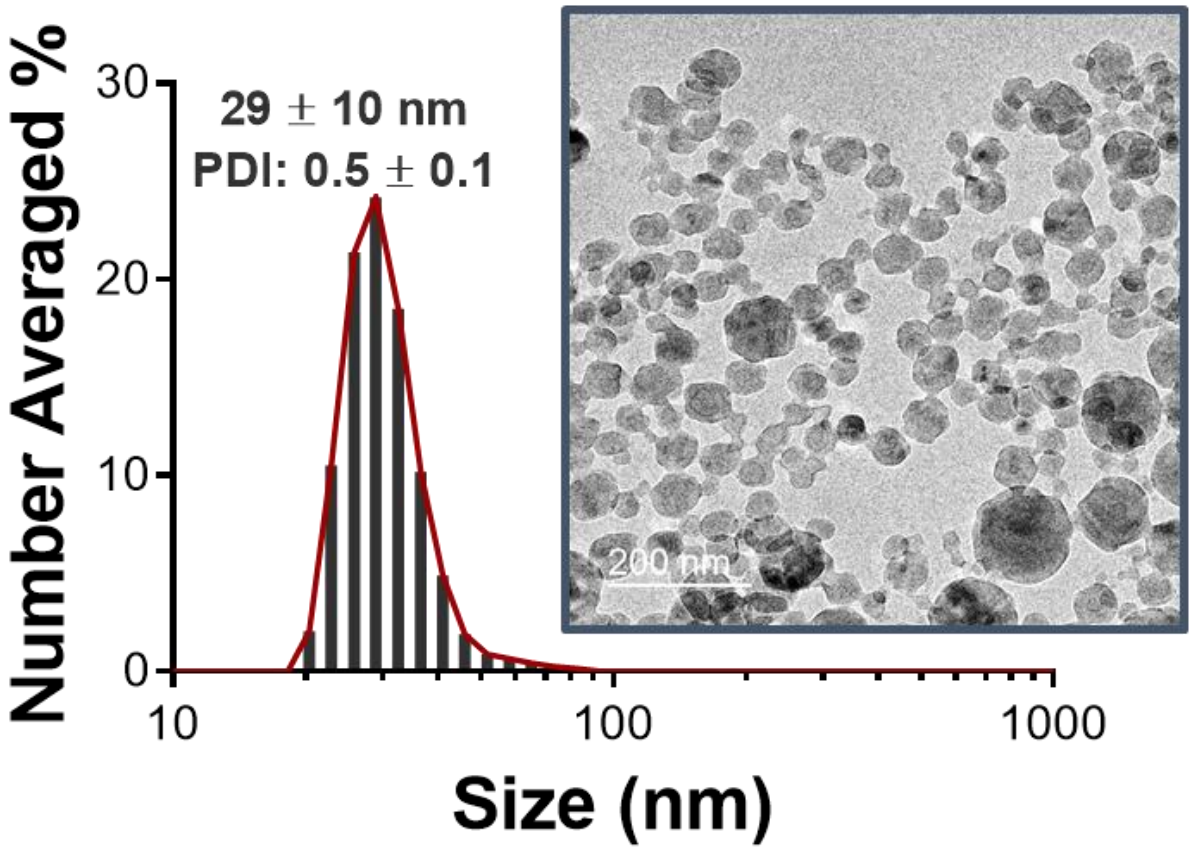

Since we hypothesized that these nanoparticles were robust for systemic use and would enhance intracellular delivery, we analyzed their surface charge and stability profile. Since nanoparticle surface charge is a well-known determinant of cellular internalization efficiency and systemic stability,[10,11] we investigated the NCAPs' Zeta potential. Zeta readings showed the NCAPs registered at -25 ± 5 mV, which falls in the ideal range between −20 mV and −40 mV and is suitable for cellular internalization and multi-environment stability. To measure their stability profile, we placed the NCAP in the following aqueous solutions at 37 °C and monitored its hydrodynamic diameter by DLS over the course of 1 week: nanopure H_2O, dPBS (pH 7.4), pH 4.5, pH 7.4, pH 12 (pH was controlled with HCl and NaOH). The NCAPs were found to be significantly stable over time in each environmental formulation except for the pH 4.5 solution (Figure 4.10). This sudden change in stability is indicative that severely acidic conditions, such as the localized environment of a tumor,[12–14] is ideal for NCAPs' disassociation and payload release.

To test the NCAPs' release profile, we measured Doxorubicin-loaded NCAPs, Doxorubicin-loaded liposomes (prepared according to literature standards; Lee et al.[15]), and free Doxorubicin for Doxorubicin content by UV-VIS over one day while dialyzed in a 10,000 MW cassette against nanopure water (18 MΩ). As expected, free Doxorubicin dissipated from the dialysis cassette within minutes, while the liposome variation took 1.5 hours to release 69.6% of its payload. Contrarily, the Doxorubicin-loaded NCAPs released 63.2% of its payload after 3.5 hours of dialysis (Figure 4.11).

Figure 4.10: One week assessment of the NCAP's Hydrodynamic diameter stability in various environments.

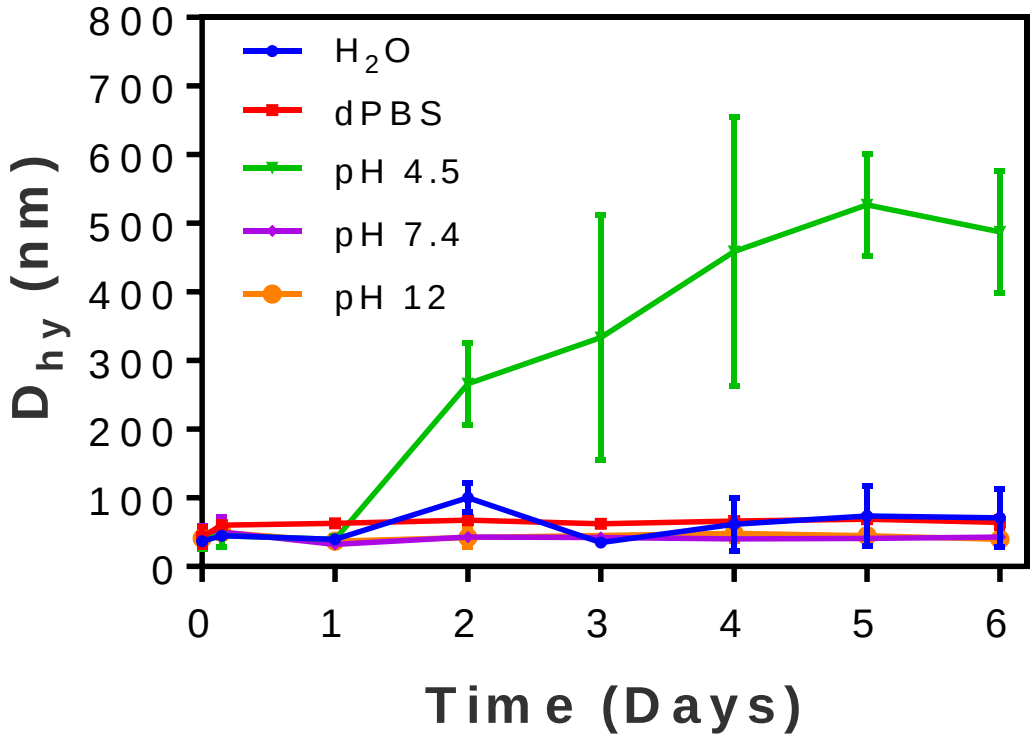

Figure 4.11: Dialysis release profile of doxorubicin from liposome and NCAP samples over 7 hours, compared to free doxorubicin.

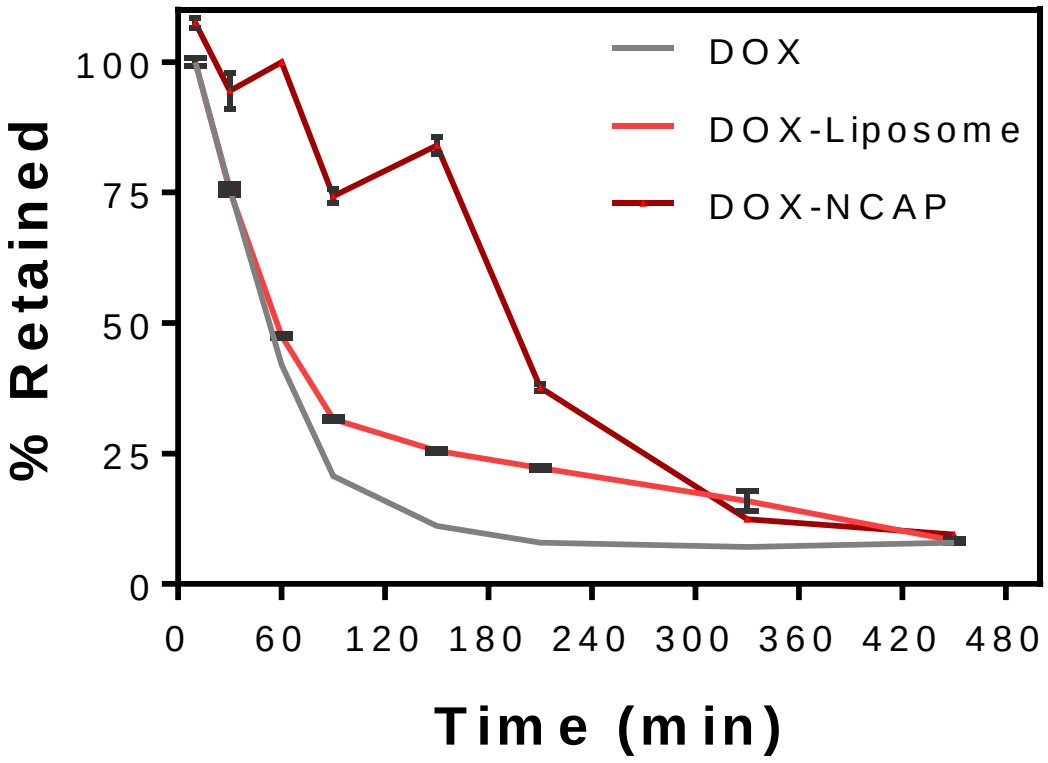

Cellular Delivery and Uptake Profile

To create a biological characterization profile of the NCAPs, we performed an initial toxicity test with Doxorubicin exposure to the triple-positive breast cancer cell line MCF-7. The samples chosen for treatment included a control sample of the NCAP alone, NCAP loaded with Doxorubicin, and a sample of Doxorubicin alone at the equivalent concentration of the NCAP loaded version. Using the standard MTT assay, we found that the NCAP performed better at delivering the payload contents intracellularly and thus proved to be more toxic than the free Doxorubicin treatment. The control NCAP sample did not show signs of toxicity because of it's makeup of biocompatible materials (Figure 4.12).

For a more thorough quantification of the NCAPs' nano-delivery efficiency as compared to liposomal delivery, we labeled both nanoparticle types with the fluorescent lipid 1,2-Dioleoyl-sn-Glycero-3-Phosphoethanolamine-N-(Carboxyfluorescein) (F-PE) and measured their treatment efficiencies on MCF-7 cells by flow cytometry. The fluorescence data showed two separate and unique histograms of each particle variant where the NCAP sample clearly exceeds the liposomal sample in arbitrary intensity units (Figure 4.13). To quantify this difference, we subtracted the histograms according to the Cumulative-Overton method; the results then indicated that 69.93% of NCAP-treated cells were deemed positive (had significantly higher F-PE expression) over liposome-treated cells (included in Figure 4.13).

Figure 4.12: Percent change in MCF-7 cell viability at different treatment concentrations.

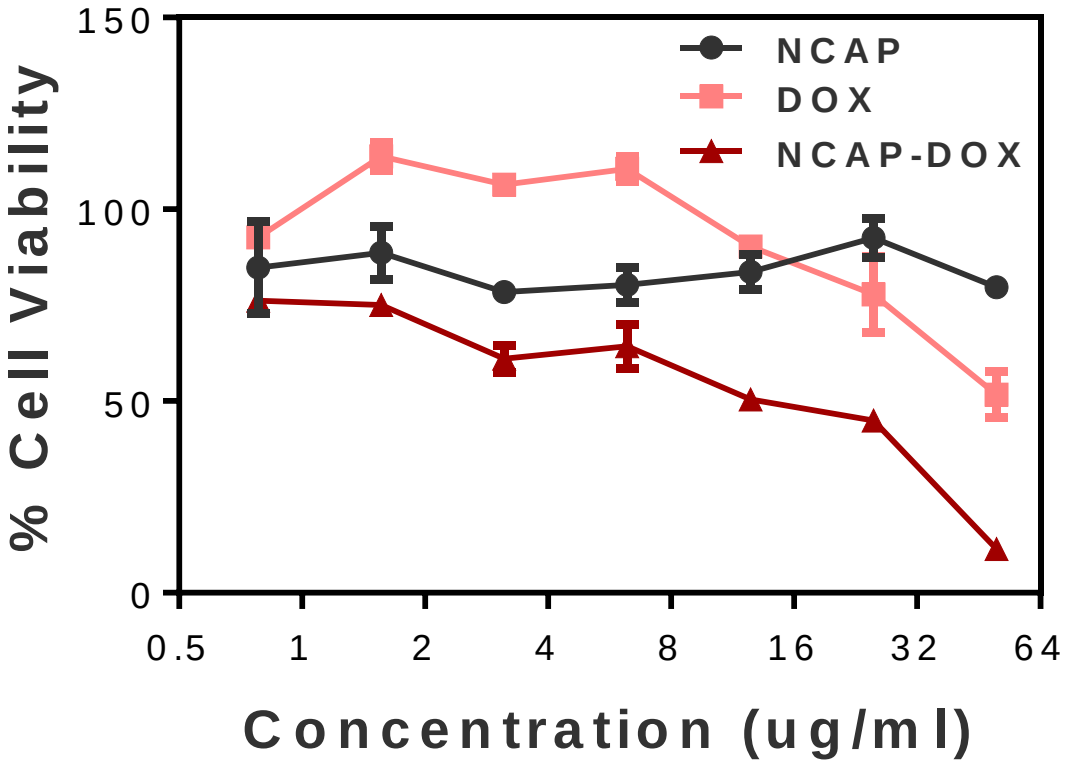

Figure 4.13: Flow cytometry histogram analysis of cells treated with an F-PE labeled Liposome, and an F-PE labeled NCAP. The liposome histogram was subtracted from the NCAP histogram by Cumulative Overton method, and NCAP-Treated cells which were identified to have more fluorescence expression than liposome-treated cells are labeled in dark red. A histogram of control cells is shown for reference.

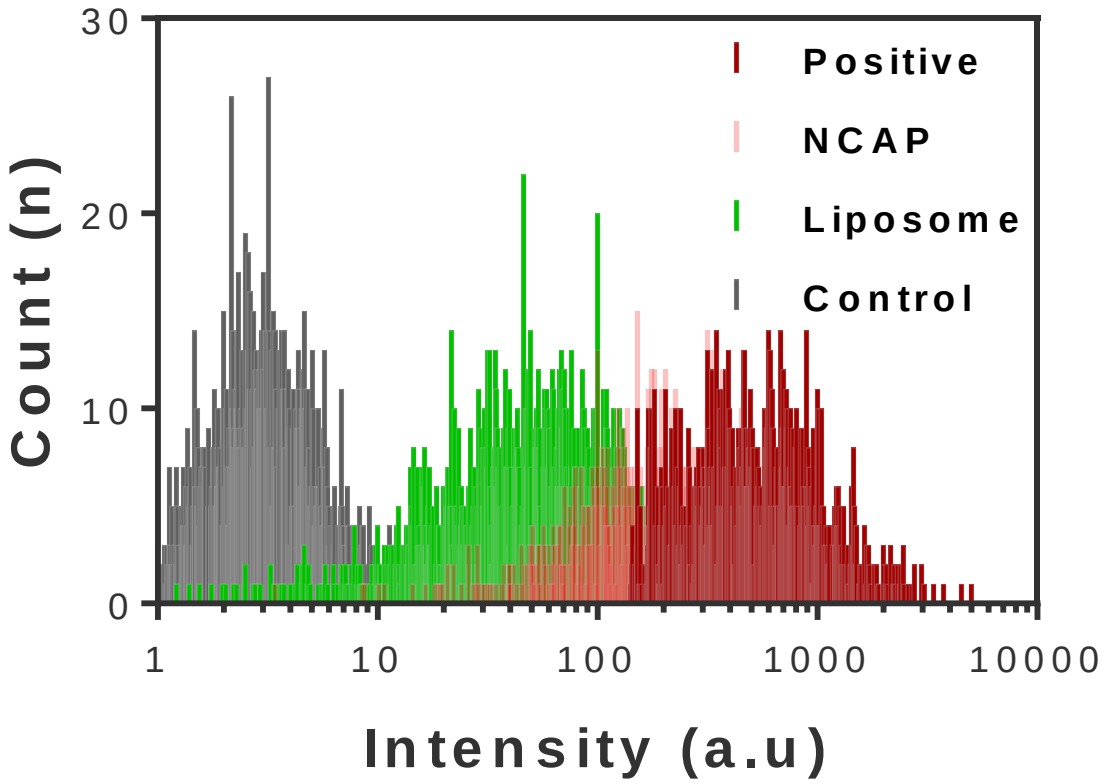

To visualize this interaction at the cellular level, we employed confocal microscopy on MCF-7 cells treated with both the liposome and NCAP variants; both samples were loaded with Rhodamine B and labeled with F-PE. Our confocal micrographs demonstrate that both nanoparticle variants delivered their Rhodamine B payload within the cells; however, the entire NCAP structure was were delivered intracellularly along with its payload, whereas the liposomes only bonded with the lipid-rich cell membrane (Figure 4.14a, b). Furthermore, liposome-treated cells showed a high frequency of localized nanoparticle clusters at the perimeter of the cell, whereas NCAPs were localized within the cell lumen (white arrows in Figure 4.14a, b). The difference in localization indicates that the NCAPs' delivery system is more efficient in cellular internalization than liposomal particles; this is an important consideration for theranostic applications involving prodrugs or lipid-labeled imaging agents that require the whole particle to be internalized to be effective. A final observation to consider is the presence of large numbers of fluorescent nanoparticles within the nucleus of the NCAP-treated cells, which suggests that the NCAP is either able to penetrate the nucleus, or that the nanoparticle breaks down within the cell, and its material compositions then disperses into the nucleus. Nonetheless, this NCAPs' phenomenon is superior to the liposomal method of delivery for DNA-disrupting therapeutic agents.

Figure 4.14: Confocal images of MCF-7 cells treated with an F-PE labeled a) liposome or b) NCAP. Both samples were loaded with rhodamine to visualize delivery capability. (40x objective).

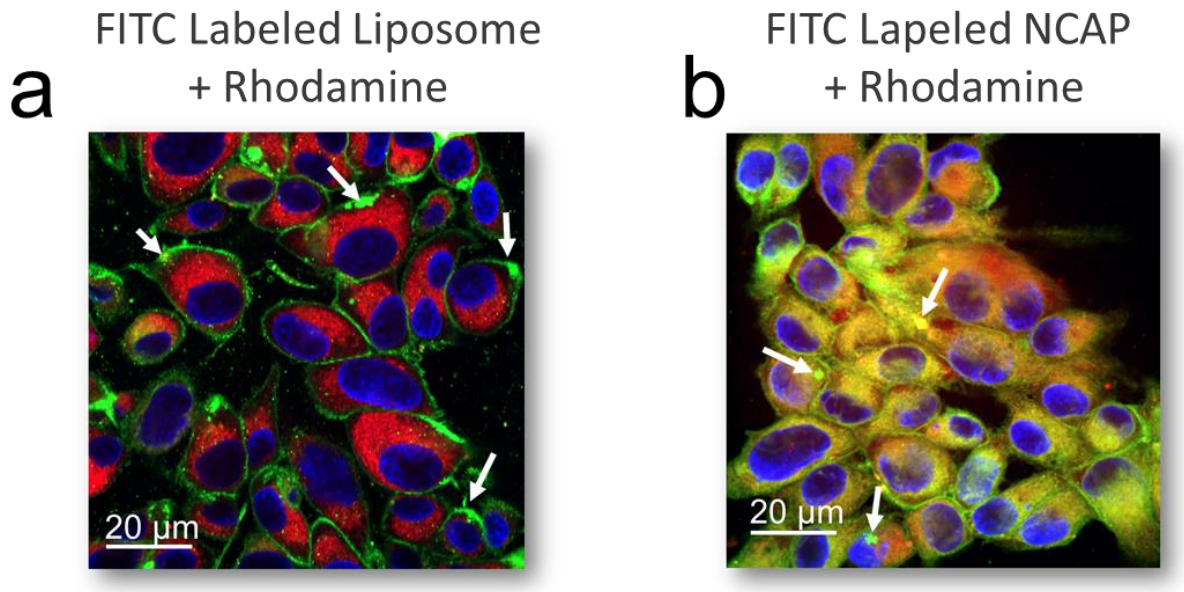

The distinct phenomenon of NCAPs' protrusion into cellular nuclei prompted us to undertake an in-depth examination of the NCAPs' interactions with cells. Thus, we employed live confocal imaging to visualize this interaction *in vitro*. Live cells were stained with DAPI 30 minutes prior to treatment with F-PE labeled liposome or NCAP samples. Cells were then treated and imaged every 5 seconds to monitor their interactions with the fluorescent liposomes. We found that cells treated with fluorescent liposomes began to show stained cell membranes within 1 minute, similarly to what was viewed in static confocal microscopy (Figure 4.15, Video 1: F-PE Labeled Liposome[2]). Conversely, the fluorescently-labeled NCAPs were found inside of the cells as fluorescent artifacts after only 5 minutes of imaging (Figure 4.16, Video 2: F-PE labeled NCAP[3]). This behavior supports our predictions that liposome-based delivery is efficient at reaching the cell, yet the unique nanoarchitecture of the NCAP allows for higher-throughput cellular internalization and agent retention.

[2] Live confocal Images of MCF-7 cells being treated with F-PE labeled liposomes. White arrows point to areas of cells where the liposomes collected at the cell membranes. Images were taken once every 5 seconds. (40X Objective)

[3] Live confocal Images of MCF-7 cells being treated with F-PE labeled NCAPs. White arrows point to areas of cells where the NCAPs internalized within the cell's cytoplasm. Images were taken once every 5 seconds. (40X Objective)

Figure 4.15: Still confocal images of MCF-7 cells while treated with an F-PE labeled liposome. Stills were taken from live recording at 0, 5, and 300 Seconds. White arrows point to collection of F-PE liposomes which were collected on cell surfaces. Arrows are maintained through the time series for consistency (40x objective).

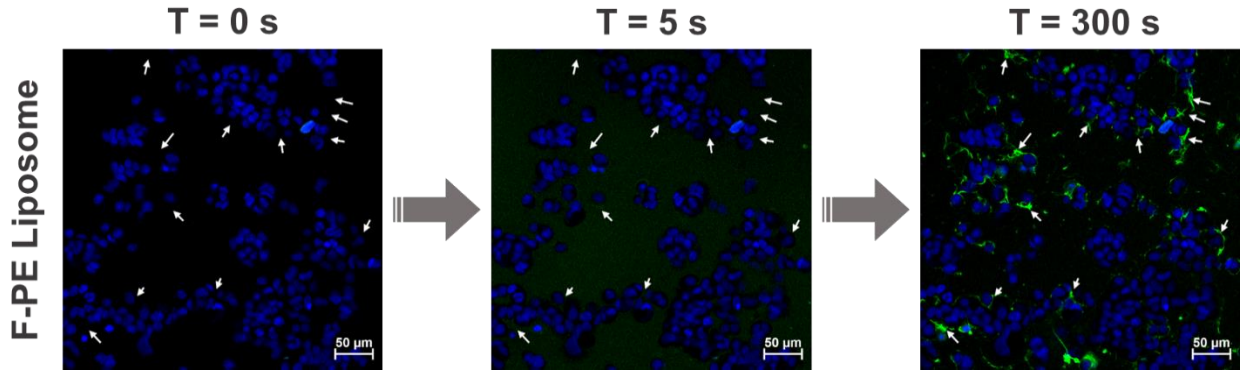

Figure 4.16: Still confocal images of MCF-7 cells while treated with an F-PE labeled NCAP. Stills were taken from live recording at 0, 5, and 300 Seconds. White arrows point to fluorescent NCAP artifacts being consumed by cells. Arrows are maintained through the time series for consistency (40x objective).

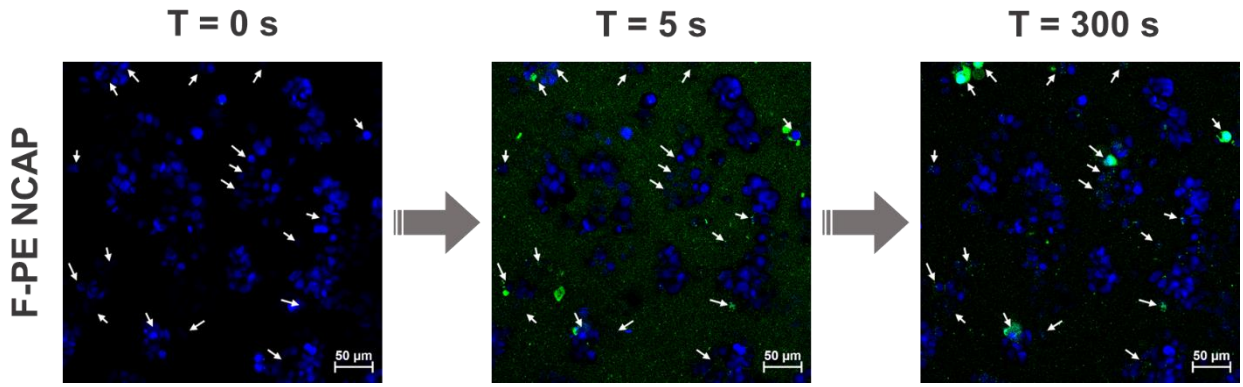

Conclusion

Here we have investigated the next generation of nanoparticle delivery by designing a nano-architecture, termed NCAP, for high-throughput internalization into cells. This type of nano-delivery vehicle is adaptable for a multitude of theranostic uses and has the potential to improve the efficacy of theranostic agents for inhibiting or detecting intracellular activity. Furthermore, the NCAPs' lipid-based shells make them ideal nano-delivery vehicles for combinatorial therapy that combines lipid-based molecules (such as imaging labels, targeting moieties, or prodrugs), and a hydrophilic agent entrapped within the NCAPs' inverted micelle capsules.

Within this detailed investigation into the possible functions of such a versatile capsule, we considered pushing its chemical boundaries by propagating the encapsulation of multiple dyes with differing molecular structures. We then transferred these capsules into aqueous and biocompatible nanoparticles facilitated by a simple lipid wrapping technique and tested their intracellular delivery capabilities on the metastatic breast cancer cell line, MCF-7.

We then compared the NCAPs' cellular interactions with the commonly used liposome nanoparticles through quantitative and visual data. Flow cytometry experiments indicated that the NCAPs were 69.93% more effective at labeling MCF-7 cells over liposomes, while confocal-based imaging and live video recordings detailed the NCAPs interactions at the cellular level. These fluorescent techniques demonstrated the NCAPs' ability to surpass cell membrane interactions and, in fact, deliver their contents into the cell's lumen, while liposome treatments were confined to membrane interactions alone.

Additional investigations are warranted in the future for the capability of the NCAPs to entrap material other than small molecules, such as biological matter or inorganic compounds.

Additionally, the NCAPs' *in vivo* adaptability and systemic clearance must be established to translate this novel delivery platform into clinical use.

Methods

Unless stated otherwise, all material and reagents were purchased from Sigma–Aldrich, St. Louis, MO, and were used without further purification. Solvents were used as received and without further purification.

Inverted Micelle Transfer

An equal volume ratio of 50 mM of dodecanoic acid dissolved in chloroform and an aqueous suspension of either Rhodamine B (100 µg/ml) or Doxorubicin (100 µg/ml) was added into a 1-dram (3.7 ml) vial and vigorously shaken for several seconds to homogenously mix the layers. The vials were then allowed to separate and settle for a prolonged period of time. At this point, the small molecule variation of choice had clearly transferred into the chloroform layer.

Nanocapsule Formation

The inverted micelle-dye/drug composite, while suspended in chloroform, was added to a glass bulb along with phosphatidylcholine (PC, Coatsome, NOF Corporation, Tokyo, Japan), 1,2-Dioleoyl-sn-glycero-3-phosphatidylethanolamine (PE, Cayman Chemical Company, MI, USA), and cholesterol at an optimized w/w ratio of 10:9:1:0.5 of dodecanoic acid:PC:PE:cholesterol. The chloroform in the glass bulb was evaporated by a rotary evaporator (RE200, Yamato Scientific Co., Ltd. Japan) in a 55 °C water bath to produce a thin film layer of the materials. The sample was then placed in a desiccator (Labconco, Kansas City, MO, USA) for 30 minutes. Water (pH 7.4, 18 MΩ Millipore H_20) was added to the bulb at a volume to produce a final concentration of

0.8 mg/ml. The sample was subject to probe sonication for 30 seconds (Amp: 1, On: 2 sec, Off: 2 sec). The samples were then immediately placed in an ice-bath and incubated for one hour at 4 °C. Following incubation, the samples were filtered through a 0.22 μm PTFE syringe filter and dialyzed against a 10,000 molecular weight cut off cassette (Thermo Scientific Product # 87730, Rockford IL, USA).

Dynamic Light Scattering Measurements

Hydrodynamic diameters were determined using a Malvern Zetasizer ZS90 particle size analyzer, while the scattered light was collected at a fixed angle of 90°. A photomultiplier aperture of 400 μm was used with the incident laser power adjusted to obtain a photon counting rate between 200 and 300 kcps. Diameter values depended on measurements whereupon the measured and calculated baselines of the intensity autocorrelation function had to agree within ±0.1%. All determinations were made in multiples of three consecutive measurements of 15 runs each. Organic samples were measured in a quartz cuvette.

Determination of Electrophoretic Zeta Potential

Zeta potential (ζ) values for each nanoparticle formulation were determined with a nano series Malvern Zetasizer Zeta potential analyzer (Fredrick Seitz Material Research Laboratory, University of Illinois at Urbana-Champaign, (MRL facility, UIUC)). Data were acquired in the phase analysis light scattering (PALS) mode following solution equilibration at 25 °C when calculation of ζ from the measured electrophoretic mobility (μ) employed the Smoluchowski equation, which is expressed as:

Equation 4.1 $$\mu = \varepsilon\zeta/\eta$$

where ε and η are the dielectric constant and the absolute viscosity of the medium, respectively.

Measurements of ζ were reproducible to within ± 2 mV of the mean value given by three determinations of 15 data accumulations.

Cryo-Transmission Electron Microscopy Imaging

Two µL of nanoparticle suspension was applied to carbon-coated TEM grids. Grids were then rapidly blotted, and immediately plunged into liquid methane kept at -200°C. The samples were stored in -200°C liquid methane until imaged on a JEOL 2100 Cryo-TEM machine via a Gatan UltraScan 2k × 2k CCD camera (MRL facility, UIUC).

Cell Viability Assay

The cytotoxic effect of nanoparticle formulations were investigated with a 3-(4,5-dimethylthiazole-2-yl)-2,5-diphenyltetrazolium bromide (MTT) assay. The MCF-7 (human estrogen receptor positive breast cancer) cell line was plated on a 96-well plate at a density of 12,000 cells per well (Greiner CellStar® 96 well plates, Sigma-Aldrich, MO, USA) and exposed to nanoparticle formulations after 24 hours at 37 °C. Followed by a 48 h exposure time, 20 μL (5 mg/mL) of MTT solution was added to each well and cells were further incubated for another 4 hours. After exposure, media was aspirated, and 200 μL of dimethyl sulfoxide (DMSO, ≥99%, MP Biomedicals, USA) was added to dissolve formazan crystals. The optical density of samples was determined by Synergy HT (BioTek, USA) with a reference wavelength of 570 nm. The following equation determined percentage cell viability:

Equation 4.2

$$\%Viability = \frac{A_{570}(treated) - A_{570}(background)}{A_{570}(control) - A_{570}(background)}$$

Flow Cytometry

Flow Cytometry samples were performed on cells (cell density: 500 cells/µL) treated with 10% v/v of each sample and measured on a Guava® EasyCyte Plus Flow Cytometer. For each sample data from 3000 single cell events were collected within 3 minutes at an excitation of 488 nm. Measurements were run in triplicates.

Confocal Microscopy

For static confocal microscopy, the MCF-7 cell line was plated on poly-L-lysine coated circular coverslips at a cell density of 400,000 cells per 25 mm coverslip. After 24 hours, cells were treated with respective components (Nanoparticles, F-PE, and/or Rhodamine) and then fixed using 8% paraformaldehyde. Cells were then stained with DAPI containing Vectashield mounting medium prior to imaging. Imaging was carried out using a Zeiss LSM 710 confocal scanner with the following lasers: 405 nm for DAPI, 488 for F-PE, and 561 nm for Rhodamine (all lasers were used at 2% laser power).

For live confocal, samples the MCF-7 cell line was plated on poly-L-lysine coated Ibidi µ-Slide 8 well plates at a cell density of 30,000 cells per well. After 24 hours, cells were placed in a Zeiss LSM 880 Airyscan confocal scanner with an attached incubation chamber. Cells were kept in the chamber at 37.1°C with a constant flow of CO_2 at 5.3% and humidity levels at 87%. Cells were replenished with fresh media as needed prior to imaging. Cells were pre-stained with DAPI (AAT Bioquest) 30 minutes prior to imaging, at a concentration of 5 µM. Cells were imaged at 1 frame per 5 seconds with a 405 nm laser at 4% laser power for DAPI and a 488 nm laser at 4% laser power for F-PE. Once imaging commenced, cells were treated with respective components (Nanocapsules and/or F-PE).

References to Chapter 4

(1) Ryu, J. H.; Lee, S.; Son, S.; Kim, S. H.; Leary, J. F.; Choi, K.; Kwon, I. C. Theranostic Nanoparticles for Future Personalized Medicine. *J. Control. Release* **2014**, *190*, 477–484.

(2) Sercombe, L.; Veerati, T.; Moheimani, F.; Wu, S. Y.; Sood, A. K.; Hua, S. Advances and Challenges of Liposome Assisted Drug Delivery. *Front. Pharmacol.* **2015**, *6*, 286.

(3) Barenholz, Y. (Chezy). Doxil® — The First FDA-Approved Nano-Drug: Lessons Learned. *J. Control. Release* **2012**, *160* (2), 117–134.

(4) Luo, D.; Carter, K. A.; Razi, A.; Geng, J.; Shao, S.; Lin, C.; Ortega, J.; Lovell, J. F. Porphyrin-Phospholipid Liposomes with Tunable Leakiness. *J. Control. Release Off. J. Control. Release Soc.* **2015**, *220* (Pt A), 484–494.

(5) Subramanian, S.; Khan, I.; Korale, O.; Alhnan, M. A.; Ahmed, W.; Najlah, M.; Taylor, K. M. G.; Elhissi, A. A Simple Approach to Predict the Stability of Phospholipid Vesicles to Nebulization without Performing Aerosolization Studies. *Int. J. Pharm.* **2016**, *502* (1–2), 18–27.

(6) Soo Choi, H.; Liu, W.; Misra, P.; Tanaka, E.; Zimmer, J. P.; Itty Ipe, B.; Bawendi, M. G.; Frangioni, J. V. Renal Clearance of Quantum Dots. *Nat. Biotechnol.* **2007**, *25* (10), 1165–1170.

(7) Sapra, P.; Allen, T. M. Ligand-Targeted Liposomal Anticancer Drugs. *Prog. Lipid Res.* **2003**, *42* (5), 439–462.

(8) Ulrich, A. S. Biophysical Aspects of Using Liposomes as Delivery Vehicles. *Biosci. Rep.* **2002**, *22* (2), 129–150.

(9) Forssen, E.; Willis, M. Ligand-Targeted Liposomes. *Adv. Drug Deliv. Rev.* **1998**, *29* (3), 249–271.

(10) Hunter, R. J. *Zeta Potential in Colloid Science: Principles and Applications*; Academic Press, 2013.

(11) Riddick, T. M. *Control of Colloid Stability through Zeta Potential*; Livingston Pub. Co: Wynnewood, Pa., 1968.

(12) Warburg, O. On the Origin of Cancer Cells. *Sci. (Washington, DC, U.S).* **1956**, *123* (3191), 309–314.

(13) Som, A.; Raliya, R.; Tian, L.; Akers, W.; Ippolito, J. E.; Singamaneni, S.; Biswas, P.; Achilefu, S. Monodispersed Calcium Carbonate Nanoparticles Modulate Local pH and Inhibit Tumor Growth in Vivo. *Nanoscale* **2016**, *8* (25), 12639–12647.

(14) Daza, E. A.; Misra, S. K.; Schwartz-Duval, A. S.; Ohoka, A.; Miller, C.; Pan, D. Nano-Cesium for Anti-Cancer Properties: An Investigation into Cesium Induced Metabolic Interference. *ACS Appl. Mater. Interfaces* **2016**, *8* (40), 26600–26612.

(15) Lee, R. J.; Low, P. S. Folate-Mediated Tumor Cell Targeting of Liposome-Entrapped Doxorubicin in Vitro. *Biochim. Biophys. Acta - Biomembr.* **1995**, *1233* (2), 134–144.

CHAPTER 5: A FACILE CHEMICAL STRATEGY TO HYDROPHOBICALLY MODIFY SOLID NANOPARTICLES USING INVERTED MICELLES FOR EFFICIENT INTRACELLULAR DELIVERY

Graphical Abstract

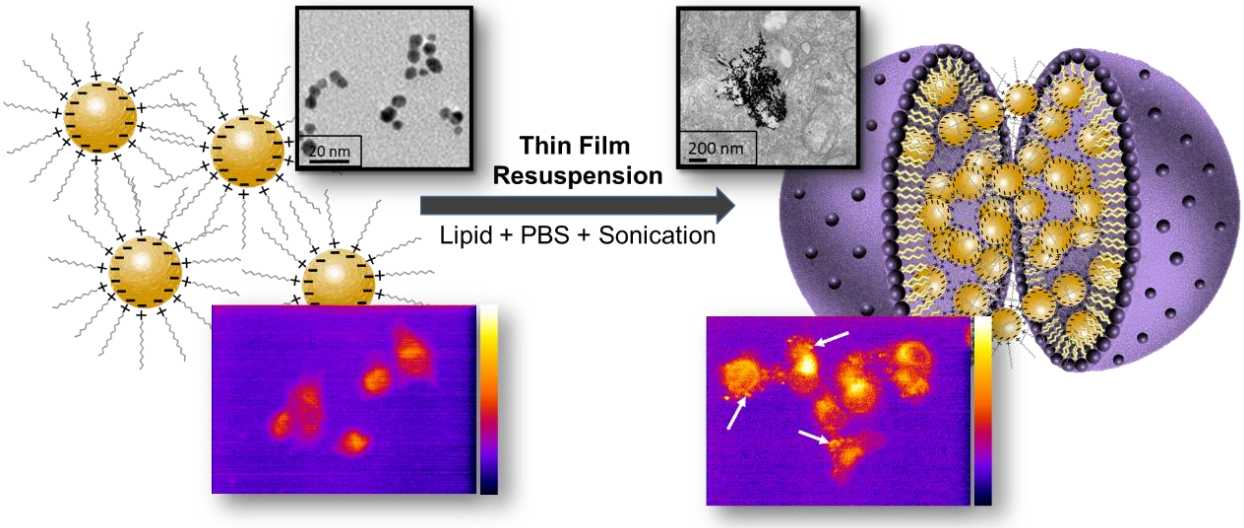

Abstract

Theranostic nanoparticles have incredible potential for biomedical applications by enabling visual confirmation of therapeutic efficacy. Numerous issues challenge their clinical translation and are primarily related to the complex chemistry and scalability of synthesizing Nanoparticles. We report a 2-step chemical strategy for high-throughput intracellular delivery of organic and inorganic solid nanoparticles. This process takes an additional step beyond hydrophobic surface modification, towards the packing of multiple solid nanoparticles into a soft-shelled lipid capsule, termed the Nano-MultiCapsule (NMC). This technique is high yielding and does not require the complex purification steps in anaerobic/hydrophobic reactions for hydrophobic modification. To demonstrate the efficacy across different material compositions, we separately entrapped ~10 nm gold and carbon nanoparticles (AuNP and CNP) within NMCs, then quantified their internalization in a human breast cancer cell line. For encapsulated AuNPs (NMC-AuNP), we confirmed greater cellular internalization of gold through ICP-OES and TEM analyses. Raman spectroscopic analysis of cells treated with encapsulated CNPs (NMC-CNP) also exhibited high degrees of uptake with apparent intracellular localization as opposed to free CNP treatment.

Keywords: Intracellular Delivery, Carbon nanoparticle, Gold Nanoparticle, Inverted Micelle.

Introduction

Nanoparticles have shown significant potential to redefine conventional medicine. Biomedical applications of nanoparticles are mainly centered around early detection and treatment of a disease. Some cases demonstrate that 'theranostic' nanoparticles allow physicians to track the effectiveness of their treatment in patients.[1,2] Although there have been comprehensive preclinical studies of these agents, the eventual success of clinical translation has not been fully realized. Numerous issues related to their development, such as scale-up feasibilities, regulatory aspects, and commercialization challenges their clinical translation. The chemistries involved in theranostic nanoparticle engineering allow for precise tuning of shape, size, and surface chemistry to better enable circumstantial requirements to serve a specific, or a multitude, of purposes.[3–6] Although the size of nanoparticles is directly correlated to retention time,[7,8] particles for systemic use have an ideal nanoparticle diameter of 10 nm or less because the glomular filtration apparatus in the kidney possesses an effective size cut-off at 10 nm.[9] As a result of this cut off size, nanoparticles with sizes under this threshold tend to rapidly clear the body's blood stream, thus decreasing chances of accidental particle accumulation, and nanoparticle exposure to vital organs.[10–15] From these physiological paradigms, which pose issues for both small (<10 nm) and large (10-300 nm) particles, there has been only marginal success in solid nanoparticle applications. There is great value for synthetic methodologies which may alleviate certain constraints in attaining FDA approval for nanoparticle based treatments. Towards this aim, we disclose a simple chemical strategy for high throughput intracellular delivery of <10 nm solid nanoparticles. This unique process involves a simple hydrocarbon 'wrapping' technique driven by inverted micelle formation to encapsulate <10 nm solid nanoparticles. The technique is high yielding and does not require an anaerobic hydrophobic reaction that normally involves complex purification steps. Parallel to

improving the *in vitro* delivery of 10 nm nanoparticles, this methodology is unrestricted to inorganic or organic material varieties, thus making it a versatile method for high throughput nanoparticle delivery.

One challenging aspect of rendering nanoparticles has been the requirement to stabilize its surface with biocompatible and nonreactive coating agents. The nanoparticle encapsulation vehicle should allow the colloidal system to stay suspended in aqueous media for a desired period and avoid unfavorable interactions with hydrophilic counterparts in systemic circulation. Furthermore, and equally as important, the nanoparticle capsule should facilitate any type of surface functionalization intended to diagnose or treat the intended delivery target. Without such a robust and multifunctional coating, proteins may absorb non-specifically to the surface leading to poor efficacy in nano-delivery. Currently, phospholipids and polymers are used to coat hydrophobically modified inorganic oxides or metal nanoparticles. Unfortunately, hydrophobic surface modifications can be particularly challenging for solid nanoparticles since some synthesis methods may require the use of organic media in an anaerobic environment. A simple yet universal coating strategy for nanoparticles is thus desirable to convert pristine cores without requiring complex chemistries. An avenue to address these issues consists of a 'particle-in-particle' approach by encapsulating nanoparticles within inverted micelles independent of their material composition. Based on these factors, we chose to investigate two commonly used solid nanoparticle compositions, i.e. gold and carbon for this study. Gold nanoparticles (AuNP) have been extensively characterized for theranostic approaches because of their attractive bio-compatibility and facile modification of surface functionalities.[16–18] Application's for AuNPs range from nucleic acid functionalization,[19,20] drug delivery,[21] contrast agents across an array of modalities,[22–24] and even photothermal therapy.[25,26] Carbon nanoparticles (CNP) are rising for their incredible

properties with fluorescent,[27–30] infrared,[27] and Raman imaging.[27–30] CNPs have been tuned with various passivations to control size, surface chemistry, and biocompatibility.[27] Concurrently, CNPs have been used for delivery of various small molecules,[31,32] nucleic acids,[33] and enzymes.[34]

Our strategy utilizes inverted micelles composed of fatty amines as a container to hydrophobically and non-covalently modify/encapsulate solid nanoparticles as a prerequisite to induce hydrophobic-amphiphilic self-assembly within lipid capsules, termed the Nano-MultiCapsule (NMC). With our research methodologies, we found that *in vitro* treatments of AuNP encapsulated by NMCs were quantifiably superior at cellular uptake compared to AuNP interactions alone. Furthermore, the NMC delivery vehicle showed similarly high-efficacy for intracellular CNP delivery, as measured by *in vitro* spectroscopic Raman analysis. Both cases show that the NMC nano-architecture proved to surpass the passively treated intracellular delivery of ~10 nm particle.

Results and Discussion

Nanoparticle characterization and inverted micelle induced passivation

AuNPs were synthesized via sodium borohydride reduction and capped with trisodium citrate. Ratios of gold chloride ($HauCl_4$), trisodium citrate ($Na_3C_6H_5O_7$), and sodium borohydride ($NaBH_4$) were optimized to ensure ~10 nm nanoparticle formation and consistency per batch while maintaining strong surface plasmon characteristics. To determine the AuNP size distribution and to confirm that particles meet limitations for renal clearance, we measured the hydrodynamic diameter of the AuNP suspension by dynamic light scattering (DLS). The optimized AuNPs had a measured hydrodynamic diameter of 8 ± 2 nm with a polydispersity index (PDI) of 0.5 ± 0.1 when measured for 'Population-by-Number' (Figure 5.1). A 'Population-by-Intensity' DLS

measurement revealed a sub-population of particles with a hydrodynamic diameter of 214 ± 56 nm and a PDI of 0.2 ± 0.1 prior to filtration (Figure 5.2). Transmission electron micrographs (TEM) of AuNP samples supported our assumption that the smaller sized AuNP population was the most abundant in the suspension (Figure 5.1 inset). Additionally, anhydrous diameters were measured by ImageJ to be 5 ± 0 nm (n = 264), due to dehydration and loss of ionic corona. Nonetheless, large particles were allowed to settle and were filtered out (0.22 μm) before *in vitro* treatments. UV-Vis analysis resulted in a characteristic plasmonic absorbance peak at 528 nm (red in color) (Figure 5.3, Figure 5.4). The addition and agitation of the AuNP aqueous suspension with a 16.2 mM solution of dodecylamine in chloroform resulted in the spontaneous transfer of the water-soluble AuNPs into the organically soluble inverted micelles. The sample was labeled as 'IM-AuNP' for inverted micelle encapsulated gold nanoparticles. This spontaneous phase transfer did not occur in a control sample where the organic solution lacked the fatty amine (Figure 5.4). The favorable electrostatic interactions between the carboxylate groups on the surface of the citrate-capped AuNPs and the amine group of dodecylamine provides a plausible mechanism for this spontaneous phase transfer; thus, resulting in a non-covalent hydrophobic hydrocarbon coating on the gold nanoparticle's surface (Figure 5.4). To confirm these surface interactions, the vibrational energies of the surface chemistry were analyzed by fourier transform infrared (FTIR) analysis. The IM-AuNP organic suspension revealed peak shifts of the Amide I (1648 → 1671 cm^{-1}) and Amide II (1556 → 1565 cm^{-1}) peaks (Figure 5.5), confirming that the amine-carboxylate interaction is the primary driving mechanism for inverted micelle encapsulation. A DLS analysis of the remaining aqueous supernatant (after transferring AuNP's into the inverted micelle) revealed that the larger AuNPs were still present and the small AuNP population had disappeared (Figure 5.2). This result implies that the inverted micelle encapsulation process acts as a size

selective barrier to ~10 nm particles. Additionally, we observed that the AuNP's color and plasmon characteristic remained after transferring into the organic layer (Figure 5.4), indicating that the dodecylamine shell protects AuNP from the harsh organic environment. A follow-up UV-Vis spectral measurement of the IM-AuNP in chloroform solution revealed the surface plasmon peak shifted from 528 nm to 518 nm, supporting our conclusion that the larger AuNP population is not present in the organic solution (Figure 5.3).[35]

To synthesize CNP, we modified a method based on Misra et al. and Daza et al. which uses agave nectar as the primary carbon source and polyethylene glycol (PEG) as the capping agent.[36,37] We chose the optimized mass ratio of 1:10 (agave: PEG) to form small biocompatible and highly spectroscopic CNPs. The CNPs were then characterized by DLS (hydrodynamic diameter: 9 ± 2 nm, with PDI of 0.3 ± 0.0) and TEM (Figure 5.6) (anhydrous diameter: 7 ± 1, n = 145) to ensure they met our <10 nm particle diameter qualifications.

While the AuNP's SPR characteristics work well for IR imaging based applications,[16,38] CNPs have a spread of unique optical and fluorescence based properties.[36] We characterized the spectroscopically active CNPs by their fluorescence profile which revealed two separate excitation wavelengths at 210 nm and 350 nm, while maintaining a common emission wavelength at 450 nm (Figure 5.7). The robustness of CNP's fluorescent property can be analyzed by assessing the carbon-carbon bond arrangement through Raman spectroscopy since it is well known that adequate graphene stacking can promote spectroscopic activity from π -π interactions due to resonant electron relaxation.[39] A Raman spectral analysis revealed that CNPs are dominantly graphitic due to the graphitic and diamond band intensity ratio (I_G/I_D ratio) of 1.13 (Figure 5.8), indicating that sp^2 bond hybridization is more prevalent within the system. Therefore, CNPs can be considered spectroscopically robust, and thus, qualify for further probing into theranostic applications.

Figure 5.1: Histogram representing the number averaged (%) of AuNPs with an inset of a TEM micrograph for nanoparticle visualization.

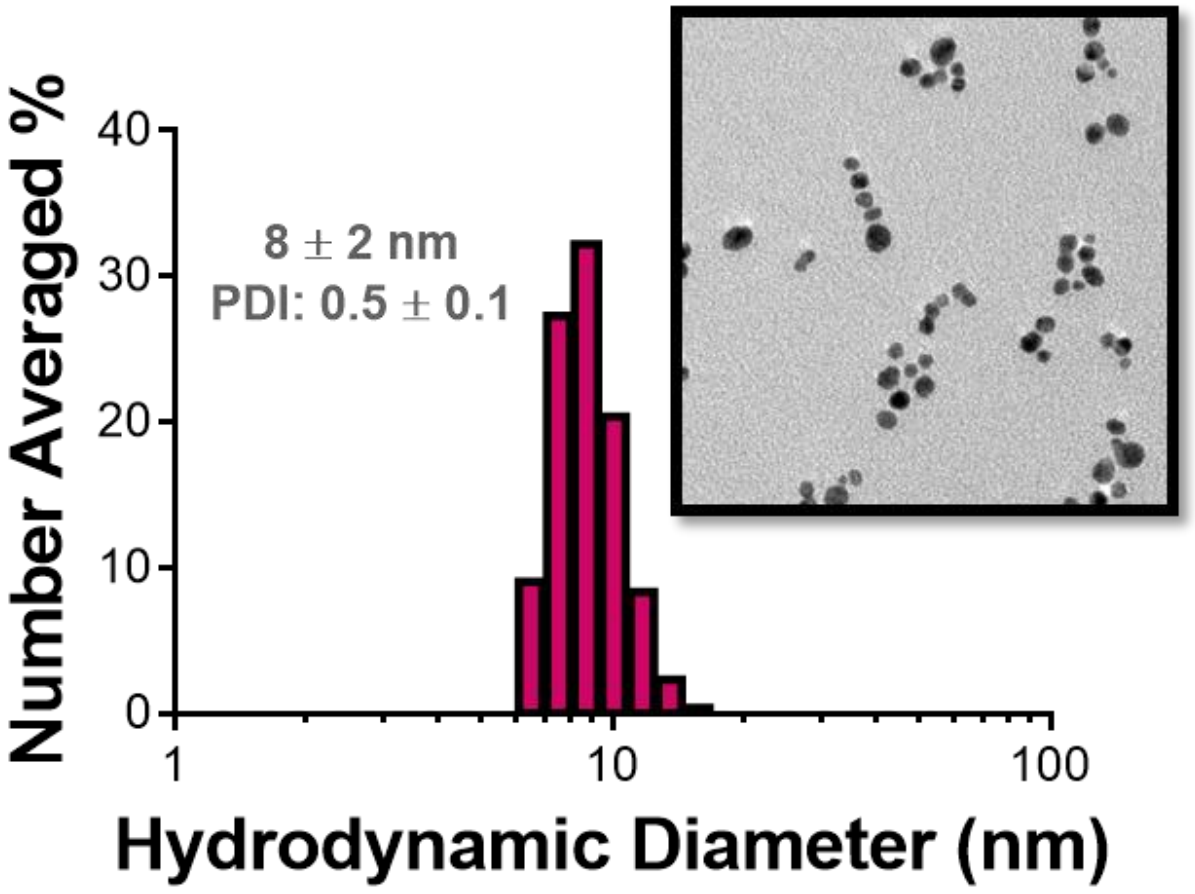

Figure 5.2: An overlaid histogram comparing the intensity averaged (%) of the AuNP stock suspension (magenta) and the 'post-transfer' supernatant (dark purple).

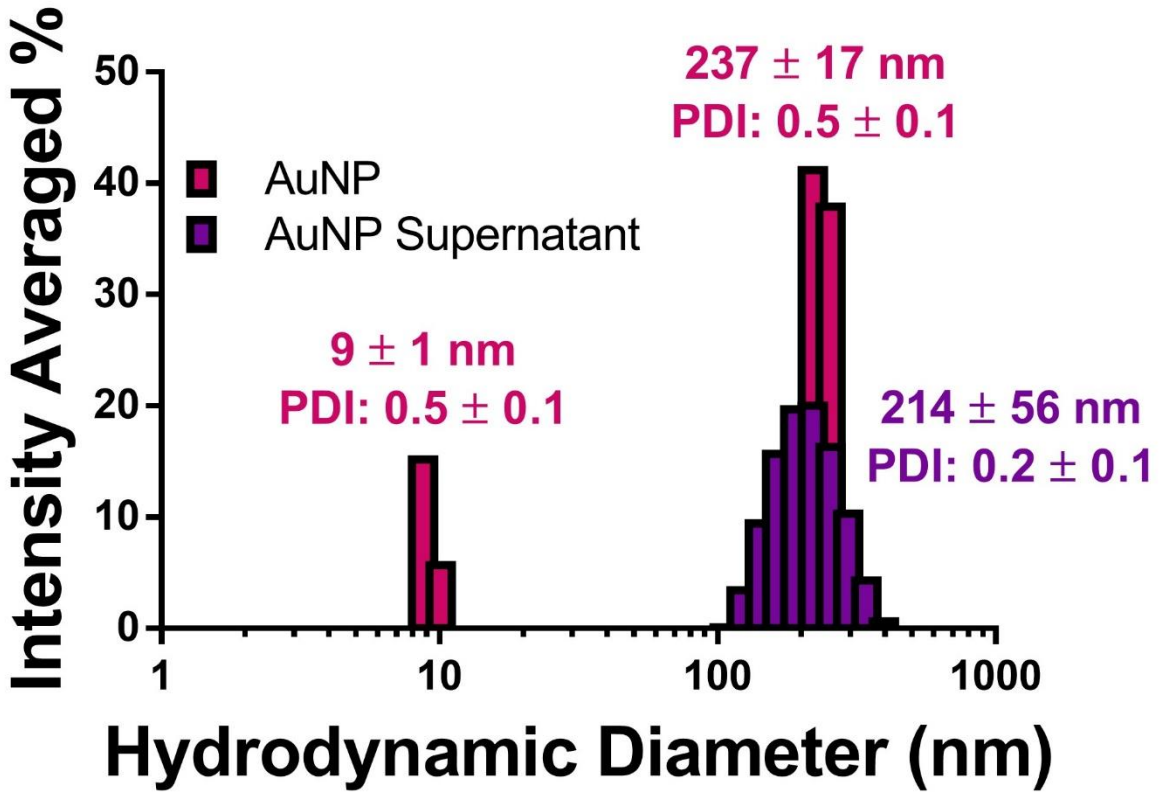

Figure 5.3: UV-Vis absorbance measurements of the AuNP stock suspension (magenta) and post transfer organic layer (dark purple).

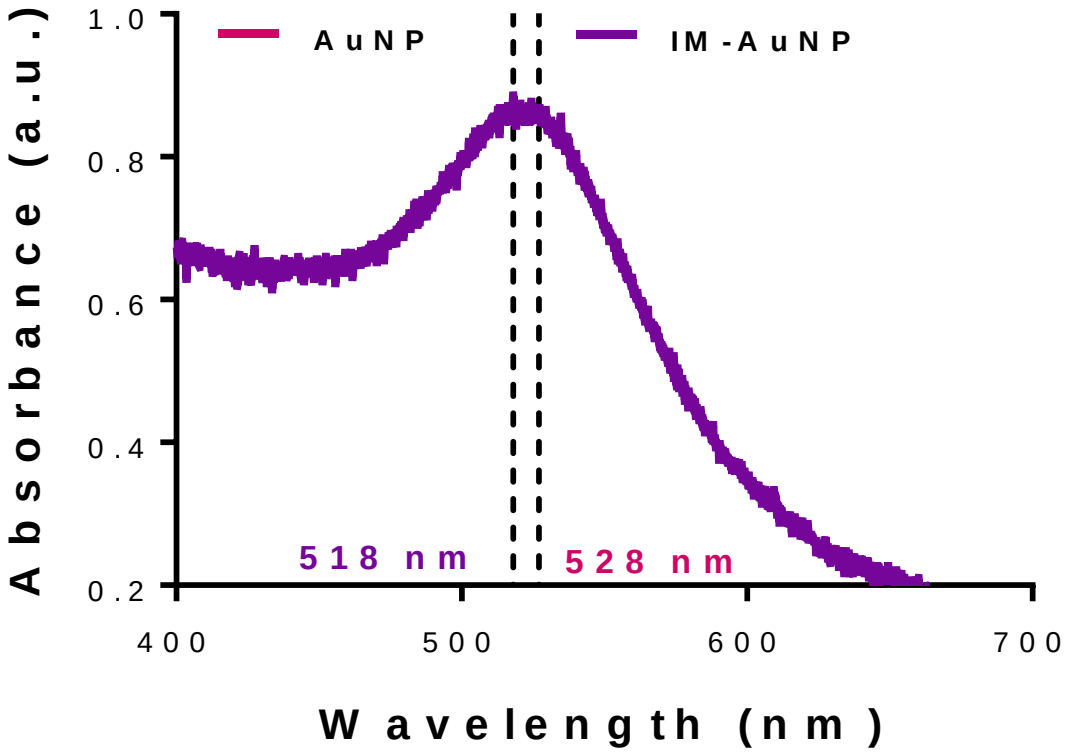

Figure 5.4: Schematic representation of solid nanoparticles transferring from aqueous to organic layers into inverted micelle capsules. Image of actual samples are shown adjacent to schematic.

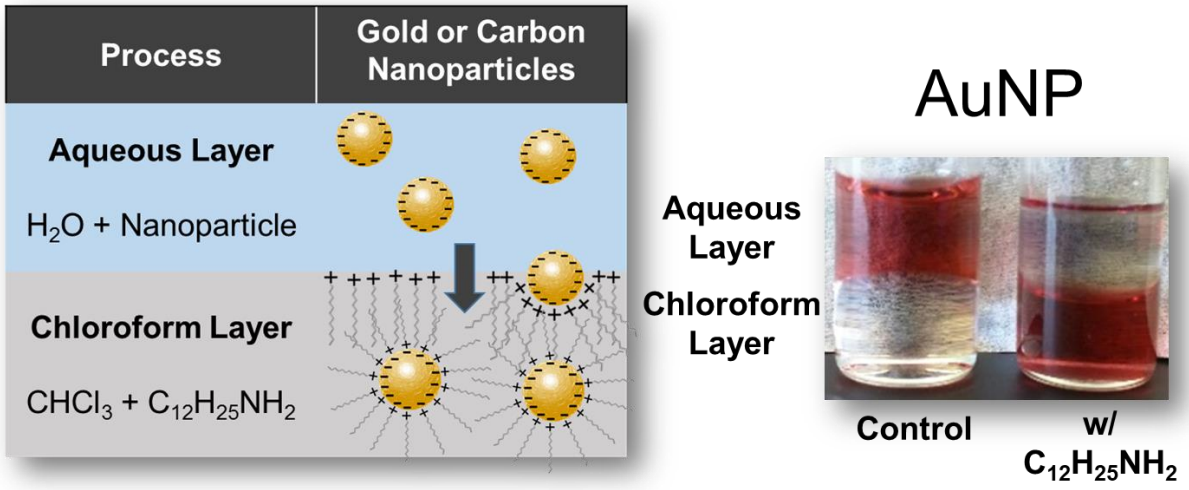

Figure 5.5: FTIR Spectral analysis of AuNP, dodecylamine ($C_{12}H_{25}NH_2$), and IM-AuNP with respective peak wavenumbers.

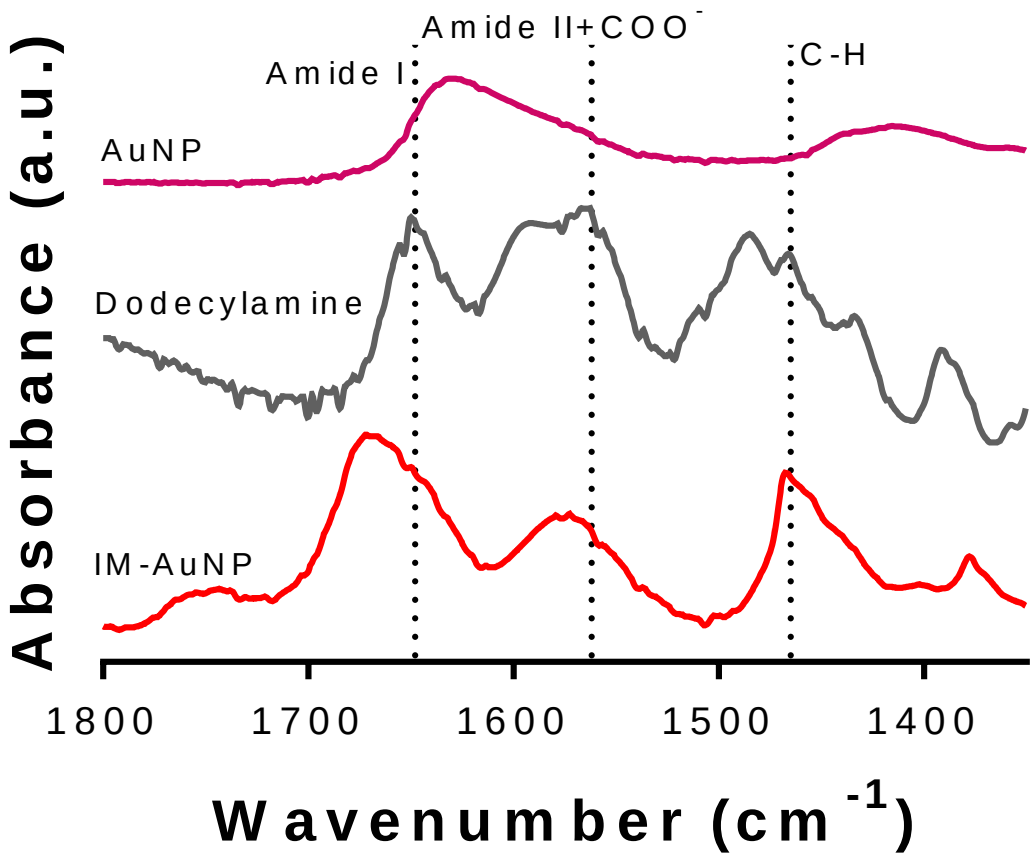

Figure 5.6: Histogram representing the number averaged (%) of CNPs with an overlaid image of a TEM micrograph of the CNPs for nanoparticle visualization.

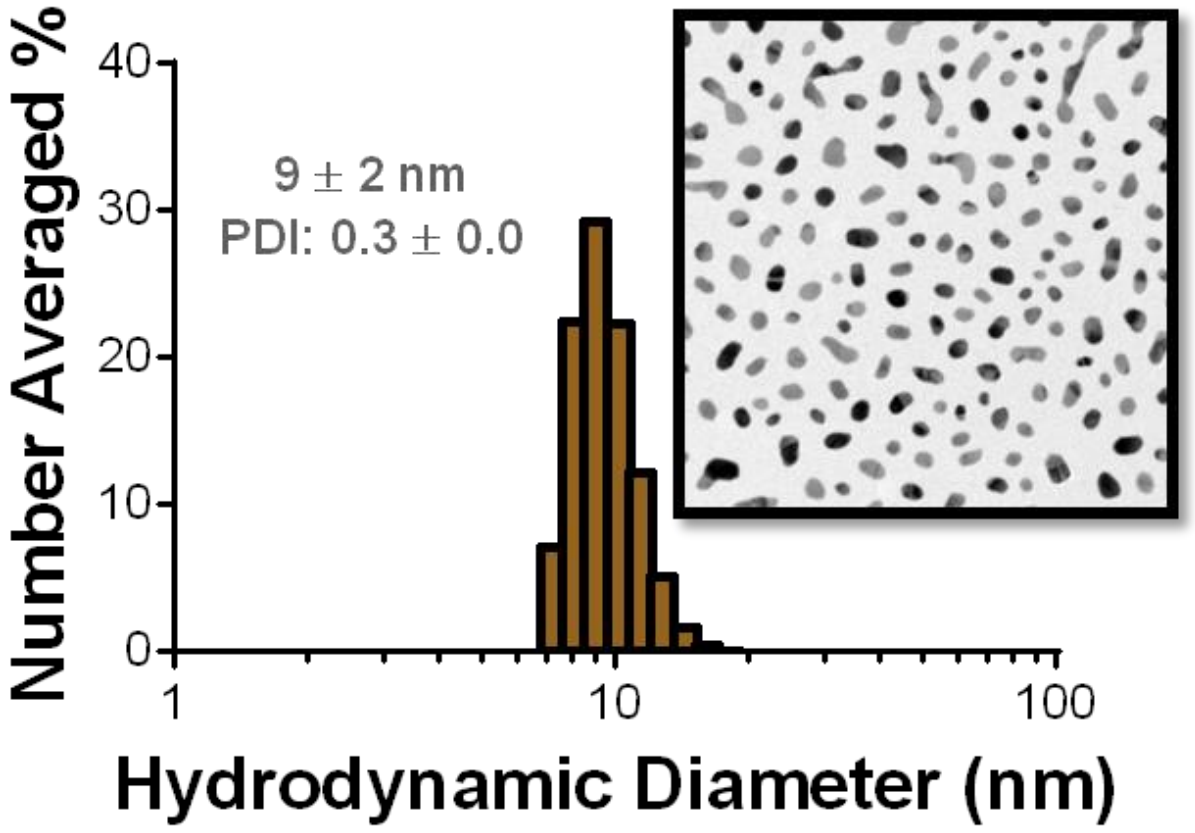

Figure 5.7: A characteristic EEM fluorescence spectral map of the CNP.

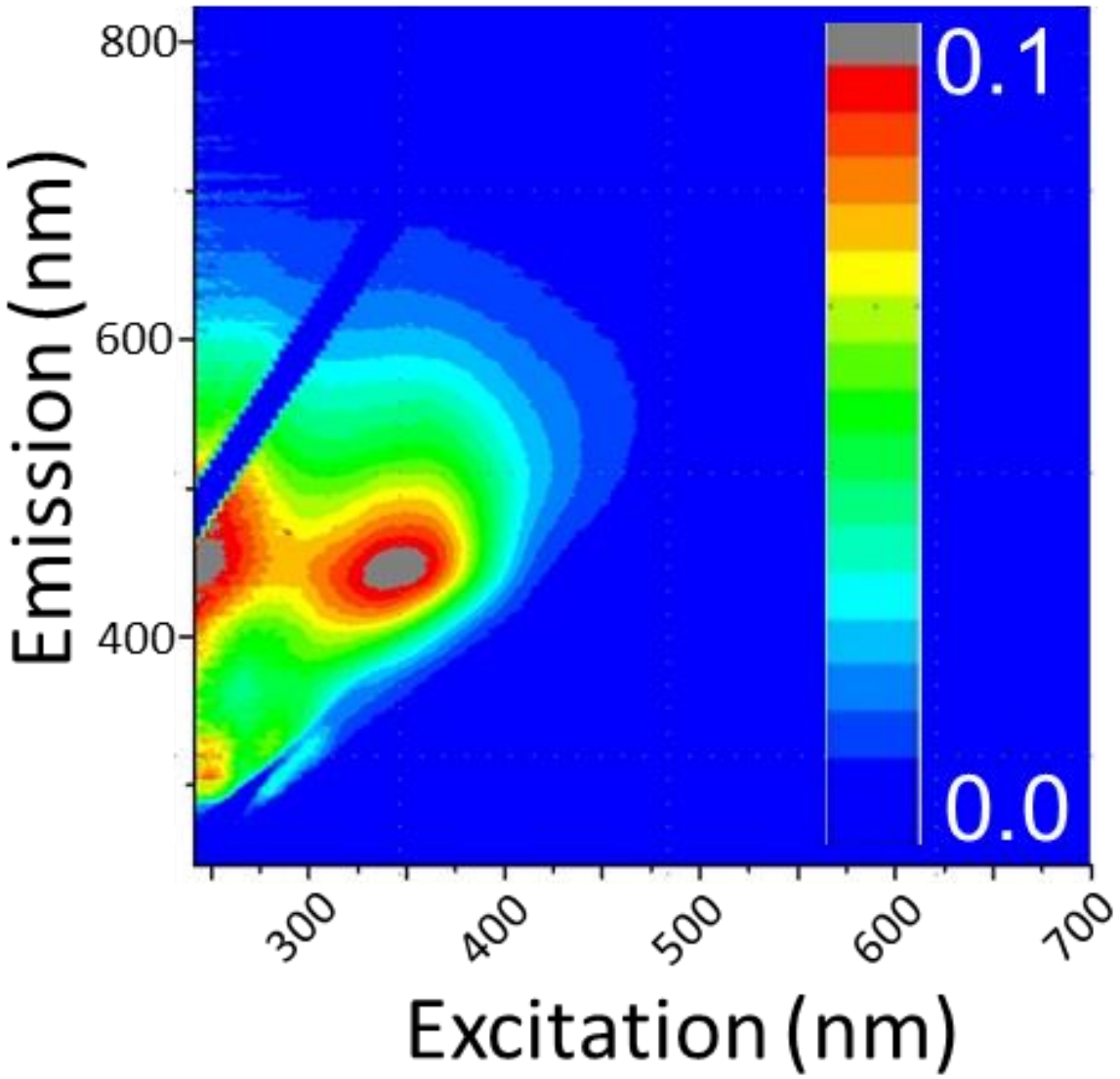

Figure 5.8: Raman spectral analysis of the CNP's graphitic and diamond-like characteristics with respective peak wavenumbers.

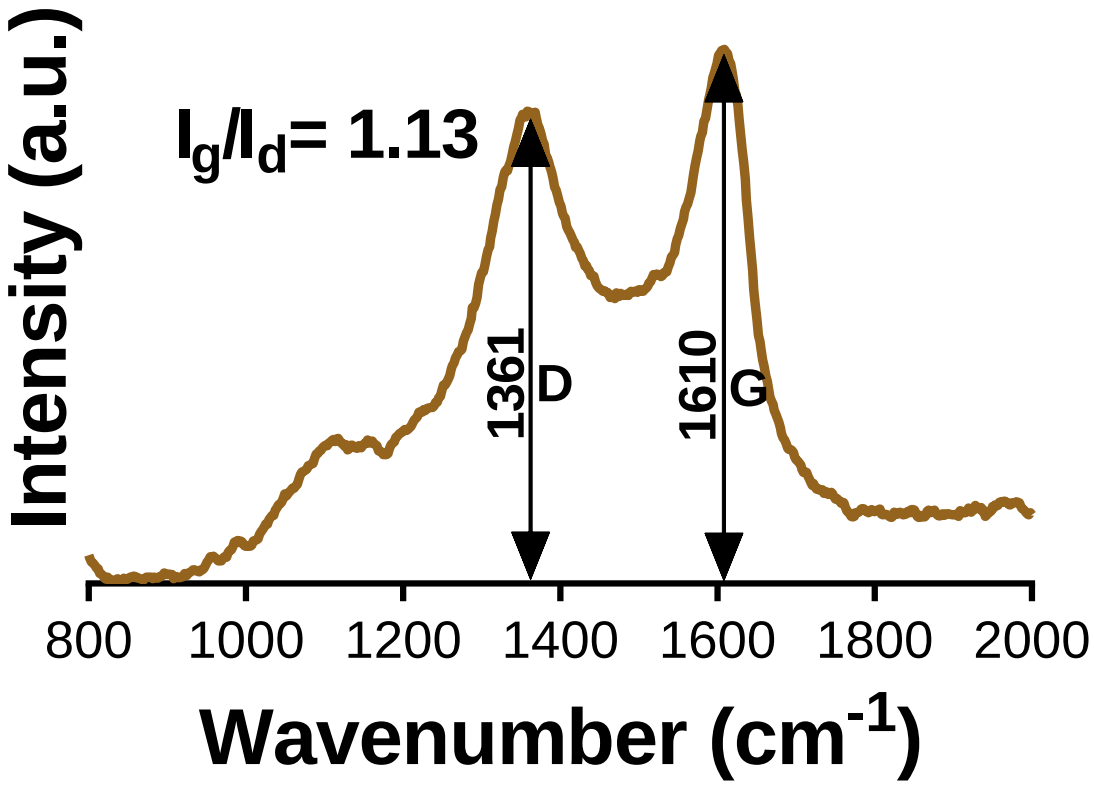

To ensure nanoparticle compatibility with fatty amine driven encapsulation, we measured the chemical composition of the CNP's surface by FTIR spectral analysis. CNP spectrographs show reoccurring hydroxyl peaks and significant artifacts indicating C-OH stretching at 3350 cm^{-1} which is indicative of H-bonding occurring within the system (Figure 5.9). This h-bonding activity is imperative to initiate inverted micelle transfer between the carboxylic acid groups on the CNP's surface and the amine groups on dodecyl amine. Similar to the AuNPs, the CNP suspension successfully transferred to the 16.2 mM dodecylamine-chloroform solution as expected (Figure 5.10), while the control sample (lacking dodecylamine) did not initiate a CNP transfer to the organic layer.

Design and synthesis of the Nano-MultiCapsule

The outer shell of the NMC system is strategically composed of soybean-derived lecithin because of its history of physiological biocompatibility and FDA approval. To produce each NMC variation, soybean lecithin was added to the organic suspension of inverted micelle encapsulated nanoparticles (IM-AuNP or IM-CNP) then processed through a rotary evaporator to remove the organic solvent. The exact proportion and composition of materials in the organic suspension was optimized to generate NMCs in the 10-100 nm range to undergo the enhanced permeability and retention effect.[40] The thin film was subsequently resuspended in pH 7.4 Dulbecco's phosphate buffered saline (dPBS) and probe sonicated to produce colloidal NMCs (Figure 5.11). These samples were then analyzed by DLS to compare their colloidal hydrodynamic size changes to the encapsulated solid nanoparticles

Figure 5.9: a) FTIR spectral analysis of CNP's chemical composition and (b) a near infrared spectrum of black box outlined in (a) Peaks are assigned to common molecular structures found in CNP.

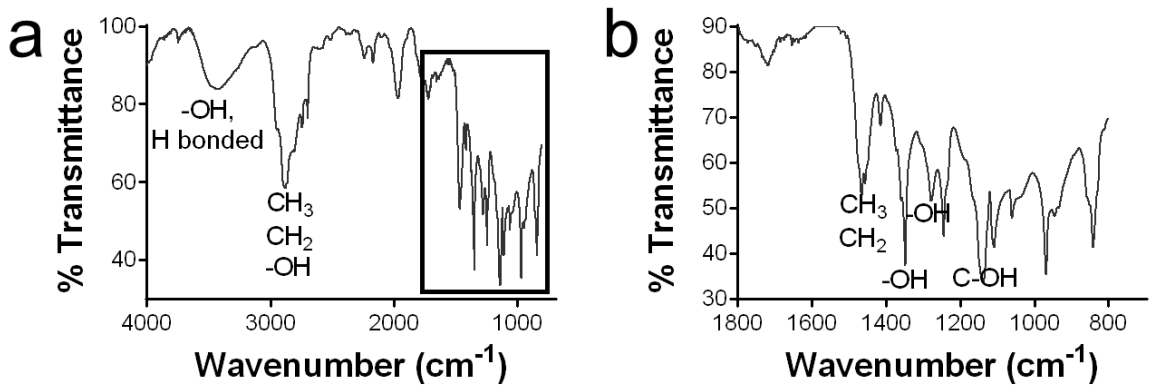

Figure 5.10: Sample image of aqueous CNP suspension and transfer into dodecylamine organic solution.

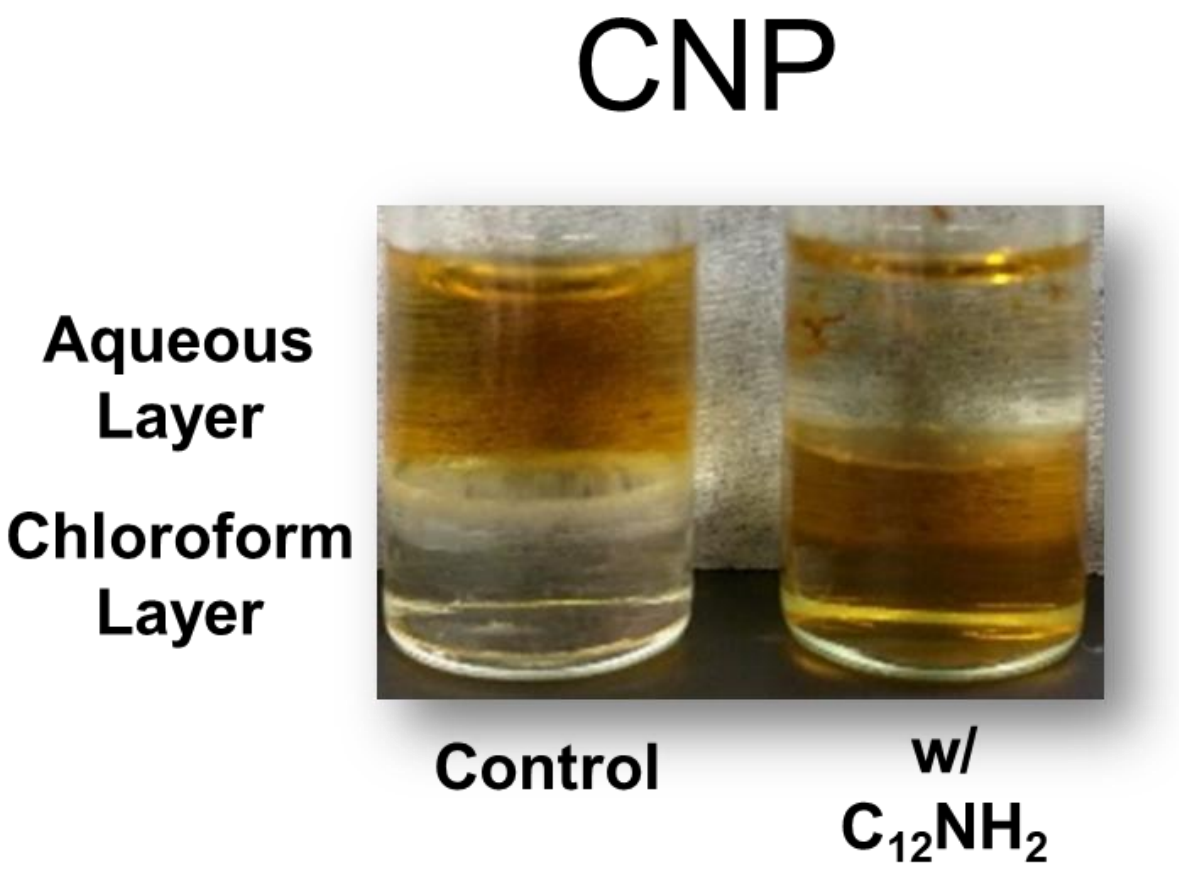

Figure 5.11: Schematic representation of the NMC synthesis process from the inverted micelle capsule to the NMC particle.

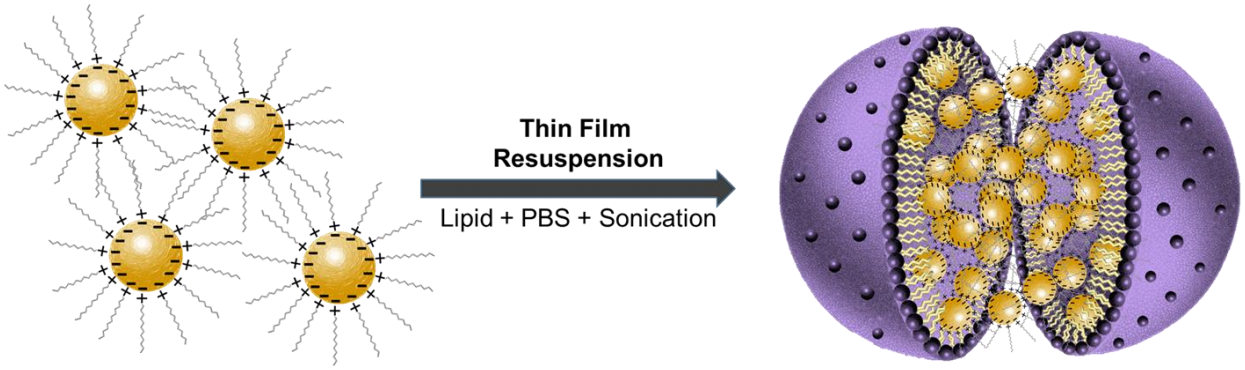

For naming convention, a group of AuNPs encapsulated in an NMC is labeled as NMC-AuNP, and a group of CNPs encapsulated into an NMC is labeled as NMC-CNP. The hydrodynamic diameter of NMC-AuNPs was measured to be 31 ± 10 nm with a PDI of 0.5 ± 0.1, while NMC-CNPs was measured to be 40 ± 6 nm with a PDI of 0.4 ± 0.1 (Figure 5.12). If we assume that the solid nanoparticles randomly pack within the NMC architecture, we can predict that the average particle per NMC-AuNP is 37 and NMC-CNP is 56 based on the Kepler random packing density coefficient, η = 0.64 (Equation 5.1).[41,42]

Equation 5.1

$$\frac{\eta * \frac{4}{3} * \pi * {r_{NMC}}^3}{\frac{4}{3} * \pi * {r_{NP}}^3} = \#\ of\ Encapsulated\ Nanoparticles$$

Nanoparticle surface charge is a well-known determinant of cellular internalization efficiency and systemic stability. In fact, receptor mediated endocytosis (RME) is dependent on the electrostatic interactions occurring between nanoparticles and cell membrane proteins on the molecular level[43,44]. For this reason, we investigated nanoparticle Zeta measurements on each NMC formulation to determine their electrophoretic potential. Zeta potential readings confirmed our initial findings that both solid nanoparticle variations had strong negative surface charges due to carboxylate-based surface chemistries. The adjacent NMC variations had 'less negative' Zeta readings which predicts a higher rate of cellular uptake while maintaining a negative charge necessary for systemic stability (Figure 5.13).[44]

Figure 5.12: An overlaid histogram representing the number averaged (%) of the NMC-AuNP and NMC-CNP colloidal hydrodynamic diameters.

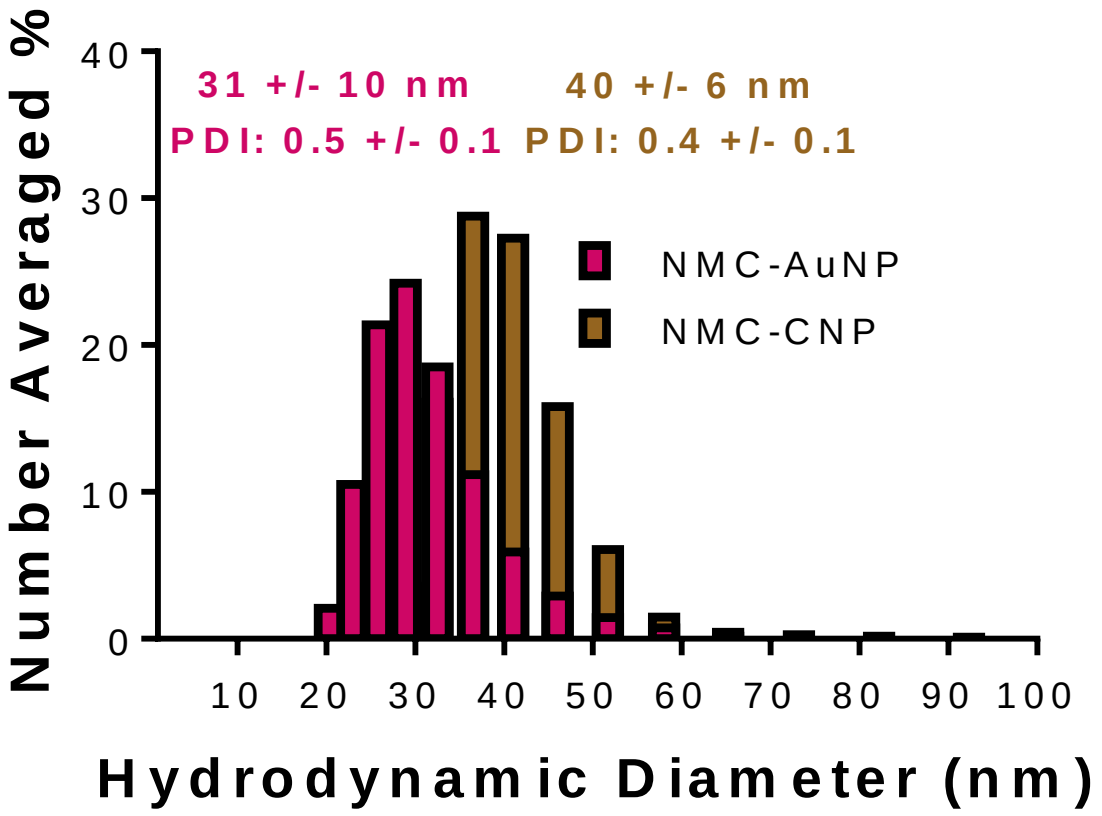

Figure 5.13: Surface charge as measured by Zeta potential of each nanoparticle formulation.

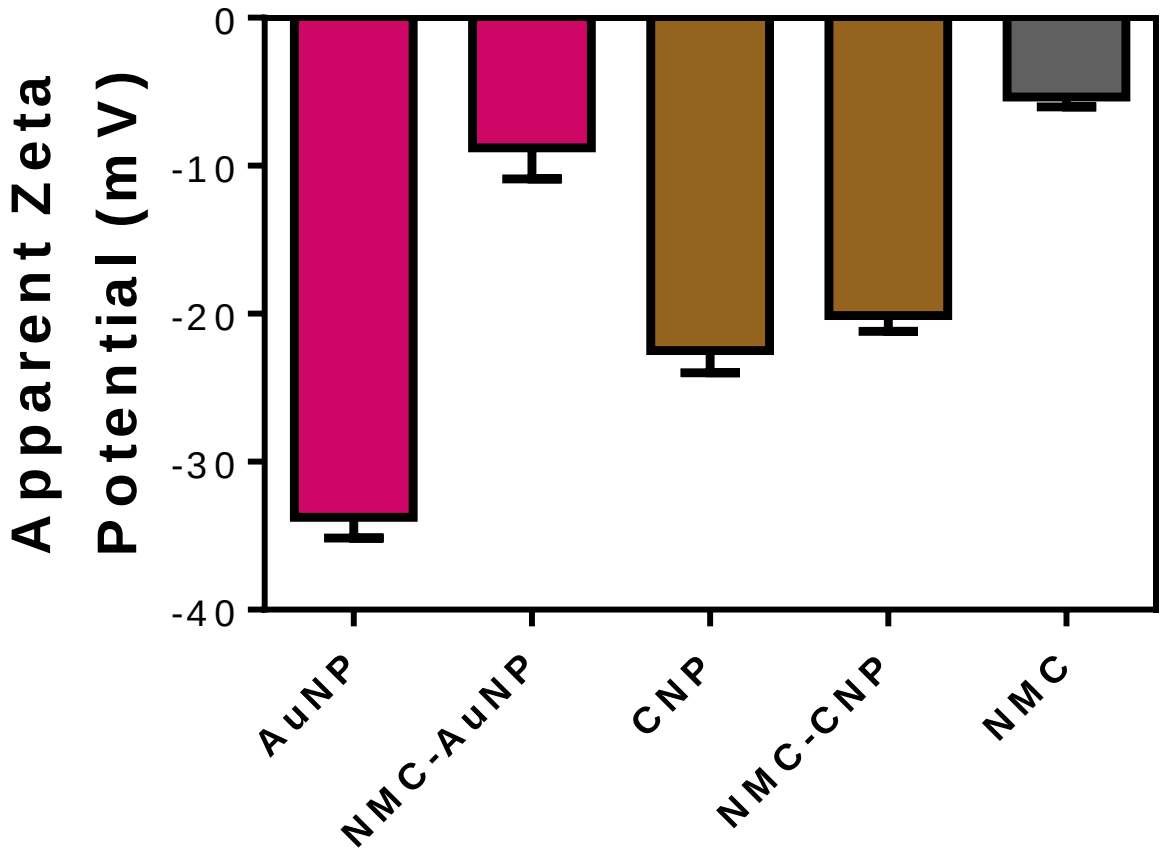

To understand the dynamic stability of the NMC architecture, the hydrodynamic diameter for each NMC variation was monitored for one week at 37 °C in the following environments: Low pH H_2O (pH 4.5, HCl), dPBS (1x, pH 7.4), high pH H_2O (pH 12, NaOH), and fetal bovine serum (FBS, 1%). Both NMC-AuNP and NMC-CNP remained consistent with their hydrodynamic diameter integrity (Figure 5.14), which was additionally supported by long-term stability studies at 4 °C over 1 month of observation (Figure 5.15). TEM micrographs of NMC-AuNP particles revealed a large population of AuNP aggregates with anhydrous diameters similar to the reported hydrodynamic diameters (Figure 5.16). Furthermore, a UV-Vis absorbance analysis on the NMC-AuNP suspension revealed a red 20 nm peak shift to 526 nm, commonly seen through aggregation (Figure 5.17). To further probe that the NMC-AuNP structure displays shell-like characteristics, samples underwent small angle X-Ray scattering (SAXS). The X-Ray patterns revealed a strong q band intensity at 0.54 nm^{-1} indicating the presence of an 11.6 nm artifact (Figure 5.18). Since the AuNP's have diameters of 8 ± 2 nm and the dodecylamine shell adds an additional 3.68 nm to the diameter (1 dodecylamine ~ 1.84 nm; 1.84 nm *2 = 3.68 nm) then the 11.6 nm SAXS artifact falls within an expected range for the hydrophobically passivated AuNPs.

TEM micrographs of NMC-CNP particles also showed a commonly sized population corresponding to the measured hydrodynamic diameters. A TEM inset at a higher magnification reveals the smaller groupings of individual CNPs with the NMC (Figure 5.19). A normalized UV-Vis absorbance measurement of the NMC-CNP suspension showed a decrease in the typical CNP absorbance peak at 282 nm as compared to the stock CNP spectra (Figure 5.20). This decrease is a result of the NMC phospholipid outer shell obstructing light interactions with the CNP's surface chemistry that determine the CNP's inherent optical properties.

Figure 5.14: Seven-day assessment of (a) NMC-AuNP and (b) NMC-CNP Hydrodynamic diameter stability in various environments.

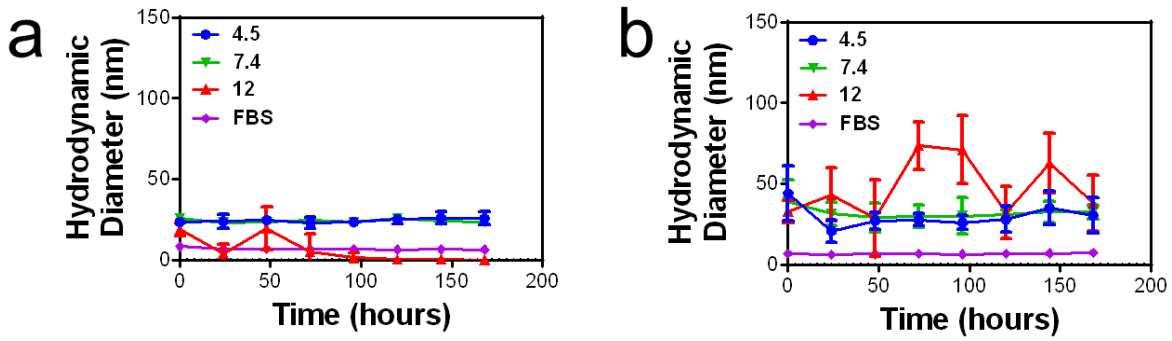

Figure 5.15: A 30-day assessment of the NMC Hydrodynamic diameter shelf life stability at 4 °C.

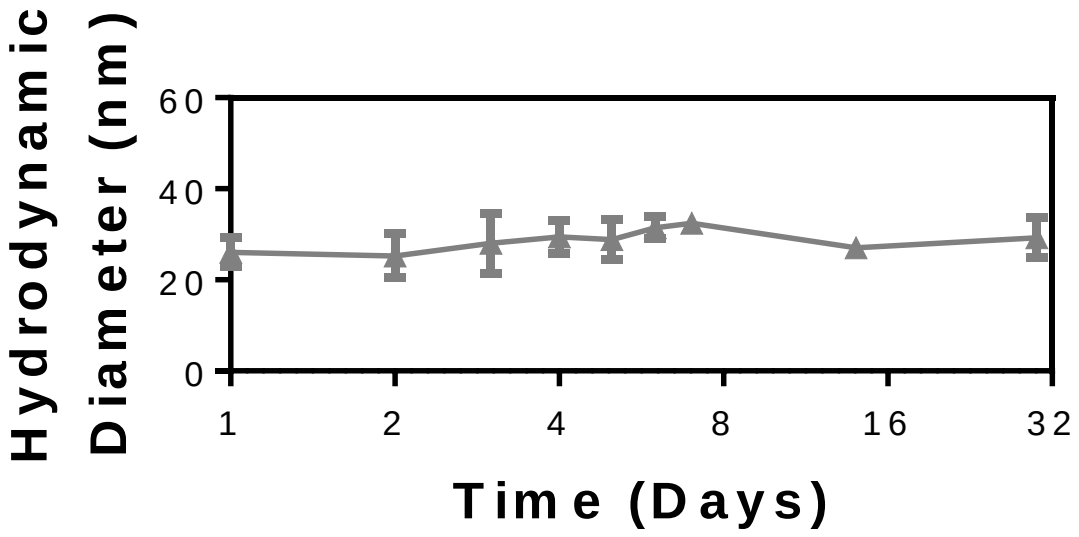

Figure 5.16: TEM micrographs of NMC-AuNP with an inset at a higher magnification.

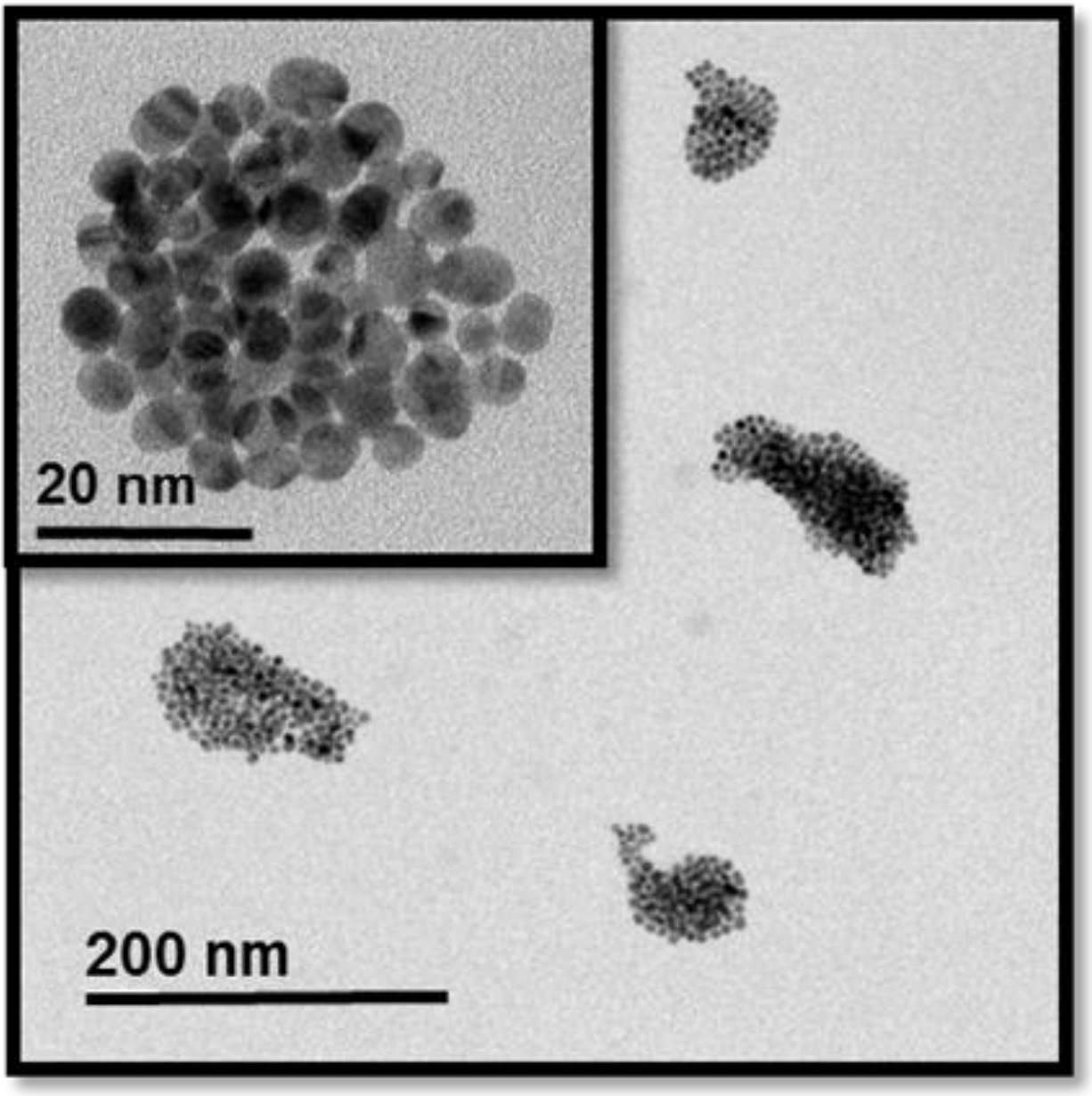

Figure 5.17: UV-Vis absorbance measurements of the AuNP stock suspension (Magenta) and NMC-AuNP (dark purple). The direction of the shifted peak is labeled with an arrow.

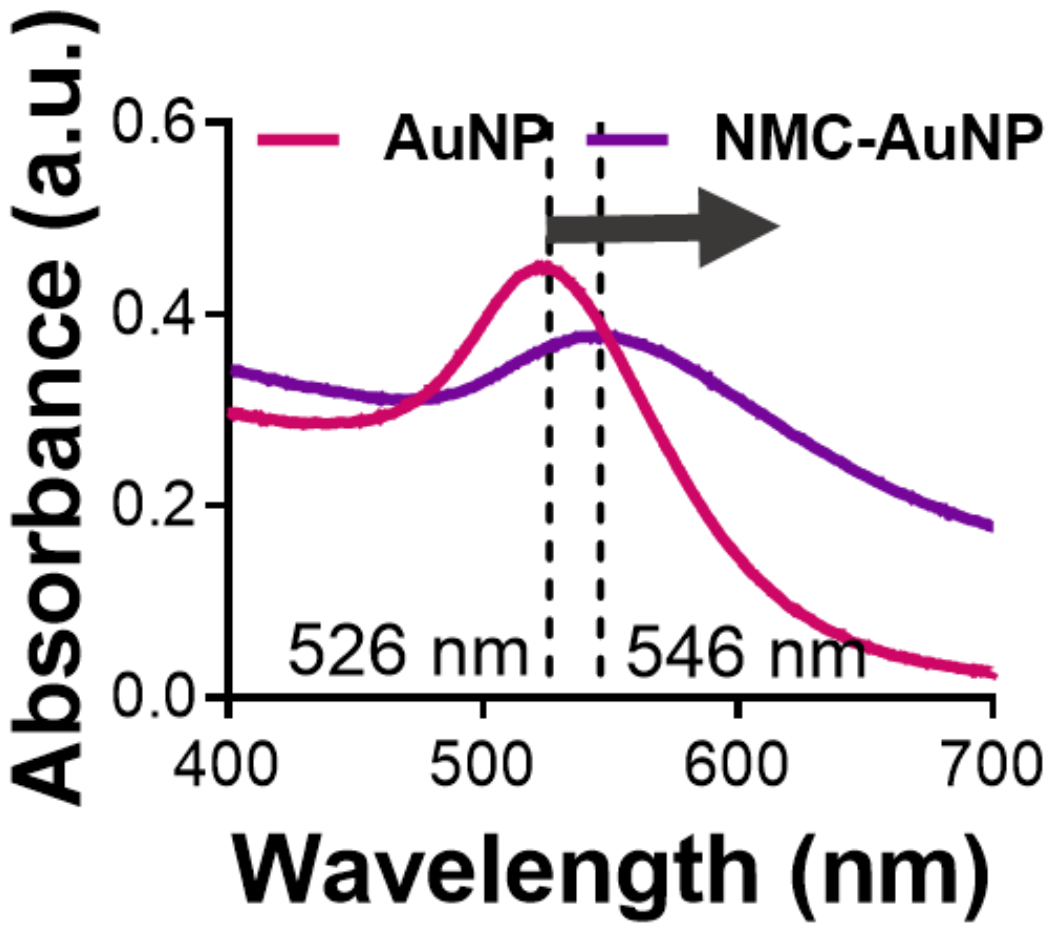

Figure 5.18: a) SAXS intensity versus q (nm^{-1}) with visible feature indicated by black arrow. a) SAXS band formation colored by intensity.

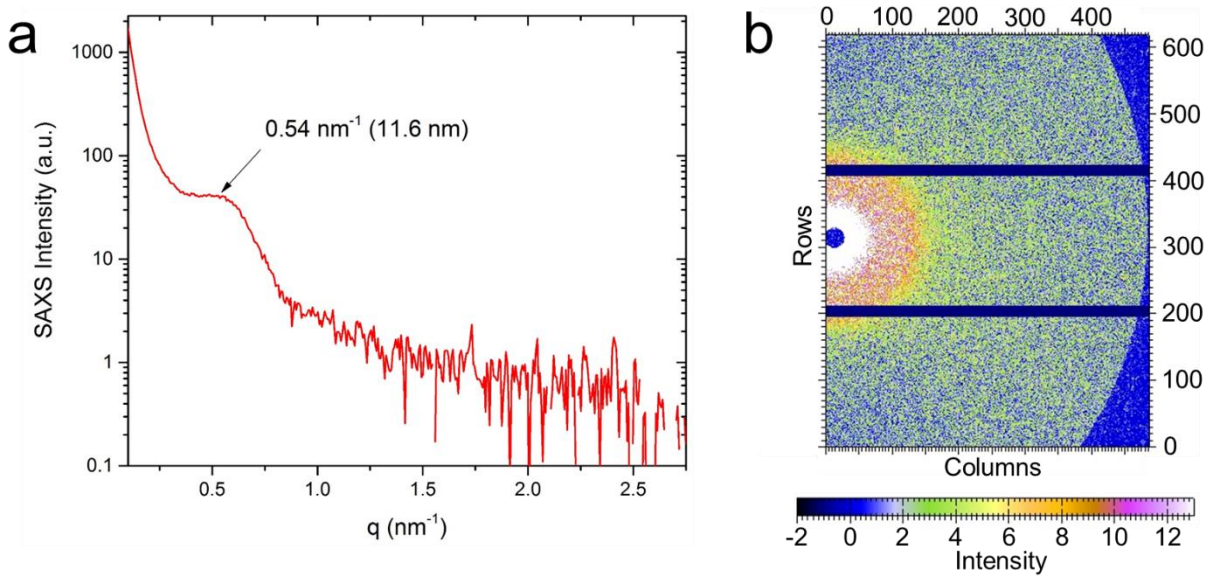

Figure 5.19: TEM micrographs of NMC-CNP with an inset at a higher magnification. Arrows reveal individual particles entrapped within the NMC-CNP complex.

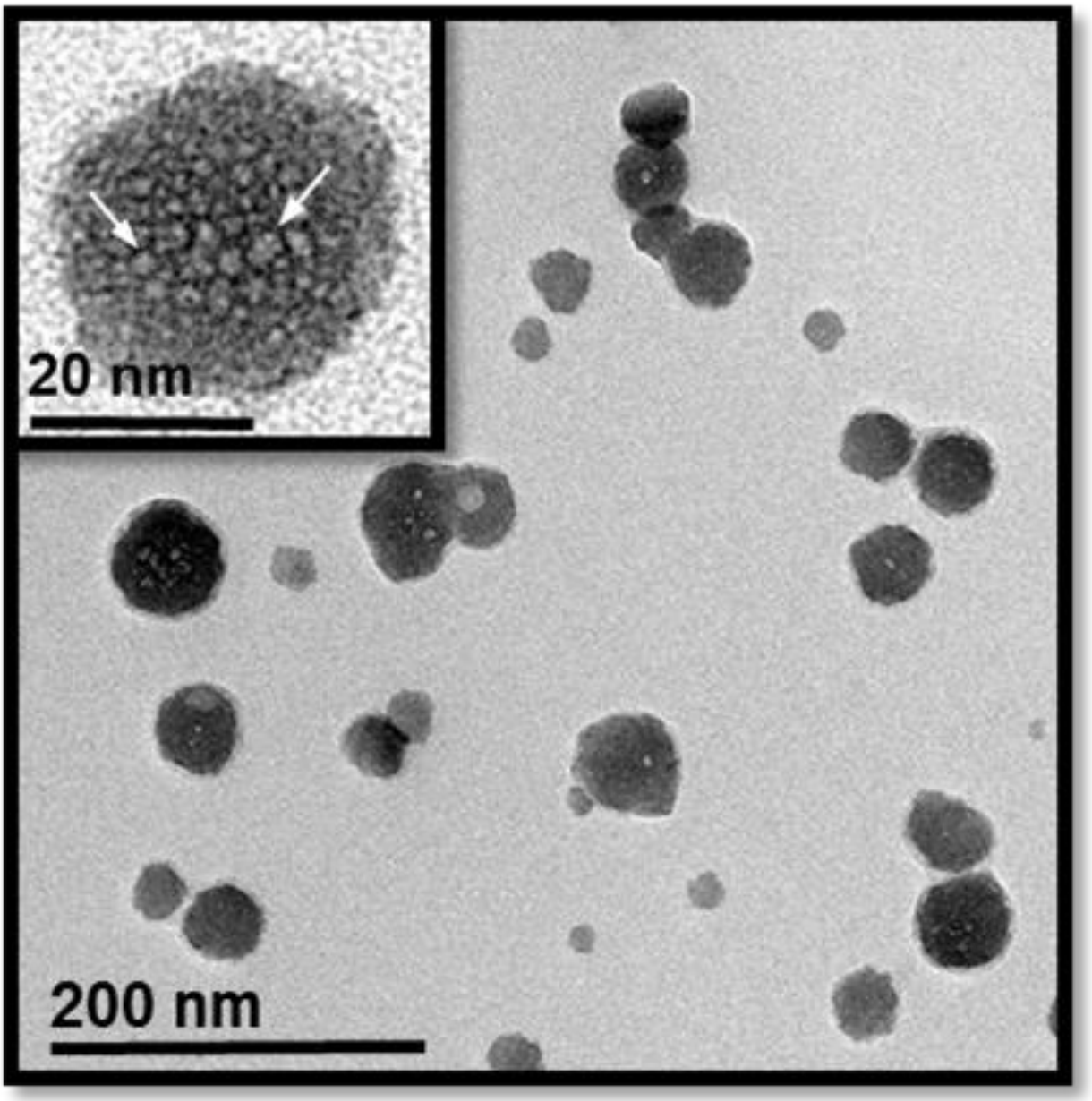

Figure 5.20: UV-Vis absorbance measurements of the CNP stock suspension (dark) and NMC-AuNP (light). The direction of peak shift is labeled with an arrow.

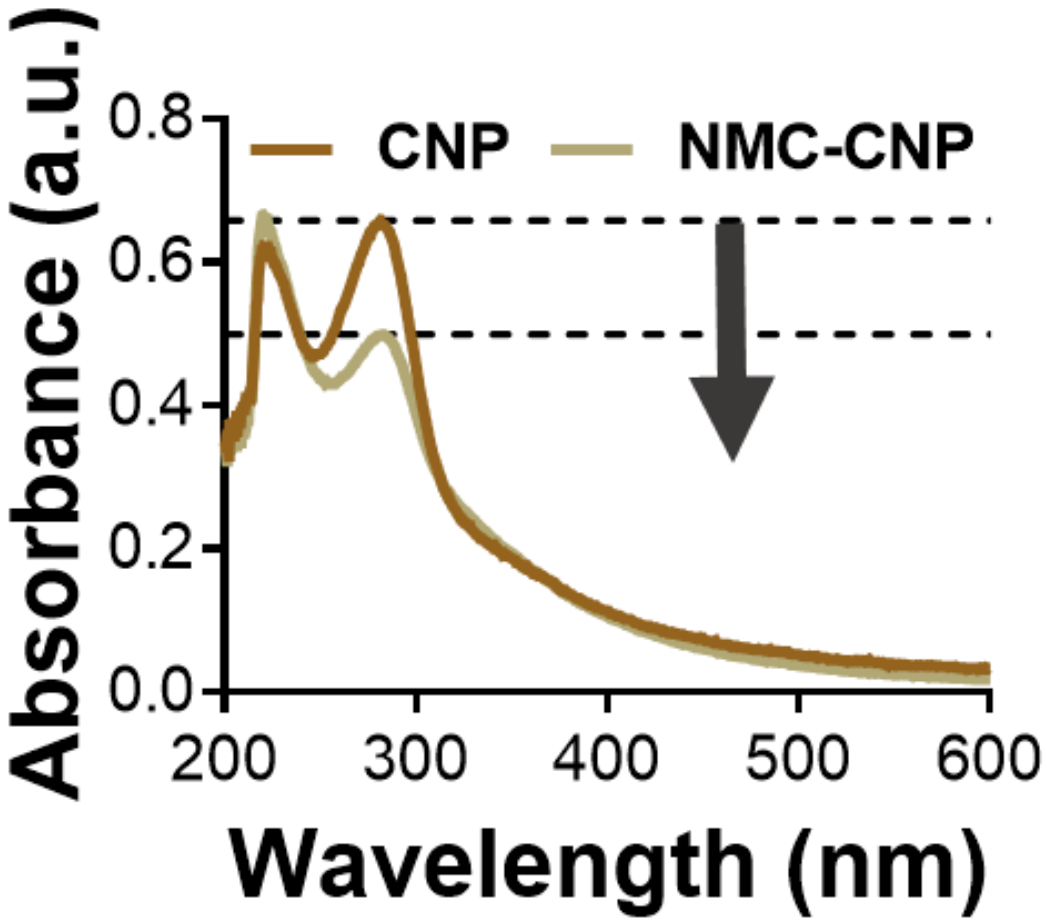

NMC biocompatibility profile and cellular internalization analysis

Since many studies show that AuNPs and CNPs have minimal to no biological interference,[36,45] we investigated the biocompatibility of the NMC-AuNP and NMC-CNP to ensure biocompatible consistency after nanoparticle encapsulation. To test biocompatibility, a 2-D culture of MCF-7 was seeded in triplicate, at a density of 10,000 cells per well, for nanoparticle cytotoxicity measurements by an MTT reduction assay. MCF-7 cells were then subject to various concentrations of AuNP, CNP, NMC-AuNP, NMC-CNP, and an empty NMC shell. After 48 hours of exposure, AuNPs and CNPs showed cell viability trends at or above 100% as expected due to their known bio-inert characteristics (Figure 5.21a).

Agreeably, both the NMC-AuNP and NMC-CNP counterparts supported trends at or above 100% cell viability for expected treatment concentrations. These results are expected since the empty NMC capsules showed no signs of severe toxicity due to its material composition except at the highest concentration tested where the cell population dipped to roughly 80% viability (Figure 5.21b). To be certain that the NMC particles did not physically disrupt cellular morphology, we examined bright field images of MCF-7 cells at the highest treatment concentrations (0.1 mg/ml) to ensure that cellular structure was not compromised. After 48 hours of exposure, we found that both treatment variations did not create noticeable morphological impairments, but instead closely resembled the control cells (Figure 5.22a-c). Both MTT and bright field experiments indicate that the NMC encapsulation process of hard nanoparticles did not affect the particle's biocompatibility, which is significantly relevant when investigating alternative methods for high-throughput delivery of small nanoparticles.

Figure 5.21: a) Percent change in MCF-7 cell viability of AuNP and CNP. b) Percent change in MCF-7 cell viability of NMC-AuNP, NMC-CNP, and an NMC control particle.

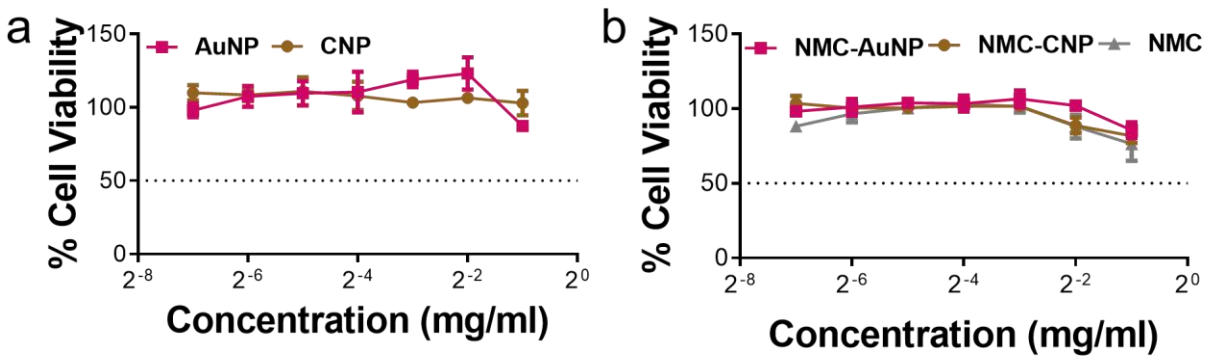

Figure 5.22: a-c) Bright field images of MCF-7 cells treated at 0.1 mg/ml of the labeled samples. Images were taken with a 10x objective (Scale bar: 50 μm).

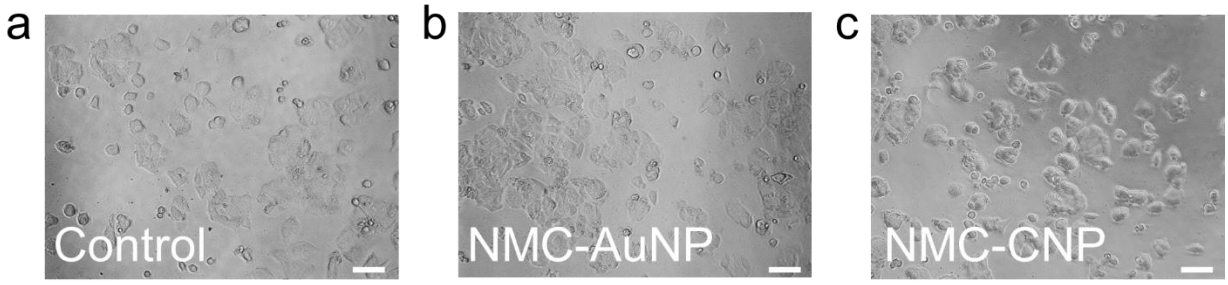

Enhanced ~10 nm AuNP cellular internalization

To validate our hypothesis that the NMC architecture improves solid nanoparticle internalization into diseased cells, we used inductively coupled plasma – optical emission spectrometry (ICP-OES) to quantify the content of gold internalized per cell for AuNP and NMC-AuNP samples. MCF-7 treatment concentrations of NMC-AuNP were optimized at 0.5 mg/ml to deliver minimal but noticeable results, while AuNP treatments were performed at a gold content equivalence to the NMC-AuNP. Cells were exposed to these formulations for four hours (2×10^6 cells/ dish), washed with dPBS (pH 7.4) three times, trypsinized, and collected for ICP-OES. A duplicate treatment underwent 3x heparin-sulfate washes instead of dPBS to remove any AuNP that might have remained on the surface of cells to differentiate from endocytosed AuNP.[46] In each case, ICP-OES results determined that the NMC-AuNP delivered a significantly larger amount of elemental gold within the cell than treatments of free AuNPs (Figure 5.23). When each formulation was compared to its duplicate heparin sulfate wash, the AuNP sample decreased in gold-per-cell by more than half, while the two NMC-AuNP samples (dPBS wash vs. heparin wash) did not significantly differ.

Figure 5.23: ICP histogram analysis of elemental gold per cell after treatments with AuNP, NMC-AuNP, and a duplicate of each variation with an added heparin sulfate wash (indicated by '-H' after the treatment name).

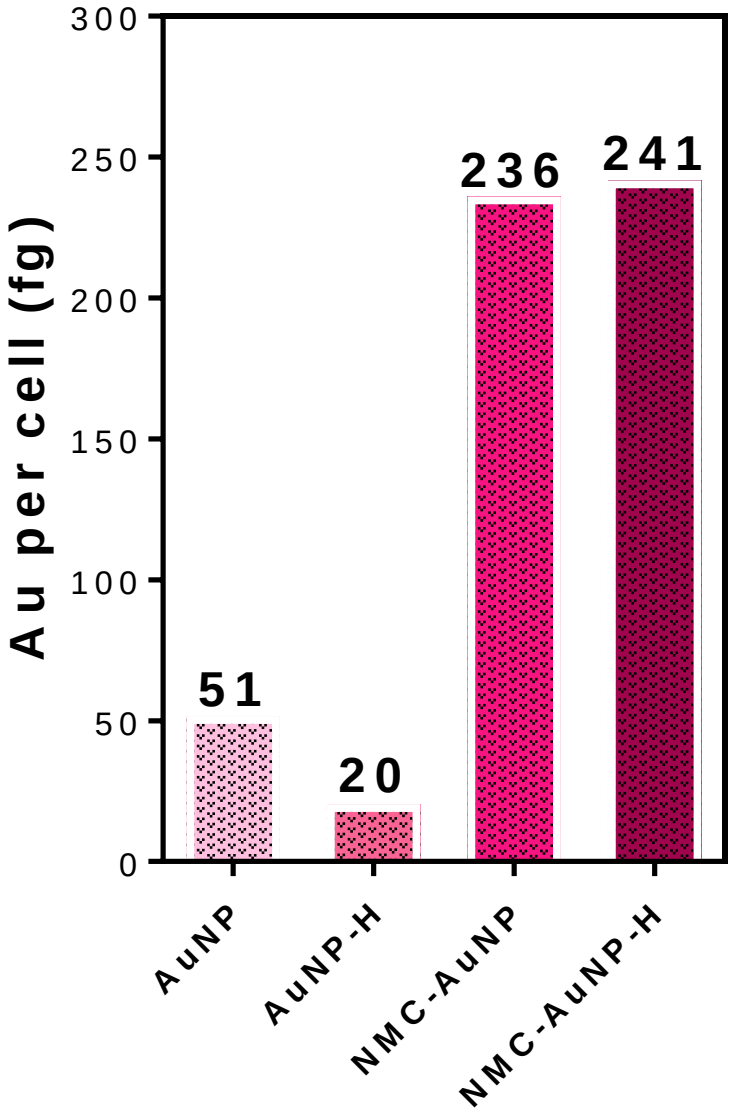

This difference in elemental gold content within the cell is indicative that the ~10 nm AuNP treatment must collect on the surface of the cell membrane and cannot activate sufficient receptors for RME as compared to the NMC-AuNP variant which carried a packaged payload of the smaller AuNPs. Therefore, we can conclude that the NMC architecture drives high-throughput intracellular nanoparticle internalization. To visualize this AuNP uptake phenomenon, we considered cellular TEM imaging after a 2-hour treatment of each variation at 5x the normal treatment concentrations. MCF-7 cells were treated with concentrations similar to ICP-OES measurements and then fixed with glutaraldehyde. TEM micrographs of cells treated with just AuNPs showed infrequent and disperse particles (Figure 5.24a). In some cases, intercellular vesicles were found to have ~10 nm gold nanoparticles lining the vesicle perimeter suggesting RME may have driven cellular uptake (Figure 5.24b), although this was not frequently observed. When compared to TEM micrographs of NMC-AuNP treatments, there was an abundant amount of internalized AuNP clusters indicating that the NMC architecture facilitated the high-throughput cellular internalization of AuNPs (Figure 5.25a-b). Occasionally, cells were seen to have disrupted membranes, possibly due to the high treatment concentrations (as seen in Figure 5.25a), but this was rarely seen and not correlated to the aggregation of AuNP in the cytoplasm.

Figure 5.24: a-b) TEM micrographs of cells treated with AuNP alone. Both images contain insets at higher magnifications.

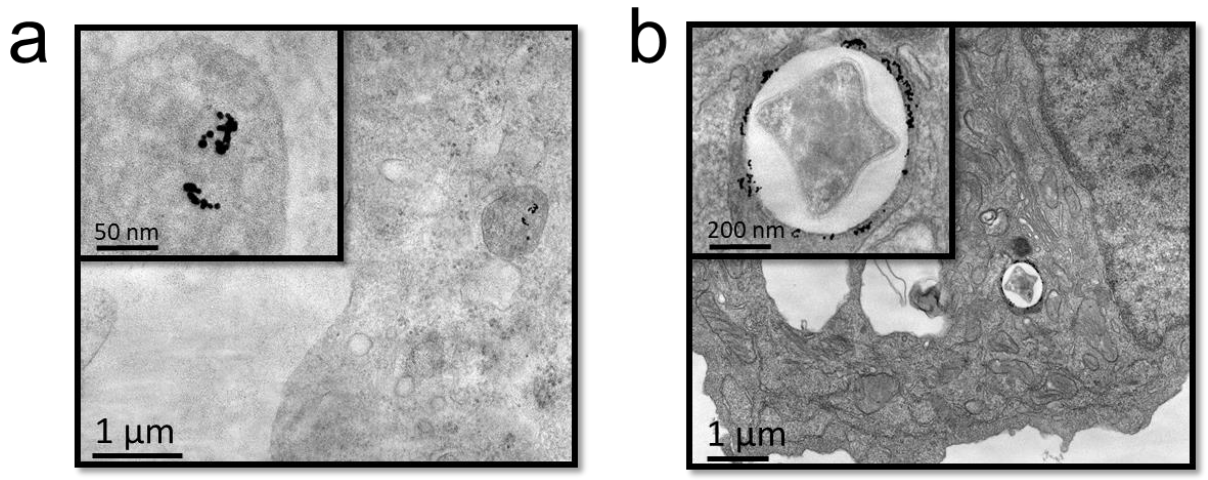

Figure 5.25: a-b) TEM micrographs of cells treated with NMC-AuNP. Both images include insets at higher magnifications.

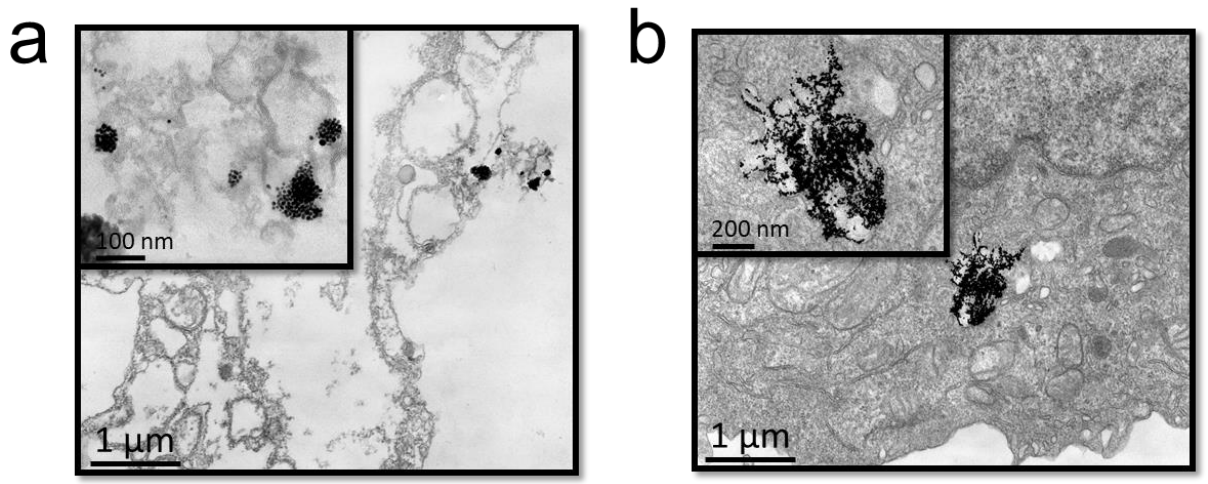

Enhanced ~10 nm carbon nanoparticle cellular internalization

To further probe into the NMC's ability to deliver an assortment of nanomaterial compositions, we analyzed the cellular Raman activity of spectroscopically active CNPs and their NMC-CNP counterpart. CNP treatment alone generated high intensity artifacts within the Raman Micrographs, but these treatments were not as prevalent or at the magnitude of NMC-CNP treatments (Figure 5.26a-c). Furthermore, when compared to bright field images, cells treated with NMC-CNP had a majority of the CNP fluorescence intensity come from localized spots within the cells (white arrows in Figure 5.26c), while the treatment of CNP alone led to high intensity spots localized along the cells perimeter (Figure 5.26b). This difference in localized Raman hot spots leads us to believe that the sub-10 nm nanoparticles are aggregating outside the cell on the membrane, while the larger NMC-CNP is facilitating a higher degree of high-throughput CNP delivery within the cell.

An averaged spectral analysis of cells did not explicitly reveal the CNP G and D band characteristics due to the low laser power needed for sample preservation. However, since Raman intensity is directly correlated to the fluorescence intensity caused by the presence of CNP, we can discern that the higher Raman readings from NMC-CNP treated cells is due to the high-throughput CNP internalization facilitated from the NMC packaging (Figure 5.27). This was also supported by Image-J pixel intensity measurements (Figure 5.28) which displayed a notably higher reading for NMC-CNP cell treatments.

Figure 5.26: Raman-generated intensity heat maps (and respective bright field images) of MCF-7 cells treated with the labeled formulations.

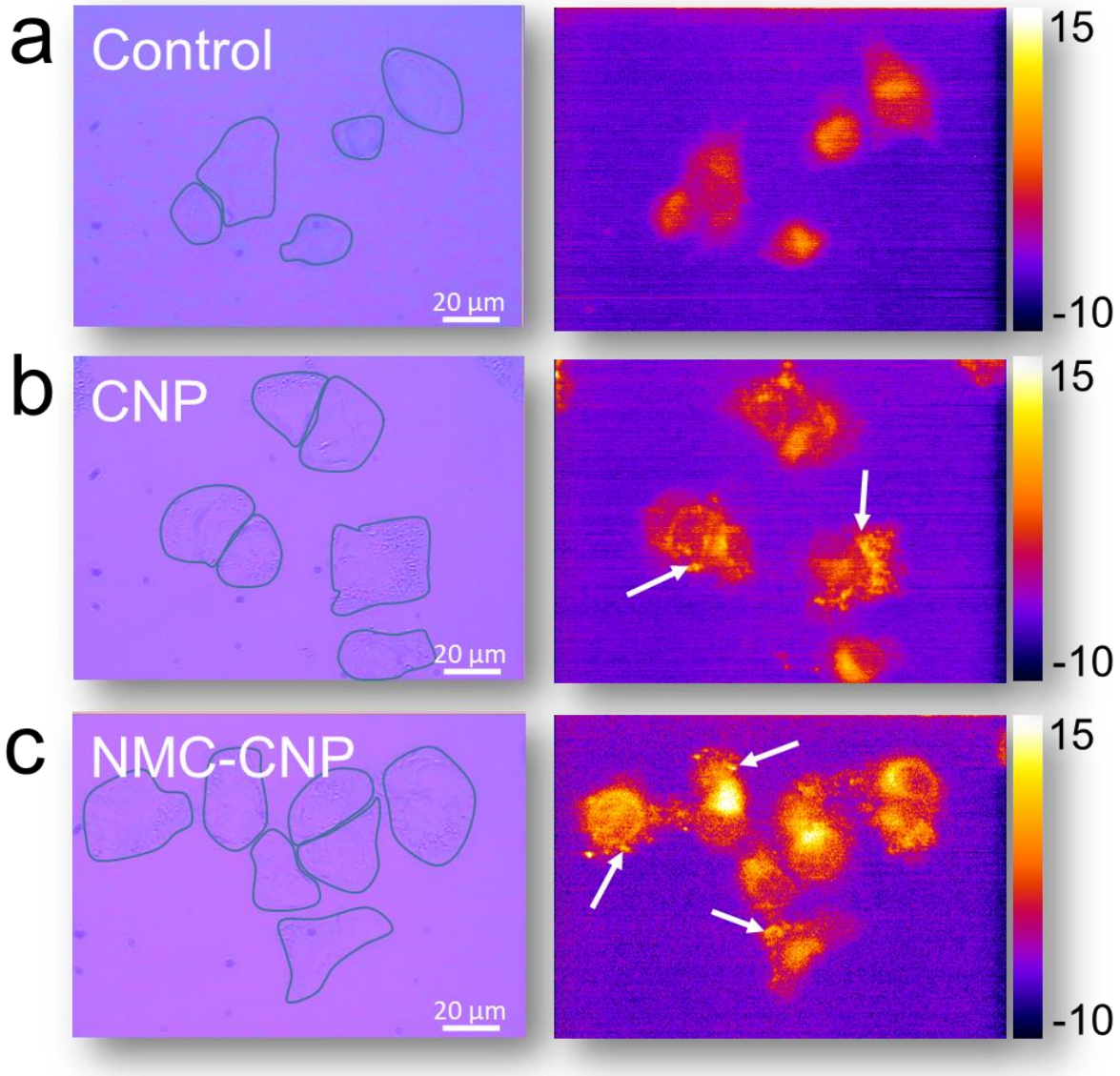

Figure 5.27: Raman-generated spectral analysis of cells with their respective chemical peak associations.

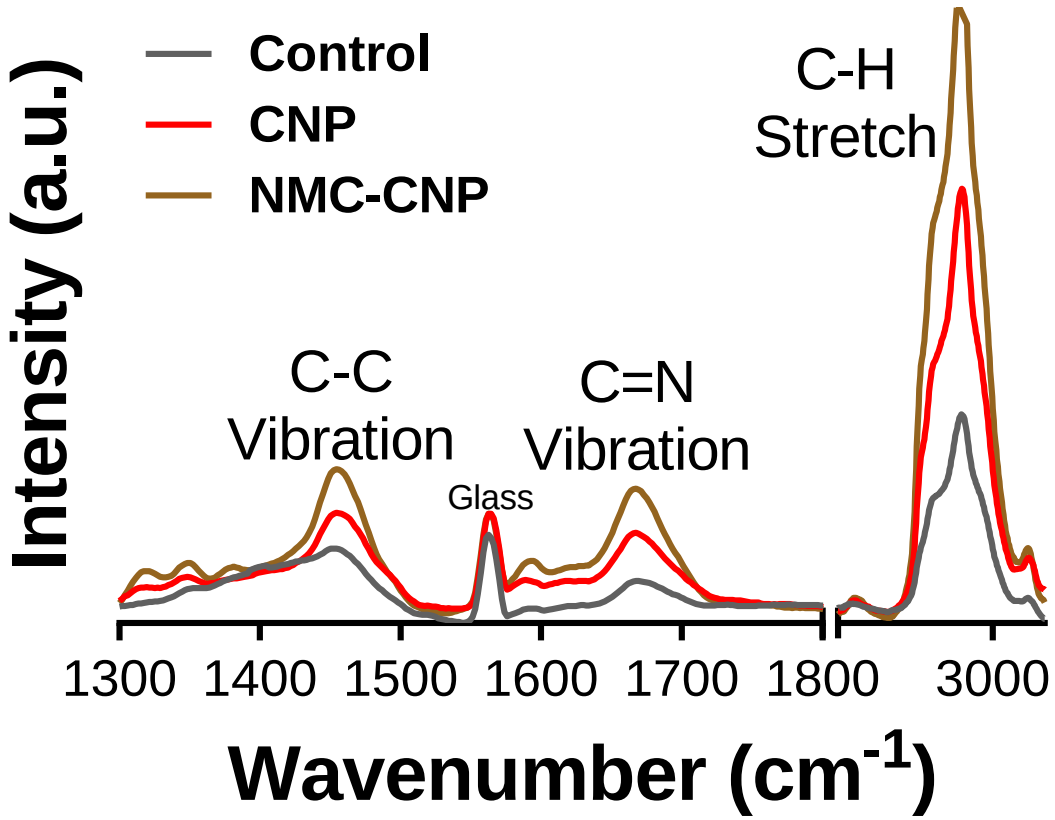

Figure 5.28: Bar chart representing pixel intensity per cell of respective treatment formulations measured by Image J.

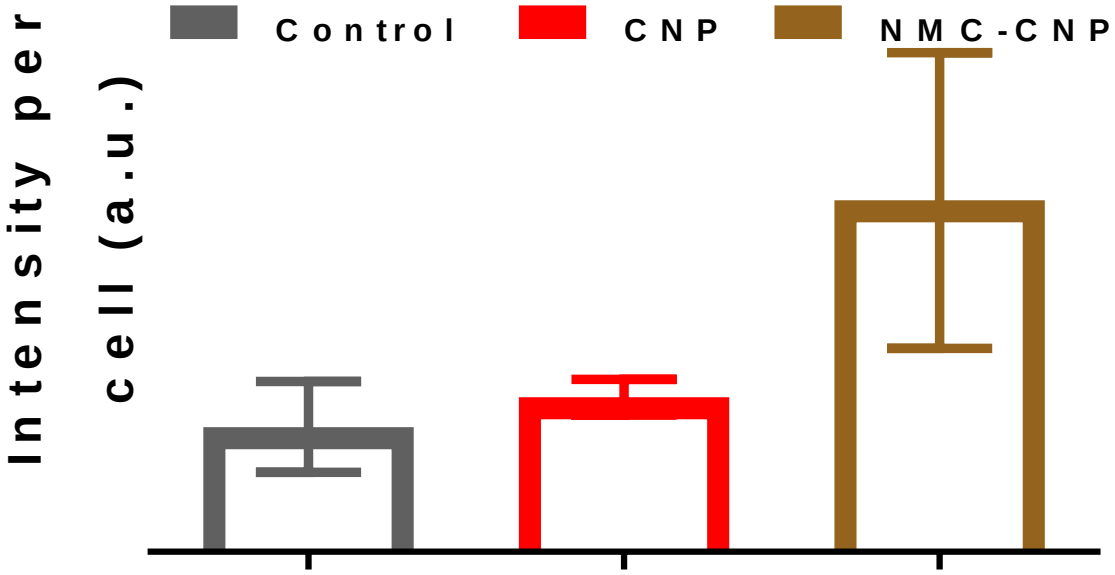

Conclusion

Here we have investigated the next generation of nanoparticle delivery by designing a nano-architecture for the high-throughput delivery of <10 nm particles, and thus alleviating the common complications associated with cellular uptake due to size restrictions and systemic clearance. Such a capsule uses simple electro-chemical interactions to entrap <10 nm particles within a hydrophobic shell, which is subsequently encapsulated into a larger phospholipid capsule. The materials composing the NMC architecture were carefully chosen to promote biocompatibility and facile cellular internalization as compared to unassisted solid nanoparticle treatments. For a detailed investigation into the possible functions of such a versatile capsule, we considered propagating the delivery of <10 nm AuNPs, which are adaptable for a multitude of theranostic uses. We found that NMC's (either NMC-AuNP or NMC-CNP) lead to a significantly larger quantity of internalized AuNPs among the metastatic cell line MCF-7. Additionally, TEM micrographs visually confirmed that cells physically consumed larger clusters of NMC-AuNP, with much higher throughput than free AuNP treatment. To expand upon the NMC's delivery ability amongst nanoparticles of different compositions, we encapsulated spectroscopically active CNPs and measured their Raman activity. Raman-generated intensity micrographs revealed that NMC-CNPs led to a higher degree of intracellular CNP fluorescence, while the treatment of CNP alone led to nanoparticle accumulation among the cell's perimeter to a much lower degree than NMC-CNP. Further investigations are warranted for the capability of the NMC to entrap material other than solid particles, such as biological matter or small drug molecules. Additionally, the NMC's *in vivo* adaptability and systemic clearance must be established to translate this novel delivery platform into clinical use.

Methods

Unless stated otherwise, all materials and reagents were purchased from Sigma–Aldrich, St. Louis, MO, and were used without further purification.

Gold nanoparticle preparation

AuNPs were prepared based on previous literature.[47] A 20 mL aqueous solution containing 400 µM HAuCl4 and 200 µM Trisodium Citrate (the capping agent) was prepared in a conical flask and cooled to 4 °C. Next, the reducing agent, $NaBH_4$, was pre-dissolved in a small volume of 4 °C nano pure water (18 MΩ) and quickly added to the solution while stirring to bring the $NaBH_4$ concentration of the entire system to 1.45 mM. The solution turned dark purple immediately, indicating gold nanoparticle formation (AuNP), then slowly changed to its final red color. The AuNP suspension was collected and filtered by a 0.22 µm filter (33mm PVDF membrane, Millex, Tullagreen, Ireland).

Carbon nanoparticle preparation

CNPs were prepared based on previous literature.[36,37] A mixture of agave nectar and polyethylene glycol (PEG) (Mn = 10,000) was taken in a glass sample vial at a 1:10 ratio (w/w). Nano pure water (18 MΩ) was added to suspend agave and polymer at concentrations of 25 mg/mL and 250 mg/ml, respectively. The sample was vortexed to form a homogenous mixture. For CNP nucleation, samples were placed on a hot plate surface (maintained at 270 °C) uncapped to allow slow evaporation of water. After 45 minutes, the reaction mixture darkened in color. The dark suspension was supplemented with nano pure water (18 MΩ) for a final concentration of 36 mg/ml and then probe sonicated for 10 minutes (Q700TM, Q sonica Sonicators, CT, USA) (Amp:1, On: 2 sec, Off: 1 sec) in an ice bath to reduce heat from sonication. The CNP suspension was collected

and filtered by a 0.45 μm filter, followed by a 0.22 μm filter (PTFE membrane, Jet Biofil®, Guangzhou Jet Bio-Filtration Co., Ltd., Guangzhou, China).

Inverted micelle nanoparticle transfer

An equal volume ratio of 16.2 mM of dodecylamine dissolved in chloroform and an aqueous suspension of either AuNP or CNP was added into a 1-dram vial and vigorously shaken for several seconds to homogenously mix the layers. The vials were then allowed to separate and settle for a prolonged period of time. At this point, the nanoparticle variation of choice had clearly transferred into the chloroform layer retaining its respective color.

Nano-MultiCapsule particle formation

The following method was used to encapsulate the inverted micelle-nanoparticle composite into a lipid nanoparticle (NMC-AuNP for AuNP entrapment, or NMC-CNP for CNP entrapment). The inverted micelle-nanoparticle composite suspended in chloroform was added to a glass bulb along with phosphatidylcholine (PC, Coatsome, NOF Corporation, Tokyo, Japan), 1,2-Dioleoyl-sn-glycero-3-phosphatidylethanolamine (PE, Cayman Chemical Company, MI, USA), and cholesterol at an optimized w/w ratio of 10:9:1:0.5 of dodecylamine:PC:PE:cholesterol. The chloroform in the glass bulb was evaporated by a rotary evaporator (RE200, Yamato Scientific Co., Ltd. Japan) in a 55 °C water bath to produce a thin film layer of the materials. The sample was then placed in a desiccator (Labconco, Kansas City, MO, USA) for 30 minutes. dPBS (pH 7.4) was added to the bulb at a volume to produce a final concentration of 0.8 mg/ml. The sample was subject to probe sonication (Amp: 1, On: 5 sec, Off: 3 sec). The samples were then immediately placed in an ice-bath and incubated for one hour at 4 °C. Following incubation, the

samples were filtered through a 0.22 μm PTFE syringe filter and dialyzed against a 10,000 molecular weight cut off cassette (Thermo Scientific Product # 87730, Rockford IL, USA).

Dynamic light scattering measurements

Hydrodynamic diameters were determined using a Malvern Zetasizer ZS90 particle size analyzer, while the scattered light was collected at a fixed angle of 90°. A photomultiplier aperture of 400 μm was used with the incident laser power adjusted to obtain a photon counting rate between 200 and 300 kcps. Diameter values depended on measurements whereupon the measured and calculated baselines of the intensity autocorrelation function had to agree within ±0.1%. All determinations were made in multiples of three consecutive measurements of 15 runs each.

Determination of electrophoretic surface potential

Zeta potential (ζ) values for each nanoparticle formulation were determined with a nano series Malvern Zetasizer Zeta potential analyzer (Fredrick Seitz Material Research Laboratory, University of Illinois at Urbana-Champaign, (MRL facility, UIUC)). Data were acquired in the phase analysis light scattering (PALS) mode following solution equilibration at 25 °C when calculation of ζ from the measured electrophoretic mobility (μ) employed the Smoluchowski equation, which is expressed as:

Equation 5.2 $$\mu = \varepsilon\zeta/\eta$$

where ε and η are the dielectric constant and the absolute viscosity of the medium, respectively.

Measurements of ζ were reproducible to within ± 2 mV of the mean value given by three determinations of 15 data accumulations.

Raman and FTIR spectroscopy

All Raman measurements were taken on a Nanophoton Raman instrument (MRL facility, UIUC) with a 532 nm wavelength laser. For each spectrum, a grating (600 l mm^{-1}) scan was taken over the range of 120–2700 cm^{-1}. Point scans were performed at 0.2% laser power for one minute using a 20x objective. An average of 20 spectra were recorded and averaged per sample. For Raman micrographs, samples were imaged using line scans at 20% laser power and a 5× objective for 20 seconds per scan.

For FTIR analysis, aqueous suspensions of particles were drop cast onto MirrIR IR-reflective glass slides (Kevley Technologies, Chesterland, Ohio, USA) and measured using a Nicolet Nexus 670 FTIR (MRL facility, UIUC). For each measurement 100 × 100 μm images were collected at 1 cm^{-1} spectral resolution with 64 scans per pixel and a 25 × 25 μm pixel size and individual spectra were corrected for atmospheric contributions.

Transmission electron microscopy imaging

Two μL of particle suspension was applied to carbon-coated TEM grids. Grids were then blotted, air dried, and imaged on a JEOL 2100 Cryo-TEM machine via a Gatan UltraScan 2k × 2k CCD camera (MRL facility, UIUC).

Cell viability assay

The cytotoxic effect of nanoparticle formulations was investigated with a 3-(4,5-dimethylthiazole-2-yl)-2,5-diphenyltetrazolium bromide (MTT) assay. The MCF-7 (human estrogen receptor positive breast cancer) cell line was plated on a 96-well plate at a density of 10,000 cells per well (Greiner CellStar® 96 well plates, Sigma-Aldrich, MO, USA) and exposed

to nanoparticle formulations after 24 hours at 37 °C. Followed by a 48 h exposure time, 20 μL (5 mg/mL) of MTT solution was added to each well and cells were further incubated for another 4 hours. After exposure, media was aspirated, and 200 μL of dimethyl sulfoxide (DMSO, ≥99%, MP Biomedicals, USA) was added to dissolve formazan crystals. The optical density of samples was determined by Synergy HT (BioTek, USA) with a reference wavelength of 570 nm. The following equation determined percentage cell viability (Equation 5.3):

Equation 5.3

$$\%Viability = \frac{A_{570}(treated) - A_{570}(background)}{A_{570}(control) - A_{570}(background)}$$

Gold nanoparticle uptake as measured by ICP-OES

ICP-OES was performed on cells treated with AuNP and NMC-AuNP to measure gold content within cells. The MCF-7 cell line was plated on a poly-L-lysine coated 6-well plate at a cell density of 1 million cells per well. After 24 hours, cells were treated with duplicates of respective formulations for two hours. Before cells were trypsinized and collected, one sample from each duplicate was washed three times with heparin sulfate similar to previous reports,[46] while the rest were washed three times with dPBS (pH 7.4). Cells were collected and centrifuged to form a cell pellet. Each pellet was then subject to an aqua regia acid degradation and analyzed with a PerkinElmer 2000DV ICP-OES (Noyes Microanalysis Laboratory, UIUC).

References to Chapter 5

(1) Caffarini, J.; Kelleher, N.; Konopka, C. C.; Mazurek, M.; Nandyala, A.; Patel, D.; Slania, S.; Wang, S.; Yada, R. C.; Pan, D. Multimodal Imaging and Theranostic Application of Disease-Directed Agents; Springer International Publishing, 2015; pp 75–103.

(2) Pan, D. *Nanomedicine: A Soft Matter Perspective - Google Books*; Taylor and Francis Group: Champaign Illinois, 2014.

(3) Ding, H.; Ma, Y. Role of Physicochemical Properties of Coating Ligands in Receptor-Mediated Endocytosis of Nanoparticles. *Biomaterials* **2012**, *33* (23), 5798–5802.

(4) Zhang, R.; Cai, X.; Yang, X.; Senpan, A.; Allen, J. S.; Pan, D.; Lanza, G. M.; Wang, L. V. Photoacoustic Molecular Imaging of Angiogenesis Using Theranostic α ν β 3 -Targeted Copper Nanoparticles Incorporating a Sn-2 Lipase-Labile Fumagillin Prodrug; Oraevsky, A. A., Wang, L. V., Eds.; International Society for Optics and Photonics, 2014; p 89435I.

(5) Yang, J.; Lee, J. Y.; Deivaraj, T. .; Too, H.-P. A Highly Efficient Phase Transfer Method for Preparing Alkylamine-Stabilized Ru, Pt, and Au Nanoparticles. *J. Colloid Interface Sci.* **2004**, *277* (1), 95–99.

(6) Saxena, U.; Chakraborty, M.; Goswami, P. Covalent Immobilization of Cholesterol Oxidase on Self-Assembled Gold Nanoparticles for Highly Sensitive Amperometric Detection of Cholesterol in Real Samples. *Biosens. Bioelectron.* **2011**, *26* (6), 3037–3043.

(7) Kamaly, N.; Xiao, Z.; Valencia, P. M.; Radovic-Moreno, A. F.; Farokhzad, O. C. Targeted Polymeric Therapeutic Nanoparticles: Design, Development and Clinical Translation. *Chem. Soc. Rev.* **2012**, *41* (7), 2971.

(8) Xu, S.; Olenyuk, B. Z.; Okamoto, C. T.; Hamm-Alvarez, S. F. Targeting Receptor-Mediated Endocytotic Pathways with Nanoparticles: Rationale and Advances. *Adv. Drug Deliv. Rev.* **2013**, *65* (1), 121–138.

(9) Choi, C. H. J.; Zuckerman, J. E.; Webster, P.; Davis, M. E. Targeting Kidney Mesangium by Nanoparticles of Defined Size. *Proc. Natl. Acad. Sci.* **2011**, *108* (16), 6656–6661.

(10) Soo Choi, H.; Liu, W.; Misra, P.; Tanaka, E.; Zimmer, J. P.; Itty Ipe, B.; Bawendi, M. G.; Frangioni, J. V. Renal Clearance of Quantum Dots. *Nat. Biotechnol.* **2007**, *25* (10), 1165–1170.

(11) Choi, H. S.; Liu, W.; Liu, F.; Nasr, K.; Misra, P.; Bawendi, M. G.; Frangioni, J. V. Design Considerations for Tumour-Targeted Nanoparticles. *Nat. Nanotechnol.* **2010**, *5* (1), 42–47.

(12) Zhang, X.-D.; Luo, Z.; Chen, J.; Wang, H.; Song, S.-S.; Shen, X.; Long, W.; Sun, Y.-M.; Fan, S.; Zheng, K.; et al. Storage of Gold Nanoclusters in Muscle Leads to Their Biphasic in Vivo Clearance. *Small* **2015**, *11* (14), 1683–1690.

(13) Zhang, X.-D.; Luo, Z.; Chen, J.; Shen, X.; Song, S.; Sun, Y.; Fan, S.; Fan, F.; Leong, D. T.; Xie, J. Ultrasmall Au $_{10–12}$ (SG) $_{10–12}$ Nanomolecules for High Tumor Specificity and Cancer Radiotherapy. *Adv. Mater.* **2014**, *26* (26), 4565–4568.

(14) Xie, J.; Lee, S.; Chen, X. Nanoparticle-Based Theranostic Agents. *Adv. Drug Deliv. Rev.* **2010**, *62* (11), 1064–1079.

(15) Luo, Z.; Zheng, K.; Xie, J. Engineering Ultrasmall Water-Soluble Gold and Silver Nanoclusters for Biomedical Applications. *Chem. Commun.* **2014**.

(16) Singh, M.; Harris-Birtill, D. C. C.; Markar, S. R.; Hanna, G. B.; Elson, D. S. Application of

Gold Nanoparticles for Gastrointestinal Cancer Theranostics: A Systematic Review. *Nanomedicine Nanotechnology, Biol. Med.* **2015**, *11* (8), 2083–2098.

(17) Pan, D.; Pramanik, M.; Senpan, A.; Wickline, S. A.; Wang, L. V.; Lanza, G. M. A Facile Synthesis of Novel Self-Assembled Gold Nanorods Designed for Near-Infrared Imaging.

(18) Schwartz-Duval, A. S.; Misra, S. K.; Mukherjee, P.; Johnson, E.; Acerbo, A. S.; Pan, D. An Anisotropic Propagation Technique for Synthesizing Hyperbranched Polyvillic Gold Nanoparticles. *Nano Res.* **2016**, 1–15.

(19) Yan, J.; Hu, C.; Wang, P.; Zhao, B.; Ouyang, X.; Zhou, J.; Liu, R.; He, D.; Fan, C.; Song, S. Growth and Origami Folding of DNA on Nanoparticles for High-Efficiency Molecular Transport in Cellular Imaging and Drug Delivery. *Angew. Chemie* **2015**, *127* (8), 2461–2465.

(20) Ding, Y.; Jiang, Z.; Saha, K.; Kim, C. S.; Kim, S. T.; Landis, R. F.; Rotello, V. M. Gold Nanoparticles for Nucleic Acid Delivery. *Mol. Ther.* **2014**, *22*, 1075–1083.

(21) Ghosh, P.; Han, G.; De, M.; Kim, C.; Rotello, V. Gold Nanoparticles in Delivery Applications☆. *Adv. Drug Deliv. Rev.* **2008**, *60* (11), 1307–1315.

(22) Pan, D.; Pramanik, M.; Wickline, S. A.; Wang, L. V.; Lanza, G. M. Recent Advances in Colloidal Gold Nanobeacons for Molecular Photoacoustic Imaging. *Contrast Media Mol. Imaging* **2011**, *6* (5), 378–388.

(23) Alric, C.; Taleb, J.; Duc, G. Le; Mandon, C.; Billotey, C.; Meur-Herland, A. Le; Brochard, T.; Vocanson, F.; Janier, M.; Perriat, P.; et al. Gadolinium Chelate Coated Gold Nanoparticles As Contrast Agents for Both X-Ray Computed Tomography and Magnetic

Resonance Imaging. *J. Am. Chem. Soc.* **2008**, *130* (18), 5908–5915.

(24) Cheheltani, R.; Ezzibdeh, R. M.; Chhour, P.; Pulaparthi, K.; Kim, J.; Jurcova, M.; Hsu, J. C.; Blundell, C.; Litt, H. I.; Ferrari, V. A.; et al. Tunable, Biodegradable Gold Nanoparticles as Contrast Agents for Computed Tomography and Photoacoustic Imaging. *Biomaterials* **2016**, *102*, 87–97.

(25) Huang, X.; Jain, P. K.; El-Sayed, I. H.; El-Sayed, M. A. Plasmonic Photothermal Therapy (PPTT) Using Gold Nanoparticles. *Lasers Med. Sci.* **2008**, *23* (3), 217–228.

(26) Rengan, A. K.; Bukhari, A. B.; Pradhan, A.; Malhotra, R.; Banerjee, R.; Srivastava, R.; De, A. In Vivo Analysis of Biodegradable Liposome Gold Nanoparticles as Efficient Agents for Photothermal Therapy of Cancer. *Nano Lett.* **2015**, *15* (2), 842–848.

(27) Mukherjee, P.; Misra, S. K.; Gryka, M. C.; Chang, H.-H.; Tiwari, S.; Wilson, W. L.; Scott, J. W.; Bhargava, R.; Pan, D. Tunable Luminescent Carbon Nanospheres with Well-Defined Nanoscale Chemistry for Synchronized Imaging and Therapy. *Small* **2015**, *11* (36), 4691–4703.

(28) Selvi, B. R.; Jagadeesa, D.; Suma, B. S.; Nagashankar, G.; Arif, M.; Balasubramanyam, K.; Eswaramoorthy, M.; Kundu, T. K. Intrinsically Fluorescent Carbon Nanospheres as a Nuclear Targeting Vector: Delivery of Membrane-Impermeable Molecule to Modulate Gene Expression In Vivo. *Nano Lett.* **2008**, *8* (10), 3182–3188.

(29) Ray, S. C.; Saha, A.; Jana, N. R.; Sarkar, R. Fluorescent Carbon Nanoparticles: Synthesis, Characterization, and Bioimaging Application. *J. Phys. Chem. C* **2009**, *113* (43), 18546–18551.

(30) Misra, S. K.; Ostadhossein, F.; Daza, E. A.; Johnson, E.; Pan, D. Hyperspectral Imaging Offers Visual and Quantitative Evidence of Drug Release from Zwitterionic-Phospholipid-Nanocarbon When Concurrently Tracked in 3D Intracellular Space. *Adv. Funct. Mater.* **2016**.

(31) Vulugundam, G.; Misra, S. K.; Ostadhossein, F.; Schwartz-Duval, A. S.; Daza, E.; Pan, D. (-)/(+)-Sparteine Induced Chirally-Active Carbon Nanoparticles for Enantioselective Separation of Racemic Mixtures. *Chem. Commun.* **2016**, *52*, 7513–7516.

(32) Ostadhossein, F.; Misra, S.; Mukherjee, P.; Ostadhossein, A.; Daza, E.; Tiwari, S.; Mittal, S.; Gryka, M. C.; Bhargava, R.; Pan, D. Defined Host-Guest Chemistry on Nanocarbon for Sustained Inhibition of Cancer. *Small* **2016**.

(33) Misra, S. K.; Ohoka, A.; Kolmodin, N. J.; Pan, D. Next Generation Carbon Nanoparticles for Efficient Gene Therapy. *Mol. Pharm.* **2015**, *12* (2), 375–385.

(34) Du, D.; Zou, Z.; Shin, Y.; Wang, J.; Wu, H.; Engelhard, M. H.; Liu, J.; Aksay, I. A.; Lin, Y. Sensitive Immunosensor for Cancer Biomarker Based on Dual Signal Amplification Strategy of Graphene Sheets and Multienzyme Functionalized Carbon Nanospheres. *Anal. Chem.* **2010**, *82* (7), 2989–2995.

(35) Ringe, E.; Langille, M. R.; Sohn, K.; Zhang, J.; Huang, J.; Mirkin, C. A.; Van Duyne, R. P.; Marks, L. D. Plasmon Length: A Universal Parameter to Describe Size Effects in Gold Nanoparticles. *J. Phys. Chem. Lett.* **2012**, *3* (11), 1479–1483.

(36) Misra, S. K.; Chang, H.-H.; Mukherjee, P.; Tiwari, S.; Ohoka, A.; Pan, D. Regulating Biocompatibility of Carbon Spheres via Defined Nanoscale Chemistry and a Careful

Selection of Surface Functionalities. *Sci. Rep.* **2015**, *5*, 14986.

(37) Daza, E. A.; Misra, S. K.; Scott, J.; Tripathi, I.; Promisel, C.; Sharma, B. K.; Topczewski, J.; Chaudhuri, S.; Pan, D. Multi-Shell Nano-CarboScavengers for Petroleum Spill Remediation. *Sci. Rep.* **2017**, *7*, 41880.

(38) K.S., U. S.; K., G.; V., G. K.; D., P.; C., A.; T., S. D.; V., K.; Changmai, N. Anti-Proliferative Effect of Biogenic Gold Nanoparticles against Breast Cancer Cell Lines (MDA-MB-231 & MCF-7). *Appl. Surf. Sci.* **2016**, *371*, 415–424.

(39) Gartia, M. R.; Misra, S. K.; Ye, M.; Schwartz-Duval, A. S.; Plucinski, L.; Zhou, X.; Kellner, D.; Labriola, L. T.; Pan, D. Point-of-Service, Quantitative Analysis of Ascorbic Acid in Aqueous Humor for Evaluating Anterior Globe Integrity Manas R. *Sci. Rep.* **2015**.

(40) Maeda, H. Macromolecular Therapeutics in Cancer Treatment: The EPR Effect and beyond. *J. Control. Release* **2012**, *164* (2), 138–144.

(41) Jaeger, H. M.; Nagel, S. R. Physics of the Granular State - ProQuest http://search.proquest.com/openview/8d32d53c48728c08c7e2648b2f1909b9/1?pq-origsite=gscholar (accessed Feb 10, 2016).

(42) Scott, G. D.; Kilgour, D. M.; D, B. J.; L, B. J. D. and F. J.; L, M. P. C. and W. E.; K, R. O.; R, R.; D, S. G.; D, S. G.; D, S. G.; et al. The Density of Random Close Packing of Spheres. *J. Phys. D. Appl. Phys.* **1969**, *2* (6), 311.

(43) Hunter, R. J. *Zeta Potential in Colloid Science: Principles and Applications*; Academic Press, 2013.

(44) Riddick, T. M. *Control of Colloid Stability through Zeta Potential*; Livingston Pub. Co:

Wynnewood, Pa., 1968.

(45) Alkilany, A. M.; Murphy, C. J. Toxicity and Cellular Uptake of Gold Nanoparticles: What We Have Learned so Far? *J. Nanoparticle Res.* **2010**, *12* (7), 2313–2333.

(46) Liu, Y.; Shipton, M. K.; Ryan, J.; Kaufman, E. D.; Franzen, S.; Feldheim, D. L. Synthesis, Stability, and Cellular Internalization of Gold Nanoparticles Containing Mixed Peptide-Poly(ethylene Glycol) Monolayers. *Anal. Chem.* **2007**, *79* (6), 2221–2229.

(47) Jana, N. R.; Gearheart, L.; Murphy, C. J. Seeding Growth for Size Control of 5−40 Nm Diameter Gold Nanoparticles. *Langmuir* **2001**, *17* (22), 6782–6786.

CHAPTER 6: CONCLUSION

Throughout this thesis, we have opened a discussion of the complexities that arise upon using modern-day treatments for common diseases. Unfortunately, contemporary medicine is still imperfect and has plenty of room for improvement. After a thorough literature review, we have reason to believe that nanotechnology can be a beacon for innovative treatment solutions and diagnostic measures to enhance modern medicine. However, multiple barriers, such as issues with biocompatibility, targeting, and retention, all contribute to the overarching theme of poor delivery efficiency and slow the adoption of nanotechnology.

Within this investigation, we addressed the profound issue of nano-delivery efficiency. We researched and developed an innovative packaging mechanism using inverted micelle self-assembly to encapsulate agents, which was followed by lipid wrapping for biocompatible use in systemic applications. This simple, 2-step nanoencapsulation technique was tested against an assortment of molecular structures and material compositions ranging from inorganic ions to organic nanoparticles. With each new encapsulated agent, the NCAP was thoroughly characterized for size, stability, structure, encapsulation efficiency, and release profile. These tests were used to verify the NCAP's versatility as a universal and robust encapsulation platform for nano-delivery.

Then, to apply this technique at the biological level, we thoroughly tested the NCAP in applications ranging from imaging to therapy, or both, and for treatment of diseases from cancer to bacterial infections. The experiments with NCAPs were carried out *in vitro* to understand their interactions in a biological setting; some were also followed by *in vivo* experiments to evaluate their clinical potential.

Within our first investigation, we used the nanocapsulation of Cs^+ ions to test the highly theorized concept of "high-pH therapy" with CsCl supplementation, as well as other possible

mechanisms initiated via *in vitro* and *in vivo* CsCl delivery. Our investigations showed that neither the extracellular delivery of CsCl nor the intracellular delivery if Cs^+ ions (facilitated by NanoCs) affected intracellular pH, thus disproving the "high-pH therapy." Furthermore, extracellular delivery of CsCl did not initiate programmed cell death. Instead, we found that the internalization of Cs^+ ions via NanoCs limits glucose internalization, which can function as an alternative mechanism for cancer therapy. These findings were gathered using fluorescently labeled glucose and ROS assays to monitor cellular starvation and cellular initiated apoptosis. *In vivo* studies showed that xenograft tumors grown in nude mice regressed to a statistically significant level after intratumorally injection of NanoCs, as compared to controls.

To expand our investigations into other disease types, we demonstrated a combinatorial approach for bactericidal applications that uses the physically destructive properties of Ag^+ ions combined with a prodrug derivative of the popular antibiotic drug, levofloxacin. This combined approach is strengthened by jointly delivering Ag^+ ions and levofloxacin directly to the bacterial cell wall. Thorough quantification showed that the combinatorial effects of Ag^+ ions and the levofloxacin prodrug in the AI-Pro-NPs are additive and yield higher toxicity than each constituent alone. After analyzing the integrity of the bacterial DNA and proteins, we showed that the AI-Pro-NPs exhibited further antibacterial effects at the molecular level. Furthermore, we visualized the effective antibacterial properties of Ag^+ delivered by the AI-NPs with bacterial TEM, which confirmed the bacterial cell wall was, in fact, compromised. Finally, live/dead assays confirmed that the combinatorial AI-Pro-NPs had a powerful antibacterial outcome as compared to Ag^+ ions or the prodrug alone.

To delve into more complex molecular structures, we propagated the encapsulation of multiple dyes and the chemotherapeutic drug doxorubicin and tested their intracellular delivery

capabilities on the metastatic breast cancer cell line, MCF-7. Through quantitative and visual data, we then compared the NCAPs' cellular interactions with those of the commonly used liposome nanoparticles. Flow cytometry experiments indicated that the NCAPs were 69.93% more effective at labeling MCF-7 cells over liposomes, whereas confocal-based imaging and live video recordings detailed the NCAPs interactions at the cellular level.

Finally, we pushed the inverted micelle's encapsulation limits by assessing its high-throughput encapsulation and delivery of <10 nm organic carbon nanoparticles and inorganic gold nanoparticles. Our aim was to alleviate the common complications associated with cellular uptake due to size restrictions and systemic clearance. We found that NMCs led to a significantly larger quantity of internalized AuNPs as measured by TEM micrographs. Similarly, the NMC-facilitated delivery of spectroscopically active CNPs led to a higher degree of intracellular CNP fluorescence, as measured by Raman imaging, while control CNP samples accumulated at the cell's perimeter.

Final Note

In short, by completing these scientific investigations, we have created a novel nanoarchitecture and tested its compatibility with a range of chemically and structurally diverse theranostic agents. Furthermore, we have determined that this nanoarchitecture is appropriate for delivering theranostic agents to target cells and we have evaluated that the encapsulated agents are effective at enhancing their intended biological effects as compared to their un-encapsulated counterparts. Thus, we have seen that in the field of nanoparticle delivery, the use of inverted micelles has shown much promise for robust encapsulation efficiency.

Further investigations are warranted for the NCAP material and biological capabilities and applications. For example, this nanoarchitecture can be used to entrap materials other than those

tested here, such as biological matter or radiolabeled compounds. More combinatorial studies should also be performed, given the NCAP's potential to upgrade this novel delivery platform towards a multifunctional, all-purpose theranostic solution. Finally, the NCAPs' long-term effects and biodistribution properties *in vivo* must be established before its translation into clinical use.

The field of nano-based medicinal treatments is looking bright as indicated by the 51 FDA-approved nanomedicines. Furthermore, 77 products are currently in clinical trials, with ~40% of trials listed in clinicaltrials.gov started in 2014 or 2015.[1] This glimpse of nanoparticles in medicine offers evidence that there has been an increase in FDA approvals and clinical trials using nanoparticles over the past three years. There has also been an increase in the complexity and variety of particles used. Bobo et al.[1] predict that this trend will continue, and our NCAP design is apt to take advantage of the new era in theranostic nanodelivery.

References to Conclusion

(1) Bobo, D.; Robinson, K. J.; Islam, J.; Thurecht, K. J.; Corrie, S. R. Nanoparticle-Based Medicines: A Review of FDA-Approved Materials and Clinical Trials to Date. *Pharm. Res.* **2016**, *33* (10), 2373–2387.